Frequency Modified Feedback in External Cavity Semiconductor Laser Systems

Yoann Noblet

Department of Physics and SUPA, University of Strathclyde

Department of Physics and Astronomy, Macquarie University

A mes parents

Abstract

This thesis presents work done on two external cavity semiconductor laser systems with different types of frequency modified feedback. The first system, based on a vertical-cavity surface-emitting laser (VCSEL) with feedback from a volume Bragg grating, is used to investigate the control of laser cavity solitons (LCSs). The temporal dynamics of a second system, relying on an edge-emitting semiconductor laser (EEL) with frequency-shifted feedback (FSF), is investigated.

LCSs are trapped in local minima of a disorder potential landscape which is created by the growth induced inhomogeneities of the cavity resonance. The positions, frequencies and thresholds of the LCSs are dictated by the disorder and as a result LCSs appear at certain locations in the VCSEL aperture. These properties are used to demonstrate a method to quantitatively characterize the disorder in a VCSEL with frequency-selective feedback.

LCSs, as any laser, have the freedom to choose their optical phase. The effects of disorder on the interaction of two LCSs are considered. We demonstrate frequency and phase synchronization of paired LCSs as their relative detuning is varied. In both theory and experiment the locking behavior is well described by the Adler model for the synchronization of coupled oscillators.

In the case of the second system, dynamics of the output of an EEL with FSF is systematically and comprehensively measured for the first time. Three fundamentally different regimes of operation are identified corresponding to low, medium and high levels of FSF. Low levels of FSF cause the emission spectrum to broaden. Medium levels of FSF are consistent with those found in semiconductor with conventional feedback systems. High levels of FSF result in periodic oscillations on a cw baseline which is similar to the pulsed comb of mode output observed in analogous FSF systems using solid state gain media when the FSF is resonant.

Acknowledgements

Thanks to my lab partner Jesus, also called Jay, for being friendly, supportive and very humble. Thanks to you, things are running very smoothly in the lab, I wish you the best with your PhD pal.

Thanks also to my flatmates in Glasgow, past and present; Pier-Francesco Caponi, Caroline, Hannah Louise Bailey, Johannes, Panchito, Ellie, Paul, Eleanor, Simona and Matt. You guys made my time in Glasgow really enjoyable, and f***, it feels good to be looking forward to going back home after work! So thank you guys for that, you all rock.

Next is a big thank you to the Sydney crew; Felix wouaaa Timmy, Philipp you're the worst character ever, Zach awesome-o, Jon, Sam, Lydia, Florian, Agathe, Marcello, Tammy, Jess, Julien and Valentine.

Thank you Zoe and Jan for making feel part of your family, you made my time in Sydney very enjoyable and I don't recall being homesick while living in Australia!

Thank you David for being so welcoming with new students. I think many people will agree with me here, you're the coolest dude in the physics department, at least you used to be since you moved to engineering. Thanks for showing me around during my time in Sydney and thank you for being my basketball buddy for the last year. I hope you manage to bring Roger's team to the top so when I come back we'll have a proper opposition!

How could I not mention my basketball friends from Glasgow. I have played with many players in different countries at different levels but Tinashe you're definitely one of the best players I've ever played with! Thank you to Kostas, Nikos, Lucio, Eric, Kokou and Mo. Mo I'm now ready to hit the courts again so you better bring your A game next time I see you!

Thanks to all the poker players I've stolen money from in the last 3 years; Loyd, Daniele, Colin, Ben, Pim, David, Louis and Jeff.

Thank you Prof. Griffin, you're now the only one who has been around since my undergraduate degree. Well done pal. Thanks for your feedback, it was needed. Let's face it, you're the only one who can speak proper English in the office! You rock dude.

Un petit merci des familles à cette vérole de Marconi qui peut pas se passer de la ramener en permanence à propos de ses solitons de merde dans sa cavité

pourrie. T'as eu la bonne idée de venir passer un peu de temps dans le froid a Glasgow, j'ai adoré !! Du coup dans le même paragraphe on retrouve ce bon vieux François Gustave qui est quand même different du Marconi il faut l'avouer, un Marconi amélioré ? Un vrai bon gars pour sûr, merci d'être venu à Glasgow passer quelques semaines, c'était le top.

A ton tour Matt, tu vas pas t'en tirer comme ça mon grand ! Ton nom ne ressemble pas à une marque de détergent mais c'est tout comme ! En gros si je suis en train d'écrire tout ça, là maintenant c'est en grande partie à cause (ou grâce c'est au choix) de toi... Et oui, si t'étais pas resté à Glasgow après ton doctorat je sais pas si j'aurais commencé le mien. Tellement de chose je pourrais dire, à commencer par expliquer pourquoi je commence à formuler mes phrases comme Yoda mais ça on reviendra pas dessus. En gros merci et merci et encore merci, cette thèse c'est aussi un peu la tienne mec !

Merci à Victor pour m'avoir donné du boulot quand c'était un peu calme au labo. J'adore ton jeu de basket !

Merci à tous mes amis d'enfance; Poulet, Wiwi, Charlot, Marcel, Lolivier et cette vérole de Mathieu qui n'a pas de surnom... On a pas eu beaucoup l'occasion de se voir durant ces 6 dernières années et plus particulièrement les 2 dernières. C'est la qualité qui compte pas la quantité, hein Wiwi ?

J'aimerais remercier ma famille et particulièrement mes sœurs et mes parents pour leur soutient et pas seulement pendant cette thèse. Je ne pensais pas arriver si loin et surtout avoir la chance de travailler dans un domaine qui me passione, merci. Merci de m'avoir laissé partir si tôt en Ecosse, ça n'a pas été facile tous les jours mais au final le jeu en valait la chandelle ! Merci pour tout, encore. Je souhaite la bienvenue a mon neveu Quentin, à un jour près tu n'y étais pas ! Je n'oublie pas ma petite nièce Madeline que j'ai vu grandir pendant ma thèse, merci de m'avoir fait tant rire.

Finally I would like to thank Lauren for her support during the last 18 months. You've been the only thing I was looking forward to after a long day in the lab. Without your support I would have been completely insane by the end of this PhD. Thank you for showing me around your beautiful country, I really had a blast, and clearly, I look forward to sharing new adventures with you.

Publications and Conference Presentations

Publications

- Y. Noblet and T. Ackemann, *Analysis of spatial emission structures in vertical-cavity surface-emitting lasers with feedback from a volume Bragg grating*, Physical Review A **85**, 053812 (2012).

- P. V. Paulau, C. McIntyre, Y. Noblet, N. Radwell, W. J. Firth, P. Colet, T. Ackemann, and G-L. Oppo, *Adler synchronization of spatial solitons pinned by defects*, Physical Review Letters **108**, 213904 (2012).

- T. Ackemann, N. Radwell, Y. Noblet, and R. Jäger, textitDisorder mapping in VCSELs using frequency-selective feedback, Optics Letters **37**, 1079 (2012).

- J. Jimenez, Y. Noblet, P. V. Paulau, D. Gomila, and T. Ackemann, *Observation of laser vortex solitons in a self-focusing semiconductor laser*, Journal of Optics **15**, 044011 (2013).

- T. Ackemann, Y. Noblet, P. V. Paulau, C. McIntyre, P. Colet, W. J. Firth, and G-L. Oppo, *Frequency and phase locking of laser cavity solitons*, in *Spontaneous Symmetry Breaking, Self-Trapping, and Josephson Oscillations*, pp. 49-87, Springer 2013.

Conference Presentations

- Y. Noblet and T. Ackemann, *Analysis of pattern formation in vertical-cavity surface-emitting lasers with feedback of a volume Bragg grating*, in *European Quantum Electronics Conference*, Optical Society of America, 2011.

- Y. Noblet, P. V. Paulau, C. McIntyre, W. J. Firth, P. Colet, G-L. Oppo, and T. Ackemann, *Adler synchronization of spatial laser solitons pinned by defects*, in *Nonlinear Photonics*, Optical Society of America, 2012.

- Y. Noblet, J. P. Toomey, and D. M. Kane, *Dynamics of a semiconductor laser with frequency shifted feedback*, in *SPIE OPTO*, International Society for Optics and Photonics, 2014.

Contents

List of Figures

List of Tables

Chapter 1

Introduction

Semiconductor lasers have become ubiquitous in application in the last few decades. Their size, cost, efficiency and reliability make them attractive in many applications such as optical data communications, medicine, sensors or optical storage systems. They are very versatile and can be designed to operate over a broad range of wavelengths from the ultraviolet [1, 2] up to a few microns [3]. Despite the fact that from a dynamical point of view, semiconductor lasers can be considered as stable class-B lasers, they are easily affected by external perturbation. Since the pioneering work of Lang and Kobayashi [4] a good deal of attention has been paid to the modeling of feedback effects on the dynamics of semiconductor lasers [5]. Such devices constitute a hotbed of creativity in which to explore temporal dynamics via countless external cavity configurations that one can think of to alter the operation of the laser.

The effects of conventional optical feedback in semiconductor lasers have been well documented and under certain conditions, i.e. very high levels of optical feedback, it is possible to achieve stabilization of the laser [4]. It was soon discovered that the single mode stabilization of the laser could be enhanced by the substitution of the plane mirror by a frequency selective element in the external cavity [6, 7]. Such a configuration is also known to greatly reduce the linewidth of the laser emission and is therefore widely used in spectroscopy [8] and optical telecommunication [9]. This scheme caught a lot of additional attention when it was discovered that it could support bistability [10, 11]. The subsequent experiments were naturally oriented towards the implementation of a vertical-cavity

surface-emitting laser (VCSEL) with frequency selective feedback. VCSELs are capable of supporting many transverse modes and the addition of a diffraction grating in an external cavity configuration can provide transverse mode control [12]. This system was then regarded as a means of creating cavity solitons (CSs) when it was discovered that such a scheme could support bistability between lasing and non-lasing states close to threshold [13]. Due to their mobility and bistable nature CSs would be good candidates for optical memory applications [14, 15] and all-optical delay lines [16].

The first semiconductor system capable of supporting CS was demonstrated in a VCSEL with an externally injected laser beam to support bistability [17]. This experiment demonstrated that CSs could be created and individually switched on and off by external injection. However, some drawbacks were rapidly identified and particularly the reliance on external injection as a mechanism to support bistability. This means that the polarization, phase and frequency of the CS is locked to that of the holding beam. The idea of creating CS in a system that does not rely on external injection to sustain bistability emerged shortly after and laser cavity solitons (LCSs) were born [18]. The first demonstration of LCSs was performed in a broad area VCSEL with a diffraction grating as the frequency selective element [18]. LCSs, in common with other lasers, are free to choose their own optical phase and additionally, if the system is isotropic, they have the freedom in their polarization and frequency (within the limitations imposed by the cavity resonances of the laser and the reflection bandwidth of the diffraction grating). This presents new opportunities for fundamental studies of LCSs and particularly interaction between them.

In the first part of this thesis I present a demonstration of phase and frequency locking of two LCSs. The system is based on a broad area VCSEL with feedback from a volume Bragg grating [19]. Preliminary results showed that such a system can sustain LCSs and, more importantly, that under favorable conditions LCSs can lock in phase and frequency [20]. Due to their intrinsic properties LCSs are mutually incoherent, i.e. they are independent microlasers. However, under certain conditions the interaction of two LCSs leads to synchronization due to phase and frequency locking. In a broader picture, where thousands of LCSs

could potentially be synchronized in the same device, it could open the door to network synchronization in a fruitful analogy with brain activity [21].

In this experiment, frequency selective feedback is used to support bistability close to threshold in an external cavity VCSEL. The external cavity allows the LCSs to lase on several external cavity modes which is a prerequisite for mode-locking. Interesting temporal dynamics in such a system have been investigated in [20]. It was discovered that under favorable conditions LCSs could mode-lock. However, this was observed in a parameter space where LCSs were not bistable, i.e. the VCSEL was operated at an injection current above the bistability curve of the LCSs. The observation of such pulses is nevertheless promising and the generation of pulsed LCSs could potentially lead to 3D solitons (2 dimensions in space and 1 dimension in time). Self-localized states in all 3 dimensions can be regarded as light bullets [22, 23] and received a lot of attention [24, 25, 26]. The main limitation for observing pulsed LCSs comes from the scheme used to support bistability. Regardless of the gain medium, frequency selective feedback is not known to achieve mode-locking, and therefore, a second external cavity scheme was studied.

The second part of this thesis deals with frequency shifted feedback (FSF). This has been used with different laser systems since the late eighties [27, 28, 29]. An FSF laser system is a gain cavity in which a frequency shifting element has been introduced. This is commonly achieved by closing the cavity on the first order diffracted beam of an acousto optic modulator (AOM). Soon after their discovery, FSF laser systems showed interesting temporal behavior and particularly the observation of short pulses in a dye laser system [30, 31]. Short pulses were later reported in fiber laser based FSF systems [29, 32] and recent studies reported the generation of picosecond pulses in Er:fiber lasers [33, 34, 35]. Despite their large gain bandwidth, it is difficult to generate pulses shorter than a picosecond with semiconductor lasers when using conventional mode-locking techniques [36]. However, the potential of mode-locked semiconductor lasers remains attractive for optical communication purposes [36, 37, 38].

The FSF external cavity setup used in this thesis is based on a quantum-well, Fabry-Perot cavity, edge emitting semiconductor laser. The temporal dynamics of such a system have never been analyzed in detail and the few reports available on

the subject belong to the last century when multi-GHz bandwidth oscilloscopes and convenient computer controlled experiments were not available. In the second part of this thesis I report the systematic study of the nonlinear dynamics of a semiconductor laser with FSF. Dynamical maps and more particularly maps of a complexity measure, the permutation entropy, have been recently generated for a similar semiconductor laser with conventional optical feedback [39]. These maps provide the necessary information to allow the difference between conventional optical feedback and FSF to be completed once a similarly comprehensive set of maps is generated for an FSF system. The results reported in this thesis focus on both the near resonance of the external cavity frequency case and the non-resonant case. The former has the potential to generate pulsed output from the system [30, 31] but this has never been demonstrated in a semiconductor laser based FSF system.

In Chapter 2 I will introduce the relevant background topics such as semi-conductor lasers, frequency selective feedback leading to the creation of cavity solitons in VCSELs as well as an overview of frequency shifted feedback laser based systems. The properties of the devices and equipment used in the experimental setup utilized to generate LCSs will be described in Chapter 3.

The spatial and spectral properties of a broad-area VCSEL with frequency-selective feedback by a volume Bragg grating will then be addressed in Chapter 4. The effects of the deviations from the self-imaging will be investigated and particularly how the pattern formation is affected by these deviations. A technique to map the variations in the cavity resonance of the VCSEL will also be introduced.

The interaction of two LCSs pinned by the defects induced by the variations in the cavity resonance of the device will be explored in Chapter 5. We will see that despite their mutual incoherence, the interaction of LCSs can lead to synchronization due to phase and frequency locking with strong similarities to the Adler-scenario of coupled oscillators.

The second experimental system based on frequency shifted feedback will be explored in Chapter 6. The dynamics of the output of an edge emitting semiconductor laser are measured and high resolution maps will be used to investigate the temporal and spectral behavior of the output power of the nonlinear system.

The results will be then contrasted with those from conventional semiconductor laser with optical feedback systems.

I will then conclude the thesis with a brief summary, together with some suggestions for future work to be conducted on LCSs and semiconductor laser based FSF systems. I will also discuss the possibility of tying together spatial and temporal dynamics in the same system.

Chapter 2

Background

2.1 Semiconductor Lasers

2.1.1 Principle

In the last few decades semiconductor lasers have become the most common type of laser. Nowadays they represent 50% of the global laser market in monetary term and about 95% of lasers sold in number [40]. There are many reasons why semiconductor lasers have become so popular. They are very compact, efficient, reliable, electrically pumped and inexpensive to produce, just to name a few. They find applications in medicine, optical data communications, optical storage devices, optical pumping of solid state lasers and many more.

The conductivity of the material used to make a semiconductor laser lies between a isolator and a conductor, hence the designation semiconductor. The simplest principle of operation of a semiconductor laser relies on a p-n junction, i.e. a combination of two semiconductor materials. The conductance can be modified by adding donors or acceptors to the material. When donors, i.e. atoms providing electrons, are added into the semiconductor material, the latter becomes n-doped and inversely when acceptors, i.e. atoms providing holes, are added into the material, it becomes p-doped. When both materials, i.e. p-doped and n-doped, are positioned next to each other, a p-n junction is formed.

Thermal equilibrium of the p-n junction, i.e. the Fermi energy level is constant throughout the junction, is obtained when no voltage is applied across the
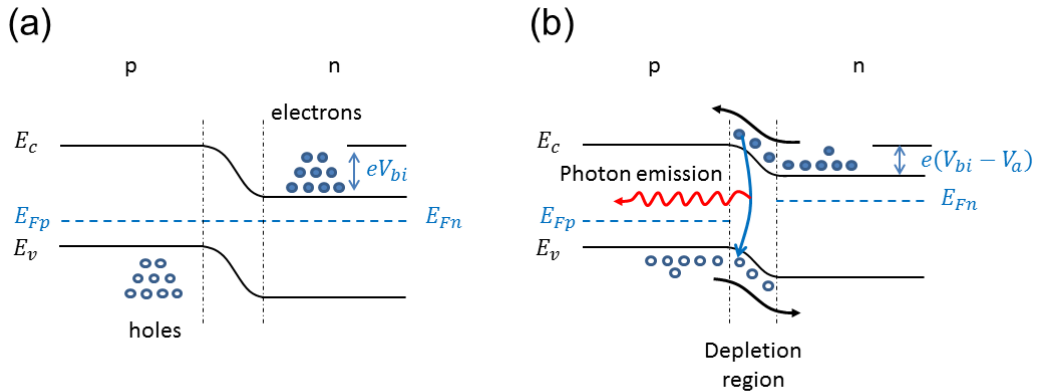
Figure 2.1: A p-n junction and its associated energy band diagram for (a) zero bias and (b) forward bias. E_{Fp} is the Fermi level of the p-type material and E_{Fn} is the Fermi level of the n-type material. E_c is the conduction band and E_v is the valence band. V_{bi} is the built in potential barrier and V_a is the positive voltage applied to the p region with respect to the n region.

junction. Because the relative position of the conduction and valence bands with respect to the Fermi energy varies between p and n regions, these bands must bend in the space charge region as illustrated Fig. 2.1(a). This implies that a large potential V_{bi} is seen by the electrons at the interface of the junction thus preventing any electron-hole recombination [41]. However, when a forward bias voltage V_a is applied to the junction, the Fermi levels become separated by the energy bandgap of the semiconductor material as seen in Fig. 2.1(b). This causes the valence and the conduction bands to bend in a small region called the depletion region where the donors and acceptors can now recombine due to the lower potential seen by the electrons at the interface of the junction. Spontaneous emission arises from the radiative recombination process and it generates photons with an energy corresponding to the energy bandgap of the semiconductor material.

Even if the first experimental demonstration of coherent light emission from a p-n junction has been established more than 50 years ago [42, 43, 44], this gain medium configuration does not form an efficient semiconductor laser. It requires extremely high currents and low temperatures in order to reach lasing threshold.

For that matter this configuration is now only used for Light Emitting Diodes (LED). These considerations led, a few years later, to the development of the double-heterostructure [45], which made cw, coherent emission possible at room temperature. A double-heterostructure design consists of two semiconductor materials with different bandgaps. A smaller bandgap material, i.e. the active layer, is effectively sandwiched between two larger bandgap materials. This means that the carriers are confined in the active layer region thus enabling greater population inversion than in a single-heterostructure configuration. Additionally, the refractive index of the active layer is larger than that of the outer layers thus providing a top-hat refractive index profile similar to what is used in optical fibers to achieve optical confinement, i.e. waveguiding. This leads to a threshold reduction such that lasing can be achieved at room temperature. Even though this configuration allows coherent emission at room temperature, nowadays most semiconductor lasers use quantum wells (QW) as the gain medium.

A quantum well is formed in a double-heterostructure laser when the thickness of the active layer is less than the de-Broglie wavelength ($\lambda \approx h/p$) of the carriers. This means that the energy states available for the carriers become discrete and as a result less electron-hole pairs are required in order to achieve lasing. This results in higher gain, higher quantum efficiency and lower lasing threshold. Due to its high efficiency, the double-heterostructure QW design is now commonly used in modern semiconductor lasers.

As with any laser, semiconductor lasers require stimulated emission in order to achieve coherent emission. In a conventional laser this is usually done by placing the gain medium in a cavity formed by high reflectivity, i.e. >99 %, mirrors. However, due to the relatively small size of semiconductor lasers, i.e. typically 100 μm × 200 μm × 50 μm, it is not desirable to implement conventional mirrors in the cavity design. Instead the Fresnel reflection at the interface between the gain medium material (high refractive index) and air (low refractive index) will often suffice to obtain reflectivities which are high enough to achieve lasing. However, if lower losses are required it is possible to achieve higher efficiency by coating the facets of the device with a high reflectivity coating.

2.1.2   Edge Emitting Lasers

Edge emitting semiconductor lasers (EELs) became popular in the early development of semiconductor laser and nowadays this design still remains widely used in many applications. A basic schematic diagram of an EEL design is shown in Fig. 2.2. Layers of n-doped semiconductor material are grown onto a substrate. The active region is sandwiched between n-doped and p-doped semiconductor layers and electrical contacts are coated on each side of the active region for pumping.

As observed in Fig. 2.2 the emission is parallel to the active region and is reflected or coupled out at the facets, i.e. cleaved edges, of the semiconductor material. EELs can exhibit a cavity, i.e. active region, length of a few hundred microns thus resulting in a high gain. This means that coherent emission is possible even when using uncoated facets with poor reflectivity (around 30% due to Fresnel reflection at the interface between the semiconductor material and air) accounting for high losses inside the resonator. The main advantage of this design is that gain can be increased either simply by increasing the length of the active region in the longitudinal direction and that losses can be reduced by applying a high reflectivity coating to the cleaved facets forming the cavity. However, increasing the cavity length will also cause more longitudinal modes to be supported by the cavity following the relationship L=q λ/2, where L is the cavity length, q is the number of modes supported by the cavity and λ is the emission wavelength.

The attractiveness of such devices comes from their compactness and makes them desirable for integration in optical networks for instance. However, this asset comes at a cost of a high beam divergence. Indeed, the small beam dimension in the direction orthogonal to the active region, i.e. around 1.5 μm, results in a beam divergence half-angle-cone at $1/e^2$ intensity point of about 20° in this direction. Similarly, the beam dimension in the plane parallel to the active region (about 6 μm) gives a divergence half-angle-cone at $1/e^2$ intensity point of about 5°. For this reason, EELs suffer from a high output beam asymmetry as illustrated in Fig. 2.2. The strong ellipticity of the beam (typically with a ratio 4:1 fast to slow axis) in both shape and divergence makes the implementation of such lasers

Electrical contact

p-Type

Active region

n-Type

Substrate
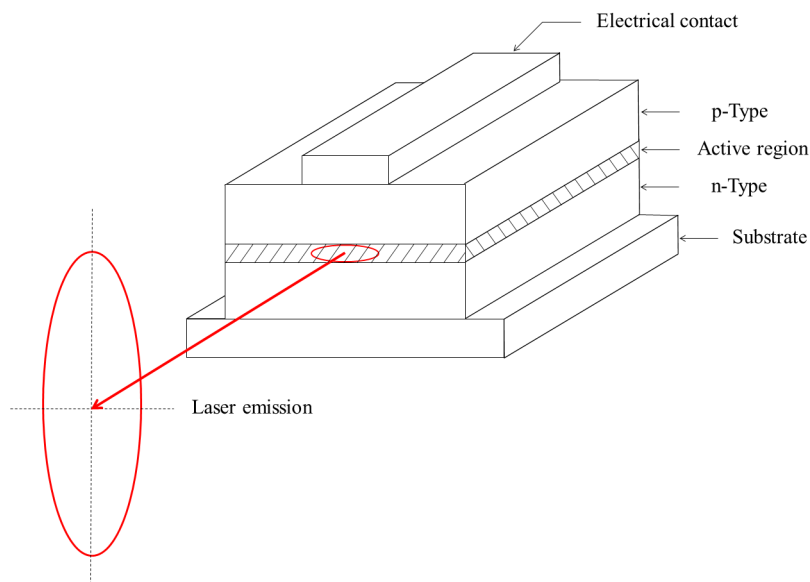
Laser emission

Figure 2.2: Schematic diagram of an edge emitting laser. The emission takes place in a plane parallel to the active region and as a result the shape of the output beam exhibits a strong ellipticity.

in communication systems not ideal despite their compactness. Indeed, optical fibers used in communication networks have circular cross sections and therefore the coupling efficiency strongly depends on the shape of the incoming beam. In addition to having a limited coupling efficiency, EELs also require a collimation optic with a high numerical aperture in order to achieve effective collimation with minimal losses.

2.1.3 Vertical Cavity Surface Emitting Lasers

Coherent emission in a plane perpendicular to the active region was first demonstrated in 1965 [46] however, vertical cavity surface emitting lasers (VCSELs) as we know them nowadays were demonstrated in the year 1990 by Iga [47, 48]. This revolutionary design combines the advantages of semiconductor lasers without the main limitation of EELs, i.e. their high beam divergence and ellipticity. The main difference between EELs and VCSELs lies in the emission direction, in
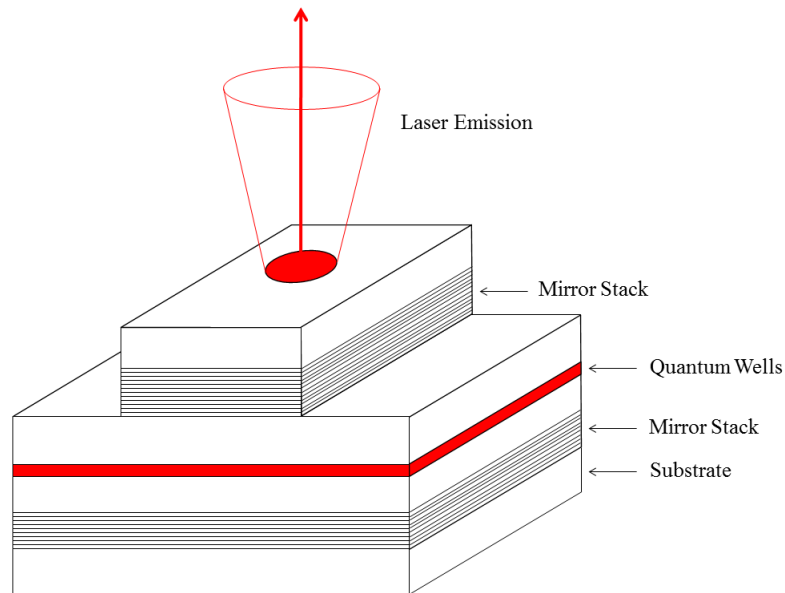
Figure 2.3:   Schematic diagram of a vertical cavity surface emitting laser. The emission takes place in a plane perpendicular to the active region.

a VCSEL the emission takes place in a perpendicular plane to the gain medium. A basic schematic diagram of a VCSEL design is shown in Fig. 2.3.

In addition to a very small beam divergence ($<5°$ for small circular single mode devices), VCSELs also provide advantages over conventional EELs. The fact the emission is perpendicular to the gain region allows the chips to be tested directly on the wafer in which they are grown as they do not require cleaving in order to achieve lasing. This design also allows the emission shape to be chosen by shaping the aperture to the required form. Due to their low beam divergence and the possibility to achieve a perfectly circular output beam, VCSELs are perfect candidates for fiber coupled telecommunication systems where compactness and high coupling efficiency is required.

However, VCSELs suffer from a very small gain. The length of the active region is very short (typically 1-3 λ where λ is the emission wavelength of the device) and therefore after a single roundtrip inside the cavity stimulated emission is less likely to occur. If with EELs lasing can be achieved with intra-cavity reflectivity around 30%, this is not the case with VCSELs where the small gain

due to the small cavity needs to be overcome to achieve coherent emission. This is done by using distributed Bragg reflectors (DBRs) which can achieve reflectivities up to 99.99%. Typically one side of the cavity has a reflectivity >99.9% while the outcoupling mirror has a reflectivity of about 99%. DBRs also have the advantage of being relatively easy to manufacture, they are made of $\lambda/4$ thick layers of alternating high and low index semiconductor material and can therefore be grown directly onto the device. With such high reflectivities greater gain can be achieved as the photon lifetime is increased and as a result the stimulated emission events are more likely to increase inside the cavity.

In VCSELs the dimensions of the gain region are somewhat fixed. Indeed, the length of the gain region in the direction perpendicular to the emission can not be increased as desired. This would lead to an increase of the number of transverse modes supported by the cavity and would thus degrade the beam shape quality of the device which is not desirable in most applications. However, in some cases such as cavity soliton generation, it is necessary to use broad area devices (>80 μm). In the direction parallel to the emission, the length of the gain region is also limited (typically 1 λ) so that single longitudinal mode operation is obtained. If the cavity length is increased, higher gain would be achieved but unwanted longitudinal modes would also be supported by the cavity thus eliminating one of the key advantages of VCSELs, their single longitudinal mode operation.

The short cavity length also accounts for small scattering and absorption losses in the active region which thus results in low threshold currents. The dimensions of the active region as well as the electrical injection are responsible for very low threshold currents in VCSELs. Indeed, the most effective technique to inject the current into the laser is achieved by the growth of oxide apertures into the structure of the device. This technique provides current confinement which induces better power conversion efficiency by focusing the carriers directly into the gain region thus avoiding diffusion through the device. Similarly to a double-heterostructure in an EEL, the oxide confinement provides optical guiding due to a high refractive index jump between the oxide aperture and the semiconductor material.

The main challenge when manufacturing VCSELs is to ensure that the wavelength selection of the gain region in the direction of the emission matches the peak of the reflection bandwidth of the DBRs. The second technological difficulty is to grow many layers of exactly $\lambda/4$ thickness to form the DBRs with high reflectivities. Because of the size restriction of the gain region, the output power of a single transverse mode VCSEL is rather low (a few milliwatts). However, due to their vertical geometry VCSELs are well suited for making large laser arrays capable of producing very high output power of up to a few kilowatts [49].

2.2 Frequency Selective Feedback

The effects of optical feedback on edge-emitting semiconductor lasers were investigated shortly after the first devices became available [50, 51]. A few years later the different behaviors were identified and a theoretical model for weak levels of feedback was introduced in the seminal experiment of Lang and Kobayashi [4]. Four regimes of operation were observed and classified depending on the feedback strength. Six years later Tkach et al. investigated the effect of high feedback levels on a 1.55 μm distributed feedback laser diode [52] and identified one particular regime which was described as regime V. This regime was found to stabilize single longitudinal mode operation of the laser regardless of the feedback phase, i.e. the length of the external cavity. In this particular regime the laser cavity acts as a small active section of a longer cavity closed by the external cavity reflector. A couple of years later it was found that the use of a dispersive element in the external cavity provides a more stable single mode operation of the laser along with a reduction of its linewidth [6, 7]. The highly coherent sources obtained via this technique are of particular interest in metrology [53], atomic physics [54] or optical telecommunication [55]. The first schemes relying on frequency selective feedback were based on a diffraction grating [6, 7], a narrow-band resonator [56], a fiber-Bragg reflector [57] or by using the transition lines of a medium inside the external cavity [58]. Due to its compactness and ease of implementation a diffraction grating constitutes a good candidate for frequency selective feedback in semiconductor lasers. In addition to greater stabilization, a frequency selective element such as a diffraction grating also provides fine frequency tuning, over a

wide range of a few tens of nm, of the laser emission [6, 7]. This configuration with EELs is however, not perfect and a few stability issues may arise such as multi-stability [7, 59, 60, 61] or mode hopping [62]. In particular bistability [10, 11] and low-frequency fluctuations [11, 60, 63] are commonly observed in such external cavity laser systems.

The bistability between different emission states found in such systems could be particularly interesting when observed in VCSELs. Their design provides strong frequency selective feedback (see Sec. 2.1.3) and as a result achieves single longitudinal mode operation. However, the addition of a diffraction grating can provide transverse mode control of the device [12]. The same scheme also demonstrated the ability of such a system to support bistability between lasing and non-lasing states close to threshold [13]. Since many transverse modes are supported in broad area VCSELs, bistability would provide a considerable asset in the excitation of spatially localized emission states, i.e. cavity solitons. Such self-localized lasing states would show great potential for information processing and particularly, due to their bistable nature and mobility, in all optical memory devices [14, 15] and in all-optical delay lines [16].

2.3 Solitons

2.3.1 History

A soliton is a solitary wave that travels without changing shape. Such a wave is formed when a fine balance of linear and non-linear effects occurs in the medium of propagation. The first observation of a solitary wave was reported by John Scott Russell in 1834 near Edinburgh in Scotland [64]. J. S. Russell was observing a boat in a canal when the vessel suddenly stopped. This caused the water accumulated at the front of the boat to form a wave of large elevation and velocity. He then followed the wave for a couple of miles along the canal without noticing any change of shape or diminution of speed. However, before losing the wave in the windings of the channel he noticed a slight diminution in its height. Russell called this phenomenon 'wave of translation'.

Russel tried to recreate this phenomenon in a tank of water and came to the conclusion that such a wave was a fundamental mode of propagation [65]. However, Russel's work failed to convince the scientific community. In particular Airy and Stokes questioned the existence of a wave that travels without changing shape above the water. Their main argument was based on the fact that the wave loses amplitude with time, which at the time they attributed as a sign that the wave was actually temporary. Russel contested these claims and attributed the diminution of amplitude to friction. It was only in the late 1870's that Russel's work was accepted and the theory describing waves in shallow water surfaces was finally demonstrated at the end of the century in 1895 by Korteweg and deVries [65].

Solitons can either be conservative or dissipative. In this section we will give a description of each category before introducing cavity solitons and cavity soliton lasers, which are different types of spatial dissipative solitons. We will here focus on optical solitons but solitons in other media such as water or plasma share similar properties.

2.3.2   Conservative Solitons

A conservative soliton is a solitary wave whose energy is conserved. In other words, the losses in the system are completely absent and the latter does not require any continuous energy input. Such solitons have been experimentally observed in systems where the losses were low enough for the solitons to be regarded as conservative [66, 67].

In optics conservative solitons exist when a fine balance of nonlinear and linear (diffraction for a spatial soliton and dispersion for a temporal soliton) effects occurs. In particular a spatial soliton is formed when the Kerr effect balances the effect of diffraction in the propagation medium. Indeed, when light propagates through a linear medium diffraction occurs, i.e. the light spatially spreads, it diverges. However, when light propagates through a nonlinear medium it can experience the so-called Kerr effect. The refractive index of this nonlinear medium is proportional to the intensity of the electric field passing through, i.e. $n = n_0 + n_2 I$, where n_0 is the linear refractive index of the medium, n_2 is the Kerr
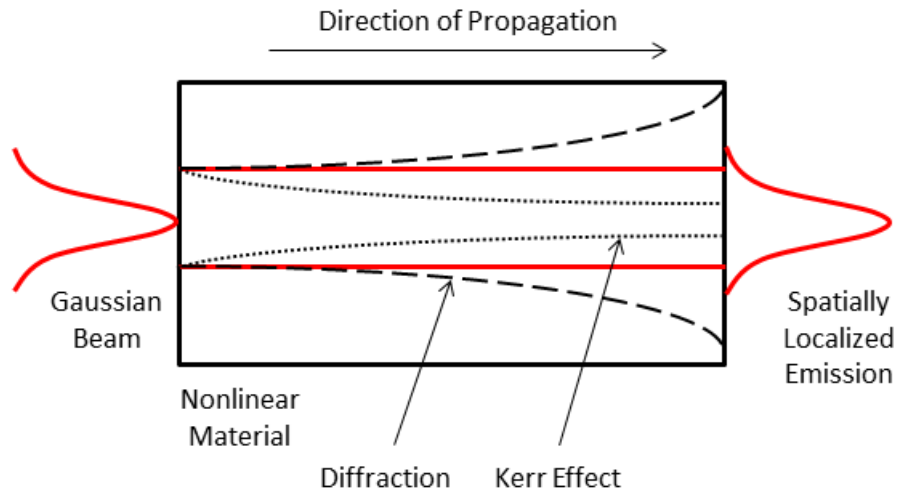
Figure 2.4: Schematic diagram of a spatial soliton supported by a fine balance of Kerr effect and diffraction in a nonlinear medium. The dashed line represents the diffraction of the light in the propagating medium. The dotted line represents the effect of Kerr lensing. The red solid line illustrates the spatial soliton, when the two effects exactly balance each other out.

coefficient and I is the intensity of the radiation [68]. In the case of a Gaussian beam the refractive index gradient takes the form of a Gaussian profile, i.e. the effective refractive index is higher in the center of the beam than in the wings. Therefore, this modified refractive index profile acts like a focusing lens.

This situation is illustrated in Fig. 2.4. If the Kerr effect compensates the diffraction of the beam such that the incoming beam retains its shape while propagating through the nonlinear medium, a spatially localized emission is obtained. This is schematically shown in Fig. 2.4 where the longer dash line represents the natural diffraction of the beam and the dotted line is the Kerr effect. The red solid line illustrates the resulting propagating beam which does not change shape while traveling, i.e. a spatial soliton, when the two effects exactly compensate for each other.

2.3.3   Dissipative Solitons

A dissipative soliton, as the name suggests, is a solitary wave whose energy is partially dissipated in the system. Experimentally, real systems exhibit losses, i.e. they lose energy, and therefore require a constant energy input in order to sustain solitons. Indeed, if the losses are too high, a soliton can only exist for a very limited distance of propagation. However, it is possible to overcome the losses by injecting energy to the system. Dissipative solitons in laser systems are a good example of optical dissipative solitons. In a laser, after each round trip inside the cavity, several photons leave the cavity thus accounting for a constant loss of energy which is compensated by gain sustained by external driving. Therefore, under favorable circumstances, i.e. fine balance of linear and nonlinear effects as well as gain counteracting the energy loss of the system, formation and stabilization of dissipative solitons occur.

2.3.3.1   Cavity Solitons

As described in Sec. 2.3.2 the refractive index variation of the nonlinear medium is intensity dependant. In order to achieve a sufficient refractive index change such that the Kerr effect balances the natural diffraction of the beam, high intensity inside the nonlinear material is required. Therefore, the nonlinear medium is placed within a cavity. This allows for greater net gain as well as high beam powers required for Kerr lensing. When dissipative solitons are formed in a cavity they are referred to as cavity solitons (CSs).

This situation is illustrated in Fig. 2.5. A nonlinear gain medium is sandwiched by two stacks of high reflectivity DBRs. The Kerr effect acts as a focusing lens and balances the natural diffraction of the beam. Due to the plane-parallel cavity, stable Gaussian modes are not supported by the cavity. However, for the reasons mentioned earlier, under favorable circumstances CSs can exist. They retain their spatial profile after each roundtrip in the cavity, i.e. locally stable cavity, and are therefore referred to as spatial cavity solitons [69, 70].

Each of these localized structures behave as an independent object and should be able to exist anywhere in the transverse aperture of the laser. Indeed, CSs are
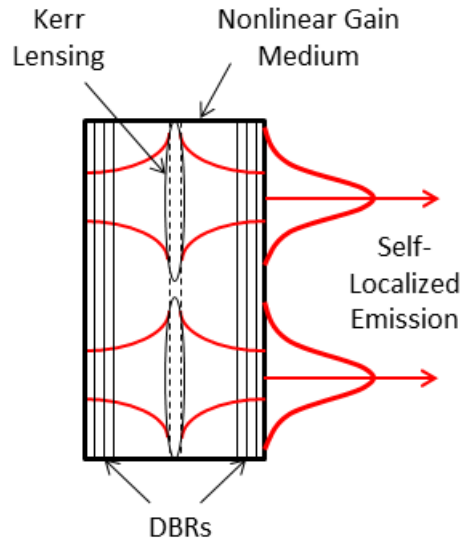
Figure 2.5: Schematic diagram of a cavity soliton sustained by a fine balance of Kerr effect and diffraction in a nonlinear medium. The gain inside the cavity is responsible for stabilizing the cavity solitons by counteracting the energy loss of the system.

independent of the system boundaries and are only stabilized by the nonlinearities. Their shape and size are governed by the system parameters. This means that several CSs should be able to coexist within the same cavity and that they can also exist in arbitrary locations within the transverse aperture of the device. They should also be able to be independently controlled which means that each CS can be independently switched on or off. Further, because they should be able to exist anywhere in the transverse aperture they should also have motion freedom.

The formation of CSs occurs because of the coexistence of a homogeneous background state and a patterned stationary state. Below threshold the background state (or off-state) is stable and as injection increases a spatially extended emission pattern forms. At this point the background is unstable whilst the patterned state becomes stable. However, below the threshold value of the patterned stationary state there exists a small region in which the background remains stable

and the CS can exist. CSs can then be considered as intermediate states between the background and the spatially extended pattern emission. This specificity means that in the CS region there exist two stable states, i.e. the background state (off-state) and the CS state (on-state). This is called bistability and opens up a whole new world of possible applications in information processing.

These properties make CSs good candidates for optical memories and potential applications in this field were first addressed in [16]. However, industrial applications become more attractive in a fast, compact and inexpensive system suitable for implementation in modern electronic devices. This is why a few years later, following the work of Brambilla and co-workers, the idea of realizing CSs in semiconductor lasers rose for possible large scale industrial applications [71]. CSs can exist anywhere in the transverse aperture of a broad area semiconductor laser and can be independently switched on or off by a local perturbation. In turn, these can be regarded as spatial logical bits. Their freedom of movement and position across the aperture of the laser make them potentially suitable for the creation of 2D matrices.

The bistability along with the mobility exhibited by CSs also seem well suited for all-optical delay lines. The speed limitation of current optical networks could be significantly increased if the information could be stored and routed optically. However, routing the information optically would also require the ability to buffer data when the router is occupied dealing with another set of data. CSs seem particularly attractive for this job. They can be written (switched on) at a certain location and then be dragged to a second location anywhere across the transverse plane of the cavity where they can be read and then erased (switched off) [72, 73].

2.3.3.2 Cavity Solitons In Semiconductor Lasers

Semiconductor lasers are compact, relatively inexpensive to produce and also exhibit fast intrinsic time scales. Fast time-scales and small spatial scales associated with a CS in a semiconductor laser make this system very attractive compared to systems based on liquid crystals [74] or atomic vapors [75]. The characteristic

time-scale for CS formation in semiconductor lasers is on the order of a nanosecond, i.e. the carrier recombination time. This, along with the dimensions of a broad area semiconductor laser lying in the hundreds of micrometers range, show the key features of a system for all-optical networking.

Broad area semiconductor lasers appear to be a preferred candidate for such applications. In particular, broad area VCSELs are a main interest. Broad area devices are required in order to support several transverse modes, thus allowing the formation of multiple CSs in the same device. VCSELs are compact, they exhibit a fast intrinsic time-scale and they also have a nonlinear gain medium. However, VCSELs alone do not support bistability and two different techniques have been proven to support bistability in broad area VCSELs. The first approach relies on the injection of a holding beam (HB) into the device whereas the second approach requires the addition of an external element in order to achieve bistability. The latter can be a frequency selective element such as a grating or a saturable absorber. The CSs emerging from this configuration are referred to as Laser Cavity Solitons (LCSs). Experimental work conducted on CSs in VCSELs up to the year 2011 is reviewed in [76].

Cavity Solitons In Driven Systems

The first experimental demonstration of CSs in VCSEL amplifiers happened at the beginning of the century [17]. Barland et al. used a broad area (150 μm) VCSEL driven by a homogenous optical beam, i.e. holding beam (HB), covering the whole aperture of the device. The VCSEL was operated below threshold but above transparency. An external beam, the writing beam (WB), derived from the HB, was used to locally ignite a region of the aperture, i.e. a cavity soliton. This confirmed that the device was operated in a bistable region. The beam size of the WB needs to be close to the size of a CS, i.e. about 10 μm, when it reaches the device. When a beam with the proper size is achieved, the switch on mechanism requires the WB to have a matching phase with the HB. Inversely, for switch off, the phase of the WB must be opposite to that of the HB.

CSs in driven systems have been experimentally observed in both electrically [17, 77] and optically pumped [78] semiconductor amplifiers. The latter experi-

ment demonstrated that there is no need for a phase reference between the HB and the WB. One of the advantages of driven systems is that the CSs are locked to the HB and therefore exhibit the same phase, polarization, and frequency as the HB. This means that a phase reference is available and that the erasure of a CS can be done by shining the WB with the opposite phase on an existing CS via destructive interference between the WB and the CS. However, shortly after the first experimental demonstration of CSs in driven systems greater flexibility was achieved as it was found in [78] that CSs can be successively generated and erased by using a WB which had no phase relationship with the HB. Note that the WB was blue detuned with respect to the cavity resonance. Short pulses (around 60 ps) emitting at a different wavelength from the HB, with no phase reference to the latter, were used both to create and erase CSs. This excitation via addition of carriers at specific locations allows for creation and erasure of a CS. However, the time scales in the writing process involved in this configuration are much slower than that of the coherent case (a few hundred nanoseconds rather than a few nanoseconds). Note that the latency in switching on a CS can be reduced by increasing the power of the WB and was later attributed to be due to local temperature effects [79]. The switch off process is, however, faster and occurs in a few nanoseconds.

The formation of CSs in such systems originated from theoretical predictions in which a translational invariant system is required. Material gradients are of particular importance in the formation and control of CSs. It was demonstrated in [80, 81, 82] that self-organized patterns have the freedom of translation or rotation and can therefore exist anywhere. This Goldstone mode implies that the CSs should be able to move under the influence of any gradient. The speed at which they would travel would make them undetectable by most CCD cameras. Gradients are always present in experimental systems and mainly originate from growth fluctuations of the semiconductor material. These gradients would in practise induce the CS to drift across the aperture of the device until the point where the CS reaches a boundary and then dies. This would make the observation of CSs practically impossible. Fortunately these gradients, i.e. defects, form stabilizing traps for the CSs. At locations where the defects are deep enough the CSs are pinned, i.e. trapped in the defects, and can therefore survive, avoiding

reaching the boundaries of the device. This was indeed verified in [17] where the CSs always appeared at the same locations. These properties were later used as a way of mapping inhomogeneities in the device [83].

The main advantage of CSs in driven systems, i.e. the phase, polarization and frequency are locked to the HB, is also the main drawback in the sense that it does not allow for many degrees of freedom. In addition to this lack of freedom, the need for both a HB and a WB in the system does not lead to compactness and, ultimately, integration for applications in optical networking.

Laser Cavity Solitons

CSs in driven systems do not currently represent a viable configuration for industrial applications. The main reason is that such systems require an external laser of high spatial and temporal coherence which removes some degrees of freedom that CSs could potentially show. A system in which each individual CS could have the freedom to choose its own phase, polarization and frequency would lead to new possibilities. This would also allow for interactions between CSs to be studied and could open up a new world of possibilities in the formation of large arrays of CSs. Therefore, the interest in laser cavity solitons (LCSs) rapidly rose a few years after the first CSs were demonstrated in driven systems. LCSs would be generated in a system where bistability would be provided by frequency selective feedback or by a saturable absorber in an external cavity configuration. Such CSs would behave as independent lasers and are therefore referred to as laser cavity solitons.

Each LCS originates from a spontaneous symmetry breaking and can thus be seen as a microlaser which has the freedom to choose its optical phase. In an isotropic system the polarization of each LCS should also be unique as there is no external influence on the system. The frequency freedom is somewhat different as, for example, in the case of frequency selective feedback, the frequencies at which the LCSs can operate are limited by the bandwidth of the frequency selective element. However, LCSs still have the possibility to be lasing on several external cavity modes. The defects in the transverse aperture of the device are also expected to play a role in the frequency distribution of LCSs. They change

the local resonance of the VCSEL cavity which causes the LCSs to operate at different wavelengths across the aperture of the device. In addition, any scheme relying on an external cavity gives the opportunity for each LCS to lase on different external cavity modes. This ability is of importance as it could lead to mode-locking which then opens up a great avenue towards pulsed LCSs. The ability for individual LCSs to arbitrarily choose their phase and frequency is of great interest as it could potentially lead to phase and frequency locking. Individually controllable yet mutually coherent LCSs would open the door to the possibility of creating large laser arrays where coherence can be established between the different emitters, even in the presence of variations in the natural frequencies of the emitters forming the array.

The first experimental realization of LCSs in a semiconductor laser was demonstrated in a system with frequency selective feedback [18]. This scheme supports bistability via the addition of a frequency selective element in an external cavity configuration. The idea of generating LCSs in a semiconductor laser started with the observation that optical injection which is slightly detuned to the VCSEL resonance can provide bistability [84, 85] and became very promising when the first CSs were demonstrated a few years later in a broad area VCSEL [17]. Therefore, by providing detuned feedback from a diffraction grating to the VCSEL, one expects that it should be enough to provide optical injection without the need of a second laser. Indeed, if the reflection bandwidth of the grating is small enough compared to the frequency band of the VCSEL emission there can exist a frequency detuning between the resonance of the VCSEL and the peak reflection of the grating. This scheme can then support bistability and allows for the creation of LCSs [13]. Bistability arises because there exist two stable states. When the VCSEL is below lasing threshold only spontaneous emission occurs resulting in a high carrier density and low refractive index. As feedback is increased, i.e. higher injection, the carrier density drops and therefore the refractive index increases. This phenomenon leads to a red shift of the VCSEL cavity resonance which in turn increases feedback and creates a positive feedback loop until a high intensity state is reached. However, lasing is not stable over the whole aperture and it sets in locally. At this point the background state is also stable thus providing

bistability to the system (see Chap. 4 Sec. 4.2.1.1 for a more detailed analysis). A discussion for small area VCSELs is given in [13, 86].

In the first experimental demonstration of LCSs in a semiconductor laser system, the frequency selective element used for feedback was a diffraction grating in a Littrow configuration [18]. A self imaging cavity was used in order to keep a high Fresnel number cavity which allows for many transverse modes to be supported by the device. LCSs were created when the peak reflection of the grating was set to be red detuned to the VCSEL cavity resonance. With increasing injection current several laser spots appeared at different locations. The threshold for each spot is different and all the spots show bistability and are almost identical in size (FWHM 10 μm) and shape. They are individually controllable and emit on axis (FWHM 10 MHz). Each spot is a small, localized, coherent emitter, i.e. a LCS. In order to demonstrate the independence of the LCSs the VCSEL is biased in a region which is known to support bistability for several LCSs. An incoherent external beam, i.e. WB, with a transverse size close to the size of a LCS is then injected onto the device at the locations where LCSs are known to be supported. This results in the switching on of the LCSs at the exact same locations. The LCSs remain switched on even after the WB is removed, i.e. they are self sustained. Several LCSs are independently switched on without affecting the state of the LCSs already present in the cavity. The LCSs also show some mobility. Indeed, the WB can be used to drag the LCSs in the transverse plane. The mobility of the LCSs mainly depends on the shape of the traps they are sitting in. Refer to [87] for a detailed analysis of the different switching techniques and [88] for a theoretical model supporting the experimental observations. The first limitation of this configuration is that the frequency selection provided by the diffraction grating is not narrow enough. This leads to the formation of LCSs with the presence of extended states, even at low injection currents. The second drawback is the non-isotropic nature of the diffraction grating [89]. The orientation of lines composing the grating imposes a polarization state in the external cavity, thus removing the desired polarization freedom that LCSs should show.

The issues related to the broadband frequency selection as well as the non-isotropic nature of the feedback element closing the external cavity led to the idea of using a different frequency selective element. A volume Bragg grating (VBG)

meets the criteria of narrow frequency selectivity and isotropic feedback. A configuration with a VBG as the frequency selective element was first demonstrated in [19]. The narrow reflection bandwidth of the VBG allows for a better contrast between the LCSs and extended states. This means that higher currents are available at which LCSs are still supported that were not available with feedback from a diffraction grating, i.e. more LCSs are observed. The VBG also increases the width of the LCS hysteresis loop [19]. In addition to fundamental LCSs, the first observation that differs from [18] is that the system shows multipeak structures. Indeed, the LCSs show a tendency to split in a particular sequence of one peak to two peaks and then a triangular arrangement of three peaks [19]. Similar observations are found in an optically pumped vertical-cavity amplifier [90] and are believed to be associated with homoclinic snaking. A WB, injected at the back of the VBG, is used to drag the LCSs across the aperture of the VCSEL, thus demonstrating some mobility. Several LCSs can be independently switched on and then switched off. In order to switch off a LCS the WB is injected in its vicinity so that it can be dragged out of its trap and then die. The location of the WB, relative to the position of the LCS, at which the switch off process is the easiest is different for each LCS. This matches the observations in configurations with saturable absorption [91, 92] which are also isotropic in contrast with feedback from a diffraction grating where the orientation of the grating breaks parity and a preference for up/down switching is observed [18, 87]. It was demonstrated that LCSs can be switched on by pulses down to 15 ns (limited by the equipment) and it was observed that for long pulse length, i.e. >100 ns, there exists a constant threshold power. Finally, given the very weak anisotropy of the VBG, this scheme gives some freedom for the LCSs to choose their own polarization which results in each LCS having a unique polarization angle [19].

Frequency selective feedback is not the only way to provide bistability in semiconductor lasers. Saturable absorption is another well known technique that can support bistability in semiconductor lasers [93, 94]. For that reason this scheme represents a good candidate for the creation of LCSs. The first experimental realization of LCSs in such systems was observed in [91]. This scheme relies on two mutually coupled VCSELs in face to face configuration. One VCSEL works as an amplifier while the second, biased below transparency, is used as a saturable

absorber. Similarly to [19], this configuration shows very little anisotropy which should result in an arbitrary polarization state for each individual LCS. The LCSs observed in such systems show similar properties as the LCSs in [19]. Monolithic integration of an optically pumped VCSEL with intracavity saturable absorber is demonstrated in [95, 96] and shows great potential for industrial applications.

The stabilization of mutually incoherent emitters inside a cavity is conducive to extensive study of their interaction. The results presented in this thesis follow the work of [20] on phase and frequency locking of LCSs in a VCSEL with feedback from a VBG. Frequency and phase locking of two LCSs was experimentally observed in [20], though no systematic characterization was conducted at the time. It was confirmed that the disorder in the VCSEL aperture was responsible for pinning the LCSs at certain locations as well as the differences in threshold and frequency between them. However, it was noted that a detuning of the self-imaging cavity could affect the locking strength. Therefore, it is essential to characterize the external cavity and particularly the effects of deviations from the self-imaging condition on the pattern formation before conducting a systematic characterization of phase and frequency locking between two LCSs. Nevertheless, due to their intrinsic nature, i.e. phase, frequency and polarization freedom, the interaction of LCSs leading to synchronization due to phase and frequency locking is an interesting topic that may open the door to network synchronization of many LCSs.

2.4   Frequency Shifted Feedback

2.4.1   Frequency Shifted Feedback Systems

In the late eighties, a new kind of external cavity laser was developed that showed unique frequency properties [30, 97]. A frequency shifted feedback (FSF) laser is a specific external cavity laser in which a frequency shifting element (commonly an acousto-optic modulator (AOM)) has been introduced [27]. A schematic diagram of an FSF laser system seeded by a cw single frequency laser in a ring cavity configuration is shown in Fig. 2.6. The seed laser is injected into the ring cavity via the AOM while the output is observed at the undeflected beam output of the
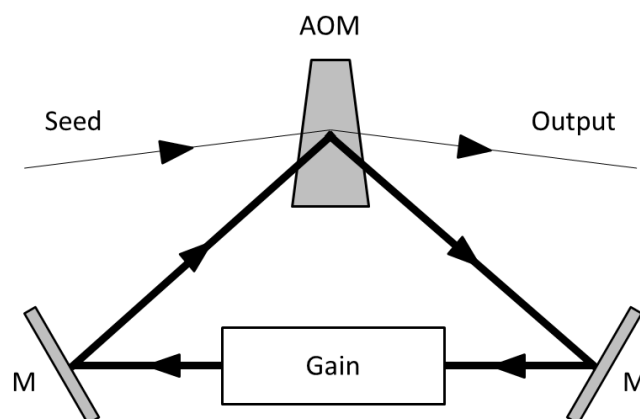
Figure 2.6:   Schematic diagram of an FSF laser seeded by a cw single frequency laser in a ring cavity configuration. Seed: cw single frequency laser, AOM: Acousto-optic modulator, M: Mirror, Gain: Gain medium, Output: Output beam of the FSF laser.

AOM. The ring cavity is closed on the first order diffracted beam of the AOM which implies that a photon experiences a frequency shift after each round trip made in the cavity. Therefore, even if regenerative amplification occurs inside the cavity such laser systems do not support constructive interference over consecutive roundtrips, i.e. the frequency of the light field fed back to the laser changes after each roundtrip. As a result such lasers do not exhibit the conventional longitudinal mode structure observed in Fabry-Perot resonators commonly used to sustain laser oscillation. The spectral profile of an FSF laser is therefore determined by the frequency dependence of the gain medium. The spectral and temporal characteristics of such laser systems show some diversity. They depend on the interplay of various nonlinearities in the system, the cavity geometry and elements, the various sources of technical and fundamental noise, along with the aforementioned laser gain medium. In particular, both the frequency shift induced by the AOM and the free spectral range of the external cavity play an important

role in the characteristics of the output emerging from FSF laser systems. When these two parameters are carefully chosen, the system can operate under different regimes. Early reports based on a dye laser FSF system demonstrated that when the frequency shift is significantly smaller than the free spectral range (FSR) of the laser the output consists of chirped comb lines, the frequency will change in a discrete step after each round trip time and can be seen as a moving comb of frequency modes [98]. However, when the frequency shift is on the order or greater than the FSR, the laser system is capable of emitting in the pulsed regime [30, 31]. Here the repetition frequency of the pulses was that of the roundtrip frequency shift for the first order of diffraction beam of the AOM which was in turn matched to the longitudinal mode-spacing of the laser cavity. This is a case of a FSF-based mode-locked laser. Broadband modeless operation from dye lasers has also been demonstrated when the roundtrip frequency shift of the first order beam from the AOM does not match that of the laser cavity [97, 99].

The first mention of an FSF laser in the literature appeared in 1971 when Taylor et al. [100] introduced an acousto optic cell inside an organic dye laser cavity for the first time. They achieved electronic frequency control of a pulsed dye laser over 78 nm, ranging from 544 to 622 nm with a laser linewidth of 0.135 nm. Nearly two decades later FSF lasers were revisited by Kowalski et al. with the idea of generating stable trains of short optical pulses [30]. The authors injected the output of a laser into a passive frequency shifted ring cavity. An AOM was placed inside the cavity so that after each round trip the light was frequency shifted. The ring cavity was designed such that only the first order diffraction beam of the AOM, i.e. the frequency shifted light, was fed back to the laser. The zeroth order output of the AOM was used to couple the external pump laser into the cavity. Short pulse generation was observed by tuning the cavity mode spacing such that it matches the AOM frequency. This particular configuration is known as the resonant condition. Their first observation was the direct relation between the number of cavity round trips of the light and the number of frequency components of the output spectrum. The authors observed a spectrum consisting of 18 distinct components but due to the short number of round trips the pulses were 1.5 ns wide, i.e. longer than hoped for. In 1988 Kowaslski et al. [97] demonstrated the use of FSF laser systems to produce laser radiation with a broadband

modeless spectrum. The authors demonstrated CW emission by placing a dye jet into a detuned FSF cavity, i.e. when the roundtrip frequency shift does not match that of the laser cavity. The modeless structure observed at the time was attributed to the fact that no discrete frequencies were coupled in. The spontaneously emitted light from the dye jet provides a broadband input and as a result the output of the FSF laser is broadband. Shortly after, this group demonstrated pulsed operation from the same laser system by having the external cavity set up to be in the resonant condition with the roundtrip frequency shift [30] and by placing etalons inside the external cavity to reduce the overall bandwidth [27]. The pulse repetition rate of the laser was directly proportional to the frequency shift induced by the AOM, ranging from 220 MHz to 1760 MHz in multiples of the frequency shift of the AOM. Short pulses have also been demonstrated by placing an AOM in a ring interferometer with cw single frequency injection [101]. Two years later Hale et al. [31] introduced a theoretical model describing the output in both the time and frequency domain for the two regimes of operation aforementioned.

Broadband lasers find applications in spectroscopy, white light cooling or can be used as a tool to explore the effect of phase and amplitude fluctuations on nonlinear optical phenomena. Developing such sources by using compact laser diodes with FSF offers advantages over solid state lasers in term of price and size. Following this statement, in 1991 Richter et al. [28] demonstrated an FSF broadband output with a controllable bandwidth of up to 5 GHz, while the laser output remained single longitudinal mode, using both near infrared and red Fabry-Perot cavity semiconductor lasers. A theoretical rate equation model was later introduced in order to describe the spectral characteristics of such lasers [102]. Subsequent research demonstrated similar results using semiconductor lasers with low reflectance facets for the internal semiconductor laser facets of the external cavity laser system aiming to generate modeless output of larger frequency bandwidth [103]. The expectation that broader FSF bandwidth would be achieved before multilongitudinal mode operation commenced was not met in the experiments. The maximum diffraction efficiency achieved with the AOM meant at most 12% of the emitted light could be fed back to the semiconductor laser in the first order diffracted beam. The coupling efficiency of this light is typically 20-30%

for the laser system used. Higher single longitudinal mode broadening was also reported by using a diffraction grating rather than a plane mirror as the closing element of the external cavity. Use of a distributed feedback (DFB) laser would also be expected to maintain single longitudinal mode output to higher FSF feedback levels but even using a DFB laser gave FSF bandwidths of a few hundred MHz [104]. This work also contrasted conventional feedback and FSF, and noted the suppression of phase dependent linewidth variation of the lasing mode using FSF. Measurements of the RMS noise level of the photodetected output power as a function of feedback level suggested that a transition to the coherence collapse dynamical regime occurred in both systems. This regime of operation had been well documented in the sequence of regimes observed for a semiconductor laser with optical feedback from an external mirror [5]. In the FSF system the transition was not the expected discontinuous switch at a single feedback level. The transition was more gradual. However, the increase in noise level was about 20 dBm/Hz in both cases. This research suggests that FSF does not dominate nor significantly modify the usual coherence collapse nonlinear dynamics that occurs in these systems and which is predicted reasonably well by the Lang-Kobayashi rate equation model [4].

The transition, in an FSF dye laser, from a broadband modeless output to a chirped comb of frequency was observed in [105]. The generation of a comb of modes spaced by the laser cavity roundtrip frequency shift was provided by a monochromatic seed laser injected into the broadband FSF laser system. Several solid state laser based optical frequency comb lasers have been reported starting with one based on Nd:YLF which generated a comb of modes with a bandwidth of 140 GHz [106]. This is essentially the full gain bandwidth of the 1.047 μm lasing transition in Nd:YLF. Fiber laser based FSF systems have been reported, such as a short pulsed Er:fiber laser at 1.55 μm [29, 32] and multi-frequency lasers for telecommunications applications [107, 108]. Er:fiber FSF laser based systems have been demonstrated for the generation of ps pulses associated with an optical bandwidth of a few nm [33, 34, 35]. Fiber FSF laser systems also allow fine tuning of the emission wavelength over a broad range (typically around 30 nm for Er doped fiber lasers) limited by the gain bandwidth of the laser [34, 109, 110, 111, 112]. Recently a numerical model for Er:fiber FSF lasers based

on the rate equation and nonlinear Schrodinger equation managed to successfully capture the spectral and temporal behaviors of such systems [113]. The gain bandwidth when the host is glass, rather than a crystal of YAG or YLF, is significantly increased. Typically by a factor of order ten. The bandwidth of the comb of modes or modeless output that can be generated has the gain bandwidth as its upper limit. The pulse duration of mode-locked pulses decreases as the reciprocal of the FSF bandwidth. The potential to generate sub-picosecond pulses from FSF systems exists but in many of the demonstrated systems it has been necessary to reduce the gain bandwidth using intracavity frequency selective elements to achieve identifiable FSF laser outputs. A titanium sapphire FSF laser has shown a range of different dynamical regimes with increasing pump power [114]. Starting at low pump powers it operated cw then transitioned through sustained spiking, low frequency pulsation on a cw baseline, high frequency pulsations with a zero baseline, and finally to cw output again at high pump powers. Much of this behavior has been predicted by a model [115], applied to simulations for Ti:sapphire, Nd:YAG, Nd:YLF and Nd:YVO4 gain media used in the FSF system. The theoretical models that capture much of the complex behavior that has been seen in FSF laser systems show they can be complex nonlinear laser systems. A careful study of the cw, broadband, modeless FSF output [116, 117] has shown that, with appropriately chosen laser parameters, the output is a chirped comb of modes spaced by the round trip frequency shift.

Early reports showed that when the frequency shift is similar or greater than the external cavity mode separation, the output of an FSF laser is modeless [97, 99]. However, when the frequency shift becomes small compared to the external cavity mode spacing, it is possible to obtain a chirped comb of frequency components without the need of a single frequency seed laser. Balle et al. reported the existence of a chirped comb of frequency components separated by the external cavity frequency. This was observed in a homogeneously broadened dye laser with spontaneous emission feeding where the chirp is stepwise. A few years later Nakamura et al. [118] used different interferometric schemes in order to demonstrate, for the first time, the existence of continuously chirped frequency components in an FSF based solid-state laser system without seeding. Their work contrasts with [98] in which the chirp is stepwise. Nakamura and coauthors based

their demonstration on the observation of a continuous change of the beat frequency through the Michelson interferometer as the path difference was varied. A year later the same group supported the existence of a continuously chirped comb by presenting a model predicting a continuous chirp across the oscillation bandwidth of a solid state laser [119]. A few years later, Kowalski et al. discussed the properties of the frequency chirped output of FSF lasers [120] directly comparing observations in [98] and [118, 119]. At the time the exact nature of the electric field emerging from such lasers was a matter of discussion and by using results and parameters from two contradictory previous studies, supporting the stepwise [98] and continuous model [118, 119], the authors tried to determine which model is appropriate to describe the output of an FSF laser. Two different kinds of interferometry, namely homodyne and heterodyne, were compared. The former requires an ultrafast time analysis of the output whereas the latter needs an extensive study of the interference pattern. Even though the study failed to give a description of the nature of the output, it paved the way for interpreting future results using homodyne or heterodyne interferometry methods. More recently Guillet de Chatellus et al. [121] demonstrated that the moving comb of frequencies model is only valid if the frequency shift is small, i.e. when it does not exceed a few percent of the FSR of the laser.

2.4.2 Applications

FSF fiber laser based systems started to draw a lot of attention in the nineties when people realized that such compact systems could be very attractive for telecommunication applications. In particular, short pulse operation has been demonstrated and shown potential in secure communications. The unique spectral characteristics of such sources, i.e. comb of equally spaced and potentially frequency stabilized lines, would make them perfect candidates for spectroscopy or metrology applications as well as distance measurement. However, one of the first applications of FSF was discovered in the early seventies when Smith introduced the concept of optical isolation via FSF [122]. He demonstrated efficient optical isolation by using an acousto-optic modulator under the condition that the frequency shift induced by the AOM does not correspond to a multiple of the

cavity resonance. Smith came to the conclusion that a frequency shift of 2 MHz between the external cavity roundtrip and the AOM is sufficient to achieve good optical isolation. Nine years later, Furch et al. achieved 40 dB isolation using an AOM in the near IR [123]. Even though Faraday isolators became more popular in the nineties they were not flawless. Optical waveguide birefringence was one of their major drawbacks. This is the reason why in 1996 optical isolation using FSF was still considered as an effective method when Benoist showed a suppression of the phase dependent noise enhancement at low feedback level for DFB lasers operating in the NIR [104]. Nowadays Faraday isolators can achieve really high isolation along with very low absorption coefficient, low non-linear refractive index and high damage threshold. Undesired thermal effects are avoided by ensuring a short optical path within the birefringent material. In addition to these features, their size and ease of alignment have made Faraday isolators a standard tool to achieve high optical isolation for a very broad range of wavelengths, therefore rendering FSF based optical isolation uncompetitive.

FSF laser systems can also be used to broaden the linewidth of a laser which finds applications in optical pumping, white light cooling or frequency combs generation. In 1998 Lim and co-workers constructed an external cavity diode laser with frequency shifted feedback from an AOM for optical pumping of Zeeman-split lines in the kilogauss regime [124]. Their new design involving a diffraction grating as a reflective surface of the external cavity allows a control of the average frequency supported by the cavity. They demonstrated a tunability of 8 nm, along with a bandwidth of 5 GHz. This design was capable of achieving simultaneous optical pumping on 85 Rb and 87 Rb, allowing for easy tuning to the D1 or D2 transition manifolds. In 2001 a wideband multiwavelength Er-doped fiber laser was demonstrated by Kim and co-workers [107]. Such sources have applications in optical communication systems such as wavelength division multiplexing (WDM) transmission systems which rely on several wavelengths being transmitted at the same time via the same optical fiber. The main challenge is to manage to achieve lasing with as many wavelengths as possible within the third transmission window (1530-1565 nm), i.e. C band, of silica fibers. A high number of channels is required to achieve high bit rate communication and the output power in each channel needs to be equal. The authors used an intra cavity gain flattening filter in order

to increase the lasing spectral bandwidth. They managed to achieve lasing of 34 channels with a 0.8 nm channel spacing across 28 nm in C band. However, it was observed that ripples as small as 0.4 dB in the spectral transmission of the gain flattening filter can lead to a 10 dB output difference between the different channels. Two years later a broader emission spectrum was obtained when Maran et al. demonstrated multiwavelength operation of an Er-doped fiber laser covering the whole C band [108]. They used the FSF scheme introduced in [107] with a fiber Bragg grating array instead of a gain flattening filter. The addition of this frequency selective element allowed lasing of 17 laser lines with an output power flatness greater than 3 dB. Even though this system is capable of emitting a few tens of lines in the C band it remains insufficient for a commercial use in optical communications. Indeed, such a system seems limited when current WDM communication systems can handle more than one hundred wavelengths within the C band. Chromatic dispersion in optical fibers is one of the factors limiting the performance of WDM systems. Therefore, in 2004, Maran proposed to use the same FSF laser scheme in order to characterize optical components and networks by measuring the optical fiber chromatic dispersion [125]. Due to the chromatic dispersion, the different wavelengths simultaneously injected into the fiber will propagate with different group delay velocities. Therefore, by capturing the time delay between the different pulses at the end of the fiber and thus allowing the differentiation of the corresponding group delays, it is possible to retrieve the chromatic dispersion of the fiber. This method, called time of flight, is capable of achieving a precision in the evaluation of pulse arrival time of 10 ps, and a repeatability of the chromatic dispersion measurement better than 0.5%. These results are on par with the standard phase-shift method commonly used for such measurements [126, 127]. This technique however, seems particularly suited for measurement of already installed fiber networks as no reference is needed between the input and the output of the fiber.

High precision distance measurements relying on optical reflectometry are a main interest in various fields such as fiber-optic component and module characterization [128, 129], biomedical imaging [130] or distributed optical sensing [131]. A common technique called optical frequency domain reflectometry (OFDR) has been widely used in the past decades for this purpose [132, 133, 134, 135, 136,

137, 138]. OFDR allows high resolution measurements ranging from short to long distances with a high dynamic range and is well suited to tomographic applications. This technique relies on a cw frequency-chirped laser to be injected into a Michelson interferometer. The beat signal from the interferometer has a frequency proportional to the path difference of the Michelson interferometer and can therefore allow accurate distance measurement and beat frequency determination with high precision. This technique is also insensitive to material phase shifts that occur upon reflection as it relies on time measurement rather than phase. It does not require the knowledge and use of a material-dependent phase shift at the surface of the measured object either. For this purpose, semiconductor lasers appear to be the most practical devices available due to their size, cost, gain medium and frequency tunability. The latter can be achieved by varying the injection current [134], the temperature [139] or by adding a diffraction grating in an external cavity configuration [140]. However, the main problem of this technique, when using a frequency chirped laser, is that there is a trade-off between range and resolution. The distance range is a function of the ratio between the frequency chirp range and the chirp rate. Nevertheless, in 1998 Nakamura et al. demonstrated that the use of an FSF laser rather than a frequency-chirped laser overcomes the limitations of the OFDR method [141]. In this first experimental work a distance of 3.7 km was measured with a resolution of 9.4 mm. Since then there has been considerable effort to demonstrate accurate ranging using FSF lasers operating in the chirped comb of modes regime. In 2000, Nakamura et al. improved the maximum operating range of their FSF laser system, i.e. a diode-pumped Nd:YVO4, up to 18.5 km with a precision of 20 mm [142]. Because the resolution is mainly limited by the frequency chirp range it was also reported that the latter can be improved by using a gain medium with a wider gain bandwidth than Nd:YVO4. Therefore, new FSF laser based systems have been used to achieve OFDR with higher resolution. Yoshida et al. proposed an Er-doped FSF fiber laser to achieve a resolution greater than 2.5 mm over distances of a few tens of a kilometer [143]. In 2004, Yatsenko and co-workers theoretically studied the limitations of phase modulated seeded FSF lasers in OFDR [144]. The authors found a link between the effective number of discrete frequency components and the spectral width of the FSF laser. They demonstrated that the

width ultimately limits the resolution by restricting the precision by which the beat frequency can be determined. Theoretically, and under favorable conditions, they showed that the errors in the beat frequency determination can allow sub-wavelength precision determination that matches what is typically achieved with conventional interferometry. Two years later Ogurtsov et al. confirmed the theoretical prediction introduced in [145]. The authors used a Yb3+ doped fiber ring FSF laser with phase modulated seed to achieve distance measurements with an accuracy better than 10 μm and resolution greater than 100 μm over distances of a few meters. It was established that the phase modulated seed laser allows the signal to be encoded in a narrow bandwidth and that it does not affect the large bandwidth signature of the FSF laser, but improves the signal to noise ratio. However, the coherence length of the seed laser limits the distance range achievable with this technique which was measured to be about 1 km. In 2006, Paul et al. demonstrated the first OFDR using an FSF laser system based on a distributed feedback (DFB) semiconductor laser [146]. However, neither the resolution nor the accuracy of the measurement were reported. The ease of implementation of this method along with the intrinsic performance offered by the gain bandwidth of such lasers make this compact, inexpensive system very interesting for commercial applications. A few months later the same group, using the same FSF system, reported the accuracy and the resolution of the system in more detail [147]. Accuracies below 0.2 mm for distances not exceeding 0.5 m were reported as well as an accuracy of 3 mm at 588 mm with an estimated resolution of 52 mm. In 2008, following up on the work presented in [145], Ogurtsov and co-workers demonstrated the use of an Er3+ doped fiber with an external phase modulated seed laser as a tool for OFDR [148]. Their system suffered from a bandwidth limitation and could only achieve distance measurements up to a few tens of meters. An accuracy better than 0.1 mm and a resolution greater than 1 mm, also limited by the bandwidth of the laser, were reported. A year later Yatsenko et al. discussed the physics behind the observation of the dramatic signal enhancement resulting from the phase modulation of the FSF seeded by a phase modulated laser [149]. The authors theoretically showed that using a PM seed enhances the interferometer output signal by a few orders of magnitude if the modulation frequency of the seed obeys a certain resonance condition. A

few weeks later the same group presented a theoretical analysis of the coherence properties of the output from a FSF laser seeded simultaneously by an external seed laser and by spontaneous emission (SE) [150]. It was established that the competition between SE and seed induces a balance which is linearly related to the control parameters rather than being exponentially related in conventional laser systems. It was also demonstrated that it is not possible to suppress the SE component of the signal which would therefore increase the performance of the system for optical ranging by increasing the signal to noise ratio. More recently, Pique demonstrated that fast long distance measurements, i.e. up to 250 m, with a good accuracy (better than 1 μm) are possible by using a pulsed FSF laser [151].

The results presented in the second part of this thesis focus on an edge emitting semiconductor laser coupled to a high reflectivity mirror in an external cavity configuration with frequency shifted feedback. The dynamics of the output of the system are systematically analyzed. Nowadays multi-GHz bandwidth oscilloscopes for real time data analysis and collection are available on the market. This state of the art equipment allows us to investigate the temporal and spectral behavior of the output power of the nonlinear system with a resolution that was not imaginable when the last similar studies were reported [28, 103, 104]. With the help of computer controlled experiments, it is now possible to collect tens of thousands of time series, as laser parameters are varied, in experiment run times that are measured in hours. This, along with a fast oscilloscope, enables us to explore a broad parameter space and could potentially lead to the observation of new dynamics. Dynamical maps of a complexity measure, the permutation entropy [152], have been recently generated for a similar semiconductor laser with conventional optical feedback [39]. These maps for conventional optical feedback provide the necessary information to allow the difference between conventional optical feedback and FSF to be conducted once a similar set of maps is generated for an FSF system. The investigations focus on both the near resonant case, i.e. when the roundtrip frequency shift of the first order beam from the AOM matches that of the laser cavity, and the non-resonant case.

Chapter 3

Experimental Equipment and Basic Properties of Laser Cavity Solitons

This chapter introduces the basic properties of the experimental equipment used in the frequency selective feedback experiment. The interaction of LCSs leading to phase and frequency locking arise from their unique properties. Therefore, a brief description of the basic properties of LCSs will be given in this chapter.

3.1 VCSEL Characterization

The VCSEL used in the experiment was fabricated by Ulm Photonics and is similar to the ones described in more detail in [18, 19, 153, 154, 155]. It is a large aperture device specifically designed for the creation of cavity solitons. Commercial VCSELs are designed such that they only support one, or a few, transverse modes. The high quality beam shape achieved by these single mode, small aperture devices is not a vital factor to create cavity solitons. A typical single mode VCSEL has an aperture diameter of a few tens of microns. This small aperture does not allow the formation of multiple CSs, which typically have a radius of about 6 μm, within the same aperture. Thus, a larger aperture device was manufactured so that multiple CSs can potentially co-exist, independent of

Figure 3.1:   Schematic diagram of the VCSEL structure. In the multi-layer structure, the curved lines indicate the resulting current paths.

boundary, within the same aperture. A recent experimental realization reported the formation of multiple CSs in an 80 μm diameter VCSEL [156]. This is, as of today, the smallest VCSEL aperture which has experimentally been demonstrated to sustain multiple CSs.

The VCSEL has a large aperture of 200 μm, allowing the formation of many transverse cavity modes of fairly high order and has an emission wavelength around 975 nm at room temperature. Figure 3.1 shows the layer structure of the VCSEL. Three InGaAs quantum wells are serving as gain medium leading to emission in the 980 nm range. The quantum wells are surrounded by passive AlGaAs spacer layers with a total thickness of one wavelength. The cavity is closed by high reflectivity distributed Bragg reflectors (DBR) with 33 layers AlGaAs/GaAs on the top side (p-contact) and 22 layers on the bottom side (n-contact). The emission takes place through the n-doped Bragg reflector and

(a)   (b)   (c)   (d)
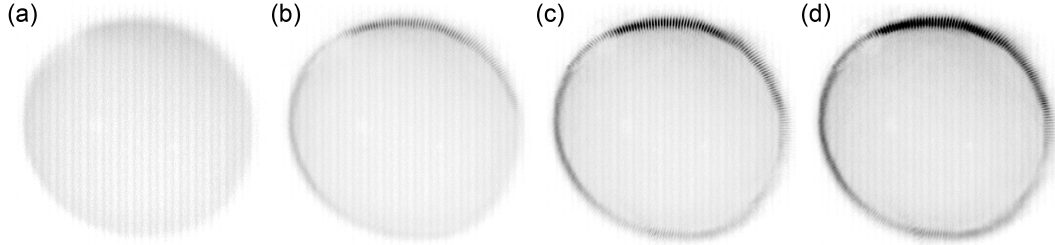
Figure 3.2:   Near field intensity distribution of the VCSEL at a temperature of 16 °C for (a) I=450 mA (this, and all other images in this chapter, depict intensity in a linear gray scale with black denoting high intensity), (b) I=500 mA, (c) I=550 mA, (d) I=600 mA. Note that the slight non-homogenous behavior of the emission (decrease of intensity from the upper left to the lower right) is due to the detection setup.

through the transparent substrate. In this so-called bottom-emitting geometry a reasonable uniformity of carrier injection can be achieved over fairly large apertures [153, 154] compared to a standard top-emitter VCSEL. A 200 μm diameter circular oxide aperture provides optical and current guiding. The oxide layer provides an abrupt refractive index jump inducing a strong optical confinement. This confines the emission to take place within the circular aperture of the device. Because the oxide does not conduct electricity, when the current is injected from the top of the device, the carriers are directly channeled into the gain region thus improving the efficiency of the device. This active diameter is much larger than the effective cavity length of about 1.2 μm. As a result, the VCSEL has a large Fresnel number allowing for the formation of many transverse cavity modes of fairly high order. An anti-reflection layer is applied in the emission window on the substrate in order to avoid back reflections into the cavity. The VCSEL is then mounted to a diamond heat spreader (see Fig. 3.1) which is attached to the top DBR in order to minimize the distance between the heat spreader and the laser cavity. This improves the thermal dissipation of the device.

In spite of the large aperture the device is still capable of lasing at low enough temperatures. The lower the temperature the lower the current required to achieve lasing. In order to be conservative the device was never operated above 600 mA, regardless of the temperature of the VCSEL. Figure 3.2 shows
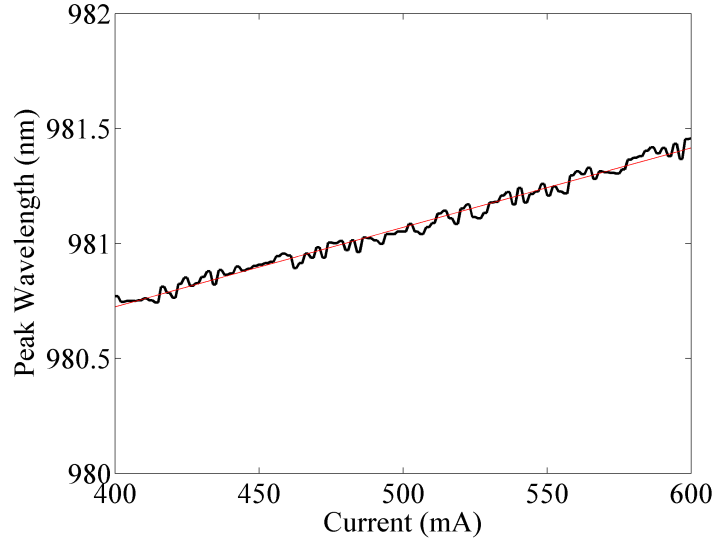
Figure 3.3: Peak wavelength position of the spontaneous emission with increasing injection current for the free-running VCSEL. The laser was operated at 70 °C and current steps of 1 mA were used. Black line is the experimental data. Red line is a numerical fit to data.

the emission pattern of the VCSEL for different injection currents at a temperature of 16 °C. The spontaneous emission is rather homogeneous below threshold (Fig. 3.2(a)) but as the current increases the intensity becomes higher at the boundaries due to current crowding at the oxide aperture [154]. Above threshold the laser starts to lase on a kind of whispering gallery mode (e.g. [155]), depicted as a ring with a substructure of fringes around the boundaries of the VCSEL (Fig. 3.2(b)). The gain is the highest around the boundaries due to the current crowding previously observed therefore leading to a lower threshold of this mode. The whispering gallery mode continues to lase up to 600 mA with higher intensity in the fringes associated with small variations in their structure as illustrated in Fig. 3.2(c-d). For further details on the free-running properties of large area VCSELs refer to [157].

As mentioned earlier, the laser emits around 975 nm at room temperature. However, this wavelength can be tuned by changing the operating temperature of the device. This can be achieved by directly changing the temperature of the

VCSEL via the peltier element attached to the heatsink of the device. This increase in temperature expands the cavity and as a result it increases the optical path length. According to the specifications of the manufacturer, this results in an emission wavelength shift of 0.066 nm/K. The emission wavelength of the VCSEL can also be tuned by increasing the injection current driving the device. Figure 3.3 illustrates the spontaneous emission wavelength shift of the free-running VCSEL at 70 °C with increasing injection current. The laser is operated at high temperature and, as indicated earlier, its emission wavelength increases at a rate of 0.066 nm/K. Therefore, the VCSEL operates around 980 nm at 70 °C. The spontaneous emission of the free-running laser shows an approximately linear increase with a rate of 0.0035 nm/mA (red fitted line in Fig. 3.3). In this case the expansion of the cavity is caused by Joule heating, i.e. heat induced by the current flowing through the device. These two phenomena allow for a very fine tuning of the emission wavelength of the VCSEL, which is a crucial parameter for the formation and control of LCSs. This is also a key parameter when trying to interact two, or more, solitons.

3.2   Devices and Experimental Setup

3.2.1   Experimental Setup

In this section the frequency selective feedback experimental setup is detailed. A schematic diagram of the experimental setup is illustrated in Fig. 3.4. The VCSEL previously introduced is temperature controlled to 0.01 K and driven by an ultra-low noise current source (Arroyo 4210). The VCSEL is coupled to a volume Bragg grating (VBG) via a self-imaging external cavity. Every point of the VCSEL is imaged at the same spatial position after each round trip therefore maintaining the high Fresnel number of the VCSEL cavity and ensuring local feedback compatible with self-localization. The VCSEL is collimated by $f_1 = 8$ mm focal length plano-convex aspheric lens. The second lens is a $f_2 = 50$ mm focal length plano-convex lens and is used to focus the light onto the volume Bragg grating (VBG). This telescope setup gives a 6.25 : 1 magnification factor onto the VBG. This cavity has a round trip frequency of 1.23 GHz which corresponds to

Figure 3.4: Experimental setup. VCSEL: Vertical-cavity surface-emitting laser, f_1=8 mm: Collimation lens, f_2=50 mm: Focusing lens, f_3=80 mm, f_4=75 mm, f_5=100 mm and f_6=200 mm: Lenses in the detection arm of the setup used to image both near and far field images of the VCSEL onto the cameras. BS: Beamsplitter, VBG: Volume Bragg grating, HWP: Half wave plate, A: Aperture, M: Mirror, PD: Photodiode, CCD1: CCD camera in far field image plane of VCSEL, CCD2: CCD camera in near field image plane of VCSEL, OSA: Optical spectrum analyzer, FP: Fabry-Perot interferometer.

a round trip time of 0.81 ns. The light is coupled out of the cavity using a glass plate (beam splitter with a front uncoated facet and a back anti reflection coated facet). The reflection is relying on Fresnel reflection and therefore is polarization dependent. The reflectivity is on the order of 10 % for s-polarized light and 1 % for p-polarized light.

An optical isolator is used to prevent reflection from the detection from passing

into the external cavity. The half wave-plate (HWP) in front of the isolator aligns the incoming polarization to match the front polarizer for maximum transmission through the isolator. Outside the external cavity, a 50/50 beamsplitter (BS) is used to couple half of the laser output to the optical spectral characterization arm of the setup. The optical spectra are recorded with an optical spectrum analyzer (OSA, Hewlett-Packard 86140A) with a resolution of 0.07 nm and/or by a custom made Fabry-Perot interferometer (FPI). The confocal scanning FPI consists of two mirrors with radius of curvature -7.5 mm and reflectivities greater than 99%. One of the mirrors is fixed and the second mirror is attached to a piezoelectric transducer thus allowing the cavity to be actively scanned (see Chap. 6 Sec. 6.1.4 for a more detailed description of an FPI). The free spectral range (FSR) of the FPI was measured at 10 GHz with a finesse of 80. This allows the FPI to achieve a resolution of 125 MHz. The remaining light is then used for images collection and power measurement via three 50/50 beamsplitters. There are two charge-coupled-device (CCD) cameras used for detection, one is used to produce images of the VCSEL emission in the gain region (near field) and the other camera produces images of the Fourier plane of the gain region (far field). A photodiode is used to measure the laser power in order to produce LI curves. The instrumentation is controlled via a computer through the software LabVIEW.

3.2.2 Volume Bragg Grating

Frequency selective optical feedback is provided by a volume Bragg Grating (VBG). VBGs are usually made out of a photosensitive glass or polymer material. It consists of alternating high and low refractive index layers of $\lambda/4$ thickness. The photosensitive glass piece is irradiated by a coherent UV beam, with $\lambda/4$ wavelength where λ is the peak reflection wavelength of the VBG, spatially modulated by an interference pattern in order to write the grating into the glass material. The reflectivity and the position of the reflection peak are determined by the number of layers and the thickness of each layer, respectively. Peak reflectivities of up to 99.9 % can be achieved. The reflectivity of a VBG relies on constructive interference caused by the reflection of the light at each interface between the different layers. This allows VBGs to achieve small reflection
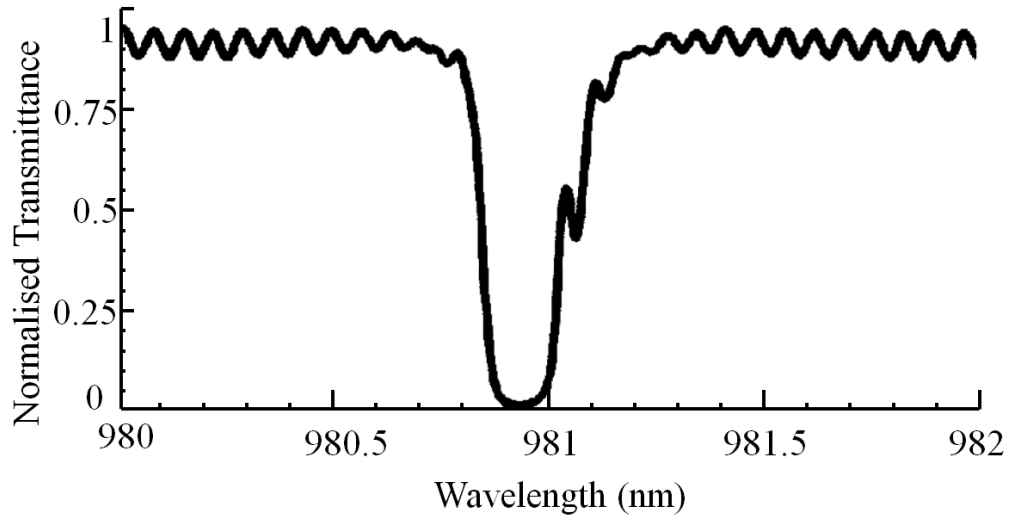
Figure 3.5: Peak reflection of volume Bragg grating 1 (VBG 1). Curve supplied by Optigrate [158].

bandwidths, typically <0.3 nm, and they are therefore referred to as frequency selective elements.

Two VBGs, with a different peak reflection, were used in the experiment. They were both manufactured by OptiGrate for the purpose of the project [158, 159]. The bulk material is crown glass and both VBGs have a size of 4×5×4.56 mm. In order to avoid interference between the grating and the facets, the grating is written with a wedge angle of 0.5°. An anti-reflection coating is also applied to the VBGs in order to prevent any interferometric effects occurring at all.

Both VBGs were characterized by OptiGrate and Fig. 3.5 shows the reflection bandwidth of VBG 1. The specifications state that the peak reflection is centered at 980.9 nm with a full-width half-maximum (FWHM) of 0.19 nm. The diffraction efficiency at the peak reflection is 99.1%. In order to ensure self-consistency in the data the peak reflection was remeasured using a tunable laser and the OSA. The emission wavelength of the laser was swept through a couple of nanometers around the stated peak reflection of the VBG and the transmission of the VBG was measured. The peak reflection was found at 981.1 nm with a FWHM of 0.19 nm. The discrepancy is probably caused by a miscalibration of

our equipment. However, since the absolute wavelength is not of interest and that only the relative detuning between the VCSEL and the VBG is important, the value of 981.1 nm will be used throughout this thesis. The second VBG used in the experiment has a peak reflection at 978.2 nm with a FWHM of 0.11 nm. The diffraction efficiency at the peak reflection is 92.0%. This grating will be referenced as VBG 2.

Optical alignment of the laser system is achieved by looking at the emission pattern of the VCSEL in both near field and far field. At high injection currents, when the VBG is perfectly aligned, the VCSEL lases in an extended pattern up to a point where the entire aperture of the device is lasing. If the VBG is not correctly aligned then the whole aperture of the VCSEL does not lase and the emission is localized on one side of the device. In far field, high injection currents lead to the formation of a ring which corresponds to off-axis emission. Similarly, if the VBG is slightly misaligned then the symmetry of the ring is broken. The alignment was carefully checked and optimized in this consistent manner before any data collection was performed.

3.2.3 Detection

3.2.3.1 Cameras and Images Collection

Two CCD cameras are used for detection, one is used to produce images of the VCSEL emission in the gain region (near field) and the other camera produces images of the Fourier plane of the gain region (far field). The near field camera (Pulnix TM-765E) has a 756×581 pixel matrix. The size of the sensor is 8.32 mm×6.39 mm, this means that each photosite, i.e. pixel, is 11μm×11μm in size. The second CCD camera, used in far field, is custom made and has the same pixel matrix of 756×581.

In order to take advantage of the large surface area of the cameras (about 5 mm×5 mm), the aperture of the VCSEL needs to be magnified by a factor 20 to fill most of the detection area of the cameras (200 μm×20=4 mm). Two telescopes, i.e. beam expanders, are set-up in the detection area of the experimental setup as illustrated in Fig. 3.4. The first telescope consists of two lenses, $f_1 = 8$ mm and $f_3 = 80$ mm, and it has a magnification factor of $f_3/f_1 = 10$.

The second telescope is formed by $f_5 = 100$ mm and $f_6 = 200$ mm which gives a magnification factor of 2. The total magnification factor is then $10\times2=20$, therefore, the aperture of the VCSEL has a size of about 4 mm$\times$4 mm. The near field camera is placed such that the spontaneous emission pattern of the VCSEL looks the sharpest. The lens f_4 is placed in between the two telescopes and provides a 1:1 image of the VCSEL aperture in order to allow spatial filtering of the beam. By placing an adjustable iris or a slit in the re-imaged plane of the VCSEL, it is possible to isolate a fraction of the VCSEL aperture such that only one, or a few, solitons are observed in the detection.

The far field image of the VCSEL is obtained after careful positioning of the camera in the far field plane of the laser. An estimate of the position of this plane is determined by placing a thin wire after the collimation lens f_1. The position of the camera is then adjusted so that the edge of the wire has the highest definition. This method is only reliable if the wire is placed exactly in the far field plane of the VCSEL, i.e. 8 mm (the focal length of the lens). However, it is not easy to precisely determine this position as the lens is rather thick and placed in a mount. Thus, this method was only used to obtain an estimate of the position of the far field plane and numerical calculations were conducted to accurately find its position. The results indicated that the plane was located 233.34 mm after f_5. Because the camera was moved manually, its position was adjusted to match this distance with an accuracy of ±1 mm.

The cameras are connected to a computer via an IMAQ frame grabber. This allows the images to be exported in LabVIEW where they can then be saved as 10-bit greyscale images. The experiment is completely automated via LabVIEW which means that images, output power or optical spectra can be recorded independently if required.

3.2.3.2 Near and Far Fields Cameras Calibration

The near field camera was calibrated after the experimental setup illustrated in Fig. 3.4 was achieved and properly aligned. The calibration was done by using a near field image of the spontaneous emission of the VCSEL similar to that shown in Fig. 3.2(a). The diameter of the lasing aperture of the VCSEL is 200 μm.

Therefore, by importing Fig. 3.2(a) into a graphics software it is possible to know how many pixels correspond to the diameter of the VCSEL aperture. Then each pixel can be converted to a distance by using the 200 μm diameter as a reference. After calculation the calibration was used to calculate the size of the LCSs or the size of the lasing structures in the aperture.

The far field camera calibration, however, requires the VCSEL to be operated outside of the external cavity. This means that the calibration has to be done before the alignment of the experimental setup. In order to calibrate the far field camera the free running VCSEL was operated outside of the external cavity without a collimation lens. As illustrated earlier the free running VCSEL lases on a whispering gallery mode which is depicted as a ring in near field. The divergence of the beam is used to calibrate the camera. The diameter of the ring observed on an IR card was calculated at two distances (about 25 cm apart) away from the VCSEL. Meanwhile an image of the VCSEL aperture was recorded at each position with the far field camera. Then it is possible to determine the angle at which the beam diverges by using a simple trigonometric function. To relate this angle to the number of pixels on the camera it is necessary to calculate the ring diameter difference in pixels between the two positions. Once this is done the pixels on the camera can be converted to mrad. Once this first calibration is achieved two far field images of the VCSEL are taken at two different injection currents (500 mA and 600 mA). From these two images the angular spread difference between the two currents is recovered. After calibration the VCSEL is then placed in the external cavity for alignment and the camera is positioned in the far field plane of the VCSEL following the procedure described in the previous section. Two far field images of the VCSEL at 500 mA and 600 mA are then recorded and a calibration of the far field camera at this position is achieved using the angular spread difference between the two injection currents previously calculated.

3.2.4   LI Curves

A Light-Injection (LI) curve measures how the laser output power varies with injection current. This is usually done by increasing the current in small steps

so that the transition to lasing can be identified with good accuracy and the threshold can be determined. However, since CSL are bistable, the injection current needs to be ramped upwards and then downwards. When bistability occurs, a different CSL output power level is observed between the up ramp and the down ramp within a small range of injection currents (typically about 2 mA).

The light output of the laser is measured using an amplified photodetector (Siemens BPW 34) with adjustable gain. The output of the power meter is then connected to a computer and controlled through a custom made LabVIEW program. The ultra-low noise current source (Arroyo 4210) can deliver currents up to 1000 mA with a precision of 0.1 mA and an accuracy of 0.05%. The current applied to the laser is increased until the specified maximum injection is reached, it is then decreased to the starting injection with the same resolution.

The maximum speed at which the current ramp can be performed was experimentally determined. Because an increase of the injection current leads to joule heating, it is necessary to ensure that the laser is thermally stable before taking a power reading at each injection current probed. If this is not the case, then, this will cause erroneous bistability. A maximum ramping speed of 1 mA/s was used in order to avoid this issue and all the LI curves presented in the next two chapters were performed at this rate.

3.3   Basic Properties of Laser Cavity Solitons

The characteristics of LCSs in the experimental setup introduced in Sec. 3.2.1 have been investigated in detail in [19, 20]. This section summarizes the basic properties of LCSs, refer to [20] for a more detailed analysis.

Frequency selective feedback is only effective if the VCSEL emits within the reflection wavelength bandwidth of the VBG. This means that at room temperature, where the VCSEL has an emission wavelength around 975 nm, the VBG has no effect (978.2 nm or 981.1 nm peak reflection wavelength). Therefore, the device must be tuned in temperature such that its emission wavelength approaches the peak reflection wavelength of the VBG. The laser must be tuned up to $70\,°C$ to reach the peak reflection bandwidth of VBG 1, i.e. 981.1 nm. The peak reflection of VBG 2, i.e. 978.2 nm, is reached when the device is operating at $40\,°C$.
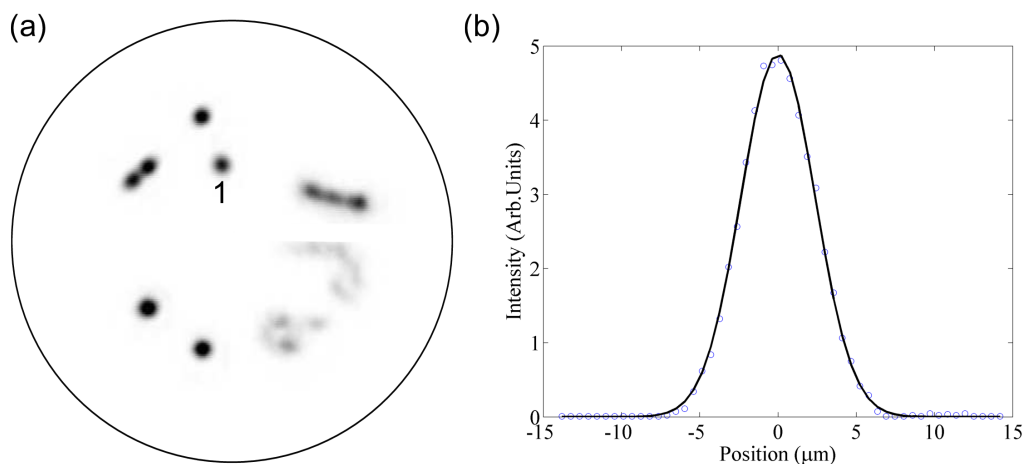
Figure 3.6:   (a) Near field image of the VCSEL aperture taken at 396 mA showing the relative position of a few solitons. (b) Near field intensity profile (points) with Gaussian fit of the soliton marked 1 in subcaption (a).

At such a high temperature the free running laser has an infinite threshold and lasing only occurs because of the feedback from the VBG.

The parameters and the description given in this section are associated with VBG 1. When increasing the VCSEL injection current, LCSs appear at specific spatial localizations. The first lasing emission occurs at currents of about 360-380 mA, depending on the exact temperature and alignment of the VBG. Figure 3.6(a) shows a typical near field intensity distribution slightly above threshold. There are several distinct spots of emission, which are approximately circularly symmetric and approximately equal in amplitude and shape. These are the LCSs. The size of a LCS is about 5-7 μm ($1/e^2$ radius) as seen in Fig. 3.6(b). The far field has also a single-lobe, well-behaved profile with a width of a few tens of milliradians [19], i.e. the LCSs have a high spatial coherence. The emission is also temporally coherent with a typical linewidth of about 6 MHz when operating on a single longitudinal mode of the external cavity [19], quite a typical value for grating-controlled lasers on millisecond and second time scales. Hence each LCS is a coherent emitter, a microlaser. By increasing the current, a soliton typically splits into a compound state with two humps, and then possibly three or four,
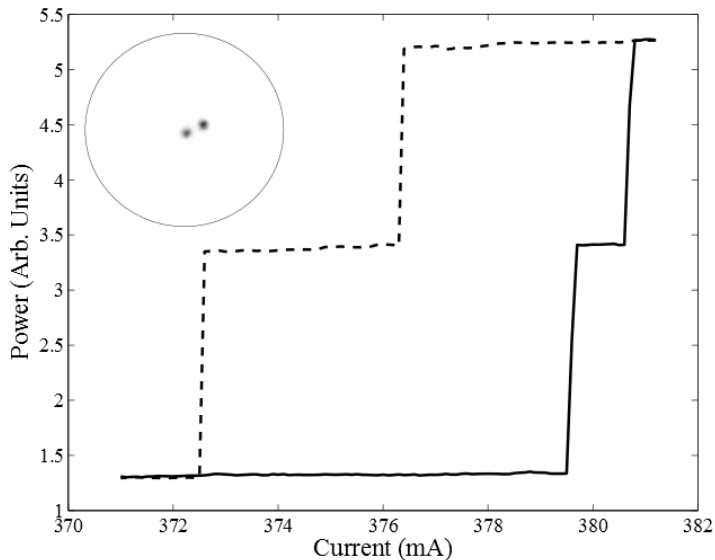
Figure 3.7: Light-current (LI) curve for two sample LCSs (shown in inset). The solid line refers to increasing current and the dashed line to decreasing current. Measurements taken at 0.1 mA intervals at a rate of 1 mA per second to avoid thermal hysteresis.

followed by disordered extended states. Evidence for these states, stemming from the LCS with the lowest threshold, is visible in the lower right part of the aperture in Fig. 3.6(a). Details on the LCSs and pattern evolution beyond threshold can be found in [19].

The appearance of each LCS is abrupt and we observe hysteresis when the current is ramped up and down, i.e. each LCS shows bistability. Figure 3.7 illustrates this phenomena for two sample LCSs shown in the corresponding inset. The right one switches on abruptly at about 379.5 mA, the left one only slightly later at about 381 mA. If the current is decreased again, the latter survives till about 376 mA, the former till 372.5 mA. In between 376 mA and 379.5 mA the two LCSs are simultaneously and individually bistable, i.e. they can be independently switched on and off by an external writing pulse [18, 19, 87]. This represents a 2-bit memory, which is interesting for optical information processing when extended to more channels that can display the potential for massive parallelism in broad-area VCSELs. The details of the hysteresis loops are different for distinct LCSs
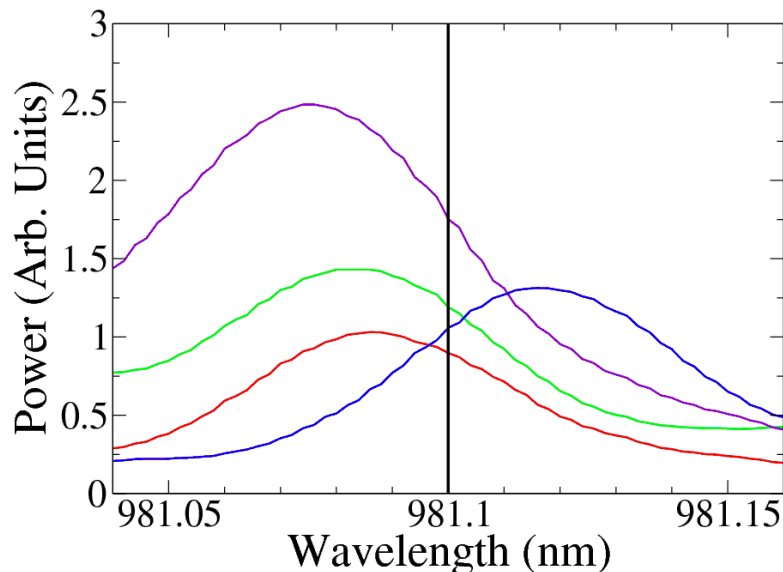
Figure 3.8: Optical spectra taken with the OSA of four LCSs just above their respective thresholds. The vertical black line denotes the peak reflection of VBG 1. The LCS denoted by the blue curve has the lowest threshold followed by red, green and purple. Extracted from [20].

and also depend on alignment. Typically switch-on occurs to the single-humped fundamental LCSs as demonstrated in Fig. 3.7. Corresponding scenarios are described in [18, 19, 87, 160], but a direct transition to multi-humped and ring-shaped states leading to single and multiple vortex solitons is also possible [161].

The reason for the difference in threshold for the different solitons as well as for the preference of certain locations lies in growth irregularities of the semiconductor material. This phenomenon will be described and illustrated in detail in Chap. 4 and is summarized here. If the cavity resonance of the VCSEL is spatially varying, the linear gap between the grating frequency and the cavity resonance is changing in space and a minimum value of the detuning for switch-on is met at different locations or different injection currents. Hence the lasing will start first at the most reddish location with the smallest gap. This is illustrated in Fig. 3.8 (extracted from [20]) which shows the absolute wavelength of four LCSs just above their respective thresholds. The emission wavelength of LCSs is usually blue detuned to the peak reflection of the VBG and increases with increasing

injection current. With increasing currents more locations reach the critical detuning value and additional LCSs switch on, whereas the LCSs formed originally may give way to high-order compound states and extended, off-axis lasing states. This motivated the idea of mapping variations in the cavity resonance of the VCSEL with a high spectral resolution and it will be explored at length in Chap. 4.

The basic properties of cavity solitons have been established but in order to be classified as cavity solitons, these micro-lasers need to fulfill four conditions. A cavity soliton must be self-localized, bistable, independent and mobile [17, 18, 162]. Localization ensures that CSs are confined by non-linearities and not boundary conditions or disorder. Independence means that CSs are not part of large pattern. Bistability was previously introduced and is illustrated in Fig. 3.7. Mobility is required to ensure that CSs have some freedom to move in the transverse aperture of the VCSEL, thus excluding that CSs are transverse modes of the cavity.

The fact that each individual spot has approximately the same size and dimensions means that their shape is determined by non-linearities and not by the spatial disorder of the aperture. This confirms the locality of these spots in the transverse aperture of the VCSEL.

Bistability is illustrated in Fig. 3.7 and confirms that in between 376 mA and 379.5 mA the two LCSs are simultaneously and individually bistable. This means that for each spot, within this injection range and for a given current, there exists two possible states, i.e. on or off.

The LI curve in Fig. 3.7 shows that each spot has a unique injection current threshold. This indicates that each spot is independent and does not belong to an extended pattern. A second approach [20, 163] to demonstrate independence will be introduced in Chap. 5. An external laser beam, injected from the back of the VBG, is used to switch different spots on and off without altering the states of the other spots.

In theory, a laser cavity soliton can exist anywhere within the transverse aperture of the VCSEL [16, 162]. LCSs will couple to parameter variations and drift [16, 164] until they either disappear from the system or reach a point in which all gradients vanish at a local extremum of the landscape imposed by the

variations. Spatial LCSs in real systems are usually pinned by defects resulting from fluctuations during the epitaxial growth process [19, 163]. These preferred locations are the ones where we find LCSs in Fig. 3.6(a) and are referred to as traps or defects. However, some minor external influence on the position of the LCSs is possible by alignment changes in the external cavity. This degree of freedom within the different traps of the aperture can be used to instigate the interaction of two LCSs. This can lead to their synchronization due to phase and frequency locking. This phenomenon will be discussed in detail in Chap. 5.

Chapter 4

Spatial Emission Structures and Disorder Mapping in VCSELs with Frequency Selective Feedback

In this chapter, the spatial and spectral properties of a broad-area VCSEL with frequency-selective feedback by a volume Bragg grating are addressed. The investigations focus on a self-imaging external cavity. Deviations from the self-imaging condition and their effects on the pattern formation are investigated. The experiment was also proven to be a reliable tool for mapping variations in the cavity resonance of the VCSEL, i.e. growth irregularities in the laser structure.

As discussed in Chap. 3, volume Bragg gratings are compact, narrow-band frequency filters which prove to be of increasing use in photonics. One particular application is the wavelength control of edge-emitting laser diodes (EELs), where VBGs can stabilize the emission wavelength very effectively against the red-shift connected to an increase of ambient temperature or to the Ohmic heating due to increasing current [165, 166, 167]. In addition, the spectral and spatial brightness of broad-area EELs can be increased significantly by the feedback from a VBG [165, 166]. Commercial versions are referred to as wavelength-locker or power-locker.

Frequency-selective feedback was proposed, and demonstrated, to provide some control of transverse modes also for VCSELs, both for medium-sized devices emitting Gaussian modes [12, 168] as well as for broad-area devices emitting Fourier modes [155]. These investigations used diffraction gratings and the only investigations using VBG were performed by our group at the University of Strathclyde with a focus on the close-to-threshold region where bistable spatial solitons are formed [19, 169]. This work reports experiments on how the solitons formed at threshold give way to spatially extended spatial structures and analyzes their properties quantitatively. Similarities and differences to the edge-emitting case will be discussed.

4.1   Analysis of Spatial Emission Structures

4.1.1   Experimental Results

This work is focused on a specific setup of the external cavity close to a self-imaging situation. The effects of deviation from the self-imaging condition on the pattern formation are investigated. These effects are not only important for pattern formation as investigated in this chapter and feedback experiments for modal control [12, 155, 168], but there is recent interest in using self-imaging, or close to self-imaging cavities, for studying large arrays of coupled lasers [170, 171] and coupled laser solitons [172]. Deviations from the self-imaging condition modify the strength of coupling between the oscillators via the non-locality introduced. Hence, a proper characterization and thorough understanding of cavity properties near a self-imaging situation is required when exploring synchronization dynamics and frequency and phase locking in these systems. These phenomena will be investigated in detail in Chap. 5.

4.1.1.1   Alignment of the Self Imaging Cavity

The basic experimental setup is illustrated and described in Chap. 3. The VCSEL is coupled to the VBG via a self-imaging external cavity. Every point of the VCSEL is imaged at the same spatial position after each round trip therefore
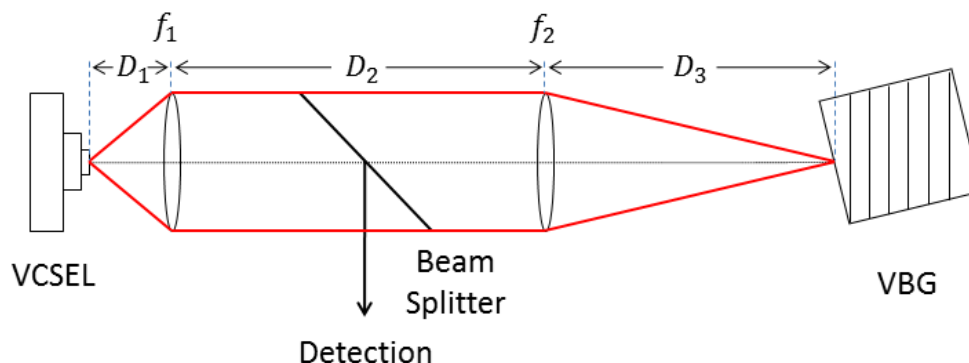
Figure 4.1: Schematic diagram of the self-imaging cavity. VCSEL: Vertical-cavity surface-emitting laser, $f_1 = 8$ mm: Collimation lens, $f_2 = 50$ mm: Focusing lens, VBG: Volume Bragg grating.

maintaining the high Fresnel number of the VCSEL cavity. The external cavity consists of an aspheric lens f_1 with a focal length of 8 mm and a plano-convex lens f_2 with a focal length of 50 mm arranged as an afocal telescope as seen in Fig. 4.1. Therefore, the magnification factor M of this telescope is determined by the ratio of the two focal lengths. The position of the first lens, D_1, is adjusted to provide the best collimation of the VCSEL output. The distance between the two intra-cavity lenses, D_2 should be $f_1 + f_2$ for an afocal telescope, where f_1 and f_2 are the focal lengths of the collimation lens and the focusing lens, respectively. In reality this is difficult to adjust because the lenses are thick, i.e. D_2 should refer to the distance between the principle planes, which is not easy to measure. In addition, there is no simple criterion for aligning D_2 just from observing images of the VCSEL output on a CCD camera. Therefore, the first alignment of the external cavity was setup with an approximate placement given by the focal lengths of the lenses. This alignment will be improved and validated as discussed later in Sec. 4.1.3.

Taking dispersion data from the manufacturer into account, the nominally 8 mm collimation lens and the 50 mm focusing lens have an effective focal length of respectively 8.07 mm and 50.79 mm at 980 nm. The principal plane of a plano-convex lens (or a nearly plano-convex lens as the aspheric lens) at the
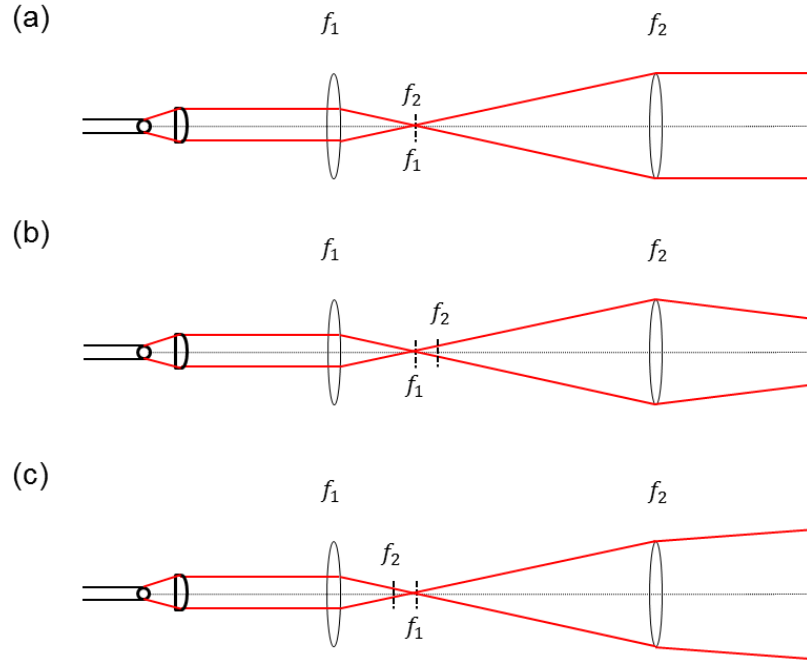
Figure 4.2: Schematic diagram of the telescope when (a) the intra-lens distance D_2 is correct, (b) the intra-lens distance D_2 is too long and (c) the intra-lens distance D_2 is too short.

curved side should be directly at the tip. The intra-cavity beam splitter (BS) makes the diffractive length about 0.8 mm shorter than the real length. Hence the distance between back (curved side) of the collimation lens and the front (curved side) of the focusing lens should be (8.07+50.79+0.8) mm = 59.66 mm. In the setup, the distance from the front side of the mount of the collimation lens to the back of the mount holding the focusing lens (each adds 1 mm) is the only convenient distance to measure and was taken to represent D_2. The thickness of our lenses is 3.69 mm and 5.3 mm for the collimation lens and the focusing lens, respectively. Therefore the self-imaging intra-cavity distance is estimated to be (59.66+3.69+1+5.3+1) mm = 70.65 mm. Obviously, adjusting this distance only by measurement with a caliper will have an uncertainty on the order of $\pm$ 0.5 mm.

In order to confirm these considerations, another experiment was set up to
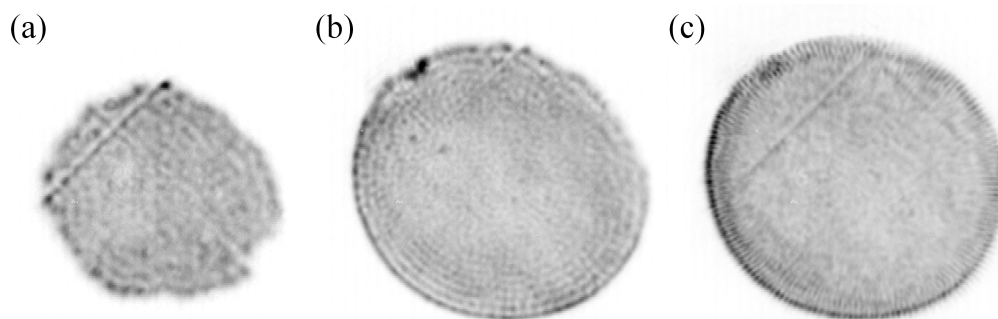
Figure 4.3: Near field intensity distribution of the VCSEL with feedback from a VBG (a,b) and a plane mirror (c). The injection current was (a, c) $I = 450$ mA, and (b) $I = 550$ mA. Other parameter: T=70°C.

study the effects of the intra-lens distance D_2 on the divergence of the beam in detail. It consists of the same telescope with the exact same optics (i.e. a collimation lens, a focusing lens and a beam splitter) as seen in Fig. 4.2. A tunable laser is coupled into a single mode fiber. The collimated output beam is then injected into the telescope from f_1. It is expected that the beam coming out of the telescope at the focusing lens, i.e. f_2, has the smallest beam divergence if the intra-lens distance D_2 is correct (see Fig. 4.2(a)). Three scenarios are illustrated in Fig. 4.2. When the intra-cavity distance is correct the output beam is collimated (Fig. 4.2(a)), when it is too long the beam is converging (Fig. 4.2(b)) and when it is too short the output beam is diverging (Fig. 4.2(c)). The best output beam collimation was found for an intra-cavity D_2=70.65 mm, within ± 0.2 mm, which is considered to be the accuracy of the distance measurement. This falls into the range of the theoretically estimated distance of 70.5 mm and will therefore be used as the reference position.

Figure 4.3 shows the near field intensity distribution of the VCSEL with feedback from a VBG (Fig. 4.3(a,b)) and a plane mirror (Fig. 4.3(c)). The position of the VBG (or the mirror) closing the cavity at D_3 is determined from images like in Fig. 4.3(b) obtained at high current. When the boundaries of the aperture are sharp and well defined this is supposedly the self-imaging position. The telescope is still imaging the intensity distribution for correct D_1 and D_3 but incorrect D_2

(see the discussion around Eq. 4.5 later). However, for self-imaging of intensity and phase profiles, the intra-cavity distance needs to be equal to $f_1 + f_2$.

4.1.1.2 Feedback with a Plane Mirror

For completeness, the case of feedback with a plane mirror was first studied, i.e. without frequency selection. Figure 4.4 depicts the near field intensity distribution of the VCSEL with feedback from a VBG at several injection currents (first three columns on the left) and intra-cavity distances, and with feedback from a plane mirror (right column). The data given in the first column of Fig. 4.4 correspond to the optimized intra-lens distance D_2 established in Sec. 4.1.1.1. The laser starts at a quite low threshold of around 170 mA. The emission is characterized by a ring with fringes perpendicular to the aperture and this is very similar to what we observe in the free-running laser at lower temperature (see Fig. 3.2(d)). This preference for the perimeter is again a gain effect due to the current crowding.

If the current is increased, the inner part of the lasing aperture also starts to lase, but a certain preference for the perimeter stays (upper image, right column, Fig. 4.4). If the current is increased further, the output power increases further but the spatial structure stays essentially the same (lower images, right column, Fig. 4.4). Figure 4.5 shows the far field intensity distribution of the VCSEL with feedback from a VBG at several injection currents (first three columns on the left) and intra-cavity distances, and with feedback from a plane mirror (right column). The emission in far field (Fig. 4.5, right column) is quite broad with a disk-shaped structure on axis surrounded by a faint halo. At the transition between center and halo, one wavenumber is somewhat enhanced leading to a ring. The latter does not change much with increasing current. This means that this wavenumber is probably the one favored by the detuning between the frequency of the gain maximum and the longitudinal cavity resonance as expected for free-running devices of this kind [157].
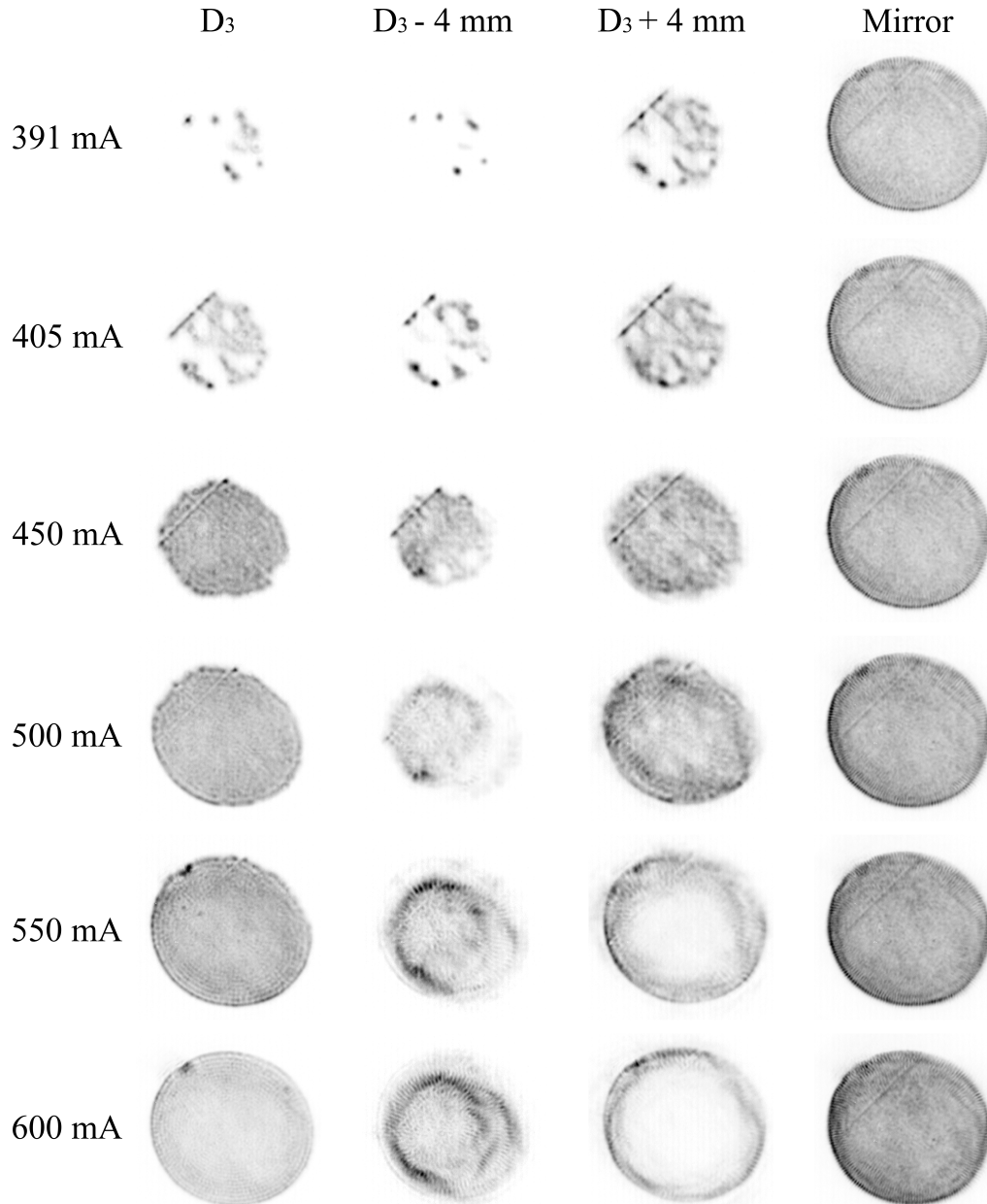
Figure 4.4:   Near field intensity distribution of the VCSEL with feedback from a VBG at different currents. Left column: D_3 at self-imaging distance; center columns: D_3 too short or too large by 4 mm; right column: Feedback with plane mirror. Other parameter: T=70°C.

	D₃	D₃ - 4 mm	D₃ + 4 mm	Mirror
391 mA				
405 mA				
450 mA				
500 mA				
550 mA				
600 mA				
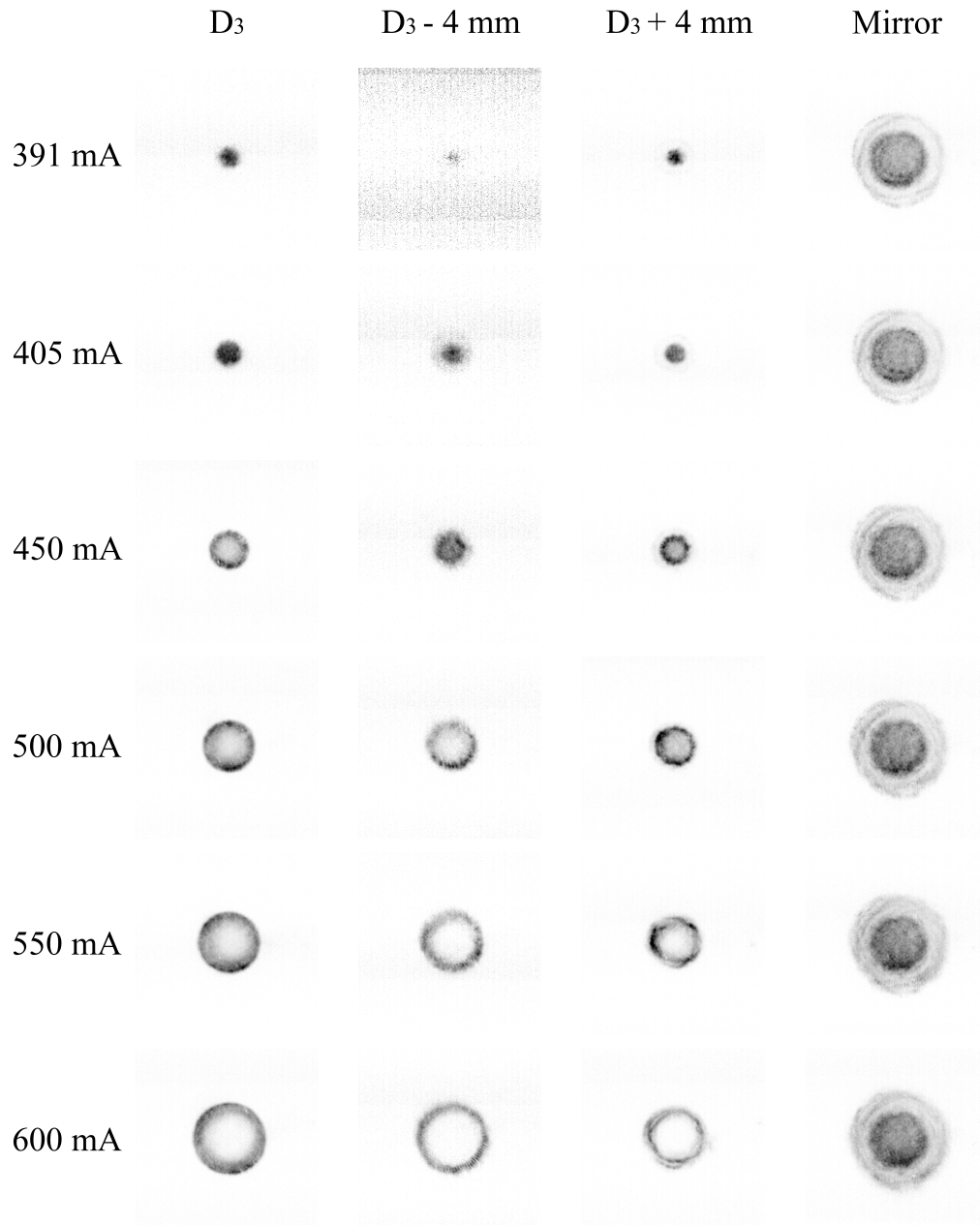
Figure 4.5: Far field intensity distribution of the VCSEL with feedback from a VBG at different currents. Left column: D_3 at self-imaging distance; center columns: D_3 too short or too large by 4 mm; right column: Feedback with plane mirror. Other parameter: T=70°C.

4.1.1.3 Feedback with a VBG

When feedback is provided by the VBG the lasing threshold is much higher (around 390 mA), and at this injection, small localized spots spontaneously appear in the near field of the laser, away from the boundaries (left column, uppermost image in Fig. 4.4). These spots are the laser cavity solitons (LCSs) investigated in [18, 19, 169] and previously introduced in Chap. 3. If the current is increased further, more LCSs appear at other locations and LCSs already formed give way to extended lasing states of lower amplitude (images in left column of Fig. 4.4). At about 500 mA essentially the whole aperture is lasing, whereas with feedback from a mirror this is already the case for about 400 mA. The patterns are actually quite similar to the ones obtained with a plane mirror, i.e. fine waves at high spatial frequency filling up the whole aperture of the device. However, the main difference is that the length scale now depends on injection current. When comparing Fig. 4.3(a) and 4.3(b), it is clear that the wavelength of these waves decreases with increasing current.

This feature can be much better investigated in far field images. The sequence depicted in the leftmost column of Fig. 4.5 illustrates that the emission is very much dominated by a single ring with negligible background, i.e. only a single transverse wavenumber is lasing. The solitons start to emit on axis and the wavenumber increases monotonically with increasing current. A quantitative investigation will be conducted in the next section.

If the distance D_3 is changed away from the self-imaging condition the far-field images do not show a significant change except for quantitative corrections to the wavenumber (analyzed in more detail in the next section), but the near-field images do. For a longer cavity (+4 mm) one observes a defocusing effect, i.e. the emission is shifting towards the boundaries of the aperture, especially at high currents. Inversely, for a too short cavity (−4 mm) the pattern seems to be focused, i.e. it contracts towards the center of the device.

Figure 4.6 gives an indication of the change of emission wavelength with increasing current of the spontaneous emission of the free-running laser (blue dashed line), with feedback from a VBG (black solid line) and feedback from a plane mirror (green solid line). The spontaneous emission of the free-running laser shows

Figure 4.6: Peak wavelength position with increasing injection current. Black solid line: Wavelength shift of one mode of the VCSEL with feedback from a VBG ($M = 6.25$). Green solid line: Feedback from a plane mirror. Blue dashed line: Spontaneous emission of the free Running Laser (FRL) at 70 °C. Red solid line: Fit to the FRL.

an approximately linear increase with a rate of 0.0035 nm/mA as discussed earlier in Chap.3. This is due to Joule heating. The VCSEL with feedback from a mirror shows a corresponding behavior, whereas the emission wavelength of the VCSEL with feedback from the VBG is essentially locked to one value (within 0.06 nm) given by the peak reflection of the VBG (981.1 nm). This matches qualitatively the observations in EELs discussed earlier [165, 166, 167]. A closer inspection shows that the wavelength is in tendency increasing, by about 0.06 nm, at the beginning (the soliton area) and then slowly decreasing (by about 0.02 nm).

4.1.2 Interpretation

The resonance conditions for a VCSEL cavity are identical to the ones of a plano-planar Fabry-Perot cavity in diverging light and were investigated in detail in [157, 173]. The dispersion relation of plane waves with a transverse wavenumber
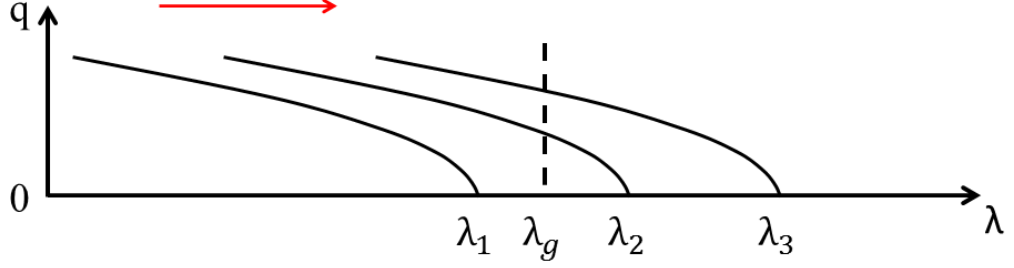
Figure 4.7: Schematic diagram illustrating the mechanism for selecting the transverse wavenumber. λ_{g}: Central reflection wavelength of the volume Bragg grating. λ_1 : VCSEL wavelength at low current. λ_2 : VCSEL wavelength at higher current. λ_3 : VCSEL wavelength at high current. The arrow corresponds to the wavelength shift induced by the increase of the VCSEL injection current.

q in the VCSEL is given by [157, 173]:

$$q_{\mathrm{VCSEL}} = \sqrt{\frac{8\pi^2 n_0 n_{gr}(\lambda_{\mathrm{c}} - \lambda)}{\lambda^3}} = \sqrt{\frac{8\pi^2 n_0 n_{gr}}{\lambda^3}} \sqrt{(\lambda_{\mathrm{c}} - \lambda)} = a\sqrt{\Delta\lambda}, \qquad (4.1)$$

where n_0 is an average refractive index of the VCSEL and n_{gr} is the group index, λ is the vacuum wavelength of the emission and λ_{c} is the vacuum wavelength of the longitudinal resonance. If the wavelength of the emission is fixed by the VBG, as indicated by Fig. 4.6, and the longitudinal resonance shifts due to Joule heating, then different transverse wavenumbers should come into resonance with the feedback starting with those at $q = 0$. This situation is schematically depicted in Fig. 4.7. λ_{g} represents the grating frequency, λ is the longitudinal resonance of the cavity, which increases with increasing temperature or current. Due to the dispersion relation of the VCSEL, one expects not only a selection of wavelength, but also of transverse wavenumber, i.e. the emission should correspond to a ring in the far field, which is exactly what is observed in Fig. 4.5. The emission angle should increase monotonically with current. Quantitatively, one expects an increase as the square root of the detuning of the VCSEL cavity, which we will be investigated below. Note that close to threshold, around $q = 0$,
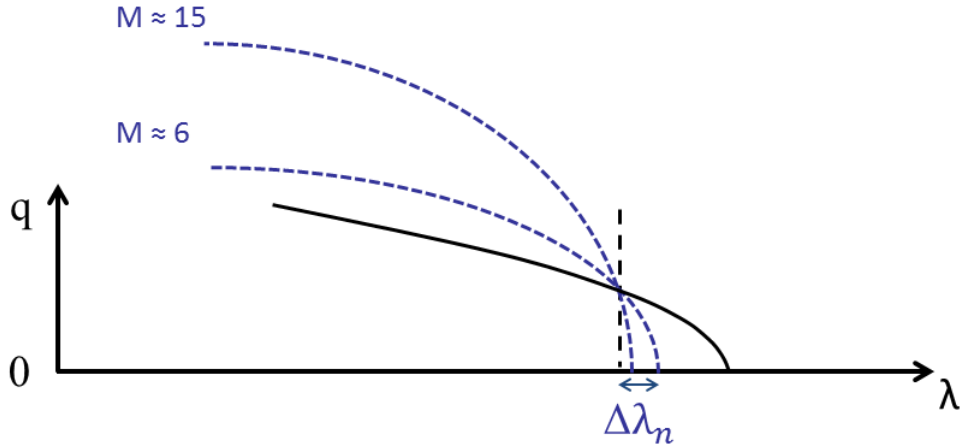
Figure 4.8: Schematic diagram illustrating the effect of the magnification M on the dispersion curve of the VBG. $M \approx 6$ corresponds to the short cavity and $M \approx 15$ corresponds to the long cavity. $\Delta\lambda_n$ is the wavelength shift between λ_g and the emission wavelength of the VCSEL.

nonlinear frequency shifts play a role leading to the possibility of bistability of solitons by reducing the wavelength gap between grating and VCSEL resonance. This increases the intensity, which reduces the carrier density, increases the refractive index and thus red-shifts the cavity resonance further. This positive feedback can create an abrupt transition to lasing [13, 18, 19] and can explain also the variation in wavelengths in the range below 420 mA in Fig. 4.6. If the cavity resonance condition is not quite homogenous then the transition to lasing takes place at different current levels. This explains the fact that the VCSEL starts to lase locally at the locations where the resonance is the most reddish, i.e. closest to the grating, and then slowly fills up the entire aperture as shown in the near field images (see left column in Fig. 4.4). This relationship can be used in order to provide a mapping of the disorder of the cavity resonance. This will be addressed later in Sec.4.2.

The small remaining wavelength shift observed in Fig. 4.6 at high currents (above 420 mA) is due to the fact that the dispersion curve of the VBG is not straight. This curvature means that there is a small difference between the operating wavelength of the device and the intercept as shown schematically in

Fig. 4.8.

From the condition that the phase shift in a single layer of the VBG should remain $\pi/4$ also at oblique incidence, the dispersion relation of the VBG can be expressed as:

$$q_{\text{VBG}} = M\sqrt{\frac{8\pi^2 n^2 (\lambda_{\text{g}} - \lambda)}{\lambda^3}} = M\sqrt{\frac{8\pi^2 n^2}{\lambda^3}}\sqrt{(\lambda_{\text{g}} - \lambda)} = b\sqrt{\Delta\lambda} \qquad (4.2)$$

λ_{g} is the peak reflection wavelength of the VBG and n is the refractive index of the glass host. From Eq. 4.2, one can see that if the telescope magnification M is increased then the dispersion curve of the VBG will straighten up thus reducing the wavelength shift $\Delta\lambda_{\text{n}}$. By equating (4.1) and (4.2), the emission wavelength for $\lambda_{\text{g}} \leq \lambda_{\text{c}}$ can be expressed as:

$$\lambda = \frac{\lambda_{\text{g}} - \frac{a^2}{b^2}\lambda_{\text{c}}}{1 - \frac{a^2}{b^2}} = \lambda_{\text{g}} - \frac{\frac{a^2}{b^2}(\lambda_{\text{c}} - \lambda_{\text{g}})}{1 - \frac{a^2}{b^2}} \qquad (4.3)$$

For $M = 6.25$, $n_0 = 3.51$, $n_{\text{gr}} = 4.1$, $n = 1.5$ and for a shift of λ_{c} by $0.0035\text{nm/mA} \times 210\text{mA} = 0.735\text{nm}$, one obtains $\lambda = \lambda_{\text{g}} - 0.10$ nm which is on the order of (though somewhat larger) what is observed in Fig. 4.6.

In order to verify the theoretical calculations from Eq. 4.3, the same experiment was performed with a second telescope arrangement, i.e. a longer external cavity, with $f_2 = 125$ mm giving a magnification factor M of about 15. Figure 4.9 illustrates the emission wavelength shift of the VCSEL with increasing injection for the longer external cavity. The shift is barely noticeable and within the accuracy range of the equipment it is not possible to quantify it. From Eq. 4.3, $\lambda = \lambda_{\text{g}} - 0.02$ nm with $M = 15.6$. This result is in good agreement with the experimental observation that the curve is essentially flat beyond the soliton region, i.e. above 430 mA. The remaining variations are below the limit of the accuracy of our OSA (about 0.03 nm relative accuracy within a single run). These results confirm the presence of frequency locking when feedback is provided from a VBG and also that the remaining frequency shift depends on the magnification factor of the external cavity. For a large magnification ($M >> 1$), $b >> a$, Eq. 4.3 gives $\lambda \approx \lambda_{\text{g}}$, i.e. perfect locking, because the dispersion relation of the VBG approaches a vertical line.
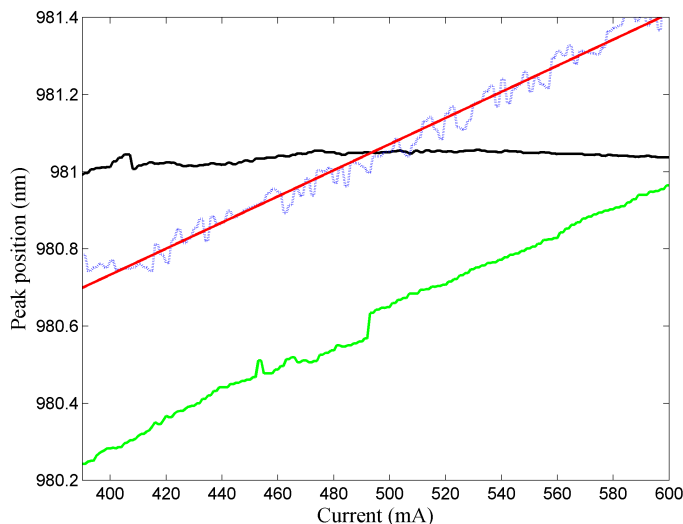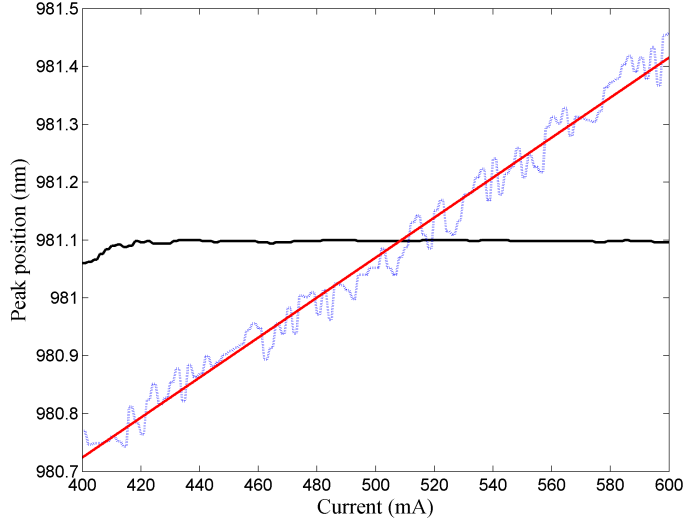
Figure 4.9: Peak wavelength position with increasing injection current. Black solid line: Wavelength shift of the VCSEL with feedback from a VBG ($M = 15.6$). Blue dashed line: FRL at 70 °C. Red solid line: Fit to the FRL.

As derived earlier in this section, the wavenumber of the emission should follow a square root behavior with detuning. This can be checked quantitatively using data like the ones obtained in Fig. 4.5. The results are shown in Fig. 4.10 which shows the transverse wave number of the emission as function of detuning between emission wavelength and longitudinal resonance. Figure 4.10 is produced by calculating the increase in diameter of the ring in far field with increasing injection current (see left column in Fig. 4.5). A plot of the wave number q as function of injection current is then produced. From this plot, the intersect I_0 and the scaling exponent s are determined by using the following fitting function $q(I) = c(I-I_0)^s$. The intercept I_0 corresponds to the zero detuning condition. The detuning scale can be then determined using the measured rate of 0.0035 nm/mA for the FRL. A fit is then applied to the wave number vs detuning curve which returns a scaling exponent with parameter error and a regression coefficient. Figure 4.10(a) shows a square-root behavior with a scaling exponent of 0.502 with a negligible parameter error (on the order of 3×10^{-3}) and a high-fidelity regression coefficient ($R^2 = 0.9989$) returned by the nonlinear fitting code.

4.1.3   Effects of Deviation from Self-Imaging

The effect of the VBG on wavelength locking is rather clear but the influence of the distances between the intra-cavity lenses and the self-imaging position, i.e. D_2 and D_3 respectively, remains to be investigated. For instance, Figs. 4.4 and 4.5 clearly indicate that D_3 has an influence on the spatial structures.

As shown in Fig. 4.1, a self imaging cavity is characterized by three distances. The first one is the distance D_1 between the laser and the collimation lens. It is found by adjusting the position of the lens until the divergence of the beam is minimal. The second distance D_2 is the distance separating both lenses also referred as the intra-cavity distance in the following; ideally it is $(f_1 + f_2)$. The last distance is the distance D_3 separating the second lens and the VBG. It is determined by moving the VBG until the near field image of the VCSEL has the sharpest boundaries. Matrix theory indicates that D_2 is not influencing the imaging condition for the intensity distribution. Since D_2 is the most poorly defined distance (in the sense that there is no obvious alignment criterion based on the VCSEL images like for D_1 or D_3, but only an estimated distance from the specifications of the lenses and the collimation experiment as explained in Sect. 4.1.1.1) it is the first distance investigated.

Figure 4.10(b) shows a dispersion relation similar to that obtained in (a) but obtained for an intra-cavity distance $D_2 = 78$ mm, away from the self-imaging condition. Even though the data follow a square-law like behavior, they are more scattered. The lower quality of the fit is also evidenced by a reduction of the regression coefficient to $R^2 = 0.9845$ and the parameter error returned is 11×10^{-3}. The scaling exponent turns out to be slightly different from the reference value of 0.502 found in Fig. 4.10(a). From Fig. 4.10(b), the fitting function returns a scaling exponent of 0.479. This scattered behavior combined with a reduction of the fitting quality and a deviation of the scaling exponent from 0.502 is typical also for other intra-cavity distances D_2 different from $D_2 = 70.5$ mm depicted in Fig. 4.10(a). For example, for $D_2 = 74$ mm, the scaling exponent is 0.508 and $R^2 = 0.9874$.

A tendency for slight variations of the details of the patterns (not the basic structure) from run to run away from $D_2 = 70.5$ mm was also observed. Hence
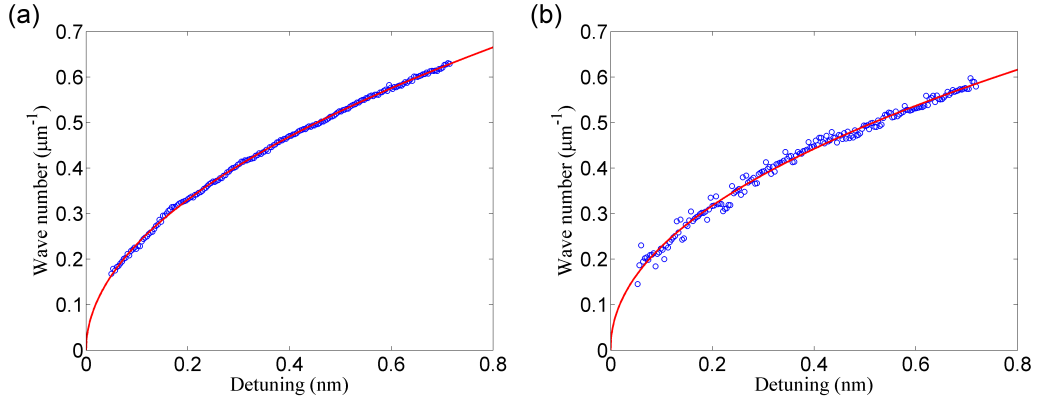
Figure 4.10: Transverse wave number of the VCSEL versus detuning between emission wavelength and longitudinal resonance (circles represent data points and solid lines fits). These plots are produced from plots of the wave number q vs current I by finding the intersect I_0 and the scaling exponent s using a fitting function $q(I) = c(I - I_0)^s$. The intercept I_0 then corresponds to the zero detuning condition. Starting from that, the rate of 0.0035 nm/mA is applied as a coefficient to define the detuning scaling, which is used to plot the fitting curve (red curve in the figure). a) For D_2=70.5 mm leading to a scaling exponent $s = 0.502$; b) for D_2=78 mm leading to a scaling exponent $s = 0.479$.

results averaged over three runs are reported in Tab. 4.1, which summarizes the effect of the intra-cavity distance on the scaling exponent over a larger range. Figure 4.11 illustrates the same results graphically. The first observation is that in general the averaged scaling exponent is oscillating around 0.500 with a tendency to larger values for smaller distances. However, there exists two positions at $D_2 = 74$ mm and 78 mm in addition to $D_2 = 70.5$ mm at which the averaged scaling exponent is again close to 0.500. However, as stated already above, the quality of the fits is lower and there is a larger variation between runs. This was characterized by calculating the standard deviation σ of the scaling exponents for the different runs (see Tab. 4.1, second to last column).

In order to get further insight into the nature of these deviations and variations, the width of the ring in Fourier space as a measure of the quality of wavenumber selection was analyzed (see last column in Tab. 4.1 and blue dashed line in Fig. 4.11). It has a minimum around $D_2 = 70.5$ mm, i.e. the anticipated self-imaging condition, and increases, except for one exception interpreted

Table 4.1: Effect of D_2 on the scaling exponent. Three rounds of data taking averaged. The data for both 70.5 mm and 72 mm are actually based on nine runs. The standard deviation σ of the scaling exponent is given as an indication of the quality of the fits. The width of the ring in Fourier space gives a measure of the quality of the wavenumber selection and it is given at 500 mA.

D_2 (mm)	Scaling Exponent	Intersect (mA)	St. deviation σ	Width (μm^{-1})
64	0.597	389	0.022	0.195
66	0.667	381	0.011	0.195
68	0.532	395	0.013	0.186
70	0.551	392	0.011	0.176
70.5	0.502	395	0.002	0.176
71	0.550	393	0.032	0.176
72	0.513	396	0.022	0.176
74	0.508	391	0.010	0.204
76	0.561	384	0.022	0.195
78	0.503	394	0.043	0.214
80	0.489	397	0.009	0.223

as scatter, monotonically away from this position. In particular, at 70.5 mm the ring is narrower than at both 74 mm and 78 mm (see also the width in Tab. 4.1). These observations reinforce the fact that the expected correct intra-lens distance $D_2 = 70.5$ mm is indeed the self-imaging position.

This can be understood by using ABCD matrix calculations. The external cavity consists of two lenses and a VBG as depicted in Fig. 4.1. Using the ray transfer matrix analysis and considering a single trip in the external cavity, i.e. before the reflection of the light by the VBG, the resulting matrix can be expressed by

$$M = \begin{pmatrix} 1 & D_3 \\ 0 & 1 \end{pmatrix} \begin{pmatrix} 1 & 0 \\ -\frac{1}{f_2} & 1 \end{pmatrix} \begin{pmatrix} 1 & D_2 \\ 0 & 1 \end{pmatrix} \begin{pmatrix} 1 & 0 \\ -\frac{1}{f_1} & 1 \end{pmatrix} \begin{pmatrix} 1 & f_1 \\ 0 & 1 \end{pmatrix}. \qquad (4.4)$$

After a round-trip through the external cavity and if $D_2 = f_1 + f_2 + x$ and
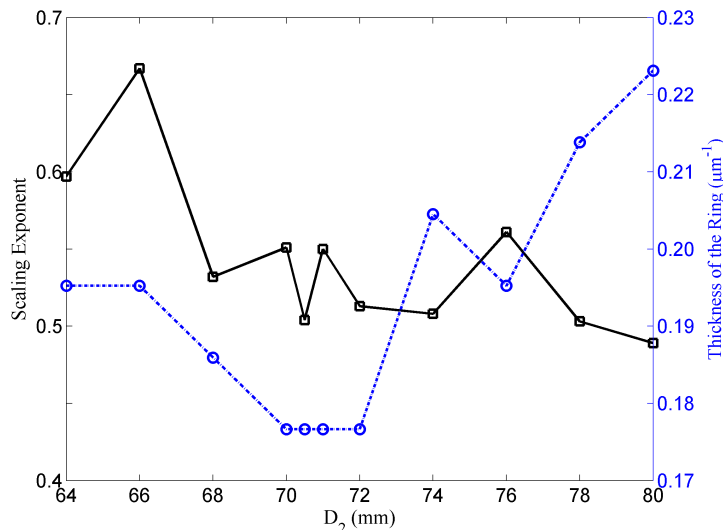
Figure 4.11: Scaling exponent and thickness of the far field ring as function of D_2. Black solid line: Scaling exponent vs. D_2. Blue dashed line: Width of the ring in far field vs. D_2.

$D_3 = f_2$ the matrix is expressed by

$$M_2 = \begin{pmatrix} 1 & 0 \\ -\frac{2}{f_1^2}\,x & 1 \end{pmatrix}. \tag{4.5}$$

A small misalignment x leads to a change of phase curvature or ray angle for the returning light. Hence the spatial Fourier spectrum broadens. Therefore, it can be assumed that the intra-cavity distance corresponding to the narrowest ring in far field, i.e. D_2=70.5 mm, corresponds to the self-imaging distance. On a quantitative level, for a ray emerging at a distance r from the optical axis, the change in angle is given by

$$\Delta\Theta = -\frac{2}{f_1^2}\,x\,r. \tag{4.6}$$

Taking $r \approx 0.05$ mm (half the radius of the VCSEL, i.e. an average r), and $x = 8$ mm (the maximal deviation investigated in Fig. 4.11), one obtains $\Delta\Theta = 1.3 \times 10^{-2}$. This corresponds to a change in wavenumber by $\Delta q = 0.08\mu\text{m}^{-1}$.

This is somewhat larger but comparable to the maximum change in wavenumber observed in Fig. 4.11. A change by $x = 0.2$ mm, i.e. the uncertainty in placing the lenses (see Sec. 4.1.1.1 for details), yields only $\Delta\Theta = 3.1 \times 10^{-4}$ and a corresponding change in wavenumber by $\Delta q = 0.002\mu\text{m}^{-1}$, supporting the notion that there is some tolerance in placing the lenses.

Finally, the influence of D_3 on the pattern formation is investigated. Figure 4.12 illustrates the variations of the scaling exponent as function of D_3. It suggests that D_3 also has an influence on the scaling exponent as well as on the manifestation of structures. It was already observed in Fig. 4.4 that for a too long cavity the near field intensity distribution seems to be pushed to the perimeter, whereas for a short cavity it seems to contract inwards. Also the boundaries are not as sharp and well defined. Similarly, these features can be explained by ABCD matrix calculations. After a round-trip in the external cavity and if $D_3 = f_2 + x$ and $D_2 = f_1 + f_2$ then the matrix is expressed by

$$M_3 = \begin{pmatrix} 1 & \frac{2f_1^2}{f_2^2}\,x \\ 0 & 1 \end{pmatrix}. \tag{4.7}$$

Because in this case D_3 is detuned, it means that the system is not imaging anymore. For a ray emitted at a radius r at an angle Θ, the returning rays hit at

$$r' = r + \frac{2f_1^2}{f_2^2}\,\Theta x. \tag{4.8}$$

This means that for $x > 0$ (too long cavity), the emission is pushed outwards, whereas for $x < 0$ (too short cavity) it is pushed inward. This is the tendency observed in the experiment. This effect should increase with increasing ray angle or wavenumber of emission, i.e. increasing current, which seems to be supported by the evolution of the near field patterns in Fig. 4.4.

A maximum variation of $x = \pm 4$ mm was investigated in Figs. 4.4, 4.5 and 4.12 and the highest transverse wavenumber in Fig. 4.10 is smaller than 0.7 μm^{-1}, i.e. about 100 mrad. Then the (single-pass) shift from Eq. 4.8 is $\Delta r < 20$ μm. For an uncertainty of $x = 0.1$ mm, it is less than 1 μm. Therefore, one can expect that D_3 can be adjusted to an accuracy such that a potentially remaining deviation from the self-imaging condition has a negligible influence on the
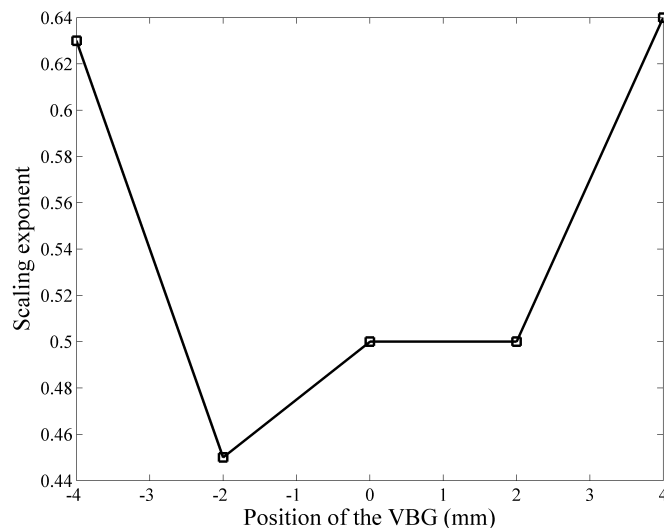
Figure 4.12: Scaling exponent as function of D_3. The zero position indicates the self-imaging position and a negative sign means that the VBG is moved towards the telescope. Inversely, a positive sign means that the VBG is moved away from the focusing lens.

pattern formation, especially in view of the fact that there is an explicit alignment criterion (sharpness of the images in near field, see Fig. 4.4). From Eq. 4.7 and Eq. 4.8 it is clear that the influence of x on D_3 evolves as f_1^2/f_2^2 leaving the variation very small for $f_2 \gg f_1$. This is in line with the expectation from geometrical optics that the depth of focus at the VBG increases for large f_2/f_1 because the incidence angles decrease. Hence, a long cavity is beneficial for reducing the sensitivity to a misadjustment of D_3 and for minimizing wavelength shifts (as discussed in Sect. 4.1.2), but comes at the expense of a large footprint and vibration sensitivity.

4.1.4 Conclusion

We have established that VBGs work as wavelength lockers for VCSELs as well as for EELs for which they are of significant importance for wavelength and modal control. VCSELs have already a lower temperature dependence than EELs because their wavelength shift is determined by the cavity shift of about 0.1 nm/K

(for GaAs based devices) compared to the gain shift of 0.2-0.3 nm/K relevant to EELs. Nevertheless, an external VBG can decrease this shift even more and the fidelity increases with increasing magnification of the imaging system, unfortunately increasing the footprint of the system.

For increasing temperature or current, the on-axis modes come into resonance first and here phase-amplitude coupling leads to the possibility of bistability [13] and, via self-focusing, soliton formation [18, 19, 169] as explained in detail in Chap. 3 Sec. 3.3. Beyond threshold, it is possible to stabilize single-wavenumber and narrow bandwidth emission with fairly high fidelity. These structures might find applications where ring-shaped foci are desired. The radius of the ring can be tuned by current or temperature. This feature constitutes an important difference between VCSELs and EELs and stems from the fact that VCSELs are intrinsically single-longitudinal mode devices. Hence, the wavelength locking is accompanied by an increase in mode order (transverse wavenumber) for increasing temperature (induced either directly via the ambient temperature or via Joule heating). In contrast, for an EEL, consequent longitudinal orders will shift into resonance. Therefore, the modal distribution will contain the mixture of low-order and high-order modes typical for broad-area EELs. However, the average mode order will not increase as much as in a VCSEL.

The effect of deviations of the external cavity from the self-imaging condition has also been analyzed. It turns out that the system is remarkably insensitive to deviations even in the millimeter range for a cavity length in the 100 mm range. This is good news for the robustness of experimental conditions. The self-imaging condition remains of interest for these kind of experiments because it allows for best feedback efficiency in terms of amplitude and phase. An autocollimation setup using only the collimation lens [12, 168] introduces an image inversion (relevant for Gauss-Hermite modes for example) but, due to the shortness of the focal lengths of typical collimation lenses, it is also likely that the length of the external cavity is larger than the perfect telescope length (an imperfect D_2 in our terminology). Hence, there is a phase curvature of the returning beam for Gaussian modes and a chance of ray direction for Fourier modes which results in an imperfect interference with the cavity mode. Also, deviations from the self-imaging condition make the returning field distribution more difficult to model,

though in principle methods like the Collins-integral are available [174]. On the other hand, a controlled deviation from the self-imaging condition might provide a convenient handle on coupling strength in arrays of lasers and laser solitons [171, 172].

4.2 Disorder Mapping

Based on the observation, in the previous section, that VBGs act as wavelength lockers for VCSELs, a simple method with a high spectral and spatial resolution for mapping variations in the cavity resonance of the VCSEL is reported in this section. The growth induced inhomogeneities of the VCSEL are of particular importance. The experiment relies only on a stand-alone laser (broad-area VCSEL) with a narrow-bandwidth passive filter (VBG) avoiding the need for an expensive tunable laser or high-resolution spectrometer.

A high uniformity of the resonance condition of laser cavities – and hence of the emission wavelength – is very important not only for laser arrays and broad-area lasers but also for the yield in gas sensing and dense wavelength multiplexing communication applications. These considerations are particularly important for semiconductor lasers due to their plano-planar cavities, but are also relevant for other monolithic laser designs with flat end mirrors. In particular, VCSELs require on the order of one hundred layers to grow and the cavity resonance is defined by the interference conditions between all these epitaxial grown layers. With modern semiconductor growth technologies like molecular beam epitaxy (MBE), metalorganic chemical vapor deposition (MOCVD) and techniques like rotating the wafer and in situ monitoring, systematic large scale gradients and inhomogeneities can be reduced to below $\pm 0.2\%$ over a 3 inch wafer [175]. However, the question of growth irregularities on small scales remains and has potentially harmful implications for applications. For example, a typical fingerprint of disorder, coherent backscattering or weak localization, is found in semiconductor microcavities [176]. Inhomogeneities limit the coherence of VCSEL-arrays [177] and hence their usefulness as high-power sources or for beam steering [177, 178]. One other repeated observation is that broad-area VCSELs tuned to emit on-axis

76

[155, 179, 180] display irregularly shaped filamentary spots instead of a fundamental mode filling the aperture. Inhomogeneities are also very important in the strong coupling regime [181, 182]. In the latter case, it is photonic disorder (cavity resonance) as well as excitonic disorder (quantum well) [181, 182]. Driven nonlinear microcavities should display an abrupt transition to self-organized spatial states like hexagons and cavity solitons [71]. In the case of extended patterns such as hexagons, experiments show that linear scattering due to disorder smears out the threshold as well as the distinct hexagonal symmetry [183, 184]. The change of length scale with inhomogeneities was proposed to characterize long range gradients [185].

As described in Chap. 3, cavity solitons [17, 169] are self-localized bistable waves in a nonlinear cavity and should be able to exist anywhere in the plane of a homogenous plano-planar cavity, but will couple to any perturbation of this translational symmetry. Therefore, gradients will lead to a drift [16, 164] which could be used in all-optical delay lines [72]. However, in reality the drift distance is found to be limited (the best result being about 40 μm [72, 87]). Hence the solitons are trapped in local minima of a potential landscape, which is created by the growth imperfections. Thus, typically experiments find them pinned to certain positions [17, 18, 19, 72, 83, 91].

It was suggested that this sensitivity of soliton position to growth imperfections can be used to probe the underlying disorder [83] instead of measuring spatially resolved reflection spectra of the micro-cavity with a tunable, narrow-linewidth laser [182, 186]. In [83] a mapping is demonstrated by looking at preferred locations of cavity solitons in a VCSEL with external injection operated below threshold, i.e. as amplifier. By spatially modulating the input beam with a fringe pattern, the solitons acquire new equilibrium positions given by local minima of the combined potential of frozen growth disorder and external modulation. Rotating the fringe pattern and averaging over the obtained distribution results in a map of preferred soliton positions including features beyond the local minima of the disorder-potential like ridges, but a quantitative interpretation is not straightforward. Indeed, an analysis of the data numerically obtained for comparison (Fig. 3 of [83]) indicates that the experiment is mainly sensitive to identifying the contour line where the cavity resonance has a certain detuning

(corresponding to the transition between the existence of solitons and extended states in a homogeneous system) to the frequency of the injected field, though this works with a high resolution. Probing contour lines corresponding to other frequencies is possible in principle but it would be very tedious in this scheme. It would imply that one needs to sweep the frequency of the injection, which is tedious in this approach, since the averaging over several fringe orientation needs to be done at every step. In addition, a tunable laser of high spatial and temporal coherence is still needed.

4.2.1 Experimental Realization

4.2.1.1 Motivations and Experimental Setup

A scheme using a VCSEL with frequency-selective feedback which can run stand-alone with any VCSEL or optically pumped VECSEL gain chip, i.e. without the need for a tunable laser, is demonstrated. It allows quantitative analysis of the fluctuations in the cavity resonance. Though, as seen earlier, it occurs in a system which shows cavity solitons at threshold [18, 19], it does not use this property but only the sensitivity of the laser losses being in or out of resonance with a narrow band filter in an external cavity. The first experimental realization of disorder mapping with the current setup was reported in [20]. However, it was not clear whether the fluctuations observed were actually related to the growth imperfections of the VCSEL aperture or to the imperfections of the VBG. Therefore, a more complete characterization of the system is considered in order to address this specific issue.

The experimental setup is illustrated and described in Chap. 3. The VCSEL is coupled to a frequency-selective element via a self-imaging external cavity. This provides a 1:1 mapping of each point of the VCSEL onto itself on subsequent round trips, thus providing a local probe needed for mapping. As described in Sec. 4.1.1.1, the imaging optics of the cavity consist of an aspheric lens with focal length 8 mm and a plano-convex lens with focal length of 50 mm arranged as an afocal telescope. This cavity will be referred to as the short cavity. In some realizations, similarly to Sec. 4.1, the second lens is replaced by one with a focal
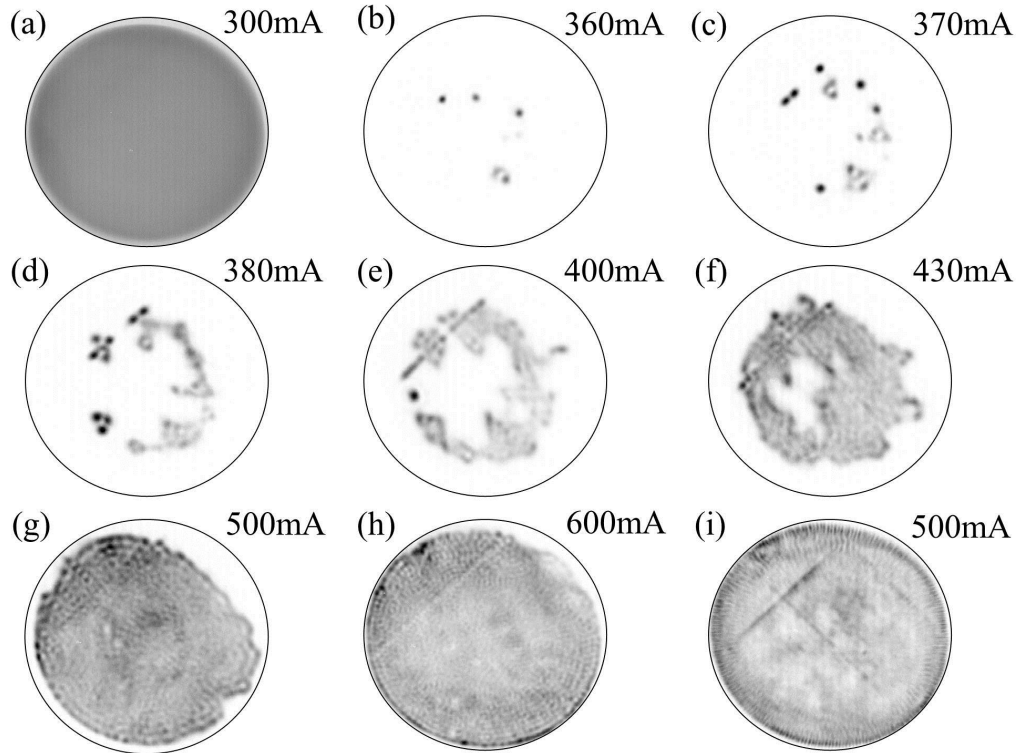
Figure 4.13: Examples of near field intensity observed for increasing current. a)-h) Feedback with VBG, i) feedback with plane mirror. The intensity is depicted in a linear gray scale with black denoting high intensity). The subpanels b)- h) are scaled to the maximum intensity occurring in the whole sequence. The black circle surrounding the near field patterns gives an indication of the boundaries of the aperture of the VCSEL. They are, however, not representative of the real aperture of the device. The slightly elongated shape of the patterns is due to the detection setup.

length of 125 mm and the external cavity length is increased correspondingly. This external cavity configuration will be referred to as the long cavity.

The VCSEL is grown by MBE and the wafer has a high homogeneity on long scales with a variation of the cavity resonance by less than 0.15% over the central 40 μm. As discussed in Chap. 3, the VBG is operated at normal incidence and provides frequency-selective feedback which breaks parity and can cause a wavefront tilt and a corresponding shift of the emission structures, thus breaking potentially locality [18, 87].

In this section another set of near field intensity images is shown. The images show essentially the same features which are already illustrated in Fig. 4.4. However, Fig. 4.13 shows a more detailed evolution of the near field intensity of the VCSEL for increasing current. Figure 4.13(a) shows the spontaneous emission emitted below threshold. It is essentially featureless, indicating that the gain is quite homogeneous. As discussed in Chap. 3, the enhancement at the perimeter is due to current crowding at the oxide aperture [154]. As a consequence the free-running laser is only operating at the perimeter and the emission is also strongest at the perimeter – and starts there at threshold – for the case of feedback by a plane mirror, i.e. without frequency-selection (see Fig. 4.13(i) and right column in Fig. 4.4). The latter shows some structures within the aperture, but with the exception of two defect lines they are not very pronounced. This is very different for the case of feedback from the VBG as illustrated in Fig. 4.13(b-h) where the laser starts to emit abruptly at very distinct spots (see Fig. 4.13(b)), the solitons [18, 19]. Increasing the current, the emission spreads over the aperture. Solitons arise at new positions (see Fig. 4.13(c, d, e, f)), and solitons formed previously give way to lower amplitude, more extended states, which correspond to off-axis emission as reported in Sec. 4.1. In other regions, the lasing intensity starts to grow in a continues way taking about 8-10 mA to reach the 90% point of emission. These observations can be interpreted in the following way: Initially, the cavity resonance of the VCSEL is at a higher frequency (blue shifted) than the reflection peak of the VBG. Ohmic dissipation due to the current increase heats the VCSEL and causes the resonance to red-shift. The first locations coming into resonance with the VBG are the most reddish ones of the disorder induced cavity resonance fluctuations. However, lasing across the whole aperture is not stable. This is the reason why lasing sets in locally and the solitons form due to nonlinear beam shaping. The blue most solitons are not stable either in this region (marked unstable soliton region in Fig. 4.14) and the frequency of the soliton cascades until a stable mode is reached which is slightly blue detuned to the peak reflection of the VBG (see Chap. 3). If the current is increased further, the cavity resonance at these reddish locations overshoots the reflection peak of the grating and on-axis states are no longer in resonance, but off-axis high-order modes are. In addition, the more bluish parts of the cavity come into resonance
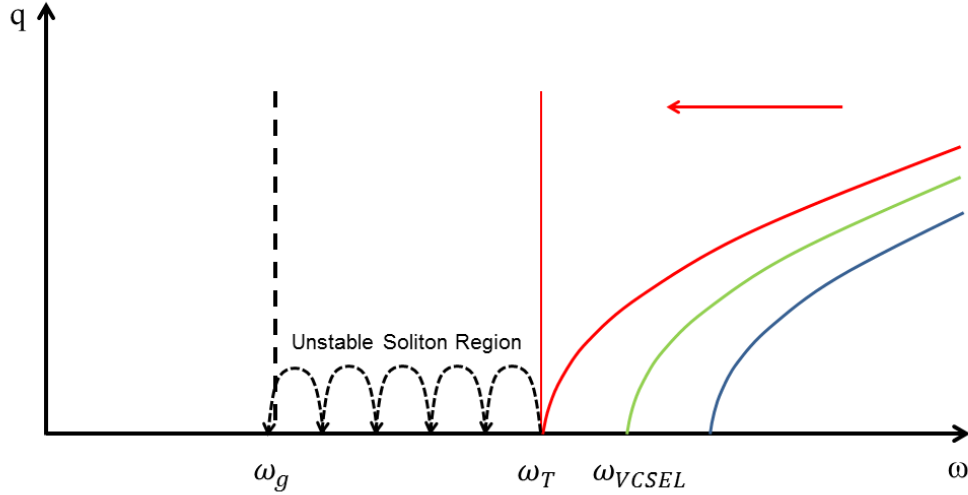
Figure 4.14: Schematic diagram illustrating the LCS switching mechanism. ω_g: Grating frequency. ω_T: Threshold frequency. ω_{VCSEL}: Cavity modes of the VCSEL. The arrow corresponds to the frequency shift induced by the increase of the VCSEL injection current. The lines representing the cavity modes of the VCSEL illustrate the dispersion relation of the transverse wavenumber vs. frequency for a plano-planar cavity as discussed in Sec. 4.1.2.

and start to emit. Hence the emission is spreading over the aperture. This scenario is illustrated in Fig. 4.14. In regions where solitons can not exist, lasing starts immediately with off-axis states as observed in Sec. 4.1.

These observations motivate the idea to use the difference in threshold at different locations to create a detuning map by using the tuning rate of the cavity, which can be measured for cavity modes without frequency-selective feedback, to convert from current to frequency. Initially, the VCSEL is biased just below the threshold for the first soliton. The current is then increased in 1 mA increments and at each current the near field intensity distribution is recorded. When all images are taken they are analyzed by a MATLAB program. The purely spontaneous emission images are disregarded and, starting from the threshold of the first LCS, the images are converted from gray scale to a binary black and white image with a threshold in between the spontaneous emission level and the lasing

states ($1/e^2$ point of intensity of the maximal amplitude). All of these binary images are then added together to produce one image in which the parts of the cavity which begin to lase first have the highest value and vice-versa. This is then normalized to a detuning using the known cavity tuning rate of 0.0035 nm/mA.

4.2.1.2 Experimental Results

Length Scales of Disorder

The disorder map of the VCSEL is shown in Fig. 4.15(a). Obviously, there is a lot of small-scale disorder within the 200 μm aperture on top of what seems to be a radial gradient. The most dark red locations are those where emission starts first. Typical length scales of disorder are about 10 μm and the span some tens of GHz. In addition to small-scale disorder, there is one distinct defect line with a width of 8 μm and a depth of about 24 GHz in the upper left part of the device running at an angle of about 45° to the horizontal, and some less expressed lines perpendicular to this. Since these are not apparent as dark or bright lines in the spontaneous emission image (see Fig. 4.13(b)) they seem to result from a dislocation line influencing cavity length and not from a defect line in the active area influencing gain. A cut through the map is shown in Fig. 4.15(b), which illustrates very well the small scale irregularities and the depth of the resulting potential wells and ridges.

The length scales observed are similar to the ones obtained in the injected VCSEL amplifier [83], but there it is difficult to assess the depth of fluctuations, as discussed in the introduction. We do not have a direct comparison with reflection measurements for our device, because our tunable laser is not of sufficient quality, but the numbers are in agreement with values in the literature [182, 186]. For a state-of-the-art material, [182] reports a variation of a few hundred μeV ($300\,\mu$eV≈ 70 GHz) and length scales of 5-20 μm. The sensitivity of the cavity resonance to length fluctuations can be numerically determined by performing a simple calculation. Indeed, for a Fabry-Perot cavity, a simple calculation shows

82
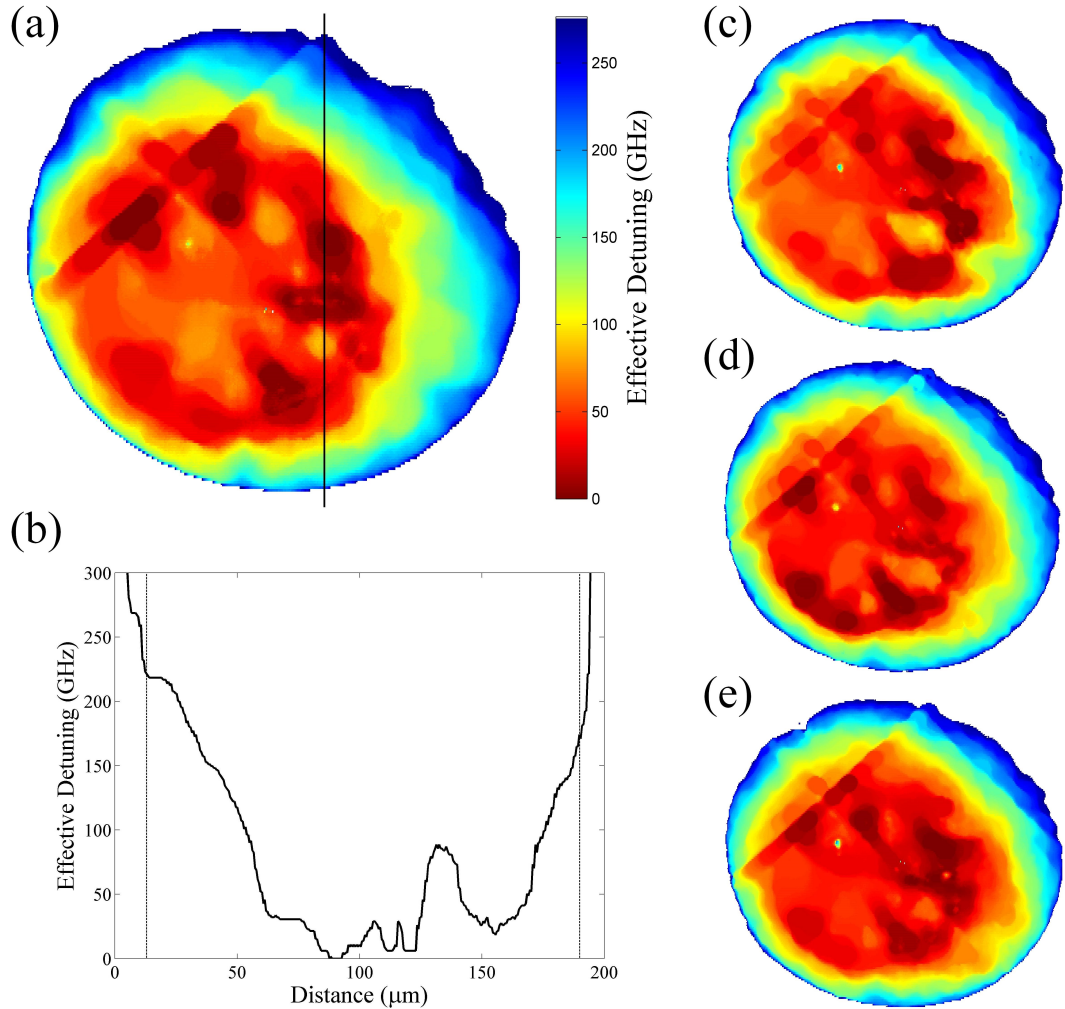
Figure 4.15: Disorder map of the VCSEL generated following the procedure described in the text. The pseudocolors denote the local detuning of the cavity resonance with respect to the location with the lowest frequency. (a) Short cavity, (b) cut through the 2D disorder map in (a) along the black vertical line, (c) long cavity, (d) and (e) long cavity with the VBG rotated by $\pm$ 90° compared to (c). The dashed lines in (b) denote the radial distances where the emission without frequency-selective feedback is, i.e. in images as in Fig. 4.13(a) and (i). Outside this range the notion of an effective detuning is not valid because the emission is strongly affected by the drop in gain and not by the properties of the cavity resonance.

that the cavity length variation ΔL induces a frequency shift

$$\Delta \nu = - \frac{\Delta L \, c}{L \lambda}, \tag{4.9}$$

where L is the cavity length, c is the speed of light and $\lambda = 980$ nm is the operating wavelength. An effective length of $L \approx 1.2$ μm is considered, which includes an effective penetration depth of the field into the distributed Bragg reflectors [187]. Then a monolayer variation of $\Delta L \approx 0.3$ nm corresponds to a frequency variation of $\Delta \nu \approx 76$ GHz. Since the cavity linewidth of a low-loss VCSEL is about 0.1 nm or 30 GHz, this explains the extreme sensitivity of the feedback patterns to disorder. Similar results are obtained with more accurate models of the multi-layer stacks forming a VCSEL [186, 188].

The measurements obtained are robust as evidenced, for example, by the images in Fig. 4.15(c-e), which are obtained in a different external cavity configuration (the longer cavity mentioned in Sec. 4.2.1.1). However, small quantitative deviations between the maps in Fig. 4.15(a, b) and (c-e) are observed. Between the subpanels in Fig. 4.15(c-e) the VBG was rotated by 90°, again leaving the map essentially the same. These checks demonstrate that disorder is probed in the VCSEL and not in the VBG. The non reproducible fine details are mainly related to minute changes of the alignment of the VBG. The major part of the deviations between different realizations is related to the impossibility to define what an optimal alignment of the VBG corresponds to. Even though the same technique, described in Sec. 4.1.1.1, was used to align D_3 there remains an uncertainty on the position of the VBG, especially for the longer cavity as discussed in Sec. 4.1.3. This issue does not affect the validity of this technique to map disorder and it remains of interest as similar sensitivity to alignment and wavefront distortion will occur if probing with a tunable laser.

Spatial Resolution

The lower limit of spatial resolution is given by the minimal area in a plano-planar resonator coupled by diffraction. In a plano-planar resonator, light will diffract over several round-trips and thus couples a finite part of the transverse

area limiting the locality of any spatially resolved measurement. This minimal area a^2 can be derived from the condition that the diffraction angle of the light multiplied by the effective propagation distance should equal the transverse size again,

$$a \approx \Theta_{\mathrm{div}} L_{\mathrm{eff}}, \tag{4.10}$$

with $\Theta_{\mathrm{div}} \approx \lambda_0/(\pi n a)$ and $L_{\mathrm{eff}} = v_{\mathrm{g}}/\kappa$. This results in the so-called diffraction parameter [189]. The mathematical derivation introduced in [189] includes a prefactor such that the diffraction parameter is defined by

$$a^2 = \frac{v_{\mathrm{g}} \lambda_0}{4\pi n \kappa}, \tag{4.11}$$

where v_{g} is the group velocity, λ_0 is the vacuum wavelength, κ is the field decay time of the cavity and n is the refractive index. The cavity transverse area divided by a^2 corresponds to the Fresnel number of the cavity. Taking into account only mirror losses, the field decay rate in the VCSEL is $\kappa \approx 90 \times 10^9$ s^{-1} leading to a space unit of $a = 4.4$ μm; adding intra-cavity losses, a field decay rate of $\kappa \approx 150 \times 10^9$ s^{-1} leads to a space unit of $a = 3.4$ μm. The exact amount of intracavity losses is difficult to estimate, but $a \approx 4$ μm and a corresponding resolution is a good estimate. This is in good agreement with the minimum length scales appearing in the subpanels of Fig. 4.15. It should be noted that – due to the disorder – the non-solitonic extended states are also changing on comparable, i.e. small, length scales as seen in Fig. 4.13(c-e) (see also [190]). The spectral resolution is given by the accuracy and reproducibility of the threshold determination. Since, in the case of a continuous switch-on, the transition between the spontaneous emission background to 90% of the final amplitude takes place in a current range of about 8-10 mA, the resolution is estimated to be better than 0.03 nm or 8 GHz. The nonlinear frequency shift at the abrupt switch-on of a soliton is in the same range, the variation of emission wavelength in the initial soliton region is about 0.06 nm for the short cavity and 0.03 nm for the long cavity as discussed in Sec. 4.1.3. This might lead to a slight overestimation of the depth of the wells (the most dark red points in Fig. 4.15) the solitons are nucleating in by up to 0.03 nm or 8 GHz. The worst case estimate can be based

on the variation of the peak of the emission spectrum with current, which stays constant within a range of 0.06 nm or 15 GHz for the short cavity and 0.03 nm or 8 GHz for the long cavity. A current increase of 1 mA corresponds to a detuning change of 1 GHz, indicating the potential for high spectral resolution.

Influence of Temperature and Carrier Variations on Resonance Condition

It is apparent from all subpanels of Fig. 4.15 that the areas close to the perimeter are strongly blue detuned. The main question is whether this is due to boundary effects or indicates a true change of effective detuning. For a clarification the radial distances at which the spontaneous emission (Fig. 4.13(a)) and the emission with a plane mirror (Fig. 4.13(i)) have maximum intensity were identified. These are identical within experimental resolution and denoted by the dashed vertical lines in Fig. 4.15(b). Outside these dashed lines, in the very proximity of the perimeter, the fairly abrupt reduction of gain at the transition to the un-pumped regions plays a role by delaying lasing and hence indicating wrongly a high detuning. Therefore, the range of the detuning map larger than about 150-200 GHz should be disregarded. However, the image with feedback from a plane mirror, Fig. 4.13(i), clearly illustrates that lasing states can exist quite close to the perimeter, but within the dashed lines, and have even higher amplitude than in the center. Hence, the more gradual blue shift outside of the center but within the dashed lines is interpreted to be related to a detuning effect and can be explained indeed with a variation of refractive index and hence cavity resonance due to radial temperature and carrier variations.

From [154], the thermal resistance of the device is $R_{\mathrm{th}} = 1/(2\lambda_c D) = 20\,\mathrm{K/W}$ with a thermal conductivity of $\lambda_c = 125\,\mathrm{W/(Km)}$ and a diameter $D = 200\,\mu\mathrm{m}$. At a current of 500 mA the dissipated power is about 1 W resulting in an increase in temperature of about 20 K. Numerical simulations indicate that the temperature in the center of the device is maximal and drops slowly by only 15% at a distance of 20 μm from the center (for a $D = 46\,\mu\mathrm{m}$ device) and the temperature drops quickly by another 15-20% thereafter [191]. Therefore, the temperature difference between the center and the perimeter of the device is about 3-9 K. The refractive

index shift of GaAs is about 2×10^{-4}/K and the refractive index difference is in the range of $\Delta n = 0.6 - 2 \times 10^{-3}$. From

$$\Delta \nu = -c\, \Delta n / (n\lambda_0), \qquad (4.12)$$

one then obtains a temperature induced detuning variation of the order of $\Delta \nu = 54 - 180$ GHz. These values and the shape of the radial profile, with a quite abrupt drop very close to the perimeter, seem to be in agreement with the findings in Fig. 4.15.

Again from numerical simulations [191], one can estimate that there are about 20% more carriers at the perimeter than in the center of the device [191]. Taking some approximate values for the phase amplitude coupling from [192], this translates into a refractive index difference of $\Delta n \approx 0.8 \times 10^{-4}$ and a frequency shift of about $\Delta \nu = 9$ GHz. This means that the carrier effect is of minor importance compared to the temperature distribution and thus the relatively high uncertainty is not important.

It has been demonstrated that the temperature is highest in the center whereas the carrier density is highest at the perimeter. Therefore, both variations lead to a reduction of refractive index at the perimeter compared to the center and thus to an increase of resonance frequency at the boundary. This confirms that the detuning obtained by this method (as well as in [83]) is actually an effective detuning, i.e. temperature and carrier variations affecting the refractive index and thus the cavity resonance in addition to the growth fluctuations.

4.2.2   Conclusion

A relatively simple and fast method to characterize quantitatively the disorder in a vertical-cavity device by frequency-selective feedback on scales relevant for device work and laser arrays has been demonstrated. This technique relies on electrical pumping but optical pumping of VCSEL or VECSEL structures should also be straightforward. The main advantage to this method is that there is no need of a high-quality tunable laser. However, since this method relies on the light emitted by the structure itself, it is only suitable to characterize hot devices, not the cold cavity, i.e. the growth-induced fluctuations alone. Since they occur

typically on different scales, this does not seem to be a major drawback. In addition, it enables probing of temperature inhomogeneities due to mounting imperfections as observed in some lasers.

Though this might be a drawback in some cases, it should be noted that the variations introduced by pumping are usually on large scales and thus the intrinsic disorder can still be resolved as demonstrated here. Obtaining a good map of the inhomogeneities would also be a first step for a compensation scheme, where the basics were recently demonstrated using the carrier-induced refractive index shift stemming from an external light beam with suitable spatial modulations to compensate the built-in length fluctuations [193].

Chapter 5

Frequency and Phase Locking of Laser Cavity Solitons

As demonstrated earlier, spatial LCSs in real systems are usually pinned by traps resulting from fluctuations during the epitaxial growth process [19, 160]. Besides fixing the position, these traps induce a shift in the LCS natural frequency [19, 194]. The diversity in natural frequencies among LCSs pinned by defects is a critical ingredient of their description in real systems. The frequency shift depends on the characteristics of the defect itself and typically is different for each of them. A demonstration of phase and frequency locking is established in this chapter. In particular, it is verified that the interaction of pinned LCSs with different intrinsic frequencies can be suitably described by the Adler locking mechanism [195]. Both experimental and theoretical investigations also demonstrate that the coupling, if strong enough, can overcome the natural disorder leading to a synchronous regime characterized by emission at a common frequency with a phase difference that has a precise dependence on the frequency difference.

5.1 Coupled Lasers and Synchronization

Lasers are a famous example of self-sustained nonlinear oscillators, which have, within the limitations of the cavity setup, the freedom to choose frequency and polarization. The phase of the oscillation of the electromagnetic field is not deter-

mined but results from the spontaneous breaking of the time symmetry present for cw pumping. Hence, the phase is a Goldstone mode of the dynamics and couples easily to perturbations, such as, for example, spontaneous emission. As a result of the induced phase diffusion [196], a laser has a finite linewidth (Schalow-Townes limit) and the mutual coherence between two independent lasers will be limited even if they have the same center frequency. Therefore, the phenomena of frequency and phase locking caught a lot of attention by which coupled lasers can synchronize their frequency and phases to achieve coherent emission [197, 198, 199, 200].

A mathematical model known as the Kuramoto model [201], named after is inventor Yoshiki Kuramoto, has been widely used during the past few decades to model the behavior of a large array of coupled oscillators with different intrinsic frequencies. In this model, coupling between the oscillators in the network happens through the sine of their phase differences. This model successfully describes synchronization in a variety of systems such as biology, physics, chemistry or neuroscience [202]. However, when the coupling between the oscillators is strong enough such that they all exhibit the same phase, i.e. one big oscillator, their interaction is well captured by the Adler model [195]. The Adler locking mechanism has relevance in biological clocks, chemical reactions, mechanical and electrical oscillators [203]. In optics, frequency locking of the Adler type was first observed in lasers with injected signals [204] with more recent generalizations to coupled lasers [199], the spatio-temporal domain [205], quantum dot lasers [206] and frequency without phase locking [207].

Laser synchronization is just a special example of synchronization dynamics of coupled oscillators, which is of high importance in all fields of Nonlinear Science [203, 208]. The first reported observation of synchronization was made by Christiaan Huygens on two pendulum clocks as early as in the 17th century. Biological examples of coupled oscillators include synchronously flashing fireflies [203, 208], pacemakers cells in the heart [209], chorusing crickets [210] or glycolytic oscillations in yeast populations [211]. Synchronization is not only limited to physics and biology but is also present in social behavior. Unintentional synchrony is found in the applause of a large crowd after a performance. Collective synchronization

can also result in undesirable effects in civil engineering where synchronous lateral excitation by pedestrians caused the Millennium bridge in London, a few days after it opened, to sway from side to side [212]. It has also been shown that people can synchronize in various ways while interacting. Several studies reported the existence of synchronization in postural sway [213, 214], walking [215, 216] or conversation pausing frequency [217]. A recent study examined the temporal structure of non-oscillatory actions such as language, facial and gestural behaviors during a conversation between two persons [218] and synchronized matching behaviors of the interlocutors was demonstrated. This confirms that synchronization is part of our everyday life and can be triggered by something as simple as human interaction.

In laser physics, frequency and phase locking has caught a lot of attention in various fields such as high power coherent emission obtained by large arrays of synchronized lasers. Robust synchronization was achieved in arrays showing discrepancies in the frequencies of the free running lasers composing the array [178, 219]. This frequency shift between the different lasers forming the array is a good analogy to the frequency discrepancies exhibited by the LCSs in our system (see Chap. 3 Sec. 3.3). High power output was also observed in large arrays of synchronized microwave oscillators [220]. Synchronization of chaotic lasers shows a lot of potential for secure communication [221, 222, 223].

As discussed in Chap. 4 spatial LCSs observed in real systems are pinned by defects caused by the growth irregularities of the semiconductor material. These defects also induce a frequency shift of the LCSs. This means that LCSs are mutually incoherent and the obvious question is whether the disorder can be overcome so that several LCSs can become coherent emitters. A method which allows for compensation of the disorder would potentially provide control of the phase and frequency of LCS arrays. This would pave the way for the synchronization of several LCSs within the same aperture, thus making possible the creation of large arrays of phase and frequency locked LCSs.

5.2   Experimental Setup and Basic Observations

The experimental setup is illustrated and described in Chap. 3. The LCSs investigated in this chapter are labeled in Fig. 5.1 which shows a near field image of the VCSEL aperture taken at 396 mA. Note that the results presented in this chapter are obtained with VBG 1 at 70 °C unless otherwise stated. As discussed in Chap. 3 Sec. 3.3, each LCS emits at a different frequency. The frequency at which each LCS emits is given by a combination of VCSEL cavity resonance and external cavity resonance (feedback phase). Hence, some control on one of the resonance conditions is required in order to achieve frequency locking. However, the choice quickly leaned towards a control of the feedback phase since a modification of the VCSEL cavity resonance is experimentally awkward and requires the use of an external tunable laser. Therefore, in order to compensate for the inherent disorder of the VCSEL, which allows phase and frequency locking of two LCSs, the precise alignment of the VBG is very important. This is achieved by tilting the VBG with a PZT which allows minute tilts of the feedback with respect to the optical axis. This leads to a differential change of the external cavity length for the two LCSs and thus to a differential change in feedback phase. The coarse alignment of the VBG is controlled by fine adjustment screws. These however, do not provide sufficient precision to achieve locking of LCSs. A more precise, computer controlled scheme with a PZT, which is stabilized against drift by a servo-loop controlled by a strain gauge, attached to the VBG mount was implemented in the experimental setup.

The tilt β induced by the PZT in the horizontal direction is schematically illustrated in Fig. 5.2. A computer controlled voltage U applied to the PZT leads to a tilt of $\delta\beta/\delta U = 2.1 \times 10^{-5}/\text{V}$, a change of the external cavity length at a rate of $\delta L/\delta U = 0.628\ \mu\text{m/V}$, and a change of the resonance frequency in the external cavity by $\delta\nu/\delta U = 1.576$ GHz/V. More importantly for what follows, there is also a differential shift for two LCSs. If their distance projected onto a plane orthogonal to the rotation axis is Δx, this shift is given by

$$\Delta\nu = \Delta x\ \frac{2\nu_{FSR}\ \sin\beta}{\lambda}, \tag{5.1}$$
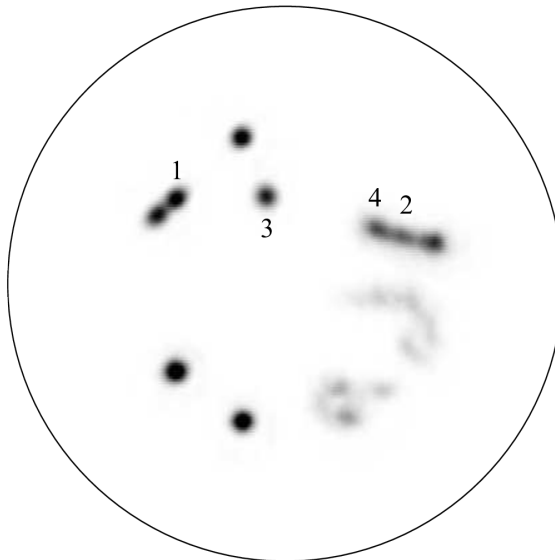
Figure 5.1: Near field image of the VCSEL aperture taken at 396 mA showing the relative position and numbering of a few solitons. Output VCSEL images, like all in the following, are in a linear gray scale with black denoting high intensity.

where ν_{FSR} is the free spectral range of the external cavity and λ is the operating wavelength of the VCSEL. The change of the ray angle after returning to the VCSEL (corrected for the magnification of the telescope) is $\theta = \beta$ M. The adjustment of the self-imaging condition is described in detail in Chap. 4 and the same procedure is applied here. After optimization the self-imaging condition is estimated to be within ± 0.2 mm with a reasonable depth of focus. However, small deviations from the self-imaging condition are not critical for the reported phenomena.

As explained in Chap. 2, LCSs will couple to parameter variations and drift [16, 164] until they either disappear from the system or reach a point in which all first order perturbations, i.e. gradients, vanish at a local extremum of the landscape imposed by the variations. These preferred locations are the ones where LCSs are found in Fig. 5.1 and, as discussed in the previous chapter, they arise from growth fluctuations in the semiconductor material. They will be referred to as traps or defects. This disordered landscape is frozen after the growth process of the semiconductor structure although some minor external
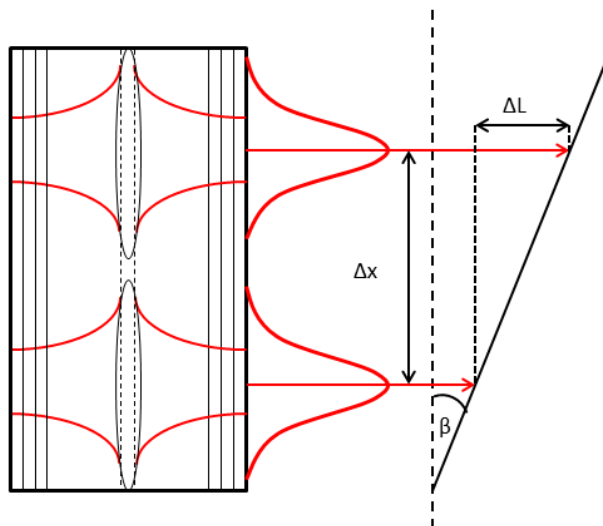
Figure 5.2: Scheme of VCSEL cavity carrying two LCSs with feedback from a tilted VBG. The tilt angle β of the VBG controls the mutual detuning of the two LCSs (see text for details). The pivot point is much further away from the optical axis in reality (about 30 mm).

influence on the positions of the LCSs is possible by alignment changes in the external cavity. In particular, a tilt of the VBG induces a tilt of the wavefront of the returning beam, which should lead to continuous drift of the LCSs in a homogeneous system. For a LCS in a trap, the tilt shifts the position where the potential minimum of the combined perturbation (frozen disorder plus tilt) lies and hence the LCS shifts to a new equilibrium position [19]. As the quantitative analysis in Fig. 5.3(a) shows, this shift is quite small. It should also be noted that the tilt is minute, about 0.15 mrad total, leading to a change of ray angle at the VCSEL smaller than 1 mrad, much smaller than the angular width of a LCS (about 50 mrad). The shift within the trap is also different for different solitons, which is expected for a disordered system because the curvature of the potential should vary randomly from trap to trap. At some critical tilt angle (larger than typically achievable with the PZT), the LCS disappears. The expectation is that the potential minimum disappears for a critical tilt and the LCS unpins and starts to drift. A corresponding transition between drifting and pinned patterns
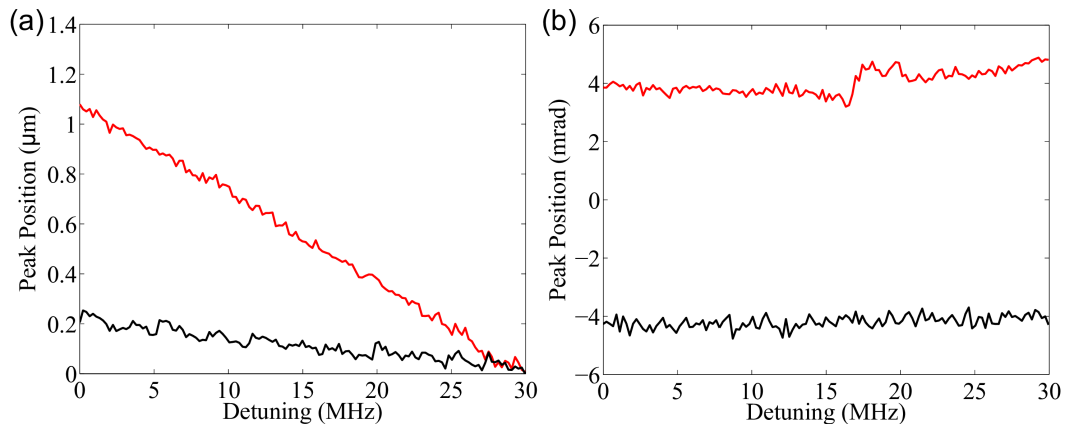
Figure 5.3: (a) Peak position of the near field profile as a function of the tilt angle for LCS 1 (red curve) and 2 (black curve); (b) Peak position of the far field profile as a function of the tilt angle. The curves are averaged over two runs and most of the undulations are likely to stem from measurement noise, although a deterministic contribution due to small-scale disorder within the trap cannot be ruled out. The zero of the y-axis in panel (b) is set at the center of the two individual angular centers of the far fields of LCS 1 and 2. For a better comparison with the results presented below the horizontal axis is scaled in the change of differential detuning between the two LCSs in the external cavity as obtained from Eq. (5.1). The total tilt is 0.15 mrad.

was found in [81]. In our system, an experimental investigation of the unpinning phenomenon requires simultaneous spatial and temporal resolution and has not been undertaken.

5.3 Experimental Results

5.3.1 Illustration of Frequency and Phase Locking of Laser Cavity Solitons

Investigations conducted on the interaction of LCSs were done on different pairs. In this chapter, results on LCSs with a separation distance between 36 μm and 79 μm are reported. The qualitative features of the observations are robust, but the details can vary a fair amount as one would expect since parameters

are affected by spatial disorder. Investigations only focus on the interactions of LCSs in different, separate traps. The coherence properties of compound, high-order states of LCSs in the same trap are a separate issue and more detailed investigations are needed in our system. This section illustrates both phase and frequency locking phenomena and a detailed analysis of the locking behavior will be investigated in Sec. 5.4 onwards. Note that VBG 2 is used in this section, thus the VCSEL was operated at a lower temperature of about $40\,°C$.

The following example illustrates the interaction of two LCSs and how the compensation of the inherent disorder of the VCSEL via the control of the external cavity, i.e. feedback phase, can lead to a synchronous regime characterized by emission at a common frequency with a phase difference that has a precise dependence on the frequency difference. The two LCSs were frequency and phase locked by both tilting the VBG and adjusting the injection current until maximum fringe visibility was achieved in far field.

To perform switching experiments the system requires an external writing beam. The WB allows switching of LCSs by shining it onto the locations which are known to support LCSs (see discussion in Chap. 2). The incoherent switching technique, i.e. no phase reference between the LCS and the WB, has been successfully demonstrated in several systems (frequency selective feedback and SA) [18, 19, 78, 91, 95] and is therefore well suited for individual spatial control of the LCSs in our experiment. The WB is an external tunable laser which is injected straight into the external cavity from the back of the VBG. The laser operates cw and the beam size is set, via a beam expander before entering the external cavity, so that it matches that of a LCS at the VCSEL surface, i.e. about 10 μm. The WB also needs careful alignment so that it is on axis with respect to the LCSs. Because the reflection peak of the VBG is very narrow, it is necessary to adjust the wavelength of the WB so that it falls outside the reflection bandwidth of the VBG and that sufficient power attains the VCSEL. The experiment described below is performed at a bias current at which both LCSs involved are individually bistable.

5.3.1.1   Observation of Phase Locking

Two spatially separated LCSs are incoherent implying that their combined far field is the incoherent sum of the intensity distributions of the individual LCSs as illustrated in Fig. 5.4(a). To overcome this a PZT is used to minutely tilt the VBG with respect to the optical axis. As a result, a pronounced fringe pattern is visible across the far field intensity profile as seen in Fig. 5.4(b). Its wavevector is parallel to the connection line between the two LCSs, i.e. the fringes are orthogonal to it. This far field fringe pattern is stable for longer than the exposure time of the CCD (20 ms), typically it can be observed for minutes to hours, once achieved. This evidences phase-coherence between the two LCSs over time spans orders of magnitude higher than the intrinsic dynamics (nanoseconds) and also higher than typical time scales of technical noise (microseconds to seconds). This indicates that this is a very robust phenomenon.

In order to evaluate both the fringe visibility and the fringe phase a cut through the fringe interference pattern is taken across the center of the far field intensity (see dashed line in Fig. 5.4(b)). Then a Gaussian profile modulated by a sine-wave is fitted to this cut as illustrated in Fig. 5.4(c),

$$y = y_0 + A \exp\left[\frac{-(\theta - \theta_0)^2}{2w^2}\right] \left[\frac{1 + M \sin(F(\theta - \theta_0) + P)}{1 + M}\right] . \qquad (5.2)$$

Here y_0 is the intensity offset, A is the amplitude, θ_0 is the peak center, θ is the angular spread, w is the width, M is the modulation depth or fringe visibility, F is the frequency of the sine modulation and P its phase. This allows us to experimentally obtain both the fringe phase and fringe visibility of the interference pattern in far field. In Fig. 5.4(c) the fitting function returns a fringe visibility and a fringe phase of about 0.6 and 1.5 π, respectively. The spacing of the fringes in far field is related to the separation of the two LCSs in near field. Indeed, from the Fourier theorem a field distribution shifted by a distance a in the near field, acquires a phase shift of $\exp(ik_\perp a)$ in the far field. Hence a, the separation of the interference source (here the LCS) in near field and the fringe period $\Delta\theta = 2\pi/F$ are related by

$$a = \frac{\lambda}{\Delta\theta}. \qquad (5.3)$$
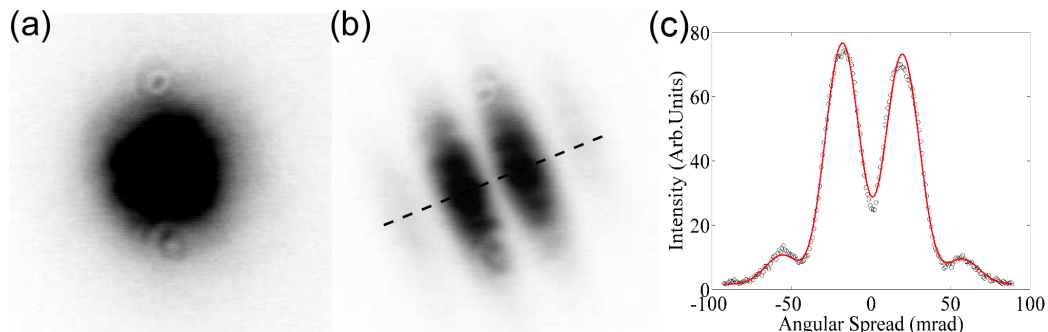
Figure 5.4: Far field images of the VCSEL for two LCSs separated by 28 μm, (a) before phase locking is achieved, (b) after careful alignment of the VBG and phase locking is obtained. (c) Cut of the far field intensity profile through the dashed line depicted in (b). The circles represent data points and the red solid line is a fit obtained with Eq. 5.2.

For a far field fringe spacing of 37.3 mrad obtained from the fit this calculation yields a near field separation of 26 μm which agrees very well with the measured LCS separation of 28 μm thus confirming that the interference comes from the two interacting LCSs.

5.3.1.2 Independent Control

LCSs are normally independent micro lasers, i.e. they are mutually incoherent. However, we have just established that under certain conditions robust phase locking can be achieved. Phase locking is only possible because LCSs can be independently controlled. It is not clear, however, whether the LCSs still show the same properties when they are in this locked state.

As discussed in Chap. 4 each individual LCS is trapped by growth imperfections in the laser. Despite the fact that LCSs are pinned in these locations, they still retain their position freedom. The local perturbations caused by the WB can affect the position of the LCSs. If the trap is large enough so that the dimensions of the LCS allow for movements within the trap, the WB can be used to move its the position within the same trap or to drag it out of the trap thus resulting in the extinction of the LCS. Similarly, it is also possible to switch on a LCS by shining the WB onto an empty trap. In order to do this the WB needs to be carefully tuned in frequency so that it is slightly blue detuned to the frequency of

the VBG peak reflection [224]. The images shown in this section were captured on the fly, both near and far field images were saved at a rate of 3 images/s. This relatively slow capture time did not allow us to capture optical spectra which would have slowed the process down to less than 1 image/s.

The investigations were done on a pair of LCSs with a separation distance of 49 μm. The images in Fig. 5.5 and Fig. 5.6 have been selected to illustrate a relevant state of the phase locking phenomenon. In total the whole process can take up to 10-15 minutes depending on the time required until switching is achieved. Figure 5.5 shows how the near and far field images evolve as the WB is moved across the laser aperture. After robust locking was achieved, with a fringe visibility of 0.43 and a fringe phase of 1.93 π between two LCSs (see Fig. 5.5(a)), the WB was shined onto the laser aperture slightly below the location of the bottom left LCS. This results in a fringe visibility being close to 0 (about 0.04) in far field, as seen in Fig. 5.5(b). Note that due to the very low fringe visibility the fitting function does not return any phase value, i.e. the far field profile is essentially Gaussian. Figure 5.5(c) shows the extinction of the bottom LCS by the WB. The latter was used to drag the LCS out of its trap in a region where it is no longer stable thus resulting in the extinction of the LCS. As a result the far field image consists of the remaining LCS seen in near field. The switch off time of a LCS is rather fast (a few ns) however, the process leading to the extinction of a LCS can take a few minutes as both the power and the wavelength of the WB need to be correctly tuned so that the interaction between the LCS and the WB is maximized. Once the bottom LCS has been switched off the next step is to switch it back on at the exact same location. This is achieved by shining the WB onto the former position of the LCS as seen in Fig. 5.5(d). In Fig. 5.5(e) the bottom LCS was switched back on at its exact former location by adjusting the wavelength of the WB until the resonance condition is achieved and a LCS appears. The fringe visibility was measured at 0.32 with a corresponding fringe phase of 1.79 π. As seen in Fig. 5.5(b, e) the WB causes a drop in visibility, i.e. the WB is not phase locked with any of the two LCSs thus resulting in a lack of coherence between the WB and the LCS. Figure 5.5(f) shows the two LCSs after the WB was switched off, the visibility was measured at 0.4 with a phase of 1.95 π. These parameters are comparable with these measured in
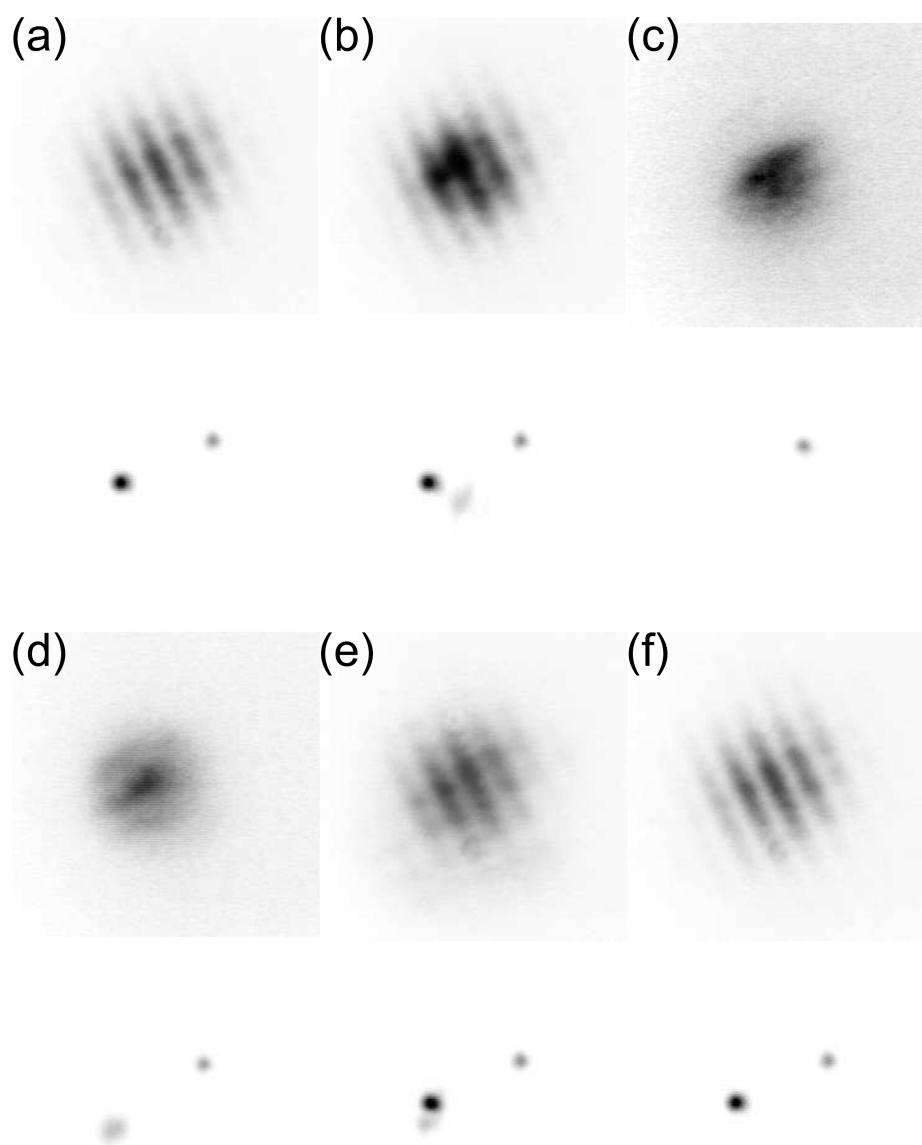
Figure 5.5: Upper row of the subcaptions: far field images, bottom row of the subcaptions: near field images. (a) Phase locking between two LCSs achieved by tilting the VBG until robust locking is obtained. (b) The WB is coupled inside the cavity through the back of the VBG, slightly below the location of the bottom LCS. (c) The bottom LCS is switched off by the WB which is then removed. (d) The WB is coupled back inside the cavity. (e) The bottom LCS is switched back on by shining the WB at its former location. (f) The WB is removed and the two LCSs remain. The VCSEL was operated at I=355 mA and T=39 °C.

Fig. 5.5(a) at the beginning of the experiment. The latter experiment was run several times and was always reproducible. When the LCSs were strongly phase locked, switching one LCS off and then switching it back on always resulted in phase locking with the same initial parameters. This confirms that when two LCSs are strongly locked the resulting state is not a single entity but two coupled LCSs. This means that the coupling between the LCSs is still weaker than their solitonic properties alone, i.e. they remain independently controllable LCSs.

For completion the same experiment was also conducted on the second LCS. The situation is illustrated in Fig. 5.6. The experiment was conducted in a similar way, the two LCSs were phase locked as seen in Fig. 5.6(a) with a visibility of 0.4 and a phase of 1.88 π. It was not possible to drag the upper LCS out of its trap either because it sits in a deeper defect and/or because it sits rather high in the bistability loop thus making the extinction much harder than the ignition. Figure 4.15(a) seems to confirm the former hypothesis as the LCS is located in a dark red region surrounded by lighter red regions of the map. Therefore, the WB is no longer used in the switching off process. Instead the feedback from the LCS was suppressed by blocking a fraction of the beam in the external cavity as close as possible to the VBG, i.e. where the magnification factor is the highest. This is only possible because the external cavity provides a large $6.25 : 1$ magnification factor. Therefore, by using a sharp object such as a razor blade, it is relatively easy to block the feedback from only one LCS. Figure 5.6(b) illustrates the situation after the feedback from the upper LCS was suppressed. In Fig. 5.6(c) the WB was turned on and no fringe pattern was observed in far field. Then as described in the previous paragraph the wavelength of the WB needs to be tuned such that it meets the resonance condition which can ignite a LCS at this specific location in the transverse aperture of the VCSEL. The result is shown in Fig. 5.6(d) where the bottom LCS was switched back on and a fringe pattern appears in far field. Note that the WB is still on at this stage thus resulting in a low fringe visibility of 0.15 and a fringe phase of 1.44π. Similarly to Fig. 5.5(e), the WB affects both the visibility and the phase of the fringe pattern in far field. The result, after the WB was turned off is illustrated in Fig. 5.6(e), the fringe pattern is very similar to the initial pattern depicted in Fig. 5.6(a) with a visibility of 0.4 and a corresponding fringe phase of 1.85π. Despite confirming
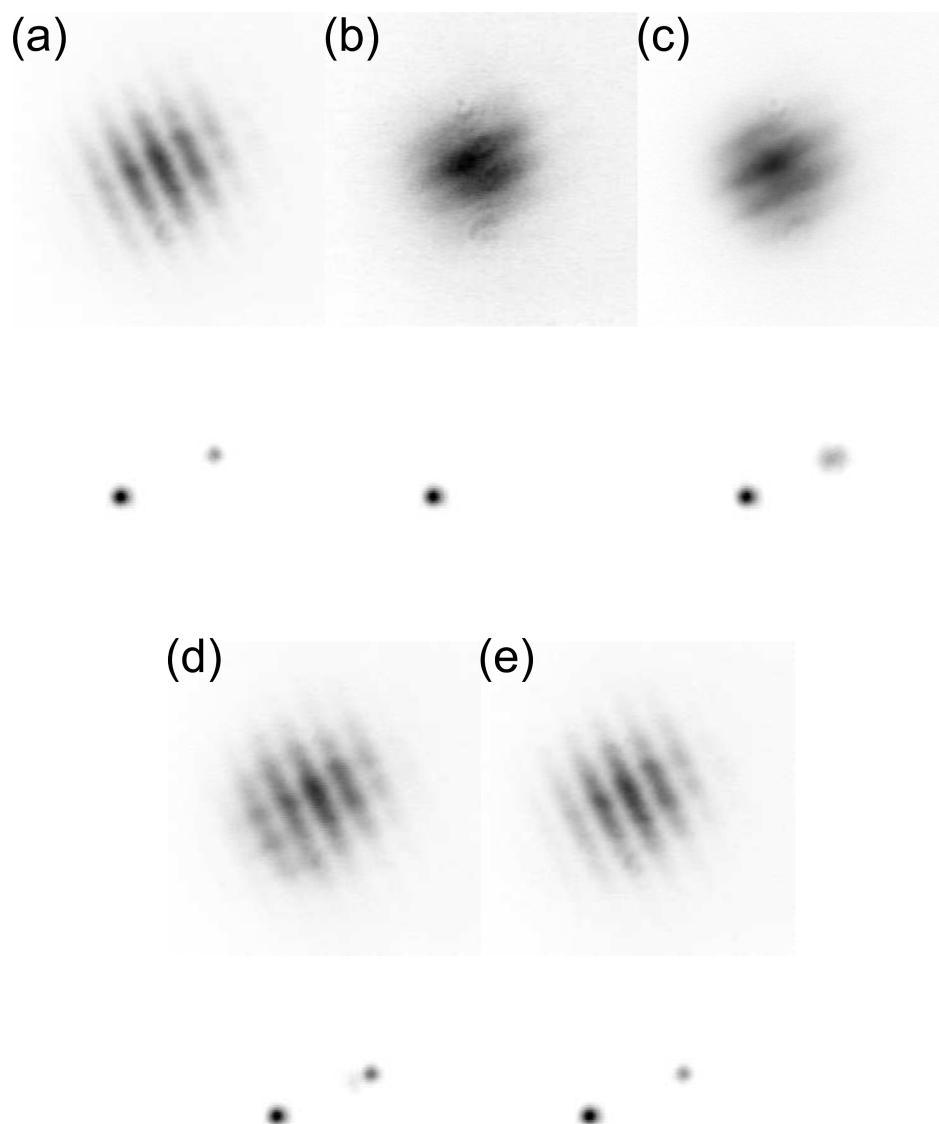
Figure 5.6: Upper row of the subcaptions: far field images, Bottom row of the subcaptions: near field images. (a) Phase locking between two LCSs achieved by tilting the VBG until robust locking is obtained. (b) The upper soliton is switched off by blocking the feedback from the WB. (c) The WB is coupled inside the cavity through the back of the VBG. (d) The upper soliton is switched back on by the WB. (e) The WB is turned off and the two solitons remain. The VCSEL was operated at I=355 mA and T=39 °C.

that the locking is weaker than the intrinsic properties of the LCS alone it also proves that once two LCSs are locked in phase, they will regain this locked state even after being independently switched off. The locking mechanism is robust and was observed for hours no matter how many times the LCSs were ignited and switched off beforehand. Phase locking was also observed after extinction of both LCSs, when switched on again they regained their locked state with the same visibility and phase they had when they were first locked.

5.3.1.3 Spectral Behavior

Robust phase locking between two independent LCSs was demonstrated in Sec. 5.5 but the spectral behavior of the LCSs associated with this locking state remains unknown. This section will focus on optical spectra data that has been recorded from the FPI along with near and far field images. A second pair of LCSs is used to illustrate the phenomenon, this pair has a smaller separation of 36 μm than the pair chosen in Sec. 5.5 because strongest locking is usually achieved with a smaller separation between the two LCSs. Similarly to Sec. 5.5, phase locking of the LCSs is obtained by tilting the VBG until strong, robust locking is achieved. Once phase locking is established the remaining adjustments to vary the feedback are done using the PZT which allows one axis of the VBG to be finely tilted. The fine adjustments from the PZT are enough to go from a complete locked regime to an unlocked state. Optical spectra as well as near and far field images are recorded for each state.

The first case discussed here is the unlocked state. It is illustrated in Fig. 5.7 and was stable and robust as expected once the VBG is tilted, i.e. the most common situation in the system as phase locking only occurs once careful alignment of the VBG is achieved. One LCS is blocked in the detection so that individual characterization of LCSs is possible. The left and right LCSs are individually shown in Fig. 5.7(a) and (b), respectively. From Fig. 5.7(a, b) it is clear that the two LCSs emit on different longitudinal modes with a similar optical power. However, the LCS located on the right of the VCSEL aperture shows side modes separated by approximately 2.5 GHz, i.e. two external cavity modes of 1.23 GHz, as seen in Fig. 5.7(b). This indicates that LCSs have the freedom to lase on
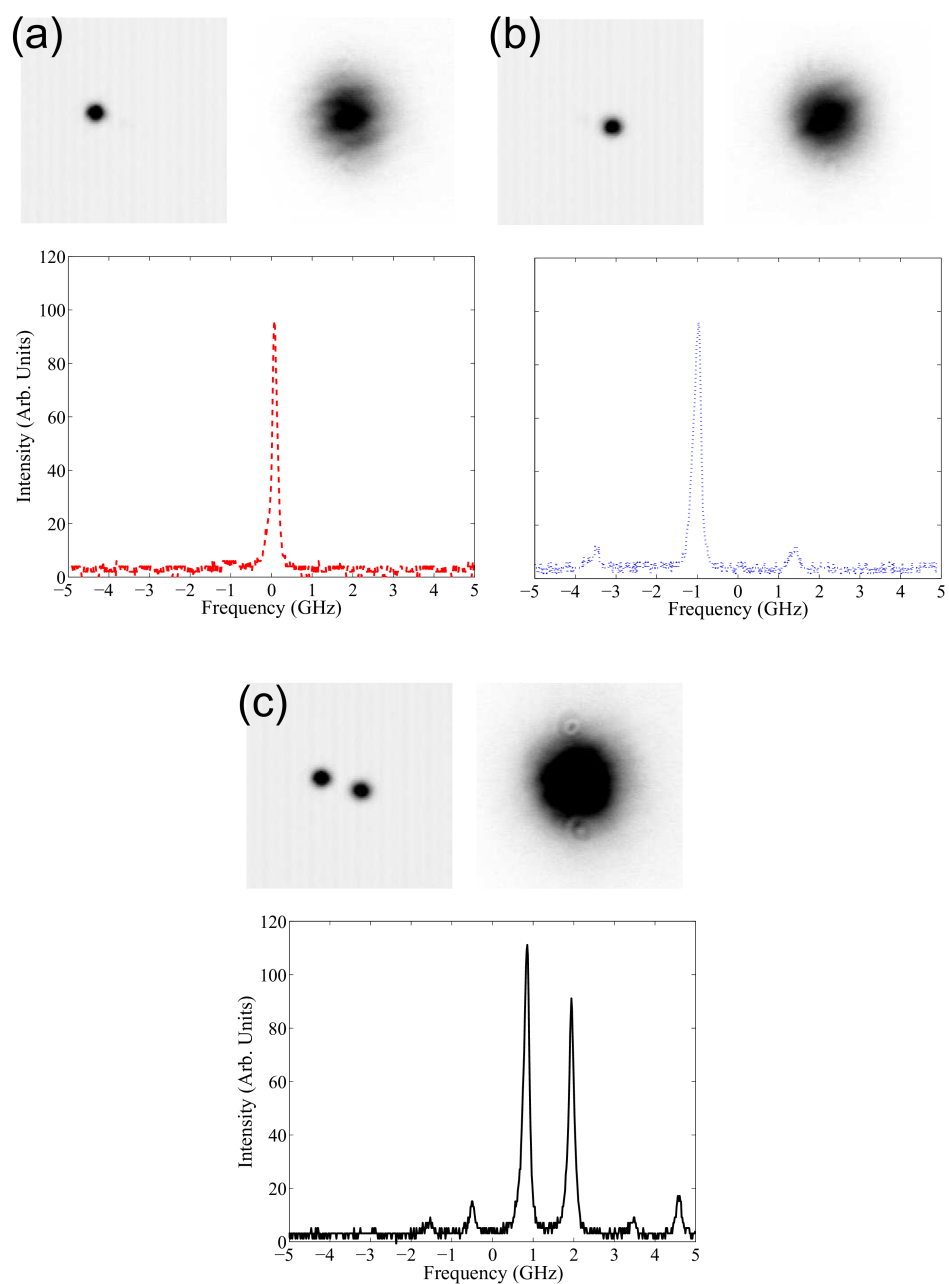
Figure 5.7: Spectral behavior of two unlocked LCSs separated by 36 μm. Upper row: near and far field images respectively, bottom row: Optical spectra. (a) The right LCS is blocked in the detection, near and far field images and optical spectrum associated to the left LCS. (b) The left LCS is blocked in the detection, near and far field images and optical spectrum associated to the right LCS. (c) Near and far field images and optical spectra of both LCSs. The VCSEL was operated at I=350 mA and T=39 °C.

several external cavity modes. It was demonstrated that, if one mode becomes suddenly unstable because of a change in the cavity resonance or in the feedback phase, LCSs have the ability to jump to the next stable neighbouring mode [20]. In Fig. 5.7(c) the optical spectrum confirms that both LCSs are emitting on different longitudinal modes and as a result the visibility in far field is very close to 0 (measured at 0.05 due to background noise). It is important to notice that now both LCSs exhibit side modes and that even if they are unlocked they show a tendency to mode hop, due to thermal drift, together during the experiment. Therefore, the frequency shift in the optical spectrum observed in Fig. 5.7(c) compared to the individual optical spectra in Fig. 5.7(a, b) is associated with the ability of the LCS to jump between stable longitudinal modes. The unlocked state is very stable and even though the LCSs are subject to mode hoping, the phenomenon is robust and unless a change of the feedback phase is applied, i.e. a tilt of the VBG, locking does not occur.

The spectral behavior of the locked LCSs is now investigated. Similarly, one LCS is blocked at the time thus allowing the characterization of individual LCSs. Figure 5.8 illustrates the locked state case where Fig. 5.8(a) shows the left soliton and Fig. 5.8(b) the right soliton individually. Both LCSs have similar intensity and seem to be separated by one external cavity mode. In Fig. 5.8(c) the detection captures both LCSs and a fringe pattern appears in far field in contrast to Fig. 5.7(c) but similar to what was observed in Fig. 5.5(f) and Fig. 5.6(e). The fringe visibility is measured at 0.61 and the amplitude in the optical spectrum corresponds to the sum of the amplitude of each individual LCS. The difference in frequency between the two LCSs is probably a confirmation that the locking state survives mode hopping. Indeed, the time required to swap LCSs in the detection for observation is enough for the LCSs to jump simultaneously on a different external cavity mode. This will be confirmed in Sec. 5.5 where the ability for the LCSs to remain locked whilst mode hopping is observed. Locking was robust and remained stable for very small tilting angles of the VBG. In tendency this LCS pair prefers to lock out of phase, i.e. fringe phase of π, as opposed to what was observed in Sec. 5.5. However, with a fine adjustment of the tilt angle the phase difference between the two LCSs can be adjusted. Indeed, after fine adjustment a fringe phase of about 0 can be achieved before locking is lost. This fringe phase
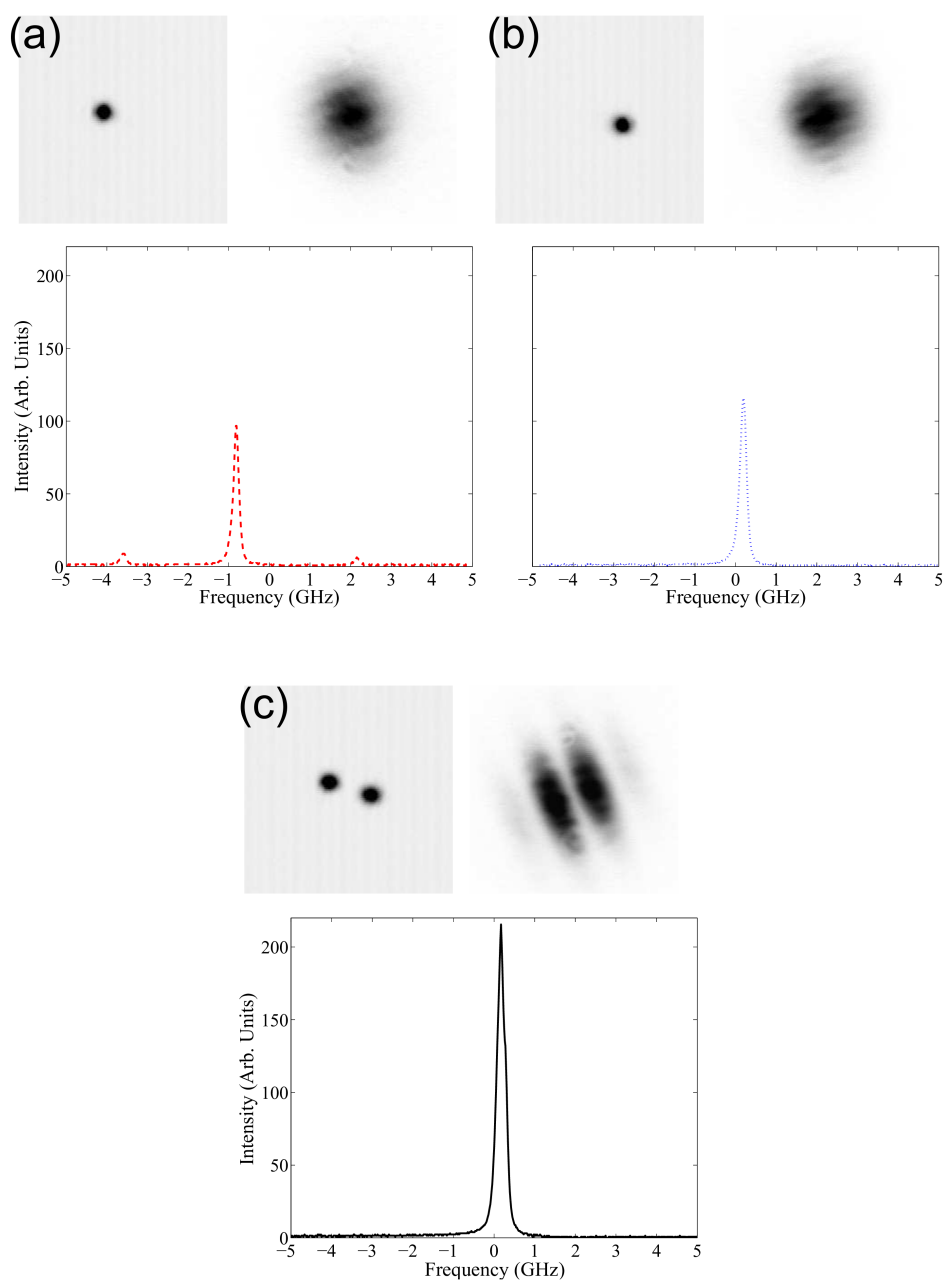
Figure 5.8: Spectral behavior of two locked LCSs separated by 36 μm. Upper row: near and far field images respectively, bottom row: Optical spectra. (a) The right LCS is blocked in the detection, near and far field images and optical spectrum associated to the left LCS. (b) The left LCS is blocked in the detection, near and far field images and optical spectrum associated to the right LCS. (c) Near and far field images and optical spectrum of both LCSs. The VCSEL was operated at I=350 mA and T=39 °C.

drift is associated with an abrupt fringe visibility reduction until locking becomes too weak and the LCSs return to an unlocked state as seen in Fig. 5.7. This VBG tilt dependence on the fringe phase shift will be investigated in detail in Sec. 5.4. The locked state was stable over minutes and locking was robust but when tilting the VBG during the transition to an unlocked state LCSs can exhibit some partial locking. However, as discussed previously the LCSs show a tendency to mode hop together regardless of their locking state. It is therefore not surprising that the partial locking state is even more difficult to investigate systematically and due to the very unstable nature of this intermediate state, it was not possible to collect systematic reliable data. From observations however, it seems that partial locking is obtained when both LCSs share the same side mode but again the instability of the phenomenon makes any interpretation difficult.

5.4 Phase Locking of Laser Cavity Solitons via Change of Current

Joule heating caused by an increase in the VCSEL injection current is responsible for a shift in the resonance condition. Therefore, increasing the injection current will result in a change in the emission wavelength of the LCSs. In this section the effect of the shift in the resonance condition on phase locking between a pair of LCSs separated by 79 μm (LCS labeled 1 and 2 in Fig. 5.1) is investigated. First the two LCSs were phase locked by tilting the VBG until robust locking was achieved with a stable injection current of 383 mA. Then the injection current scan was spanning ± 2.5 mA from the injection at which LCSs locked in a region where both LCSs are bistable. This injection range is only limited by the fact that below 380.5 mA LCS 2 switches off and that above 385.5 mA another LCS switches on thus disturbing the detection of the two previous LCSs leaving the fringe visibility close to 0 in far field. The current was scanned with 0.1 mA steps at a rate of 1 mA/s. The fringe visibility and phase are obtained from a fit of far field profiles to Eq. (5.2).

Figures 5.9(a, b) show the locking behavior of LCS 1 and 2 during an upward scan of the current. The dominant features of the spectra in Fig. 5.9(b) are multi-

(a)

(b)

(c)   (d)

Figure 5.9: (a) Fringe visibility (black line) and fringe phase (green line) as a function of current for LCS 1 and 2, 79 μm apart. The zero of the current scale corresponds to a current of 380.5 mA. (b) Evolution of frequencies; the frequency distribution is obtained from the optical spectra recorded by the FPI. The frequency separation between side modes corresponds to the free spectral range of the external cavity (1.23 GHz). (c) Far field intensity distribution at 380.5 mA corresponding to a fringe visibility of 0.55. (d) Far field intensity distribution at 385.5 mA corresponding to a fringe visibility of 0.95. Other parameter: T=69°C.

frequency emission and the common red shift of all modes due to the Ohmic heating discussed earlier. This shift is about 0.44 GHz/mA, about half the value of the free-running laser. A reduction is expected because the grating stabilizes the emission frequency as discussed in Chap. 4 and was also observed in [13]. At low current the LCSs emit on two or three different external cavity modes which corresponds to a fringe visibility close to 0.5. This indicates that the LCSs operate on different external cavity modes but share side bands, i.e. each LCS is not single mode. Then, as the current is increased, the fringe visibility increases abruptly to reach up to 0.95. At this point, only one spectral line is strongly dominant and both LCSs occupy the same external cavity mode and are then strongly frequency and phase locked. Increasing the current further leads to a jump of one LCS to an adjacent external cavity mode inducing a drop in fringe visibility back to 0.5. A similar scenario with a transition to full locking occurs at the end and high visibility is reached again. Beyond this point, a third LCS switches on in the detection area thus complicating the interpretation of the results.

Equation 5.3 gives a relationship between the fringe separation in far field and the LCS separation in near field. Using this equation for a far field fringe spacing of 12.6 mrad obtained from the fitting function this calculation yields a near field separation of 77.8 μm which agrees very well with the measured LCS separation of 79 μm thus confirming that the interference comes from the two interacting LCSs.

From Fig. 5.9(a) it is apparent that the fringe phase fluctuates apparently quite erratically during the current scan, but remains bound to a limited range close to a value slightly smaller than π. As it will be discussed below, a locking phase of π is typical for two coupled oscillators without detuning while a non-zero detuning changes the locking phase away from π. The current induced heating is a global parameter and hence it should not change the detuning condition between the two LCSs in the VCSEL cavity, in line with the fact that the locking phase is not varying by much. The operating frequency of the solitons, however, is a compromise between the VCSEL cavity resonance and the external cavity resonance leading to a transcendent equation for the operating frequency [4] (see (A.3) of [13] for a VCSEL with frequency selective feedback). With an initial, position dependent offset, a global shift of the VCSEL resonance conditions can

result in a change of relative stability and frequency of the modes of the coupled cavity system (e.g. a destabilization of an external cavity mode for one LCS but not for the other), leading to the possibility of a non-synchronous evolution of soliton frequencies and locking or unlocking. In addition, there might be small local variations either in gain or cavity resonance because the current induced temperature shift is only nominally homogeneous. These considerations indicate that the global parameter current is not a good handle to investigate the locking behavior, but one should look for a local control.

5.5 Phase and Frequency Locking of Laser Cavity Solitons via Change of Feedback Phase

Since it is experimentally difficult to change the detuning of two LCSs by locally changing the properties of the VCSEL itself, the PZT is used to minutely tilt the VBG of the external cavity with respect to the optical axis as illustrated in Fig. 5.2. As indicated by Eq. (5.1) this induces a difference in the external cavity length ΔL for the two solitons therefore leading to a difference of feedback phase and detuning in the external cavity. It is then possible to adjust the frequency difference, i.e. the detuning, between two LCSs. Indeed, the locking discussed in the previous section was achieved by aligning the VBG such that a high fringe visibility was obtained for a broad range of injection currents (about 5 mA). This follows the procedure used to control the detuning of coupled solid-state lasers, see [199, 200], but with the additional complication of coupled cavity effects due to the high reflectivity of the VCSEL out-coupling mirror, whereas the gain chip in the solid-state lasers is anti-reflection coated.

As indicated in Sec. 5.2, the tilts are actually quite small and it turns out that the soliton profiles are essentially unaffected. The width of the near field is constant to within 0.3 μm (variation ≤ 5 % of a single soliton width) and the width of the far field profiles to within 1.5 mrad (6 % of a single soliton width). When tilting the VBG both near and far field profiles of the LCSs are not affected while the positions are. As discussed in conjunction with Fig. 5.3, the positions and beam pointing of the LCSs change slightly in the trap, but the

changes are small and the differential changes are even smaller. Hence, it seems reasonable to assume that the dominant effect of the tilt is indeed the change of differential feedback phase. In order for the VBG tilt to have a significant effect, it is necessary for the different LCS pairs to be located on a horizontal plane. This ensures that the detuning between the LCSs can be controlled and automated via a computer.

Figure 5.10 illustrates the locking phenomenon between two LCSs, marked 1 and 2 in Fig. 5.1, separated by 79μm. It shows the fringe visibility, the fringe phase, the frequency distribution of the LCSs and a cut through the far field intensity distribution orthogonal to the fringe orientation as function of the detuning. The x-axis in Fig. 5.10(a), i.e. detuning, is proportional to the tilt angle of the VBG that changes the difference between the feedback phases for LCS 1 and 2. This difference is converted to a frequency scale by multiplying it by the free spectral range of the external cavity thus providing the change of the relative detuning between the two LCSs in the external cavity (see Eq. 5.1). When tilting the VBG a region of phase and frequency locking appears as illustrated in Fig. 5.10(a, c) by a range of high fringe visibility in the far field. The two dashed lines in Fig. 5.10(b) correspond to the region of strong locking, i.e. fringe visibility > 0.5. This region of high fringe visibility can last for seconds to hours depending on parameters. It confirms that locking is a robust feature once achieved by a fine alignment of the VBG.

Note that the choice to start the x-axis displaying the detuning parameter with zero is arbitrary. If one considers the locking-dynamics, it would be reasonable to expect that the zero lies at the center of the locking region. However, as the fringe phase is only approximately symmetric with respect to the center of the locking range and the details of the underlying dynamics are unknown, the position of the zero is somewhat ill-defined and no adjustments were made. Such cautious choice comes at the expense of a slightly awkward labeling: whereas the real detuning decreases in the left half (slightly) of the figure and increases in the right half, the detuning parameter chosen increases all along the x-axis.

As qualitatively apparent from Fig. 5.10(c), the fringes shift with detuning within the locking region (within a fringe visibility higher than 0.5), i.e. the locking phase changes. The quantitative analysis in Fig. 5.10(a) indicates that

Figure 5.10: (a) Fringe visibility (black line) and fringe phase (green lines) as a
function of the detuning. The zero of this detuning scale is arbitrary. The solid
and dashed green curves are obtained for scanning the tilt back and forth. (b)
Evolution of frequencies, the frequency distribution is obtained from the opti-
cal spectra recorded by the FPI. (c) Cut through far field intensity distribution
orthogonal to fringe orientation. Other parameters: T=69°C, $I = 373$ mA.

this variation is nearly linear over most of the strong locking range. The width of the locking range is close to π. If the direction of the scan of the tilt is reversed (see green dashed line in Fig. 5.10(a)) the locking phase shadows the one obtained in the up-scan which indicates that there is no discernible hysteresis. As it will be discussed in the theoretical section, these features are fingerprints of the Adler locking. The noise of the fringe phase is considerably smaller in the region corresponding to complete locking than in the partially locked regions. For even larger tilts (not achievable with the PZT), the two LCSs are completely unlocked and their phases random. Modulation depths of about 5% are due to noise in the images.

Both transitions at the strong frequency and phase locking region are rather abrupt and one might expect hysteresis at their onset. Due to the mechanical scanning, there is some jitter of the transition point. Therefore, only one sweep is shown in Fig. 5.10(a) and possible hysteresis was not investigated systematically. However, the detuning width at which strong locking occurs is very stable and no noticeable variation, within the resolution of the equipment, was observed between the different runs.

Figure 5.10(b) shows the optical spectra of the LCSs recorded with the FPI as function of the detuning and illustrates the evolution of the frequencies of the LCSs with increasing detuning. The first obvious feature is that all spectral lines are shifted due to the tilt of the VBG. The Finesse of the FPI is around 80, hence the frequency resolution is only about 130 MHz. This means that the differential frequency shift of the two LCSs cannot be resolved (it is in total about 30 MHz), but only inferred from its indirect effect via stabilization and destabilization of external cavity modes and the resulting possibility of locking and unlocking. It is worth noting that when the fringe visibility is high, i.e. >0.5, the two LCSs operate on a single frequency (region within dashed lines in Fig. 5.10(b)), they are frequency and phase locked. There is a jump in the common operation frequency of the LCSs by one FSR slightly after 15 MHz, where the fringe visibility is nearly maintained. It drops from 0.9-1 to 0.8-0.9. This indicates that the two LCSs do a common mode jump retaining phase and frequency locking, though at this point there is a change of behavior in the phase evolution (green solid line in Fig. 5.10(a)) and it becomes essentially flat. These observations reinforce the

hypothesis formulated in Sec. 5.3.1.3 regarding Fig. 5.8 and the LCSs ability to mode hop together whilst remaining locked.

Outside the locking region the two LCSs operate on two different external cavity modes (with a frequency separation of 1.23 GHz between two adjacent modes). In this region the fringe visibility is rather low (below 0.25) and the locking is very weak. Some residual coupling via side-modes is probably responsible for this residual partial locking. The observation of single LCSs in Sec. 5.3.1.3 seems to confirm this scenario. As indicated, for higher tilts, the visibility drops to a background given by noise on the order of 5% or less.

Although the transition from locking to unlocking seems to be accompanied by a transition between a one frequency to a two frequency spectrum, there are other regions in which the spectrum appears to be predominantly single-humped (possibly with weak side-modes) but with low fringe visibility. A close inspection however shows that the spectral line is wider there than in the central locking range, by around 45-55% in the region between 2-6 MHz detuning, and by 27% in the region at 19.5-20.5 MHz (close to the strong locking region). This indicates that the two LCSs are operating close in frequency so that the difference cannot be resolved within the limited resolution of the FPI (about 130 MHz). There is a third region around 26 MHz, where the spectral line seems to be slightly, but not significantly, broader and it is assumed that the frequency difference is below the resolution there.

The basic features of the scenario described for LCS 1 and 2 (79 μm apart) are also typical for other distances and other pairs of LCSs. Figure 5.11 shows phase and frequency locking for LCSs labeled 3 and 4 in Fig. 5.1, which are 49 μm apart. In this case one observes a far field fringe spacing of 19.1 mrad which corresponds to a near field separation of 51.3 μm. Again, it agrees well with the measured LCS separation of 49 μm. Similarly, there is a region of nearly complete locking with a high fringe visibility. The phase (within the strong locking region) is centered around π and varies linearly with the detuning from 0.6π to 1.4π (green curve in Fig. 5.11(a), see also Fig. 5.11(c)). The locking-unlocking transition is accompanied by a transition between a single-frequency and a two-frequency regime. Around a detuning of 4 MHz, the transition leads to a single locked state with a visibility of 0.7 dominated by a single mode, although weak side-modes
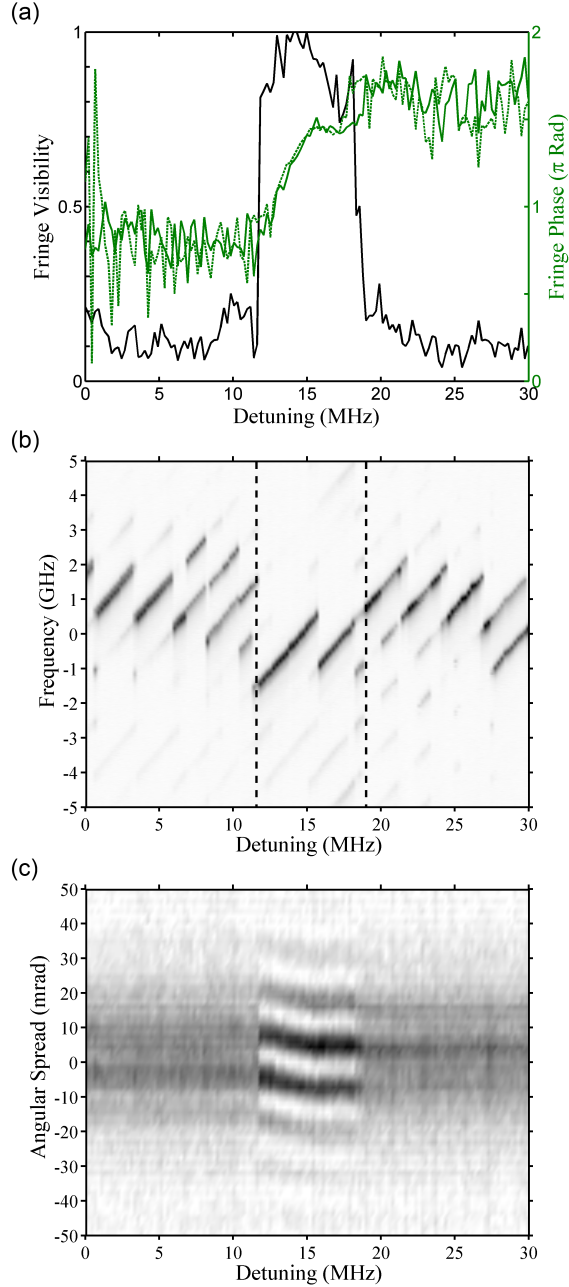
(a)

(b)

(c)
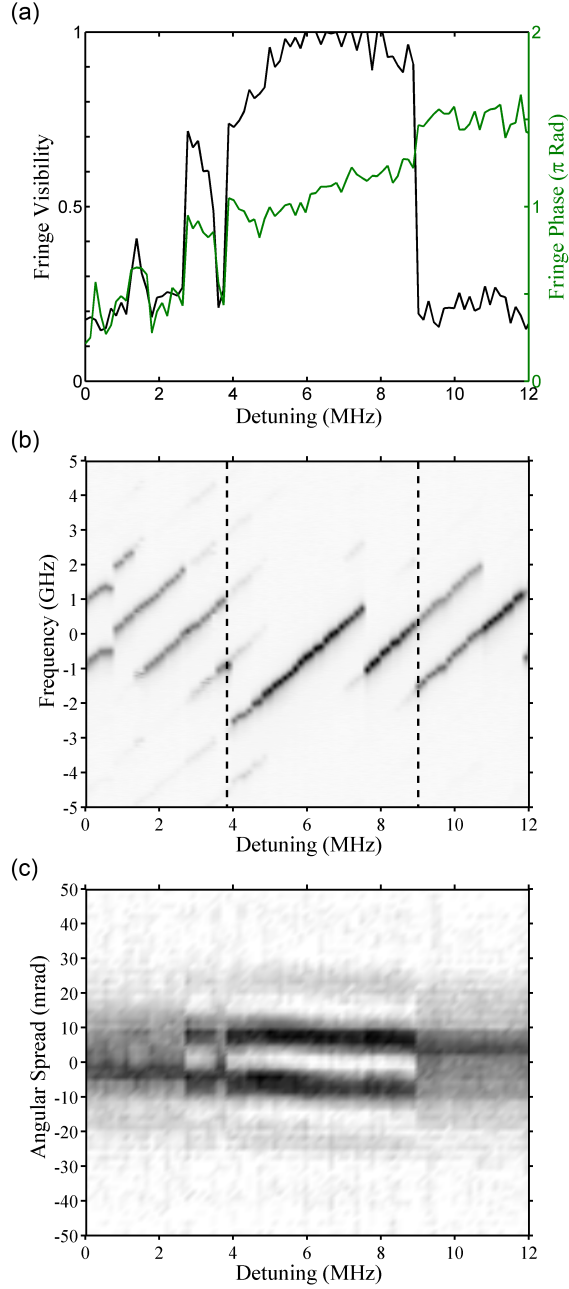
Figure 5.11: (a) Fringe visibility (black line) and fringe phase (green lines) as a function of the detuning. The zero of this detuning scale is arbitrary. The solid and dashed green curves are obtained for scanning the tilt back and forth. (b) Evolution of frequencies, the frequency distribution is obtained from the optical spectra recorded by the FPI. (c) Cut through far field intensity distribution orthogonal to fringe orientation. Other parameters: T=69°C, $I = 387$ mA.

are still present in the spectra. The latter disappears with a further increase of the visibility to the 0.9 level. Similarly to what happens in Fig. 5.10(b), the LCSs perform a common mode-hop within the locking region (around 7.5 MHz detuning), but remain locked. In contrast to the previous case, the phase evolution is not perturbed, i.e. the phase continues to grow approximately linearly. This might be related to the fact that the visibility remains above the 0.9 level, which is significantly higher than in Fig. 5.10(a).

Before the strong locking region, there are already small regions (around 1.5 MHz and 3 MHz) in which partial locking takes place. An extrapolation of the phase in the main locking region seems to match qualitatively phase values obtained in these regions. There are also some ranges of non-monotonous behavior of the phase (a decrease with increasing detuning) in the partial locking regions around 3 MHz and 4 MHz. The significance of these observations is not clear at the present stage of investigations.

A third pair of LCSs with a near field separation of 33 μm was investigated. Only one of the two LCSs is labeled, 3, in Fig. 5.1. The second one is located to the right of LCS 3. Figure 5.12 shows phase and frequency locking for this pair of LCSs. In this case a far field fringe spacing of 27.6 mrad was measured which corresponds to a near field separation of 35.5 μm. Again this result agrees well with the measured LCS separation of 33 μm which confirms that the fringes observed in far field are the result of the interference of the two LCSs. The basic features observed for the two previous pairs are also observed here. The phase (within the strong locking region) is centered around π and varies linearly with the detuning from 0.8π to 1.35π (green curve in Fig. 5.12(a), see also Fig. 5.12(c)). In this case the transition to locking is first associated with a multi-frequency regime. At the beginning of the locking region and up to a detuning of 8 MHz the LCSs operate on 3 adjacent external cavity modes. However, within this detuning range the locking is not very strong as indicated by a fringe visibility of about 0.5. In this region the two LCSs operate on 2 external cavity modes and locking seems to be the result of side-mode locking. The fact that the third frequency on which the LCSs emit in this region lies exactly in between the two individual frequencies of the LCSs in the unlocked region tends to confirm this hypothesis. Indeed, in the unlocked region, i.e. from 0 till 5.8 MHz detuning, the two LCSs do not
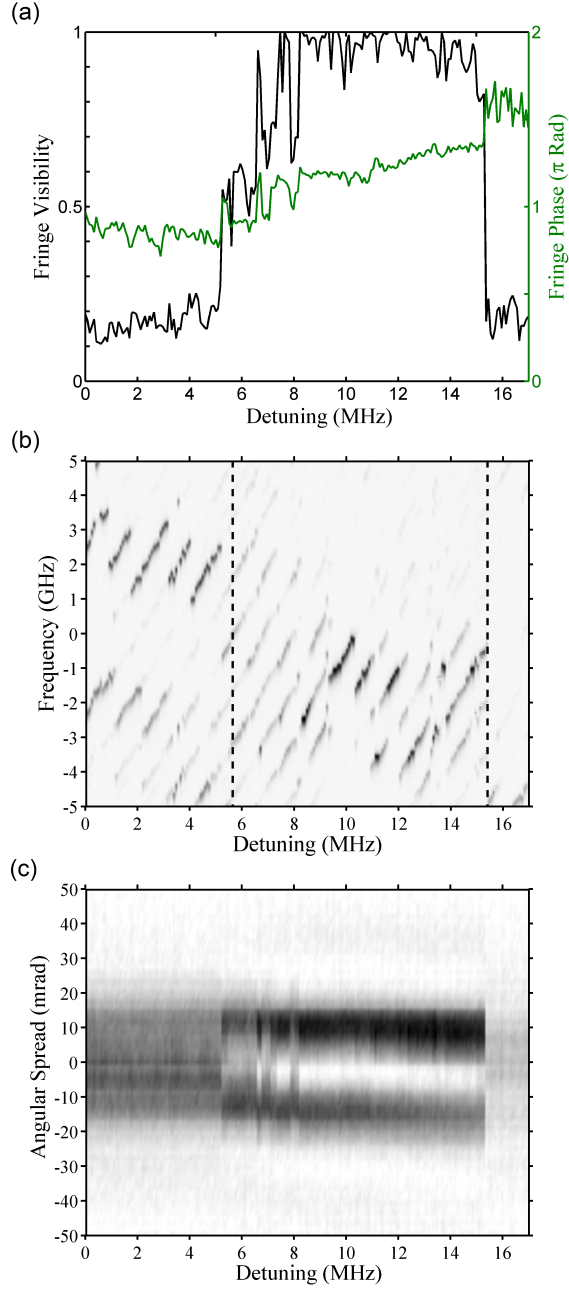
Figure 5.12: (a) Fringe visibility (black line) and fringe phase (green lines) as a function of the detuning. The zero of this detuning scale is arbitrary. The solid and dashed green curves are obtained for scanning the tilt back and forth. (b) Evolution of frequencies, the frequency distribution is obtained from the optical spectra recorded by the FPI. (c) Cut through far field intensity distribution orthogonal to fringe orientation. Other parameters: T=69°C, $I = 380$ mA.

emit on two consecutive external cavity modes but are separated by two external cavity modes. After strong locking is achieved, i.e. between 8 MHz-15.5 MHz detuning, the two LCSs mainly operate on a single frequency associated with a fringe visibility of 0.8-1. Similarly to what was observed in the two previous cases, in the strong locking region the two LCSs mode-hop together, they retain phase and frequency locking. Although, between 13 MHz and 15.5 MHz one observes weak side-modes in the spectra. Within the dashed lines (see Fig. 5.12(b)) the phase varies linearly with detuning as observed in Fig. 5.11(a) and Fig. 5.10(a). However, the variations in the phase are more pronounced between 5 MHz and 8 MHz where the visibility is >0.5. After 8 MHz the phase is not perturbed and increases approximately linearly even when the two LCSs mode-hop together. Outside the locking region the phase remains constant, i.e. the fitting function picks up noise that is not related to locking.

In summary, a variety of different dynamical behaviors for pairs of LCSs with different distances ranging from 30 μm to 80 μm were obtained. They all share the common feature of a region of nearly complete locking in which the phase is evolving approximately linearly with detuning. The locking is dominantly anti-phase (π locking phase) and the locking phase is centered around π and varies by nearly π over the locking range. Strong locking is associated with single frequency emission of the two LCSs, however they retain the ability to mode-hop together thus maintaining frequency and phase locking. We will argue in the next sections that these observations are a manifestation of the Adler-scenario. The observed variations in dynamics are expected since important parameters are associated with background disorder that cannot be controlled by the operator.

5.6 Theoretical Description

The theoretical model introduced below has been developed by the computational nonlinear and quantum optics group (CNQO) at Strathclyde following experimental guidance. The figures presented in this section were produced by Craig McIntyre and for a more detailed analysis see [225]. The CNQO, and more particularly Craig McIntyre, provided valuable insight and collaboration with the theoretical side of the interaction of two LCSs leading to frequency and

phase locking. We will see that in theory the locking behavior is well described by the Adler model for the synchronization of coupled oscillators and matches the experimental results introduced earlier in this chapter.

5.6.1   The Semiconductor Class-B Model

The behavior of semiconductor lasers with feedback has caught a lot of attention since the pioneering work of Lang and Kobayashi in 1980 [4]. In particular, the modeling of feedback effects on the dynamics of semiconductor lasers is of significant interest [5]. However, most of the work has been done by neglecting the spatial degrees of freedom in the transverse direction. Transverse space degrees of freedom are critical for LCSs, therefore they should be included in the model that describes the experimental setup discussed in the previous sections. Following [226], the dynamical evolution of the intra-VCSEL optical field E and carrier density N of a VCSEL with frequency-selective feedback can be modeled by the following system of coupled partial differential equations and mapping:

$$
\begin{aligned}
\partial_t E &= -(1+i\theta)E + i\nabla^2 E + \sigma(1-i\alpha)(N-1)E + \frac{2\sqrt{T_1}}{(T_1+T_2)}F \quad &(5.4)\\
\partial_t N &= -\gamma\left[N - J + |E|^2(N-1) + D\nabla^2 N\right] \quad &(5.5)\\
F(t) &= e^{-i\delta\tau_f}\hat{G}(t-\tau_f/2)\left\{-\sqrt{1-T_1}F(t-\tau_f) + \sqrt{T_1}E(t-\tau_f)\right\} \quad &(5.6)
\end{aligned}
$$

In Eq. (5.4), θ is the detuning of the VCSEL cavity with respect to the carrier reference frequency, σ is a coupling constant, α is the linewidth enhancement factor, and T_1 and T_2 are the transmittivities of the VCSEL mirrors. The term $\nabla^2 E$ describes diffraction in the VCSEL cavity. Note that light propagation in the external cavity is considered here without approximations typical of the Lang-Kobayashi model [227]. This allows for the consideration of large feedback reflectivities without incurring unphysical results (refer to [226] for more details).

In Eq. (5.5), J is the injection current normalized to the value at transparency. Time is scaled to the VCSEL cavity lifetime, and γ is the ratio of the cavity lifetime to the carrier response time in the VCSEL. The term $D\nabla^2 N$ describes carrier diffusion but is usually considered small and is therefore omitted.

In Eq. (5.6), δ is the external cavity carrier field detuning, τ_f the external round-trip time. See [227] for a detailed description of the external cavity. The operator $\hat{G}$ describes the frequency-selective operation of the Bragg reflector on the field envelope and is taken to be

$$\hat{G}(t) \; \{h(t)\} \; = \; \frac{r_g}{2\zeta} \int_{t-2\zeta}^{t} e^{i\Omega_g(t'-t)} \, h(t') \, dt' \tag{5.7}$$

where Ω_g is the grating central frequency relative to the reference (carrier) frequency (shifted to zero in the following), ζ the inverse of the filter bandwidth and r_g the overall reflection coefficient. Note that this description neglects the transverse wavevector dependence of the reflector response. Transverse effects of free-space propagation, i.e. diffraction, in the external cavity are also disregarded, since in the experimental setup the VCSEL output coupler is imaged directly onto the Bragg reflector as described in Chap. 3.

The validity of this model goes beyond the standard regimes of operation described by the Lang-Kobayashi (LK) model for semiconductor lasers with external feedback which only describes weak to moderate optical feedback effects, i.e. the effects of multiple round trips in the external cavity are neglected, and successfully describes the operational regimes of LCSs with high reflectivities of the VBG.

5.6.2 The Simplified Ginzburg-Landau Model

As we are primarily interested in single-frequency laser solutions, and in particular solitons, the carrier dynamics can be eliminated, reducing the model to a nonlinear equation for $E(x,t)$ coupled to a linear equation for the feedback field F. In this case we consider the simplest scenario of LCSs by setting aside complications such as delay and high-order nonlinearity. This scenario is well described by a simple generic model consisting of a cubic-quintic Complex Ginzburg Landau (CGL) equation where solitons are stabilized by coupling to a linear filter

equation [228]:

$$\partial_t E = g_0 E + g_2 |E|^2 E - i\partial_x^2 E + F + in(x)E,$$

$$\partial_t F = -\lambda F + \chi E\,,$$

(5.8)

where $E(x)$ is the intra-cavity field and $F(x)$ is the filtered feedback field. We focus here on one transverse spatial dimension but similar results are expected in 2D. The time and space coordinates (t, x) are scaled to 1 ns and 40 μm, respectively, so that g_0, describing linear gain and detuning, and g_2, describing nonlinear gain and dispersion, are dimensionless. Note that g_0 and g_2 are complex solutions and that the imaginary part of g_2 corresponds to either the strength of the self-focusing or defocusing nonlinearity. The real function $n(x)$ describes spatial variations of the cavity tuning due to background defects that predominantly perturb the material refractive index. In the second equation of (5.8) χ is the feedback strength, λ its bandwidth, and the reference frequency is set to the peak of the filter response. Small variations of $n(x)$ lead to pinning and small changes in the soliton frequency. This is analogous to tilting the VBG in the experiment, i.e. the relative detuning between the two LCSs. System (5.8) has exact solutions corresponding to stable single-frequency chirped-sech solitons [228].

5.6.3   Adler Equation

LCSs have intrinsically two Goldstone modes, namely position and phase. However, due to growth fluctuations, the positions of the LCSs is fixed by the frozen disorder of the VCSEL aperture. Thus, only one Goldstone mode remains. Since the amplitudes of the LCSs does not play a role in the locking phenomenon and that the trapped soliton pairs have a pure phase dynamics, it is possible to describe the system by an Adler equation [195], i.e. the archetypical equation describing synchronization between coupled oscillators. It can be written in the form

$$\frac{d\Phi}{dt} = \Delta\omega - \varepsilon \sin(\Phi),$$

(5.9)
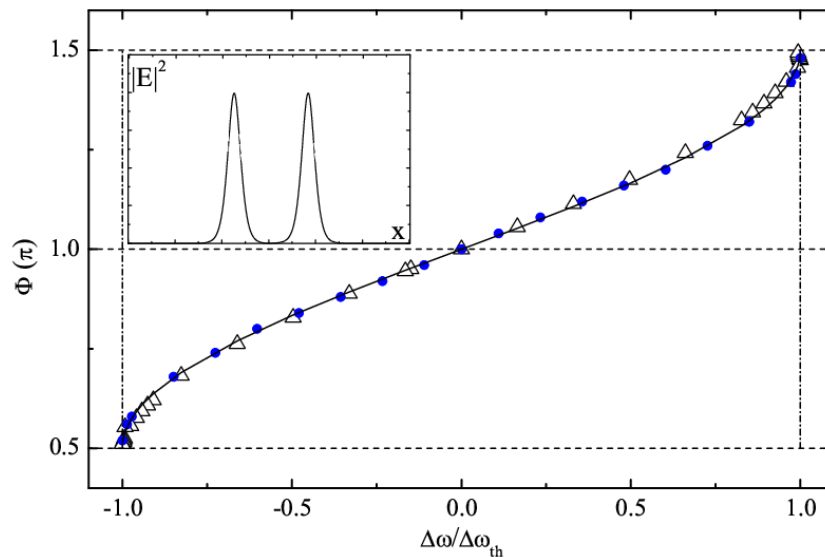
Figure 5.13: Locked phase differences Φ of pinned LCSs for different frequency detunings (controlled by the potential depths n_1 and n_2) from direct integration of Eq. (5.8) (dots, LCS separation of 5.3 soliton widths) and Eq. (5.4, 5.6) (triangles, LCS separation of 4 soliton widths). The solid line refers to the Adler equation (5.9). The inset shows the spatial profile of the near-field intensity of two interacting LCSs. Such profile is almost constant across the Adler locking region. Figure courtesy of Craig McIntyre [225].

where $\Delta\omega = \omega_2 - \omega_1$ is the trap-detuning (which is zero for $n_1 = n_2$ with $n_1 = n(x_1)$ and $n_2 = n(x_2)$) where ω_1 and ω_2 are the frequencies of the individual solitons, ε is a coupling constant and Φ is the locked phase. In-phase and anti-phase solutions are selected for $\Delta\omega = 0$, depending on the sign of the coupling. For positive ε the stable final state is $\Phi = 0$, for negative ε it is $\Phi = \pi$. A comparison of the results of the Adler equation with negative ε and the simulations of the synchronization of LCSs trapped by defects in both equations (5.8) and the class-B model equations (5.4, 5.6) is presented in Fig. 5.13. The Adler equation predictions (solid line in Fig. 5.13) show an excellent agreement with the other two models. Note that the $\pi/2$ value observed in phase locking of dissipative solitons without defects [229] is now replaced by the π value typical of Adler synchronization.

In order to characterize the Adler locking in the spatial and temporal domains, the time averaged far field images and the optical spectra are shown in Fig. 5.14
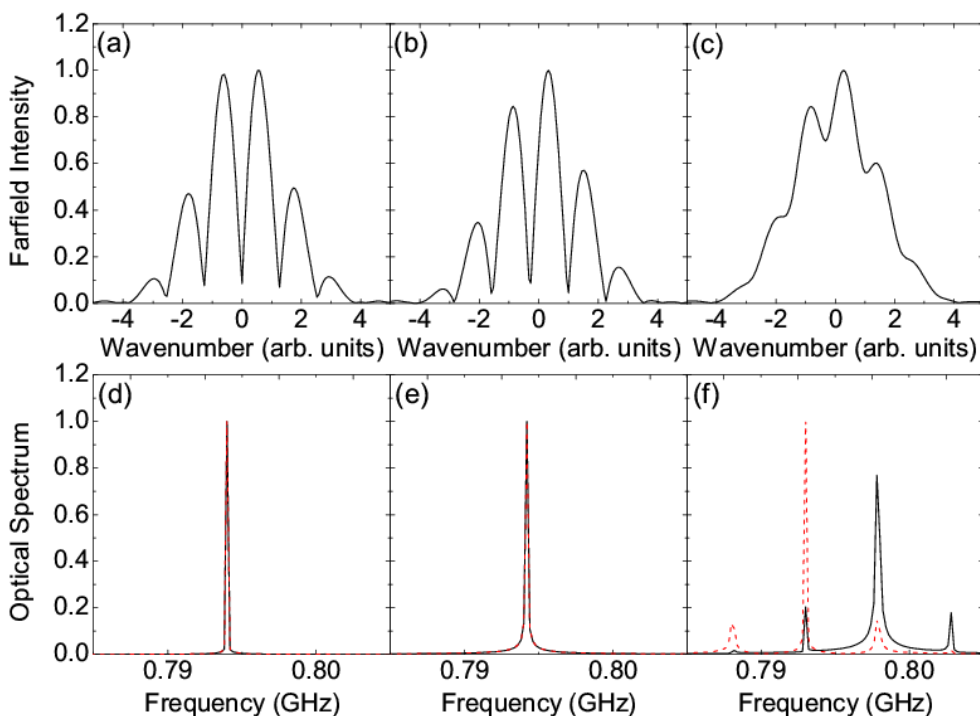
Figure 5.14: Far field fringes (a)-(c) averaged over 2 μs, and optical spectra (d)-(f) for a time window of 5 μs, for $\Delta\omega/\Delta\omega_{th} = 0$ (a,d), 0.99 (b,e) and 2.0 (c,f) obtained from simulations of the semiconductor class-B model. In (d,e) the LCS spectral peaks (dashed and solid lines) overlap. Figure courtesy of Craig McIntyre [225].

for two points inside ($\Delta\omega/\Delta\omega_{th} = 0$ and 0.99) and one outside the Adler locking region ($\Delta\omega/\Delta\omega_{th} = 2$), respectively. From Fig. 5.13 it is clear that when LCSs are in the locked state they have a fixed phase difference and the same frequency. This is demonstrated in Fig. 5.14(d, e) where the optical spectra of two values of $\Delta\omega$ inside the locked region are shown and corresponding to $\Delta\omega = \Delta\omega_{th} = 0$ and 0.99, respectively. Within the locked region, the spectra of the two LCSs overlap exactly indicating a strong interaction. There is a progressive shift of the locked frequency while scanning the Adler region. This matches qualitatively the experimental results in Fig. 5.12, 5.11, 5.10 though the absolute value is much lower. This is not surprising, because the technique used to change detuning in the experiment is different. The corresponding far field images are shown in Fig. 5.14(a, b). Interference fringes between the two locked solitons are clearly

visible. Progressive change of the LCS phase difference Φ (from π at $\Delta\omega{=}\Delta\omega_{th} = 0$ to around 1.5 π at $\Delta\omega{=}\Delta\omega_{th} = 0{:}99$) is reflected in the change in the symmetry of the fringe pattern. These features are also characteristics of the different experimental realizations where the phase difference is centered around π with a total shift of about π in all three cases investigated.

Both optical spectrum and far-field fringes change significantly as soon as one moves outside of the locking range as shown in Fig. 5.14(c, f) for $\Delta\omega{=}\Delta\omega_{th} = 2$. The spectra of the two LCSs are now clearly separated although a partial overlap of some of the peaks is still present due to the non-uniform evolution of the relative phase. Such feature affects the far-field image too where some interference maxima are still visible although progressively disappearing with increasing $\Delta\omega$. For very large difference of the defect minima (not shown), the fringe visibility is expected to disappear completely [225], as expected for two LCSs with large frequency separation. This matches the experimental results introduced earlier in this chapter and demonstrates the validity of Adler's model for two LCSs pinned by defects.

The Adler locked state between LCSs is a robust feature independent of initial conditions such as initial phases, frequencies and sequential order of creation of the two LCSs. Once the locked state is attained, one of the two LCSs can be switched off by a short, localized perturbation to the carrier density at its location. Hence, LCSs retain their solitonic properties in the phase-locked state in the sense that they are still individually bistable and optically controllable.

5.7   Conclusion

We demonstrated that locking does not affect the intrinsic properties of the LCSs, the coupling is therefore weaker than their solitonic properties alone and they remain individually controllable. We also demonstrated both experimentally and theoretically that two trapped LCSs in VCSELs with frequency selective feedback display Adler synchronization leading to phase and frequency locking. The synchronization is induced by spatial defects where the LCSs are pinned and by changing the frequency of each soliton with respect to that of its neighbor. The

presence of the defects breaks the translational symmetry, fixes the relative distance between solitons and locks the relative phase to values different from $\pi/2$ observed numerically in the absence of defects or experimentally in temporal-longitudinal systems.

Although the validity of Adler's model for only two solitons has been demonstrated, network synchronization in the spirit of Kuramoto's model (with coupling possibly controlled by the deviation from the self-imaging condition) should be possible with many LCSs in a fruitful analogy with brain activity [21] and, possibly, with spatio-temporal excitability [205].

Chapter 6

Dynamics of a Semiconductor Laser with Frequency Shifted Feedback

In this chapter experimental results of an 830 nm, Quantum-Well (QW), Fabry-Perot cavity, edge emitting semiconductor laser (EEL) coupled to a high reflectivity mirror in an external cavity configuration with frequency shifted feedback (FSF) are reported. In particular, the dynamics of the output of an EEL with FSF are investigated. Different cavity lengths, matching a multiple of the frequency shift of the optical feedback, are investigated and the results are contrasted with those from conventional optical feedback systems. Results obtained with resonant cavities are also compared with non-resonant frequency shifts giving a complete picture of the dynamics of an EEL with FSF.

The dynamics are mapped as a function of the level of FSF and the injection current. Two different external cavity configurations were investigated; when the frequency shift of the optical feedback is the fundamental or a sub-harmonic of the external cavity frequency and when the frequency shift of the feedback is off resonance with the external cavity. Multi-GHz-bandwidth real time data collection and analysis is used to investigate the temporal and spectral behavior of the output power of the nonlinear system. Three fundamentally different regimes of operation are identified for the FSF system corresponding to low, medium and

high levels of FSF. The medium FSF level regime is consistent with that found in a semiconductor with conventional optical feedback (COF) system [5]. However, for high levels of FSF the output of the system gives a noisy, near periodic output similar to the pulsed comb of mode output observed in analogous FSF laser systems using solid state gain media with a resonant cavity [105, 106, 119]. For a very small range of medium FSF levels the system exhibits spectral behavior never observed in semiconductor laser with FSF. A dual-wavelength laser emission at two widely spaced wavelengths (10 nm) was observed.

6.1 Preliminary FSF Laser Characterization

6.1.1 Experimental Setup

In this section the frequency-shifted feedback experimental setup is detailed. A schematic diagram of the experimental setup is illustrated in Fig. 6.1 and a photograph in Fig. 6.2. A quantum well, edge-emitting, Fabry-Perot cavity, laser diode emitting at 830 nm (APL 830-40) is temperature controlled to 0.01 K and driven by an ultra-low noise current source (Profile ITC-510). An output power of 12 mW was obtained with a bias current of 70 mA. The output power versus injection current (LI) characteristic for the free running laser is discussed in Sec. 6.1.3. An aspheric lens (L1) is used to collimate the output beam of the laser. However, a beam divergence of order 2 mrad remains. Frequency shifted feedback is obtained using an acousto-optic modulator (Gooch and Housego R23080-2-.85-LTD, AOM) placed inside the external cavity. The AOM is driven by a nominally 80 MHz RF generator. A 79.6 MHz frequency shift was measured in the first order diffracted light on each pass through the AOM. Optical feedback is provided by an external cavity mirror (M) mounted on a translation stage. This allows fine cavity length tuning to a precision of 0.1 μm.

A 50/50 beamsplitter (BS1) inside the cavity is used to couple light out for distribution to the diagnostic equipment. An optical isolator (OI) is used in order to prevent reflections from the detection system returning into the external cavity. Outside the laser system, a second 50/50 beamsplitter (BS2) is used to couple half of the laser output onto an ultra-fast detector (Alphalas UPD-40-VSI-P 8 GHz

Figure 6.1: Experimental setup. Solid line: Alignment on the first diffraction order beam of the AOM, Dotted line: Alignment on the zeroth order beam of the AOM. M: Mirror, L1-L4: Aspheric Lenses, BS1-BS3: Beamsplitters, AOM: Acousto Optic Modulator, OI: Optical Isolator, PD: Photodetector, PMT: Photomultiplier Tube, OSA: Optical Spectrum Analyzer, FPI: Fabry-Perot Interferometer.

bandwidth, PD). A 20 gigasample per second sampling rate digital oscilloscope with 4 GHz bandwidth (Agilent Infiniium 54854A DSO) was used to capture the output power time-series. A minimum of 20 000 points (1 μs) are sampled for each data point to allow complexity analysis to be completed. The remaining light is then split by a beamsplitter (BS3). One beam is coupled to a multimode fiber connected to an optical spectrum analyzer (Anritsu MS9710C, OSA), with a resolution of 0.07 nm. The second beam goes into a Fabry-Perot interferometer (Burleigh RC-110, FPI). The FPI is actively scanned and its cavity length can be adjusted to cover a free spectral range (FSR) from 1 GHz to 1.5 THz. The output from the FPI is measured by a photomultiplier tube (Hamamatsu R636-
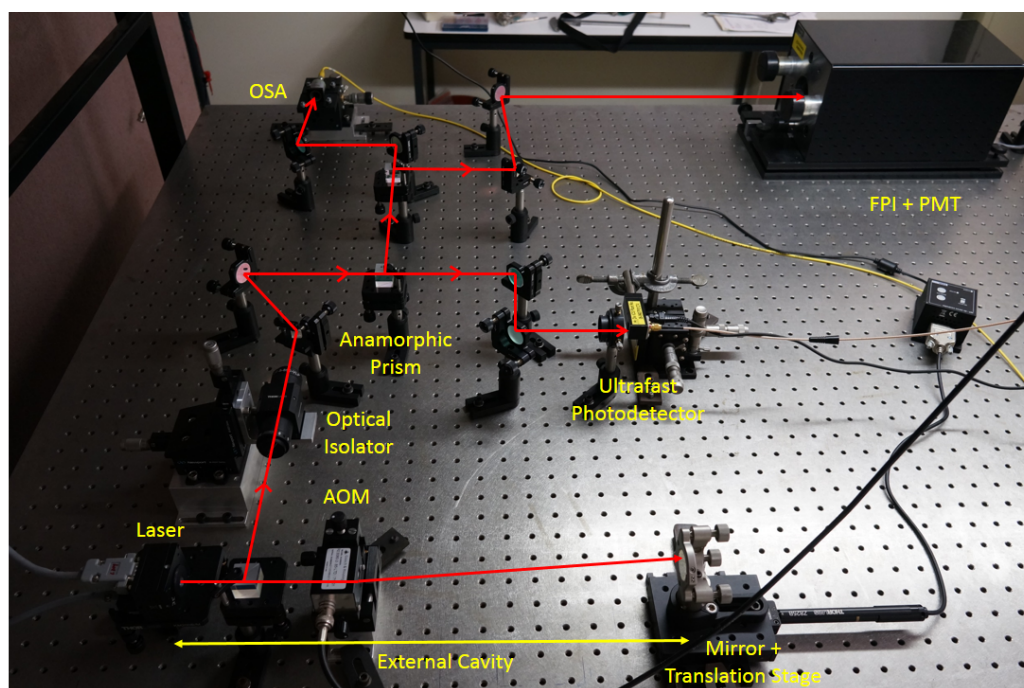
Figure 6.2: A photograph of the experimental setup. The external cavity mirror can be aligned such that it reflects the zeroth or the first order diffraction beam of the AOM. Here the first order is fed back into the laser.

10, PMT).

The translation stage, controlled via the computer to a precision of 0.1 μm, was used to tune the external cavity length such that it matched a multiple of the AOM roundtrip frequency, i.e. 160 MHz, 320 MHz, 480 MHz or 640 MHz. The shortest cavity corresponding to 640 MHz was technically possible but the angular separation between the zeroth and first order beams from the AOM was not large enough to ensure that the first order was completely coupled back into the laser without any overlap with the zeroth order. The external cavity length corresponding to a roundtrip frequency of 80 MHz was not investigated due to the fact that this frequency shift is very small compared to the expected relevant time scales of the dynamics ($\approx$ ns) and also because the roundtrip frequency shift of the AOM is 160 MHz. On top of that the external cavity length would have been too long to be set-up in a straight line on the optical table. Therefore the addition of a high reflectivity mirror inside the external cavity would be needed,

adding unnecessary complication to the already careful alignment the system requires. And because of the beam divergence, the coupling efficiency is likely to be reduced for longer cavities which means that the returning beam might not entirely pass through the AOM.

The instrumentation is controlled via a computer through the software Labview. This automated computation system allows us to capture 1001 different FSF levels for 71 injection currents in a little more than 60 minutes. The output power time-series, OSA data, and FPI spectra are all captured at the same time for each FSF level at every injection current. For a given cavity length, a complete characterization of the system requires a total number of 71 071 time-series. The characterization of the system at the highest resolution, i.e. collection of all the data, required to generate high density maps can take up to 3-4 full days to complete depending on whether the optical spectra are saved or not.

6.1.2 Acousto-Optic Modulator

Acousto-optic modulators (AOMs) are commonly used as a device to control the power or the spatial direction of a laser beam traveling through it. AOMs also find applications as frequency shifters and wavelength filters. They act as a controllable diffraction grating. They rely on the acousto-optic effect, which allows the oscillating mechanical pressure of a sound wave to modify the refractive index of a crystal. A piezo-electric transducer (PZT) is attached to the crystal such that when an oscillating electric signal is sent to the transducer it creates a sound wave in the crystal. The sound wave then generates a traveling periodic refractive index grating in the crystal which therefore causes some of the light to be diffracted. Even at maximum diffraction efficiency, a small fraction of the light remains in the zeroth order of the AOM. The frequency of the diffracted beam is then increased, but it can also be decreased depending on the propagation direction of the acoustic wave relative to the beam. The frequency of the sound wave traveling through the crystal controls the frequency shift of the diffracted beam. The diffraction efficiency is controlled via the acoustic power, i.e. the amplitude of the electric signal sent to the AOM. AOMs find many applications
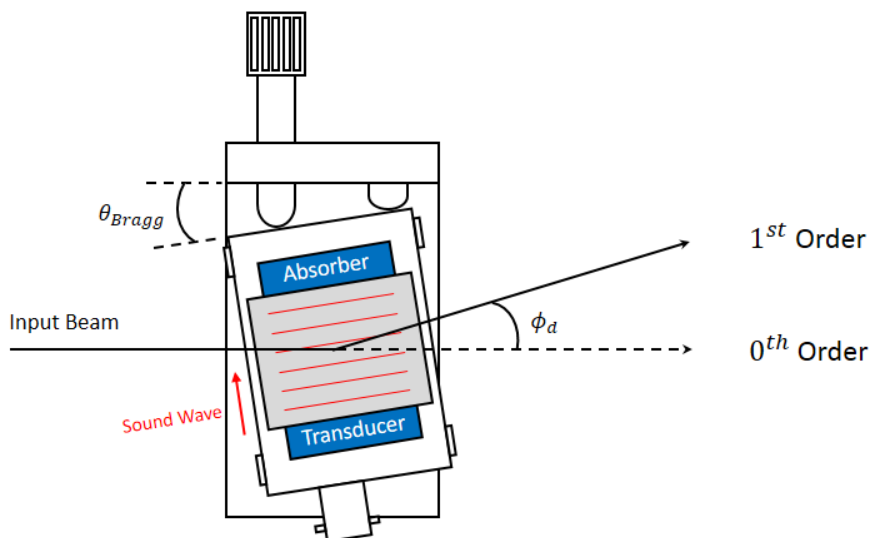
Figure 6.3: AOM Bragg adjustment. A sound wave propagating through the crystal creates a traveling periodic refractive index grating. As a result some of the light is diffracted in the 1st order with an angular separation ϕ_d corresponding to $2\theta_{Bragg}$.

such as in Q switching solid-state lasers [230], cavity dumping [231] or mode locking [232].

The modulator rise time is limited by the acoustic velocity of the modulator material and the size of the laser beam. Diffraction occurs when the acoustic wave has traveled through the optical beam. In case of a Gaussian profile the time required to cross the $1/e^2$ beam diameter is

$$\tau = \frac{D_{1/e^2}}{V} \tag{6.1}$$

where D_{1/e^2} is the diameter of the optical beam at $1/e^2$ and V is the acoustic velocity of the modulator material. The rise time is calculated from the relationship [233]

$$t_r = 0.64\tau. \tag{6.2}$$

A diagram of the angular relationship between the acoustic wave and the

131

optical beam is shown in Fig. 6.3. It illustrates a particular case known as the Bragg regime. For a specific incidence angle θ_{Bragg} only one diffraction order is generated, the others are extinguished by destructive interference. This requires the AOM to be slightly tilted off perpendicular to the optical beam so that the Bragg condition is met. The AOM was operated at the Bragg regime during the experiment as this configuration allows maximum diffraction efficiency of the AOM. The deflection angle ϕ_d illustrated in Fig. 6.3, i.e. the separation between the zeroth and first order beams, is given by [233]

$$\phi_d = 2\theta_{Bragg} = \frac{F\lambda}{V} \tag{6.3}$$

where F is the acoustic drive frequency and λ the wavelength in the crystal. Experimentally, with the shortest external cavity used, a separation of 4.00 mm ($\pm$ 2%) was obtained after a roundtrip in the external cavity between the zeroth and first order beams.

The experiment previously described in Sec. 6.1.1 relies on the frequency shifting properties of the AOM. In an FSF laser system an AOM is commonly placed inside the external cavity implying that the light experiences a frequency shift on each propagation through the AOM. The AOM is driven by an 80 MHz RF generator, thus the intracavity electric field experiences a nominal frequency shift of 160 MHz after each round trip in the external cavity. The diffraction efficiency of the AOM can be adjusted by varying the amplitude of the electric signal sent to the AOM. Increasing the voltage increases the power of the diffracted light until maximum power in the first diffraction order of the AOM is achieved for a drive voltage of 0.8 V. The transmission of the crystal was measured as 91.4% ($\pm$ 0.5%), which is slightly lower than the specification maximum transmission of 97% for the crystal. This is an indication that the collimated beam is a little too large for the aperture of the AOM. This was indeed verified by using a beam profiler. The $1/e^2$ diameter of the fast axis beam was measured at 3.35 mm and 3.21 mm before and after the AOM, respectively. It is worth mentioning that a small beam diameter difference was observed between the zeroth and first order beams and was estimated to be approximately 7% with the first order always being larger than the zeroth order beam. The size limitation of the beam could

be solved by placing the crystal at the focal spot of a telescope formed by two converging lenses thus reducing the size of the beam when propagating through the AOM. It is usually required to focus the laser beam in the crystal in order to achieve maximum diffraction efficiency. However, since the experiment requires feedback from the first order diffracted beam, i.e. the beam coming out of the AOM with an angle, the ease of the FSF alignment would suffer from it. And it is also important to avoid the extra losses induced by the telescope in order to achieve high FSF levels. But more importantly, the extra space required to place the telescope inside the cavity would not allow us to work with the external cavity corresponding to a roundtrip frequency of 480 MHz. In order to maximize the diffraction efficiency of the AOM the laser was mounted in such a way that the beam was linearly polarized, perpendicular to the acoustic propagation axis. According to the specifications of the AOM given by the manufacturer, a random polarization orientation would reduce the diffraction efficiency by at least 5%.

After careful alignment the AOM reached a maximum diffraction efficiency of 90%. Figure 6.4 shows the normalized diffraction efficiency of the AOM with increasing voltage for the zeroth (solid line) and the first order (dashed line). The diffraction efficiency is not linear with the voltage applied to the AOM. Between 0 V and 0.2 V there is no significant change in the zeroth and first order beams output power. The FSF varies from 0.03% to 0.08%. The diffraction efficiency improves quickly from 0.2 V to 0.8 V with a close to linear trend, and decreases slowly thereafter. It is worth noting that when operating with the zeroth order it is not possible to achieve complete extinction of the beam thus even for an input voltage of 1 V there is still a small amount of feedback, around 0.03%, going back into the laser if it is aligned on the zeroth order beam of the AOM. The direction of the first order beam, with respect to the zeroth order, is shifted by the AOM, as described by Eq. 6.3 and illustrated in Fig. 6.3. Thus, it is possible to optimize the feedback such that only the first order diffraction beam is fed back into the system. However, this condition is only valid if the angular separation between the first and zeroth order is large enough so that even when there is no voltage applied to the AOM the reflected light from the zeroth order does not travel back through the AOM. This was indeed verified theoretically using Eq. 6.3 and experimentally with a beam profiler for all the external cavity lengths studied
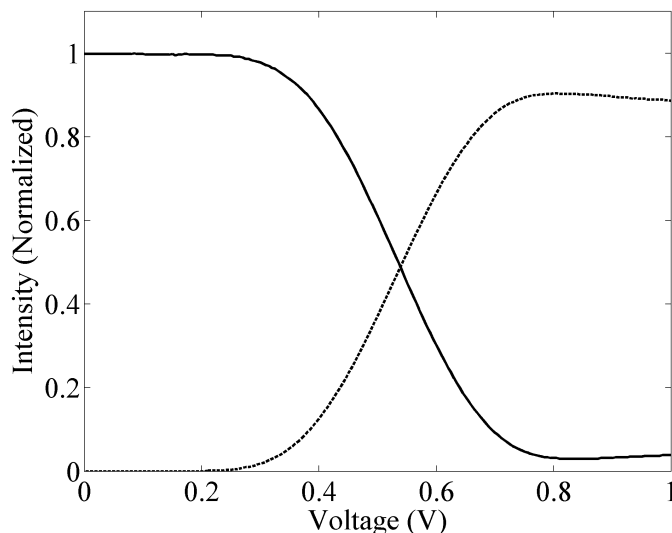
Figure 6.4: Output power of the AOM in the zeroth order (solid line) and first order (dashed line) normalized to the maximum power transmitted in the zeroth order for increasing voltage

in this chapter. A separation of 4.00 mm ($\pm$ 2%) between the center, i.e. peak power, of the zeroth and first order beams was measured after a roundtrip in the external cavity at the shortest cavity length investigated in this chapter, i.e. 480 MHz. The $1/e^2$ fast axis beam diameter was measured as 3.40 mm at this cavity length, which also corresponds to the separation between the center of the two beams. This ensures an effective separation of 0.6 mm ($\pm$ 9%) between them. Larger separations were achieved with longer external cavities. This separation was considered large enough to ensure that after careful alignment, only one beam was fed back into the system. Before any data collection the optical alignment was optimized such that the diffraction efficiency of the AOM was maximum. And when careful alignment was not enough to ensure maximum diffraction efficiency then the amplitude of the RF signal was adjusted and another version of Fig. 6.3 was generated until the diffraction efficiency was maximized and best performance of the AOM was achieved.

6.1.3   LI Curve and FSF Alignment

A Light-Injection (LI) curve measures how the laser output power varies with injection current. This is usually used to find the laser threshold point. The light output of the laser is measured using a photodetector (Ophir PD300) attached to a power meter (Ophir Nova). The output of the power meter is then connected to a computer and controlled through a custom made LabVIEW program. The ultra-low noise current source can deliver currents up to 200 mA with a precision of 0.01 mA and an accuracy of $\pm 100\ \mu$A.

The laser diode used in this experiment is a GaAlAs, quantum well, edge-emitting Fabry-Perot cavity diode. The maximum output power of the free running laser is given as 40 mW when operated below 25.0 °C. Because the laser is driven with optical feedback, it is important not to overdrive the laser. The free running laser has a recommended maximum output power of 30 mW with an injection current of 160 mA. The BS inside the external cavity transmits 50% of the light and thus, at most, half of the light reaching the external mirror is fed back into the laser, this is neglecting the attenuation of the zeroth order of the AOM which is close to 0. Taking into account the transmission of the BS and the diffraction efficiency of the first order beam after a roundtrip in the external cavity, approximately 20% of the light emitted from the laser contributes to the feedback. The coupling coefficient of the laser was not calculated but is estimated to be that of standard EEL diode, i.e. $\approx$ 20-30%, which means that at most $\approx$ 6% of the output power of the laser is fed back. Therefore, it is safe to operate the laser up to 150 mA. In order to be conservative the laser was not driven above 100 mA. When the laser diode was operated at 70 mA at a temperature of 25.0 °C the operating wavelength of the free running laser was measured as 830.8 nm using the OSA.

Figure 6.6 shows the spontaneous emission of the free running laser at 25.0 °C just below threshold with an injection current of 55 mA. From this figure the gain seems to be maximum around 829 nm which indicates that the laser apparently prefers to emit on the next longitudinal mode, i.e. 830.8 nm. However, the center of the gain bandwidth can shift at higher injection currents. Figure 6.5 shows the LI curves at 25.0 °C with maximum FSF (dashed line) and free running (solid
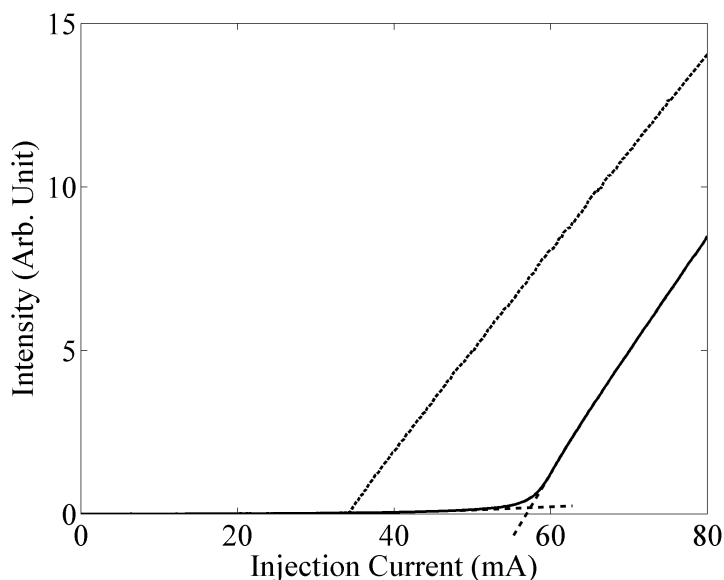
Figure 6.5: LI curves for the FSF laser (with maximum FSF) (dashed line) and the free running laser (solid line). The laser was operated at $25\,°C$ and current steps of 0.2 mA were used.

line) with a bias current resolution of 0.2 mA. The threshold has dropped from 57.2 mA to 33.4 mA with FSF, resulting in a reduction of 23.8 mA as indicated in Fig. 6.5. When FSF was applied the lasing builds up from the frequency shifting light field, not from the spontaneous emission. The sharp threshold current transition observed with FSF as compared to the gradual transition from LED operation to lasing when the laser is free running indicates the FSF laser is behaving as expected as it has been observed in other FSF laser systems with different gain media [114, 119].

Optical alignment of the laser system is achieved using the threshold minimization method. The external cavity mirror is aligned until a minimum threshold current is obtained. For optimized maximum feedback, laser threshold occurs at 33.4 mA $\pm$ 0.2 mA but as the laser was aging, towards the end of the experiment the threshold was 34.6 mA $\pm$ 0.2 mA. Figure 6.7 shows the output power as a function of the tilt of the external mirror for two different injection currents with maximum FSF. Zero mirror tilt corresponds to the alignment when minimum
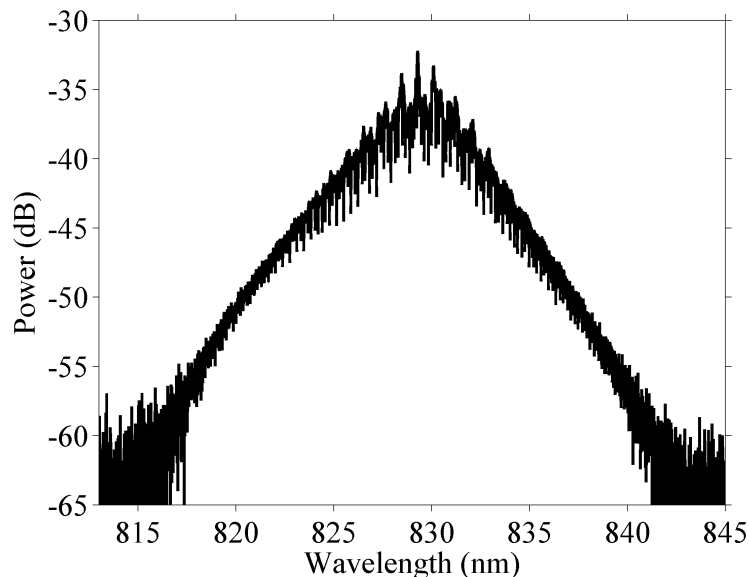
Figure 6.6: Spontaneous emission of the free running laser. The laser was operated at 25 °C and 55 mA.

threshold is achieved. For high injection current, see Fig. 6.7(b), the zero mirror tilt does not correspond to the maximum output power as observed in conventional optical feedback systems [234, 235]. Hence, the output power corresponding to minimum threshold sits in between two maxima and the feedback can not be aligned by maximizing the output power at currents well above threshold. However, when the laser is operated close to threshold, the maximum output power is reached when minimum threshold is obtained as seen in Fig. 6.7(a). Multiple realizations were performed and the large plateau at which the power is maximum and its variations very small was always observed. The small dip located in between the two maxima in Fig. 6.7(b) was present most of the time but the fact that a plateau was systematically observed for a broad range of tilt angle makes the interpretation of maximum output power rather difficult and most of the time random. Thus, the threshold minimization method was systematically used to align the mirror after the length of the external cavity was changed. Also, as it was observed that a small misalignment can cause the laser to behave in a very different way, the alignment was carefully checked and optimized in this
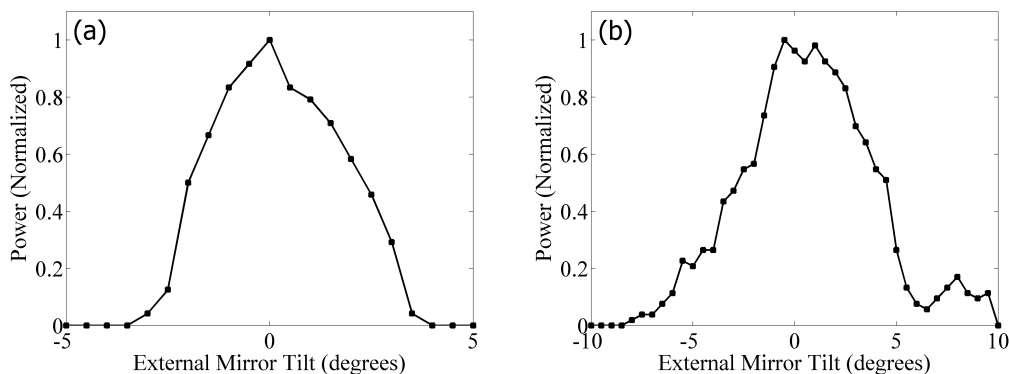
Figure 6.7: Output power as a function of the tilt of the external mirror for two different currents, 40 mA (a) and 70 mA (b), with maximum FSF. Zero mirror tilt corresponds to the alignment when minimum threshold is obtained.

consistent manner before any data collection was performed.

6.1.4 Optical Wavelength/Frequency Spectra

Two different types of instruments were used to capture optical wavelength/frequency spectra, an optical spectrum analyzer (OSA) [236] and a Fabry-Perot interferometer (FPI) [237]. The OSA relies on a high resolution diffraction grating to separate the different wavelength components the laser output may have. It has a maximum resolution of 0.07 nm or 30 GHz at 830 nm. The laser beam needs to be coupled into a single mode fiber connected to the OSA. The small diameter (typically 8 μm) of the core makes the coupling a difficult exercise, as well as being very lossy, if the beam does not have a circular shape. Therefore a pair of anamorphic prisms was used to obtain a near circular beam. Despite having a rather low coupling efficiency (less than 50%), an optical fiber is an easy and compact solution to implement in a system. An OSA is also useful to find the absolute wavelength of a laser. The main limitation of this instrument is its low spectral resolution.

An FPI was used as a second tool to measure optical frequency spectra from the system at higher resolution than the OSA. The equipment used was a plano-planar FPI. As the name suggests, the cavity consists of two high reflectivity

138

Figure 6.8: Optical frequency spectra obtained with the scanning Fabry-Perot interferometer for the free running laser. The injection current was 70 mA.

plane mirrors mounted on three carrier rails which allow the cavity length, i.e. the free spectral range (FSR) to be adjusted. One of the mirrors is fixed and the other is attached to a PZT. The coarse position of this mirror can be set to adjust the cavity length from 0.1 to 150 mm, corresponding to a FSR of 1.5 THz to 1 GHz, respectively. The FPI mirror holders and carrier rails are made of very low thermal expansion material to ensure the stability of the mirror spacing. The length of the cavity is scanned by sending a high voltage ramp to the PZT. A photomultiplier tube is placed after the cavity and is connected to an oscilloscope which triggers on the voltage ramp such that the scan of the cavity is synchronized with the detection. Multiple roundtrips inside the cavity are then responsible for creation of the interference patterns. Constructive interference is observed when the cavity is in resonance resulting in a high signal captured by the photodetector whereas an off resonance cavity leads to destructive interference. This is why a careful alignment of the cavity has to be made such that the highest signal is obtained when operating the free running laser. The Finesse (F) is a measure of the cavity resolution and is defined as the ratio of the FSR and the FWHM bandwidth of the resonance peaks $F = \Delta f / \delta f$ (see Fig. 6.8) [237]. If F becomes too small then the peaks will overlap each other resulting in a poor resolution of
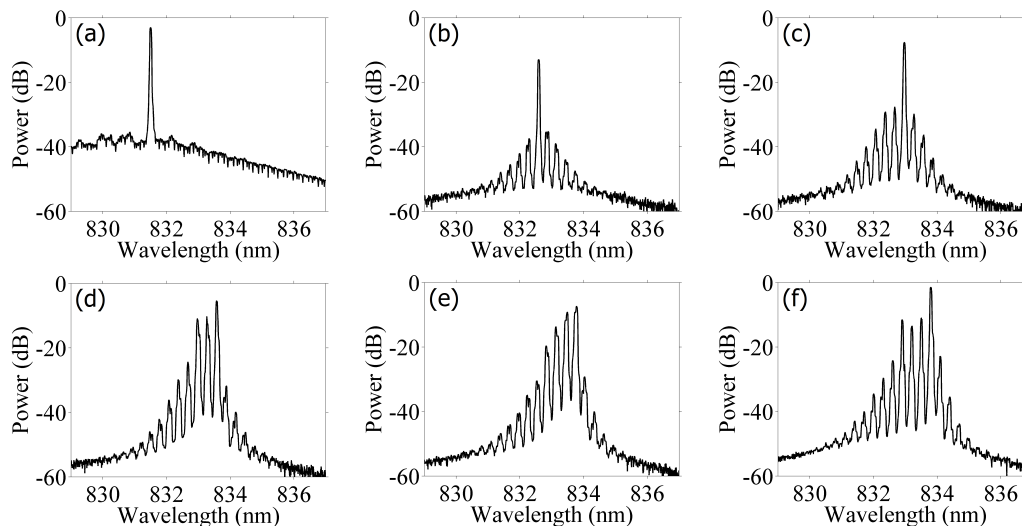
Figure 6.9: Optical spectra obtained with the optical spectrum analyzer for the free running laser operated at 70 mA (a), for the FSF laser with maximum FSF at 40 mA (b), 50 mA (c), 70 mA (d), 80 mA (e) and 100 mA (f).

the measure. A finesse of 70 ± 5 with a FSR of 7.7 ± 0.3 GHz was measured using the experimental trace shown in Fig. 6.8. These parameters give a maximum resolution of 110 MHz meaning that the 160 MHz features associated with the roundtrip FSF were resolvable, if they were present. The determination of the FSR of the cavity is critical when working with such a short cavity. Any drift, any instability could lead to a change in the FSR and thus in the FPI spectra. The easiest way to determine the FSR is to characterize the frequency drift of the laser induced by Joule heating. This can be done by recording the optical spectra from the OSA with increasing temperature. This is only valid if the laser does not show mode hopping during the temperature scan. However, due to the insufficient frequency range without mode hopping achieved by the laser, this method was not implemented. Instead a tunable laser, (New Focus 6226), tunable from 829-856 nm) with a resolution of 0.02 nm was used to calibrate the Fabry-Perot cavity. The high stability of the laser output along with the very fine tuning of the laser wavelength allowed the FSR to be determined to a precision of 300 MHz, i.e. 7.7 GHz ($\pm$ 4%).
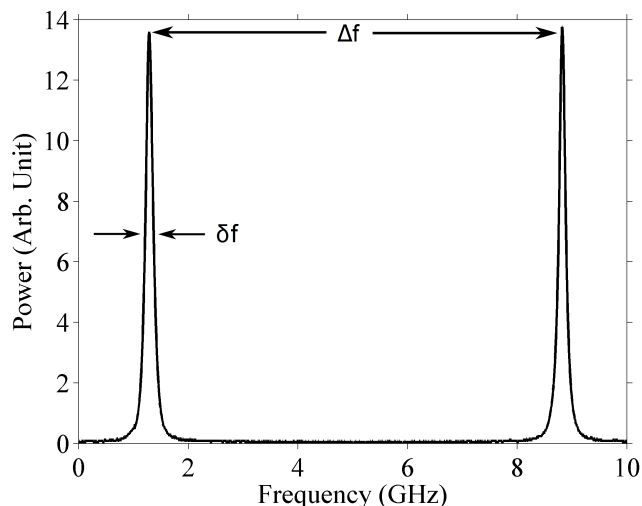
The optical frequency spectrum of the output of the system was measured at
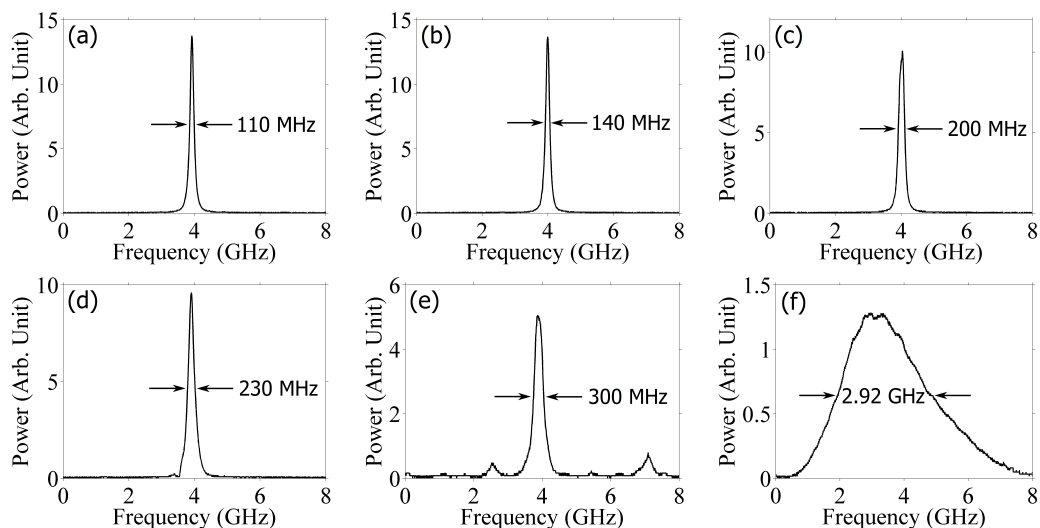
Figure 6.10: Optical frequency spectra obtained with the scanning Fabry-Perot interferometer for the free running laser (a), for the FSF laser with a FSF of 0.08% (b), 0.25% (c), 1.15% (d), 1.50% (e) and with maximum FSF (f). The injection current was 70 mA.

several injection currents and with several levels of frequency shifted feedback. Fig. 6.9 shows the optical wavelength spectra measured by the OSA. The free running laser at 830.8 nm shows a single longitudinal mode, with at least 25 dB of suppression for the neighbouring modes, at an injection current of 70.0 mA Fig. 6.9(a). When maximum FSF is applied the threshold drops, as seen previously in Fig. 6.5. The laser operates on a single longitudinal mode, with several low-power longitudinal modes as illustrated in Fig. 6.9(b), for an injection current of 40 mA. When the injection current is increased to 50 mA, see Fig. 6.9(c), the output power of the longitudinal modes starts to increase but the laser remains single mode as the side mode suppression relative to the main mode is greater than 20 dB. In Fig. 6.9(d) the laser is operated at 70 mA and it is now clear that the laser no longer operates on a single longitudinal mode, one can observe 3 modes with less than 25 dB of side mode suppression relative to the main mode. As the injection current increases the output power of the longitudinal modes increases as seen in Fig. 6.9(e). When the laser is driven at 100 mA with maximum FSF it operates on 4 longitudinal modes with less then 25 dB of side mode

suppression as depicted in Fig. 6.9(f). A higher injection current also means more power in the side modes as observed in Fig. 6.9(e) and 6.9(d). The main mode has a higher power at 100 mA than 80 mA but the power in the three side modes flattens out and they show similar power with $\approx$ 10 dB suppression to the main mode. Figure 6.9 shows that the power in the side modes increases gradually with injection current while maintaining a similar power level to that of the free running laser in the main mode. This multiple longitudinal modes operation of the laser with increasing injection current means that overlap of FSF broadened features associated with these multiple longitudinal modes may be increasing the apparent laser bandwidth in Fig. 6.10(f). The slight modulations in the spectral envelope also indicate this. One can also notice that the center of the optical wavelength spectrum shifts to longer wavelengths with FSF, see Fig. 6.9(b).

The effect of FSF on the spectral bandwidth of the laser is illustrated in Fig. 6.10, using the FPI. The full width half maximum (FWHM) of the main free running laser mode is less than 110 MHz, the instrument linewidth, at 70 mA Fig. 6.10(a). When a FSF of 0.08% is applied the spectrum broadens to 140 MHz as seen in Fig. 6.10(b). As FSF is further increased the FWHM reaches 200 MHz with a FSF of 0.25%, see Fig. 6.10(c). The FWHM increases to 230 MHz in Fig. 6.10(d) when the FSF is still at a relatively low level of 1.15%. A FSF level of 1.50% is enough to change the behavior of the laser. Beyond this point the laser is no longer lasing on a single longitudinal mode, therefore one needs to be careful with the interpretation of the optical spectra from the FPI beyond this FSF level. With maximum FSF applied, Fig. 6.10(f), the FWHM increases to 2.92 GHz and has an approximately Gaussian shape as observed in other FSF laser systems. The FSF laser optical frequency spectrum is expected to show features spaced by 160 MHz if the laser has a pulsed output. Fig. 6.10(f) does not show such features. The output is consistent with a broad band modeless output, or a chirped comb of frequencies that are not resolved due to the slow scanning rate of the Fabry-Perot compared to the frequency-shift rate of the intracavity light field. But this interpretation of Fig. 6.10(f) may also need to be modified because, as discussed previously, at this FSF level the laser is not emitting on a single longitudinal mode.

6.1.5 Resonance Condition

The resonance condition of the external cavity was established by looking at the autocorrelation function (ACF) in combination with the fast fourier transforms (FFTs) of the output power time-series of the system. For high levels of FSF the autocorrelation function, calculated using a custom program in Matlab, shows strong, sharp peaks located at the external cavity frequency. The location of the peaks can be determined with a precision of 400 kHz. Thus, it is possible to adjust the cavity length to match the AOM roundtrip frequency to a precision of 400 kHz. The AOM roundtrip frequency is determined using the FFTs of the time-series because the AOM features occurring for low levels of FSF do not appear in the autocorrelation function. It has been found that the FFTs, for low FSF levels, exhibit peaks located at multiples of the AOM frequency, i.e. ≈ 80 MHz, ≈ 160 MHz, ≈ 240 MHz, etc. The amplitude of these peaks decreases with higher order multiples, 160 MHz being the strongest peak. This peak is always located at the same frequency regardless of the cavity length. Therefore the cavity length can be adjusted so that both features, from the AOM and the external cavity, overlap within 100 kHz. The external cavity features also appear in the FFTs of the output power time-series of the system for high FSF levels. Strong, evenly spaced, sharp peaks are observed in the FFTs and are directly related to the external cavity roundtrip frequency. However, these peaks are jittering in frequency a little more than the autocorrelation peaks, therefore the absolute frequency can only be determined with a precision of 1 MHz ($\pm$ 10%). It is also common that for certain parameters these peaks do not appear in the FFTs. This usually happens for low injection currents when the system is more likely to be dominated by the FSF (see Sec. 6.4). Thus, the FFTs will only be used to know the frequency shift introduced by the AOM and the autocorrelation functions for a precise measurement of the external cavity roundtrip frequency. The 320 MHz case will be described in this section but the same procedure was applied for all the different cavity lengths studied in this chapter.

For a given injection current a fast fourier transform was performed on each of the output power time-series for every FSF level. The AOM voltage controls the FSF level, i.e. the fraction of the incoming light transmitted through the first
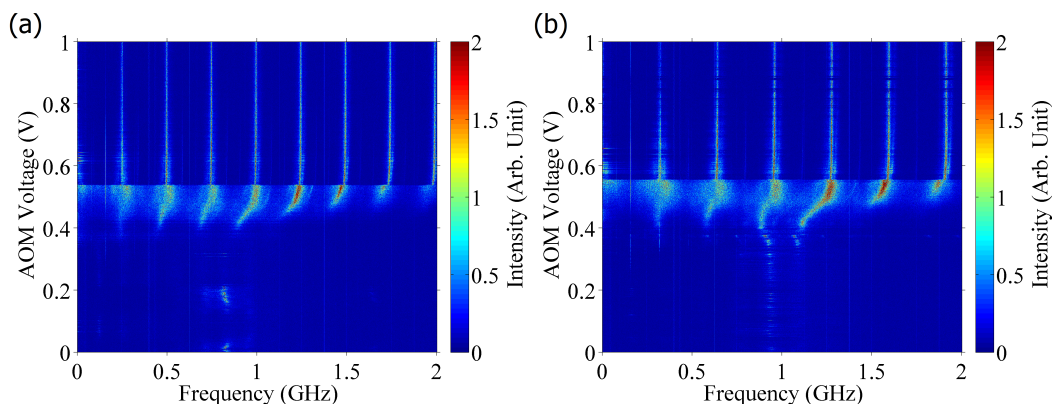
Figure 6.11: Map of the FFTs of the output power time-series for increasing FSF (a) with an off resonance cavity of 248 MHz and (b) with a resonant cavity of 320 MHz. The injection current was 70 mA.

order beam. It ranges from 0 V to 1 V, with 1 V corresponding to maximum FSF. For each injection current a total of 1001 time-series have been captured with 0.001 V steps applied to the AOM. The FFTs are then used to produce a color map of the RF spectra as a function of FSF as illustrated in Fig. 6.11.

The frequency axis in Fig. 6.11 spans from 0 to 2 GHz but the bandwidth limit of the oscilloscope allows us to observe dynamics up to 4 GHz. Beyond this frequency the amplitude drops, even though it is still possible to observe features up to 5 GHz with good clarity. Figure 6.11(a) illustrates the non resonant case with an external cavity length corresponding to a roundtrip frequency of 248.1 MHz. Peaks located at 248.1 MHz (see online version for better clarity) and its integer multiples are observed in Fig. 6.11(a) for high FSF levels. When the cavity length is modified to match the frequency shift of 318.4 MHz induced by the AOM, as seen in Fig. 6.11(b), the location of the peaks changes and now matches the frequency roundtrip of the cavity length. This means that the features observed for high FSF levels match the external cavity roundtrip time. The external cavity frequency has be observed in the literature with conventional optical feedback systems [238, 239, 240]. However, the frequency jitter of these peaks is too large to allow precise determination of the external cavity roundtrip frequency. Indeed, both the location and the frequency spacing between the peaks is not constant and it is common to observe variations due to the frequency jitter
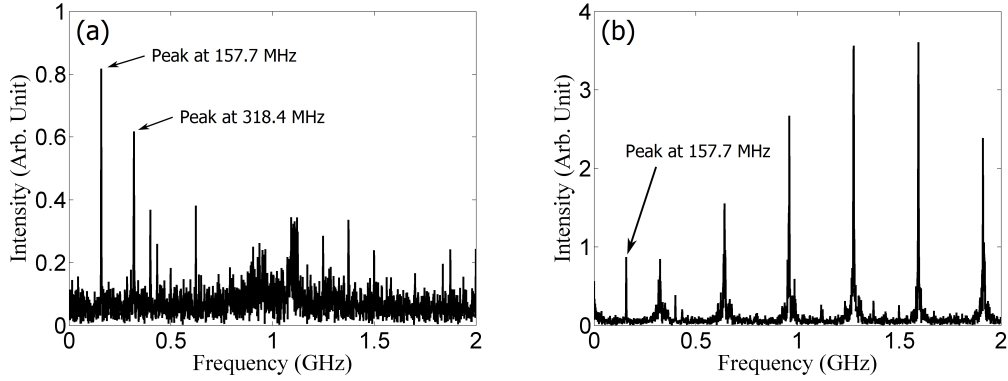
Figure 6.12: FFTs of the output power time-series for two FSF levels, (a) 0.34 V and (b) 0.7 V. The injection current was 70 mA.

on the order of a few MHz, making FFTs an unreliable tool to determine the cavity roundtrip frequency. However, a strong, sharp peak located around 160 MHz and appearing for low FSF levels up to maximum FSF is also observed in both graphs in Fig. 6.11. It is worth noting that all the low amplitude peaks observed for the entire FSF range are not features related to the dynamics of the system but noise related to the oscilloscope. Those peaks are low in amplitude and always appear at the same frequencies, they are more easily visible in the digital version of the manuscript.

Figure 6.12 shows two slices extracted from Fig. 6.11(b) at 0.34 V and 0.7 V in order to have a closer look at the peak located $\approx$ 160 MHz. The amplitude of the peak observed at 157.7 MHz is almost constant with increasing FSF and when the cavity is in resonance a second peak located at 318.4 MHz corresponding to the first multiple of the peak appearing at 157.7 MHz is observed, as seen in Fig. 6.11(b) and 6.12(a). This second peak is lower in amplitude and appears for higher FSF levels than the main peak at 157.7 MHz, probably suggesting that the external cavity is in resonance with the frequency shift of the AOM. Note that the 0 frequency of the FFTs is slightly offset so that the high amplitude peak located at 0 does not appear in the graph for better clarity. This offset explains the appearance of the second peak in Fig. 6.12(a) at 318.4 MHz rather than the expected 315.4 MHz, the same offset was applied to the ACF. However, the
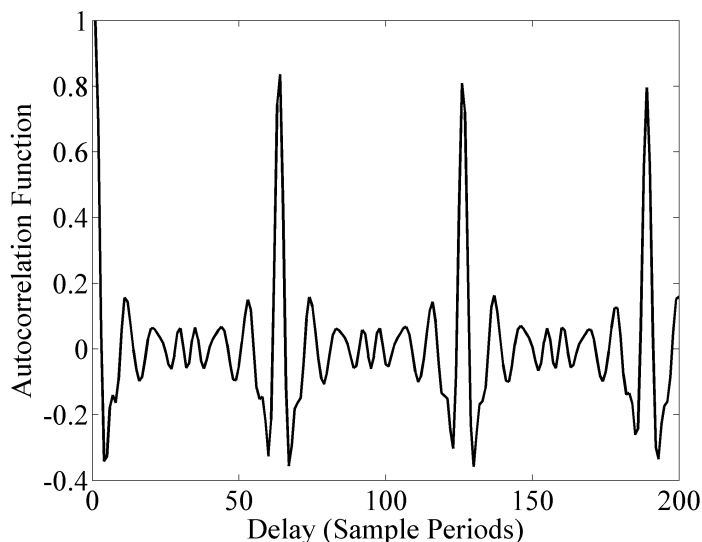
Figure 6.13:   Autocorrelation function at 70 mA and 0.6 V. One sample period=50 ps.

frequency spacing between the two peaks can be determined with confidence and was measured at 160.7 MHz. Note that the linewidth of the peak associated with the AOM is much narrower than the ones of the external cavity related peaks, as observed in Fig. 6.12(b), and remains constant for all FSF levels. Figure 6.13 shows the autocorrelation function at 70 mA and 0.6 V. The strong peak, and its integer multiples, corresponding to a delay of 63 sample periods observed in Fig. 6.13 is directly related to the time delay introduced by the external cavity. Note that this delay is constant with increasing FSF. This delay of 63 sample periods corresponds to a frequency of 318.1 MHz ($\pm$ 500 kHz) and this result agrees, within the uncertainty of the measure, with the location at 318.4 MHz of the AOM peak observed in the FFTs. Thus, the external cavity was assumed to be resonant, within this uncertainty, with the frequency shift introduced by the AOM. The peak associated with the frequency shift of the AOM for low FSF levels and the peak related to the external cavity roundtrip frequency for high FSF levels can be seen overlapping in Fig. 6.11(b) and confirms that the external cavity is now resonant.

6.2 Theoretical Models

The effects of optical feedback in semiconductor lasers have been studied since the late 70s [241, 242]. A few years later, in 1980, Lang and Kobayashi published a paper [4] explaining the effects of optical feedback on semiconductor lasers. They demonstrated that high level of external optical feedback can make the injection laser multistable and can also cause hysteresis phenomena. The authors attributed these effects to be related to the gain medium characteristics of semiconductor lasers such as the strong dependence of the refractive index on carrier density in addition to a broad gain spectrum. This paper also introduces the widely used model of a semiconductor laser with optical feedback. The present experimental setup, however, requires the inclusion of the frequency shift undergone by the carrier frequency of the field and high reflectivity of the feedback mirror.

6.2.1 Overview and Description

Since the first FSF laser systems have been demonstrated, their unique properties found various applications in diverse fields. But the precise nature of the field emerging from such lasers is still being discussed [120]. One of the reasons is that FSF lasers can operate in various regimes, ranging from a broadband modeless operation [97, 99, 102, 243], to pulsed output [27, 30, 31, 101, 244], and also a chirped comb of frequency components [98, 116, 118, 245, 246], depending on controllable parameters such as the amount of gain, the external cavity roundtrip frequency and/or the frequency bandwidth of the laser. Broadband modeless output originated from the observation that the build up of the intra cavity light field by regenerative amplification after multiple roundtrips in the cavity does not apply anymore. The frequency shift experienced by the electric field after each roundtrip in the cavity prevents constructive interference from occurring at fixed frequencies determined by the cavity length. Thus, the generation of radiation exhibiting a continuous spectral profile is possible. The Fabry-Perot structure of such radiation no longer exists but it retains the common features of conventional laser sources. However, when the cavity length matches a multiple of the AOM

147

frequency shift the system shows pulsed output. As it is not possible to obtain an electric field which is identical in phase and frequency after several roundtrips in the cavity, mode locking is a result of temporal overlap of consecutive passes through the cavity which then leads to constructive interference. A few years later, the nature of the broadband modeless output was reinvestigated [98]. Despite previous observations it was made clear that the output of an FSF laser showed a mode structure, precisely a chirped comb of frequencies. This moving comb consists of a superposition of the optical modes separated by the AOM frequency whose instantaneous frequency chirps with time at a rate proportional to the intracavity frequency shift. The chirp rate is such that any mode structure would be washed out in the detection of a Fabry-Perot interferometer or an optical spectrum analyzer which were the only optical spectral characterization tools used in the early reports. This is why two-beam interferometry studies are required to characterize the true nature of FSF laser systems. In a two-beam interferometer, the beat frequency between the two beams (shifted by the time-delay introduced by the interferometer) is directly related to the difference in the instantaneous frequencies of the modes of the the two beams. Therefore the observation of extra beat notes at the output of such an interferometer has been attributed to be a chirped comb of frequency components [118]. This model is generally accepted to describe the nature of the electric field emanating from FSF laser systems [246] and it has been experimentally demonstrated with FSF systems based on a broad range of gain media [98, 118, 245, 247].

Theoretical models have been developed to support two different views of the nature of the field emerging from FSF lasers; either the discrete set of frequencies which describes the FSF laser as a static comb of frequencies [31, 248, 249] or the moving comb model where the electric field is seen as a moving comb of chirped frequencies [29, 116, 119, 250]. More recently a study from Yatsenko and coauthors [246] presented a new approach for treating the coupled equations linking electric field output and population inversion for a FSF laser based on a unification of both models previously introduced in the literature.

In a nutshell, several models have been developed for an FSF laser and most of them describe the dynamics of solid state lasers with FSF [114, 115, 119, 144, 246]. Other models have been developed for FSF semiconductor laser systems [251, 252]

but none of them is as complete as the solid state laser based systems previously mentioned. None of these models have been used to conduct simulation studies of the system because they fail to describe the dynamics of a semiconductor laser with FSF. Developing a new model would require a lot of time which was not available during my time at Macquarie University and could potentially be a PhD project on its own.

6.3 Time-series Characterization Tools

6.3.1 Root Mean Square Amplitude

The first tool used in order to characterize the system is the root mean square (RMS) amplitude of the output power time-series. Detailed maps of the RMS amplitude of the system can be produced for a broad range of injection/feedback parameter space. These maps help us in understanding the complexity of the dynamics of the laser under various injection/feedback regimes and illustrate where the system shows fluctuations in the output power. These fluctuations are a good indication of where the coherence collapse region is located in the injection/feedback parameter space. The coherence collapse region has very distinct boundaries when the laser is operated with conventional optical feedback [253] but shows a gradual rather than a discontinuous shift with FSF [104]. The relatively low computing power required to perform the RMS calculations and then produce the maps makes this tool very appealing for identifying regions of instabilities of the system.

The RMS amplitude, also known as the quadratic mean, is a statistical measure of the magnitude of the power of the output time-series of the system. Consider a set of n values of a discrete distribution $\{x_i, ..., x_n\}$, the RMS is mathematically expressed by

$$x_{RMS} = \sqrt{\frac{x_1^2 + x_2^2 + ... + x_n^2}{n}} = \sqrt{\frac{\sum_{i=1}^{n} x_i^2}{n}}. \tag{6.4}$$

In order to produce a high resolution map of the system the RMS amplitude was calculated for the 71071 output power time-series collected for the characterization of the system, and a color map was generated from the RMS calculations in order to show how the dynamics of the system evolve as a function of injection current and optical feedback parameters.

6.3.2   Permutation Entropy

The second tool used to characterize the dynamics of the system is a measure of entropy, i.e. the permutation entropy (PE), and has been first introduced by Bandt and Pompe [152] as a tool of complexity measure for chaotic time-series. This measure of entropy, used here, is different from the famous Shannon entropy [254] or the Kolmogorov-Sinai entropy [255]. The Shannon entropy does not take into account the temporal order of values in a time-series which can be problematic when looking at dynamics evolving on the time scale of the time-series. The Kolmogorov-Sinai entropy is computationally expensive. The PE method has demonstrated to be similar to Lyapunov exponents [256], computationally more efficient and also less sensitive to noise. It is therefore more suitable for experimental data analysis.

The Bandt and Pompe methodology is described in detail in [152]. It is summarized here. PE is a measure of time series complexity based on the entropy of ordinal permutations. The ordinal pattern symbols are determined by looking at the relative amplitudes of the points forming the ordinal patterns in the time-series. Two parameters, the ordinal pattern length D and the delay τ, need to be carefully chosen in order to obtain meaningful information from the PE. Consider a vector of length D. There exist $D!$ possible permutations (see Fig. 6.14) so the choice of D is directly influenced by the length n of the time-series to be analyzed. In order to obtain reliable statistics distribution it is assumed that n must be much larger than D [257]. But if D becomes too small, i.e. smaller than 3, then it is quite likely that the statistics distribution will be biased by experimental noise. In our case the time-series collected consists of 20000 data points, therefore in most cases $D = 5$ was chosen. It gives $D! = 120$ possible ordinal permutations, which is a good trade off between calculation time and insight into the types

Figure 6.14: Illustration of the 6 possible permutations π for an ordinal pattern of length $D = 3$.

of dynamics shown by the system. The delay τ is the time separation between the points used to construct the vector D and it corresponds to a multiple of the signal sampling period. The complexity of the system can be investigated at different time scales by changing the delay. The investigation of complexity maps generated from permutation entropy calculations at different time scales has been reported in [39].

Consider the example shown in Fig. 6.14, where $D = 3$ was chosen. It means that there exists $D! = 6$ possible ordinal permutations. Each permutation is then assigned with a unique symbol π, then by sweeping through a complete time-series and counting how many times each ordinal pattern symbol appears, it is possible to generate a probability distribution as illustrated in Fig. 6.15. The permutation entropy is then calculated from this probability distribution.

Given a time-series $\{x_t, t = 1, 2, ..., N\}$, an ordinal pattern of length D, a delay τ, and an embedding procedure forms a vector

$$s \rightarrow (x_{s-(D-1)\tau}, x_{s-(D-2)\tau}, ..., x_{s-\tau}, x_s). \tag{6.5}$$

At each time s the ordinal pattern of this vector can be converted to a unique
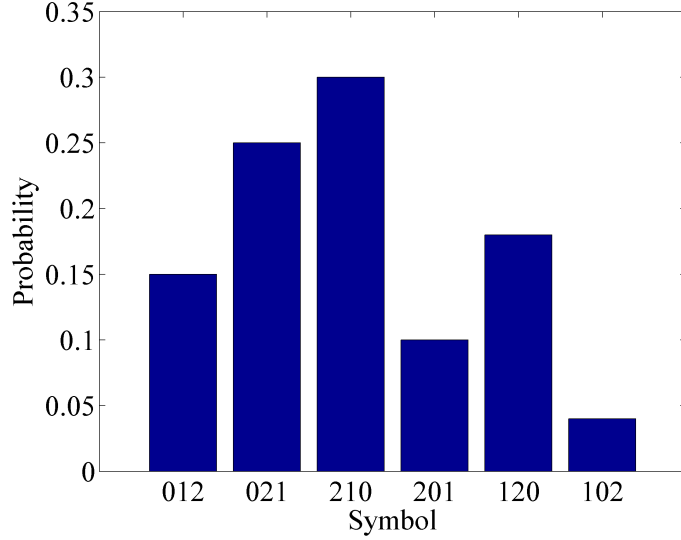
Figure 6.15:   Example of a probability distribution of the 6 possible permutations associated with an ordinal pattern of length $D = 3$.

symbol $\pi = (r_0, r_1, ..., r_{D-1})$ given by

$$x_{s-r_o\tau} \geq x_{s-r_1\tau} \geq ... \geq x_{s-r_{D-2}\tau} \geq x_{s-r_{D-1}\tau}. \qquad (6.6)$$

For each of the $D!$ permutations π of length D we determine the ordinal pattern probability distribution $P = \big\{ p(\pi_i), i = 1, ..., D! \big\}$. The normalized permutation entropy is then defined as

$$H_s = \frac{- \sum_{i=1}^{D!} p(\pi_i) \ln p(\pi_i)}{\ln D!}. \qquad (6.7)$$

The normalized permutation entropy ranges between 0 and 1, with 1 corresponding to a completely stochastic process with a uniform probability distribution and 0 to a completely predictable time-series.

6.4 Experimental Results of the Effects of the Cavity Length on the Dynamics of the System

In this section the dynamics of a semiconductor laser with FSF are investigated. High resolution dynamic maps depicting the RMS amplitude and the PE as a function of laser injection current and FSF level are produced. These allow us to investigate the complexity of the system for a broad range of this parameter space. Three different cases, corresponding to 3 cavity lengths, are reported. As discussed previously in Sec. 6.1.5, the external cavity length was matched with a multiple of the AOM roundtrip frequency. Near resonant FSF is used which has the potential to generate pulsed output from the system [30, 31]. The nature of the nonlinear gain and group velocity dispersion in single section semiconductor lasers is such that poor mode-locking usually results if any mode-locking occurs at all in single section devices [258, 259]. These results are also compared with the non-resonant case where the AOM roundtrip frequency does not match the external cavity frequency where broadband modeless output has been seen in other FSF laser systems [97, 99].

The gain in semiconductor lasers is sufficiently different from that in many other laser media that it is to be expected that the spectral and temporal output of a semiconductor-laser-based FSF laser will be different from that in other FSF laser systems. Early reports of semiconductor laser with FSF systems demonstrated an FSF broadband output with a controllable bandwidth of up to a few GHz, while the laser was operating on a single longitudinal mode [28, 103]. However, broader FSF bandwidths associated with single longitudinal mode operation of the laser could not be achieved as multi-longitudinal mode operation was observed beyond an FSF level of 12% [103]. Similar results were also obtained in [124, 245, 251, 260]. The effects of FSF on DFBs were reported in [104] and even though such devices offer better spectral selectivity than conventional EELs, FSF bandwidths of a few hundred MHz were observed. In the same study, the comparison with conventional optical feedback was also conducted and showed that the

transition to the coherence collapse dynamical regime occurred in both systems, however with a more gradual transition in the FSF system.

The previous studies on FSF semiconductor systems were performed using low resolution acquisition methods and focused on the optical and RF spectral behavior of the system [28, 103, 104, 245]. Here, the temporal and spectral behavior of the output power time-series are investigated by means of multi-GHz-bandwidth real time data collection and LabVIEW controlled experiments that can collect tens of thousands of time series, as laser parameters are varied, in experiment run times that are measured in hours. High resolution maps were recently generated for a semiconductor laser with conventional optical feedback [39] and such maps provide the necessary information to allow conventional optical feedback and FSF to be contrasted once a similarly comprehensive set of maps is generated for an FSF system.

This section is divided in 6 subsections, a brief summary of the main results is introduced in the first subsection which is then followed by 5 sets of results for different cavity lengths corresponding to 4 roundtrip frequencies, 160 MHz, 248 MHz, 320 MHz and 480 MHz are introduced. Three of these (160 MHz, 320 MHz and 480 MHz) match a multiple of the frequency shift of the optical feedback. A discussion contrasting this work with earlier work done on semiconductor laser with FSF will follow. The last section introduces the results from the zeroth order diffraction of the AOM, i.e. conventional optical feedback, with a cavity corresponding to a roundtrip frequency of 320 MHz. Overall, the results give a complete picture of the dynamics of an EEL with FSF. The new insight gained by the high resolution data collected helps understand the system better and will support the development of a theoretical model capable of describing the dynamics of such a system.

6.4.1   Main Results

Four different external cavity lengths have been studied and are reported here. Three of these (160 MHz, 320 MHz and 480 MHz) match a multiple of the frequency shift introduced by the AOM. Permutation entropy maps are specially suited to identify regions exhibiting different temporal dynamics. Figure 6.16

shows the normalized PE as a function of FSF and injection current corresponding to the four different external cavity configurations. Each map is labeled with a set of numbers corresponding to several regions of the map, above an FSF level of 0.7 V, where the temporal dynamics are noticeably different. Indeed, below this FSF level the four maps are identical and show the same dynamics. The first observation is that the four maps have common features, the regions marked 1, 2, 3 and 5 are present in each of them. Region 1 is depicted as a narrow pale green band of injection current near threshold. It is associated with PE values <0.9. Region 2 appears for higher injection currents and it is associated with PE values <0.8. In these regions the temporal dynamics show well defined periodic oscillations on a cw baseline. The lower PE values observed in region 2 indicate more periodic dynamics in this region. In both regions, however, the laser is strongly single mode. Region 3 is associated with high PE values >0.9 and the dynamics are dominated by the external cavity delay with strong peaks at multiples of the external cavity frequency in the FFT spectra. Region 5 shows PE values >0.95 and it is associated with cw, multi-mode operation of the laser. In this region the external cavity delay observed in region 3 does not affect the dynamics of the system.

The external cavity corresponding to a roundtrip frequency of 320 MHz, i.e. Fig. 6.16(b), shows a region where the dynamics are different from the other maps. This region, marked 4, shows dynamics which are similar to that observed in regions 1 and 2, i.e. periodic oscillations on a cw baseline with single mode operation of the laser, and it also shares the same PE values.

Region 6 appears when the external cavity has a roundtrip frequency of 480 MHz, i.e. the shortest cavity, and is depicted in Fig. 6.16(c) as a narrow pale green band. This region shows dynamics which are similar to that found in region 1. Both regions share the same PE values and are associated with single mode operation of the laser.

The first observation is that there is no fundamental difference between resonant and non resonant external cavity configurations. The main effect is related to the FSF strength. Indeed, the main difference is the range of injection currents at which regions 1 and 2 occur. The two longer cavities, i.e. 160 MHz and 249 MHz, show a narrower region 2 (about 1 mA) with PE values varying from
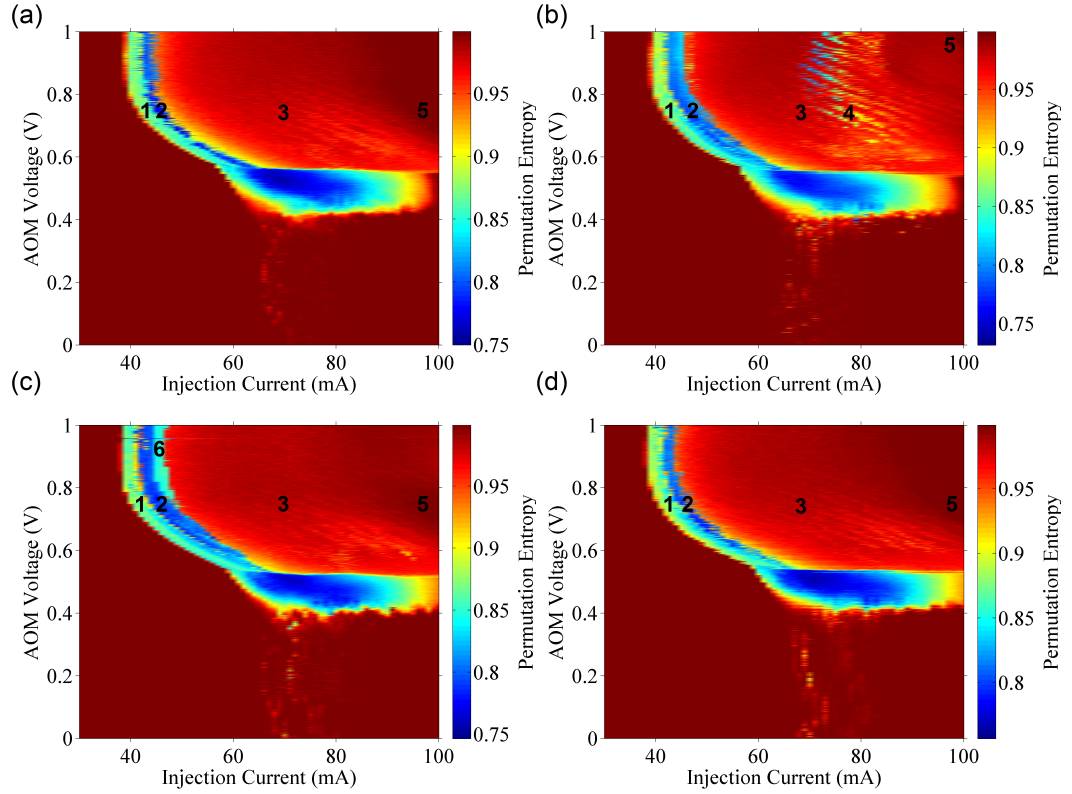
Figure 6.16: (a) Maps of the normalized permutation entropy ($D = 5$, $\tau = 2$) as a function of FSF and injection current with a cavity roundtrip frequency of (a) 160 MHz, (b) 320 MHz, (c) 480 MHz and (d) 249 MHz. The numbers 1-6 refer to six distinct regions, above 0.6 V, where the dynamics are noticeably different.

0.78 to 0.95. The shortest cavity shows periodic time-series on a cw baseline over a range of 6 mA with FSF levels >0.8 V. The fact that one observes a gradual increase of the injection range at which the system shows periodic time-series on a cw baseline with shorter cavities is related to the FSF strength. This is due to the remaining divergence of the laser beam after collimation. The longer external cavities suffer from higher losses when the beam travels back through the AOM compared to short cavities as explained in Sec. 6.1.2.

The following subsections describe in details the temporal dynamics of the system for the four different external cavity configurations. PE maps are very useful to identify regions of the map where the dynamics are different but in order to have a complete picture of the dynamics it is necessary to compare both

temporal and optical data. The following subsections introduce different high resolution maps such as FFTs, ACFs, optical spectra and RMS amplitude maps in order to characterize the system.

6.4.2   160 MHz Cavity Roundtrip Frequency

The color map of the RF spectra as a function of FSF depicted in Fig. 6.17(a) was produced following the procedure described in Sec. 6.1.5. A color map showing the dominant frequency of the FFTs of the output power time-series as a function of FSF and injection current was also produced, see Fig. 6.17(b). Color maps depicting the root-mean-square (RMS) amplitude of the time-series and the normalized permutation entropy as a function of FSF have also been produced in order to show how the system dynamics evolve. Figure 6.18 shows (a) the RMS amplitude of the output power time-series of the system and (b) the normalized PE. Three distinct regions were identified in these maps where the dynamics of the system are fundamentally different. The FSF levels indicated in this chapter, all refer to the percentage of light transmitted after passing through the AOM. For an estimation of the portion of the light fed back to the laser see Sec. 6.1.2. Regions of low, medium and high FSF levels correspond to FSF levels of 0-12% (0 V-0.40 V), 15-57% (0.42 V-0.56 V) and 57-100% (0.56 V-1 V) of the light reflected from the external mirror, respectively.

In Fig. 6.17(a), a strong peak is located at 157.7 MHz for low FSF level, i.e. below 12% (0.40 V) of the reflected light. This peak first appears around 0.25 V, which corresponds to an FSF level of 0.4%, and is seen up to 0.40 V. Below 0.25 V any effect of FSF is too small to be discerned in this experiment. This is confirmed by the fact that, in this region, the laser operates cw which leads to the observation of noise in the FFTs as seen in Fig. 6.17(b) where the dominant frequency of the FFTs seems rather random compared to the rest of the map. The RMS map shown in Fig. 6.18(a) indicates that the dynamics of the system are not affected at these low levels of FSF, although the output power of the laser seems a little more stable for high injection currents, 82 mA and above, and low FSF level, below 0.40 V. This higher stability of the laser is also seen in the optical spectra
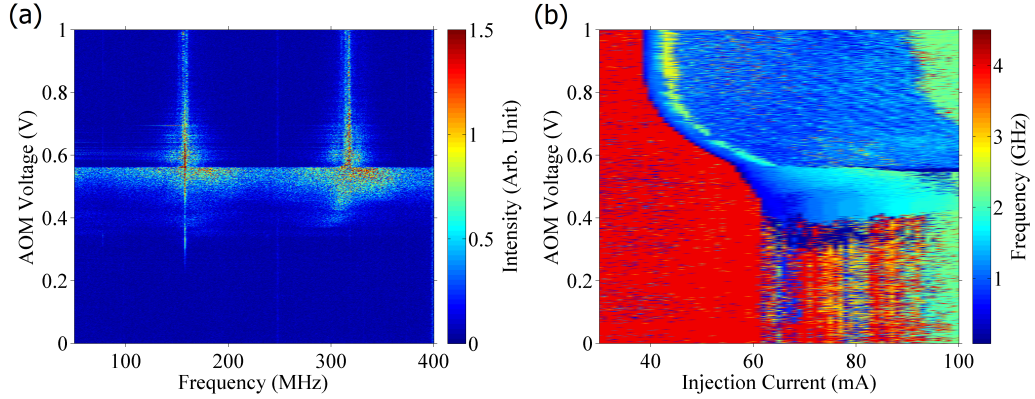
Figure 6.17:   (a) Map of the FFTs of the output power time-series for increasing FSF at 70 mA. (b) Map of the dominant frequency of the FFTs of the output power time-series as a function of FSF and injection current.

where mode hopping is also completely absent in this region. The laser operates cw within this FSF and injection range (dark blue region in Fig. 6.18(a)) as areas of low RMS amplitude correspond to cw operation of the laser or the laser is below threshold. The optical frequency spectra associated with this low FSF regime are illustrated in Fig. 6.10(a,b,c,d,e), where a broadening of the laser line of up to 300 MHz with an FSF level of 1.5% was observed. Optical spectra of the system taken with the FPI are only available up to this FSF level because above this level the laser is not operating on a single longitudinal mode as discussed in Sec. 6.1.4. These observations are comparable with previous work done on semiconductor laser systems with low FSF level in [28, 103, 104, 251]. Figure 6.18(b) shows detailed maps of the normalized permutation entropy. The PE was calculated for an ordinal pattern of length $D = 5$ and a delay $\tau = 2$. The delay of two sampling periods was chosen so that the fastest laser oscillations could be captured, yet allowing the dynamics to be distinguished from noise. With low FSF level the PE approaches 1 ($H_s \geq 0.98$) and corresponds to complex time-series associated with noise on a cw output or when the laser is below threshold. In these regions the AC recorded signal is principally photodetector and oscilloscope noise. This low FSF region is characterized by a high value of PE ($H_s \approx 0.98$) which matches the RMS amplitude results where the laser is operating cw. Figure 6.19(a) shows a dynamic map of the number of longitudinal modes lasing as a function of FSF
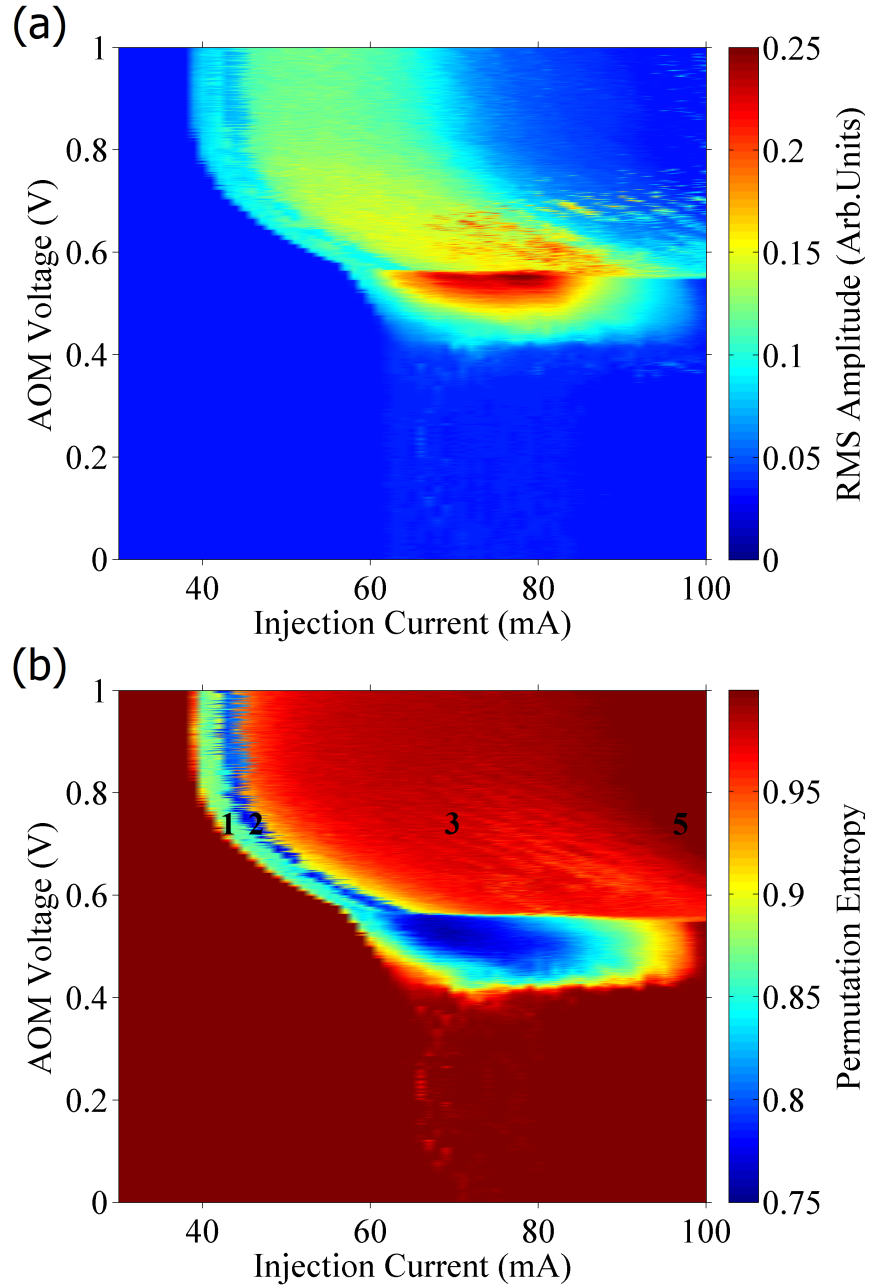
Figure 6.18: (a) Map of the RMS amplitude of the output power time-series as a function of FSF and injection current. (b) Map of the normalized permutation entropy ($D = 5$, $\tau = 2$) as a function of FSF and injection current. The numbers 1, 2, 3 and 5 refer to four distinct regions where the dynamics are noticeably different.
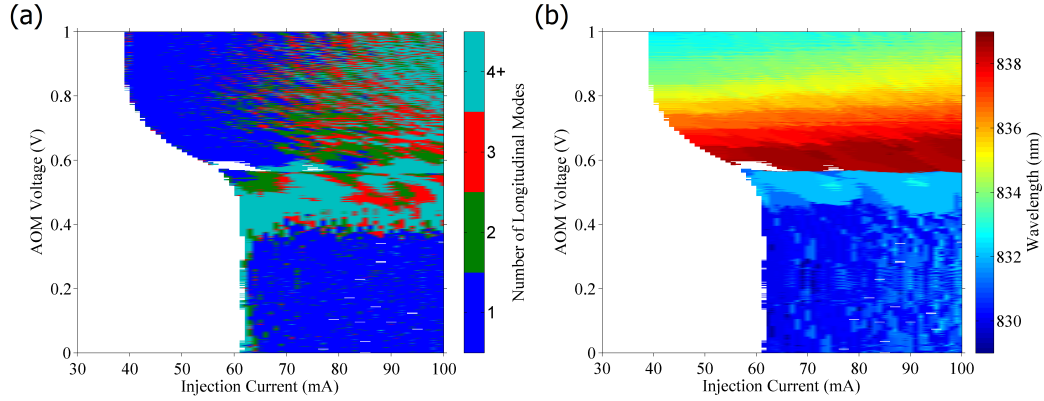
Figure 6.19:   (a) Map of the number of longitudinal modes lasing as a function of FSF and injection current. The threshold for side mode suppression was set at 15 dB. (b) Map of the emission wavelength of the main lasing mode as a function of FSF and injection current.

and injection current. The map was produced by determining the number of maxima, with at most 15 dB of side mode suppression relative to the main mode, extracted from the OSA spectra. Even though a side mode suppression of 20 dB is commonly required to consider a laser single mode, the maximum of 15 dB suppression was chosen for clarity of the map. When the laser is operating with low FSF level, it is mainly emitting on a single longitudinal mode, see the dark blue region in Figure 6.19(a). Several longitudinal modes start appearing with an FSF level as low as 1.5% (0.3 V) resulting in a side mode suppression of about 20 dB at this FSF level which means that multiple modes cannot be observed in Fig. 6.19(a). Note that the threshold current is not affected by low levels of FSF and remains constant in this region. Figure 6.19(b) shows the emission wavelength of the most intense mode extracted from the OSA spectra. With a low level of FSF, the emission wavelength is around 829 nm. It increases gradually towards longer wavelength with increasing injection current as expected from the thermal expansion of the laser cavity by Joule heating.

The temporal dynamics of the system for low FSF level are either not, or, are weakly affected by FSF, with no instabilities in the output time-series where the laser is operating cw. The sharp peak, related to the AOM RF signal, in the FFTs is the only temporally distinctive feature associated with the low FSF level

region. However, the spectrum is affected by very low FSF level ($\leq$ 1.5%). A significant broadening ($\approx 300\ MHz$) of the laser bandwidth was observed in the FPI spectra associated with single longitudinal mode operation of the laser.

The dynamics of the system radically change once FSF levels reach 12%, i.e. 0.40 V, as seen in Fig. 6.18(a). One can notice a region of instabilities associated with a high RMS amplitude depicted in red in Fig. 6.18(a). This region is located between 0.48 V and 0.56 V, respectively corresponding to 31% and 57% AOM transmission. It covers a broad range, 60-90 mA, of injection currents. This behavior is primarily the well known coherence collapse and has been observed in many laser systems with conventional optical feedback [5]. Recent studies have investigated the complexity of the output in this regime and the system more completely [39, 240]. In this region the sharp peak located at 157.7 MHz gradually disappears and broad, low amplitude peaks appear centered at the external cavity frequency multiples in Fig. 6.17(a). This transition in the dynamics is also illustrated in Fig. 6.18(b) where the PE value, for small time delay, reaches a lower complexity ($H_s = 0.75$) compared to the fundamental and technical noise. Figure 6.20 shows a typical time-series and the corresponding FFT spectrum in the coherence collapse region. In this region the RF spectra show broad, low amplitude peaks with low power at high frequencies (>2 GHz) and separated by the external cavity frequency roundtrip as illustrated in Fig. 6.20(b). The FWHM of the envelope of these features is approximately 2 GHz. The transition to the coherence collapse regime is abrupt and can be looked at as a discontinuous switch for most of the parameter space investigated. The switch occurs within the AOM voltage step resolution of the experiment, i.e. 0.001 V, and is located at the transition between high PE values ($H_s \approx 0.99$) and lower PE values ($H_s \approx 0.9$) as illustrated in Fig. 6.18(b). As discussed in Sec. 6.1.2 and illustrated in Fig. 6.4, the first order beam diffraction efficiency of the AOM with increasing voltage is not a linear function. Therefore, a step of 0.001 V at 0.40 V (where the transition to the coherence collapse occurs) and 0.56 V (where the second transition occurs) corresponds to an FSF increase of 0.2% and 0.38%, respectively. The longitudinal mode spectral behavior of the system is also affected when reaching the coherence collapse regime. In this region the laser operates on
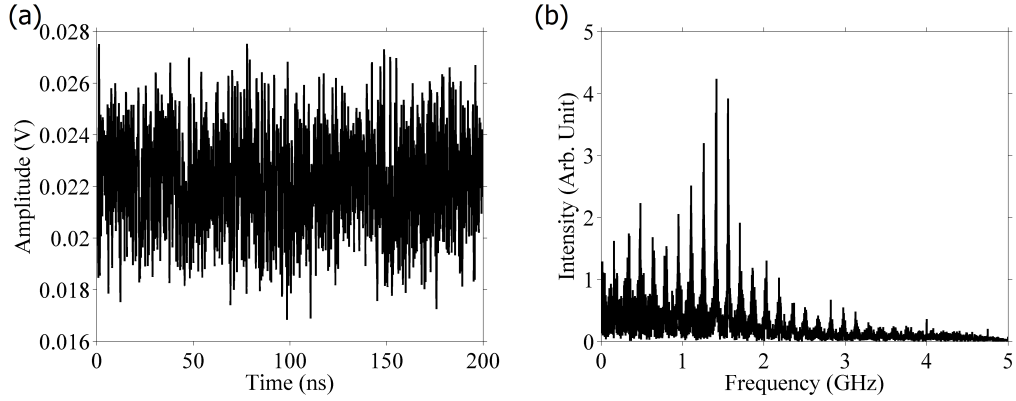
Figure 6.20: (a) Output power time-series with an FSF level of 47% (0.53 V) at 70 mA and (b) corresponding FFT spectrum.

multiple longitudinal modes (mostly on at least 3 modes) as seen in Fig. 6.19(a). The emission wavelength of the main mode is also shifted towards longer wavelengths. The most intense mode of the laser is also mainly operating at the same wavelength in this region despite a significant increase in the injection current as illustrated in Fig. 6.19(b). One can also notice a slight reduction of the laser threshold current. The characteristic drift towards longer wavelength expected with increasing injection current and observed with low FSF level does not occur with this medium FSF level which seems to stabilize the main emission wavelength of the laser. The individual spectra recorded by the FPI show a gradual broadening of the laser linewidth with increasing FSF up to 1.9 GHz with an FSF level of 57% (0.56 V). This bandwidth is comparable with that observed in Fig. 6.20(b) where the envelope of the frequency features exhibits a bandwidth of approximately 2 GHz. This observation reinforces the moving comb of frequency output theory suggested previously.

Both temporal and spectral dynamics of the system are strongly affected by medium levels of FSF, the system reaches the coherence collapse regime with an FSF level of 12% and enters a new regime of operation beyond 57%. In this region, the time-series show power fluctuations, the RF noise increases and external cavity peaks appear in the RF spectra. This is accompanied by further broadening of the optical spectrum and associated with multiple longitudinal mode

operation of the laser with a small reduction of threshold.

Beyond an FSF level of 57% the system switches to a third different regime. The FSF reduces the laser threshold by $\approx 20\ mA$ as seen in Fig. 6.19. The rate at which threshold reduction occurs is also higher than that of the coherence collapse region. The system shows an abrupt shift towards a longer wavelength of the main mode as the FSF level reaches 57% then gradually shifts back towards shorter wavelengths with increasing FSF as depicted in Fig. 6.19(b). There are two competing effects in this region as the FSF shifts the emission towards shorter wavelengths whereas the injection current shifts it in the opposite direction as illustrated by the different color bands with positive slopes in Fig. 6.19(b). It is, however, clear that the FSF is the dominant effect here as it induces the largest shift on the emission wavelength. Four distinct regions, marked 1, 2, 3 and 5 in Fig. 6.18(b), were identified where the PE values are noticeably different. Note that there is no region marked 4 in this map and that the corresponding region will be introduced later in this chapter. The first region (marked 1 in Fig. 6.18(b)) is depicted as a narrow pale green band of injection current near threshold associated with PE values ≈ 0.87. In this band, the time-series show periodic oscillations on a low amplitude cw baseline, see Fig. 6.21(a), and the FFT spectra show a high amplitude peak located at the external cavity roundtrip frequency f_e. The FFT spectra also show strong peaks precisely located at $7f_e$, $14f_e$ and $21f_e$. It is worth noting that the location of the main peak is not always the same but most of the time it is 6 or $7f_e$ as illustrated in Fig. 6.17(b). It always corresponds to a multiple of the external cavity roundtrip frequency. Figure 6.21(a) shows a time-series extracted from region 1 (see Fig. 6.18(b)) and its corresponding FFT spectrum and autocorrelation function (ACF). The latter shows fast oscillations with a delay of 18 sampling periods corresponding to a frequency of 1.113 GHz ($\pm 7\ MHz$) which matches the main peak located at 1.106 GHz ($\pm 1\ MHz$) in the FFT spectrum. The envelope of the ACF has a delay of 127 sampling periods which corresponds to a frequency of 157.7 MHz ($\pm 200\ kHz$) and matches the external cavity roundtrip frequency. The time-series in the second region, marked 2 in Fig. 6.18(b), also show periodic oscillations on a cw baseline. The higher amplitude of the cw baseline observed in this region is due to higher injection current
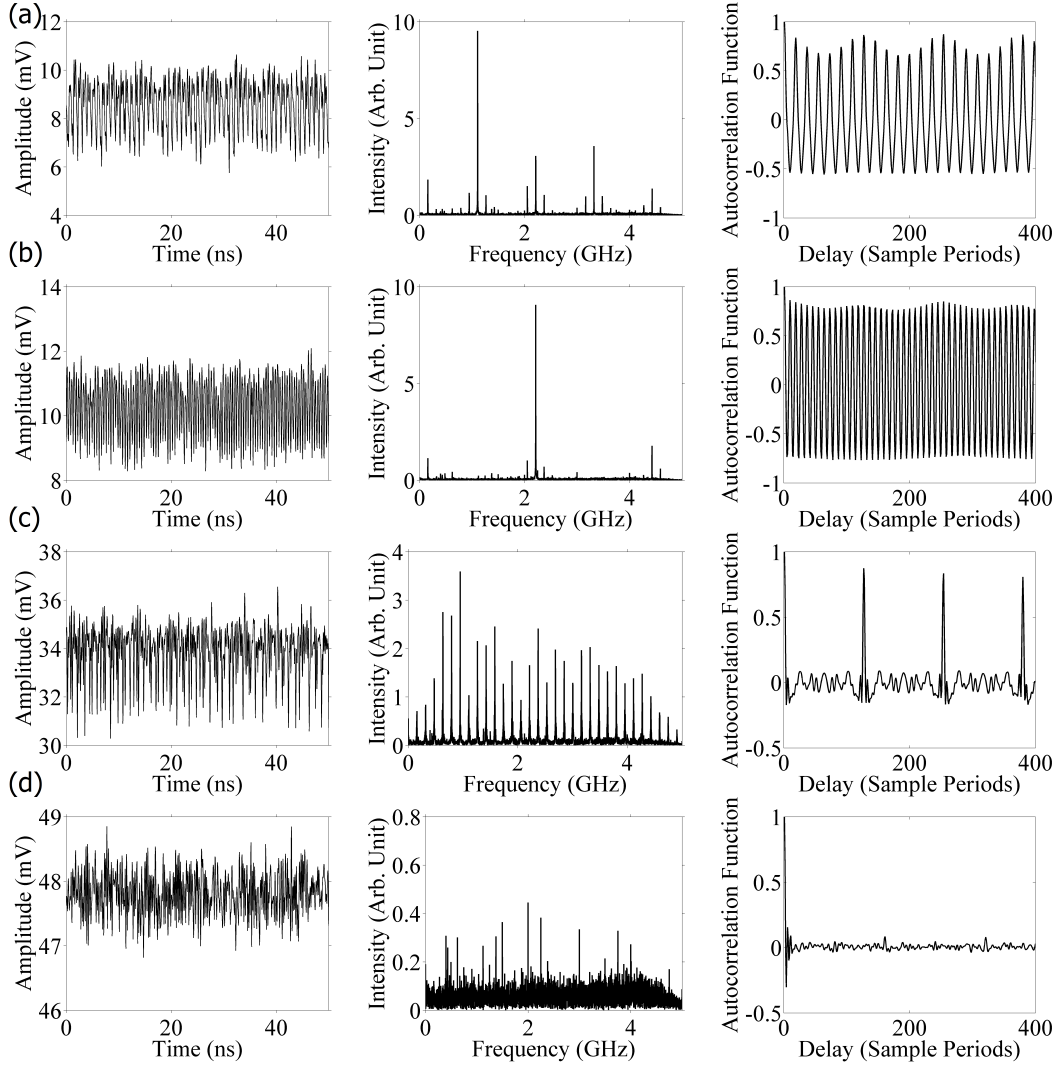
Figure 6.21: Output power time-series and corresponding FFT spectra and autocorrelation function for different regions of the parameter space as marked in Fig. 6.18(b). One sample period=50 ps. The FSF level was 97.5% (0.75 V) and the injection current was (a) 1=44 mA, (b) 2=45 mA, (c) 3=70 mA and (d) 5=100 mA.

operating the laser. This region is identified as the narrow blue band following the pale green band in the PE map. Here, the PE values drop to ≈ 0.77 and the main peak in the FFT spectra is shifted towards higher frequencies (around 2 GHz), i.e. $7f_e$, as seen in Fig. 6.17(b). The dominant frequency in the RF spectra is now

$14f_e$ with a lower amplitude peak at $21f_e$. However, the frequency bandwidth of the oscilloscope does not allow the observation of higher order multiples. The main peak frequency is measured at 2.212 GHz ($\pm 1 \ MHz$) in the FFT spectrum and matches, within the uncertainty of the measure, the measured delay of 9 sampling periods of the ACF oscillations. This corresponds to a frequency of 2.226 GHz ($\pm 24 \ MHz$). The delay of the envelope of the ACF oscillations remains 127 sampling periods, i.e. 157.7 MHz ($\pm 200 \ kHz$), even though they are not as pronounced as in region 1. Note that even if the case illustrated in Fig. 6.21 shows a frequency doubling of the main period in the FFT spectra as compared to region 1, it is not always the case and other scenarios are possible. It is quite likely that the RF spectra show a stepped (at the external cavity frequency) frequency shift of the main component with increasing injection current as the resolution of the measure, i.e. 1 mA, does not allow such characterization. In both regions, i.e. 1 and 2, the laser is emitting on a single longitudinal mode as seen in Fig. 6.19(a) with a greatly enhanced side mode suppression (>55 dB). The average power is rather low and the dc offset is small thus indicating that the laser shows periodic fluctuations on a cw baseline. This is also confirmed in Fig. 6.18(a) where the RMS amplitude is low in these regions. The spectra recorded with the FPI indicate that the linewidth of the laser mode increases with increasing FSF up to about 2.4 GHz. However, the linewidth decreases with increasing injection current, which means that the highest bandwidth is obtained at threshold with maximum FSF. Region 3 shows another differentiated region of dynamics with higher values of PE (≈ 0.94), indicating a higher complexity of the time-series. There is then a gradual increase in complexity as the system parameters approach high injection and FSF values identified as region 5 in Fig. 6.18(b). In region 3, the FFT spectrum shows strong peaks at multiples of the external cavity frequency (157.7 MHz), right up to the bandwidth limit of the measurement equipment, see Fig. 6.21(c). Their bandwidth and location indicate that they are associated with the external cavity roundtrip frequency. These peaks are a common feature of semiconductor lasers with high level of conventional feedback and have already been reported in the literature [4]. In most cases the dominant frequency of the FFT spectra is <2 GHz as seen in Fig. 6.17(b). The strong influence of the external cavity delay on the dynamics of the system is also

seen in the ACF where strong peaks corresponding to a delay of 127 (157.7 MHz) are observed. Here the laser is emitting on 2 or more longitudinal modes with a gradual increase of the number of longitudinal modes with increasing injection current as illustrated in Fig. 6.19(a). The increase in complexity associated with increasing injection current corresponds to cw operation of the laser (within the bandwidth resolution of the equipment). These observations in regions 1, 2 and 3 suggest that there is a competition between FSF and delayed feedback in this region. This is reinforced by the observation of slow temporal dynamics in regions 1 and 2, i.e. envelope corresponding to the external cavity delay. In region 5, the laser is strongly multi-mode (≥ 4) as seen in Fig. 6.19(a), but operates cw as discussed before. A typical time-series from region 5 and corresponding FFT spectrum and ACF is shown in Fig. 6.21(d), and here the time-series is essentially fundamental, photodetector noise. The dynamics associated with the external cavity delay in region 3 are here completely absent and resemble that of low level of FSF, see Fig. 6.17(b).

Very high levels of FSF affect the dynamics of the system in different ways. Close to threshold (regions 1 and 2) the dynamics become more regular with periodic time variations (lower PE values) associated with single longitudinal mode operation of the laser but multiple external cavity modes. The bandwidth of the laser is the largest at threshold with maximum FSF. For higher injection currents (region 3) the dynamics are dominated by the external cavity delay with strong peaks at multiples of the external cavity frequency in the FFT spectra. The gradual increase in complexity (higher PE values) is associated with an increase of the number of longitudinal modes the laser is operating on. For the highest injection currents and FSF levels (region 5) the high complexity (highest PE values) corresponds to cw, strong multi-mode operation of the laser. The external cavity delay does not affect the dynamics of the system anymore and results in noisy time-series similar to that obtained with low FSF level.

6.4.3   320 MHz Cavity Roundtrip Frequency

The external cavity is now set up such that it matches another multiple of the AOM frequency shift, i.e. 318.4 MHz. The resonance condition was determined
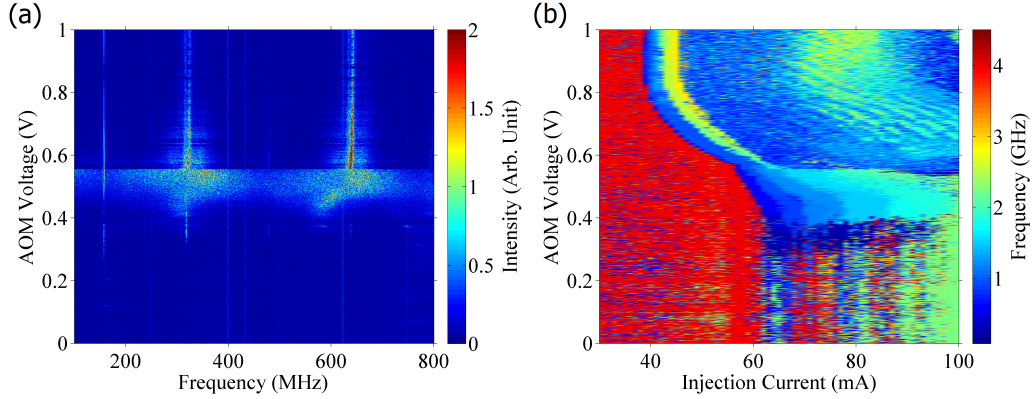
Figure 6.22:   (a) Map of the FFTs of the output power time-series for increasing FSF at 70 mA. (b) Map of the dominant frequency of the FFTs of the output power time-series as a function of FSF and injection current.

by following the procedure described in Sec. 6.1.5. The data collection was similar to that in Sec. 6.4.2 and the same figures were produced in order to allow comparison between different external cavity lengths.

Figure 6.22(a) shows a color map of the RF spectra as a function of FSF at 70 mA. A strong peak located at 318.4 MHz associated with FSF levels as low as 0.4% up to 12% appears in the RF spectra. This peak matches the external cavity roundtrip frequency and the fact that another sharp peak, sharing the same spectral bandwidth, located at 157.7 MHz also appears in Fig. 6.22(a) indicates that these peaks are directly related to the AOM frequency shift. This is also confirmed by the fact that the temporal dynamics of the system are not greatly affected with low levels of FSF as seen in Fig. 6.23. However, the temporal dynamics seem to be slightly affected when the laser is operating closer to threshold as seen in the both the RMS and PE map (see the region circled in black in Fig. 6.23(b)). Here the increase in complexity is associated with more periodic time variations than cw operation would normally exhibit. These instabilities close to threshold can also be seen in Fig. 6.24(a) where the laser is operating on several longitudinal modes. This behavior is probably the result of mode switching of the laser. Beyond an injection current of 80 mA the system is more stable with lower RMS amplitudes and higher PE values associated with single mode

167
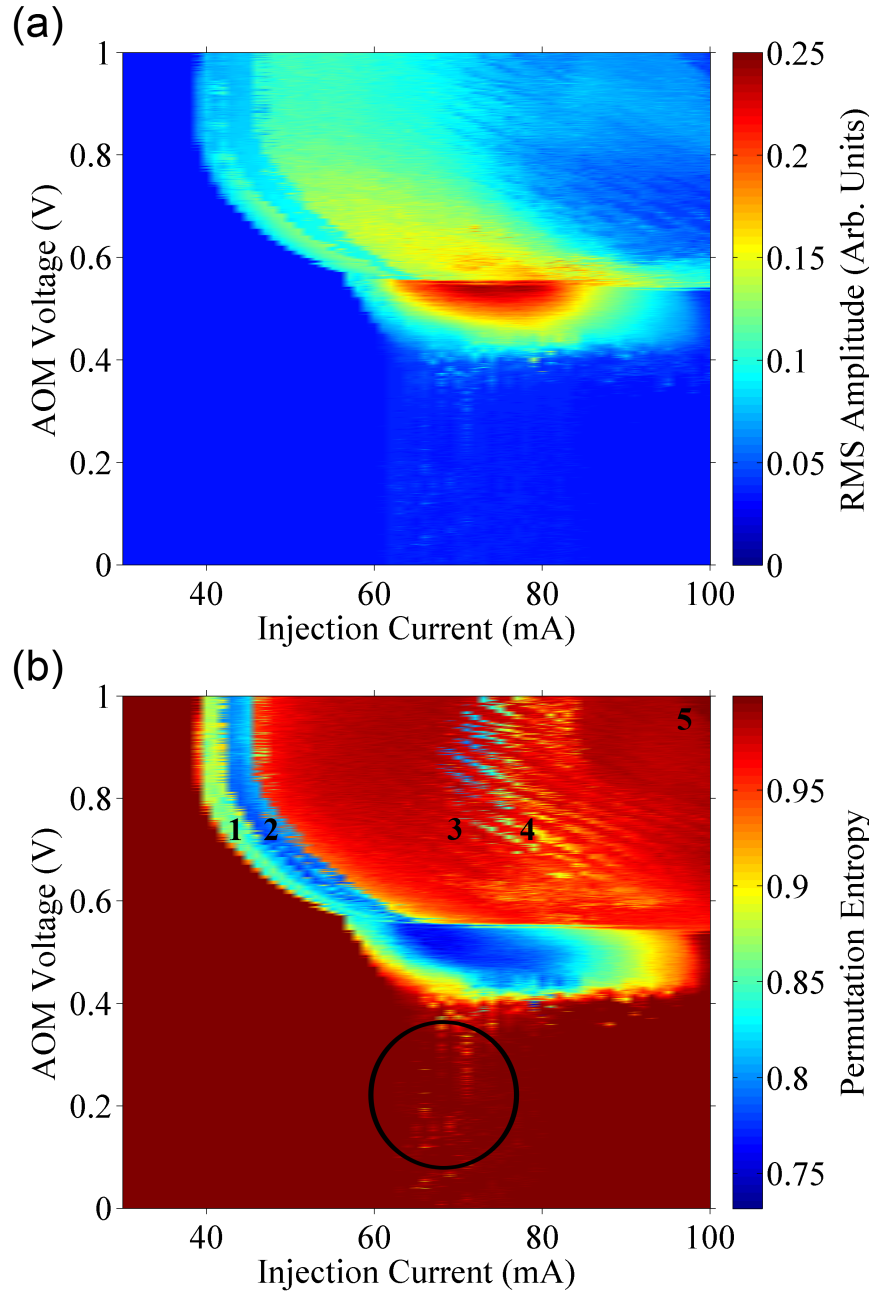
Figure 6.23: (a) Map of the RMS amplitude of the output power time-series as a function of FSF and injection current. (b) Map of the normalized permutation entropy ($D = 5$, $\tau = 2$) as a function of FSF and injection current. The numbers 1-5 refer to five distinct regions where the dynamics are noticeably different. The circle highlights another region where the dynamics are different.
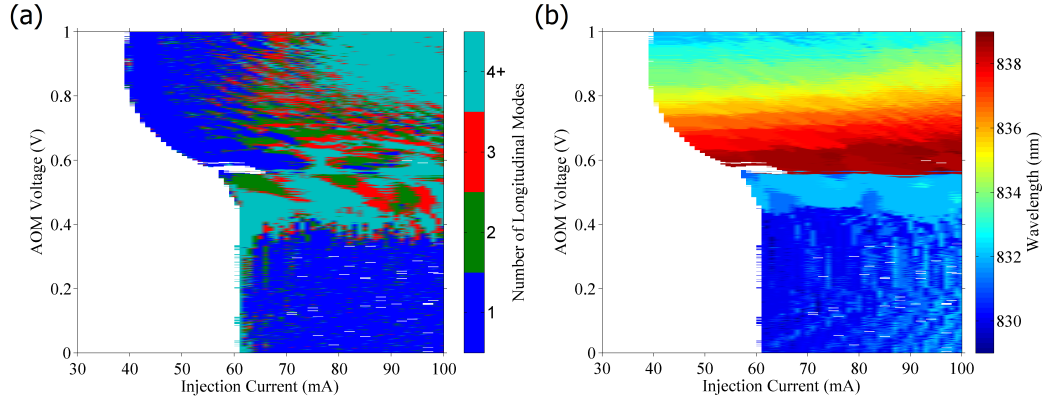
Figure 6.24: (a) Map of the number of longitudinal modes lasing as a function of FSF and injection current. The threshold for side mode suppression was set at 15 dB. (b) Map of the emission wavelength of the main lasing mode as a function of FSF and injection current.

operation of the laser. The emission wavelength of the main mode of the laser increases gradually with injection current but does not seem to be affected by low levels of FSF as illustrated in Fig. 6.24(b). The optical spectra recorded with the FPI are similar to the spectra shown in Fig. 6.10. A gradual broadening of the laser linewidth ($\approx 300\ MHz$) occurs up to an FSF level of 1.5% and beyond this FSF level the laser starts operating on several longitudinal modes. For both cavity lengths, i.e. 160 MHz and 320 MHz, with low FSF level the system shares the same dynamics. Temporal dynamics are not affected by low FSF level unless the laser is operated close to threshold where it becomes multi-mode. However, the spectral behavior of the system is affected and shows a broadening of the laser line up to an FSF level of 1.5% before the laser starts emitting on several longitudinal modes. The linewidth still broadens beyond this level of FSF but it can not be linked to the effect of the FSF alone. This multi-mode operation of the laser is associated with weak power on the side modes ($\leq 15\ dB$) as depicted in Fig. 6.24(a) where the map indicates single mode operation of the laser for low FSF levels. The threshold current of the laser remains constant with low levels of FSF as seen in Fig. 6.24(a).

Beyond an FSF level of 12% the dynamics of the system change radically.
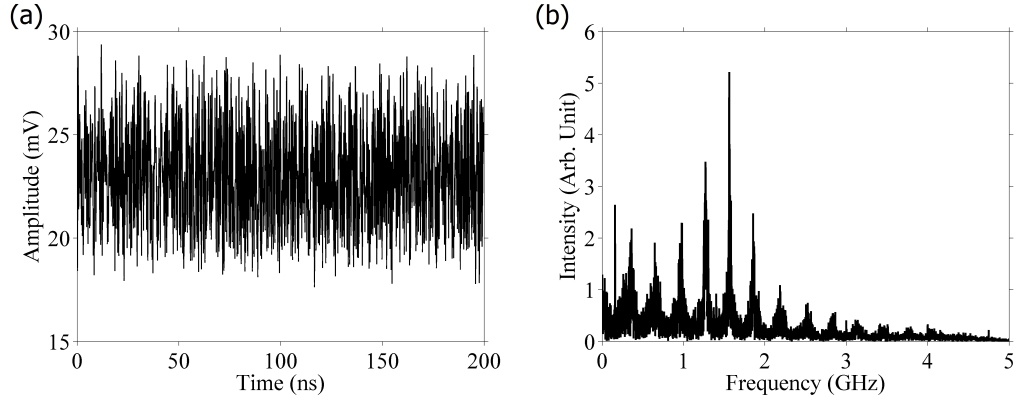
Figure 6.25:   (a) Output power time-series with an FSF level of 47% (0.53 V) at
70 mA and (b) corresponding FFT spectrum.

The strong peak located at 318.4 MHz in Fig. 6.22(a) is now replaced by a broad,
low amplitude peak centered around 318.4 MHz. However, the peak located at
157.7 MHz is still sharp and increases in amplitude with increasing FSF. This
suggests a direct pickup from the AOM power supply confirming that the AOM
induces a roundtrip frequency shift of 157.7 MHz. The coherence collapse regime
observed in Fig. 6.23(a) now occurs within FSF levels of 28% and 53%. The PE
values associated with this regime show similar complexity ($H_s < 0.75$) to that
in Sec.6.4.2. A typical time-series and its corresponding FFT spectrum extracted
from the coherence collapse regime is illustrated in Fig. 6.25. The FFT spectrum
shows broad, low amplitude peaks with low power at high frequencies (>2 GHz)
and separated by the external cavity frequency roundtrip, see Fig. 6.25(b). The
transition in and out of this regime is abrupt and occurs within the resolution
limit of the equipment, i.e. AOM step voltage resolution (0.001 V). In this region
the laser is strongly multi-mode, mostly operating on 4 longitudinal modes, as
seen in Fig. 6.24(a). The emission wavelength of the main mode is stable at about
832 nm with increasing injection current, see Fig. 6.24(b). A threshold reduction
of about 4 mA is also observed in Fig. 6.24 with medium FSF level. Similarly to
the observations in Sec. 6.4.2, the individual spectra recorded by the FPI show
a gradual broadening of the laser linewidth with increasing FSF up to 1.9 GHz
with an FSF level of 53% (0.55 V). Both temporal and spectral dynamics show

significantly different behavior with medium FSF level. The system shows large instabilities in the time-series when entering the coherence collapse regime; high RMS amplitude and lower PE values are distinctive features of this region. The delay introduced by the external cavity is prominent, the RF spectra show broad peaks separated by the external cavity frequency roundtrip. At this point the threshold is slightly reduced, the laser linewidth broadens and the laser becomes strongly multi-mode.

The dynamics of the system are radically different once the FSF level reaches 53%. A threshold reduction of about 22 mA occurs as seen in Fig. 6.24. A sudden change of the emission wavelength of the main lasing mode towards longer wavelengths (>7 nm) also occurs as the FSF level approaches 53% up until 72%. Then the emission wavelength is shifted towards shorter wavelengths (approximately 833 nm). In this region the shift is mainly controlled by the FSF and not the injection current as is the case with low FSF level. The injection current does have an effect on this shift but the FSF is the dominant effect here. At high levels of FSF, five regions have been identified where the PE values are significantly different, they are marked 1-5 in Fig. 6.23(b), four of which have already been identified and described in Sec. 6.4.2. The new region, marked 4 in Fig. 6.23(b), is associated with PE values similar to that found in region 2. Figure 6.26 shows time-series with corresponding FFT spectra and ACF for each region marked in Fig. 6.23(b). Region 1 shows periodic oscillations on a cw baseline in the time-series associated with a dominant frequency component in the RF spectrum similar to observations in Sec. 6.4.2 as seen in Fig. 6.26(a). However the ACF is slightly different, the delay associated with the oscillations still corresponds to the main frequency component appearing in the RF spectrum but the envelope corresponding to the delay of the external cavity does not appear here. This suggests that the external cavity delay does not affect the dynamics of the system. The dominant frequency peak in the FFTs is still located at about 1 GHz ($3f_e$) as illustrated in Fig. 6.22(a). In region 2, see Fig. 6.26(b), the time-series are also periodic on a cw baseline but the main peak in the RF spectra is now located at about 2 GHz ($8f_e$ as depicted in Fig. 6.22(b). The delay of the oscillations in the ACF is also related to the frequency of the peak in the
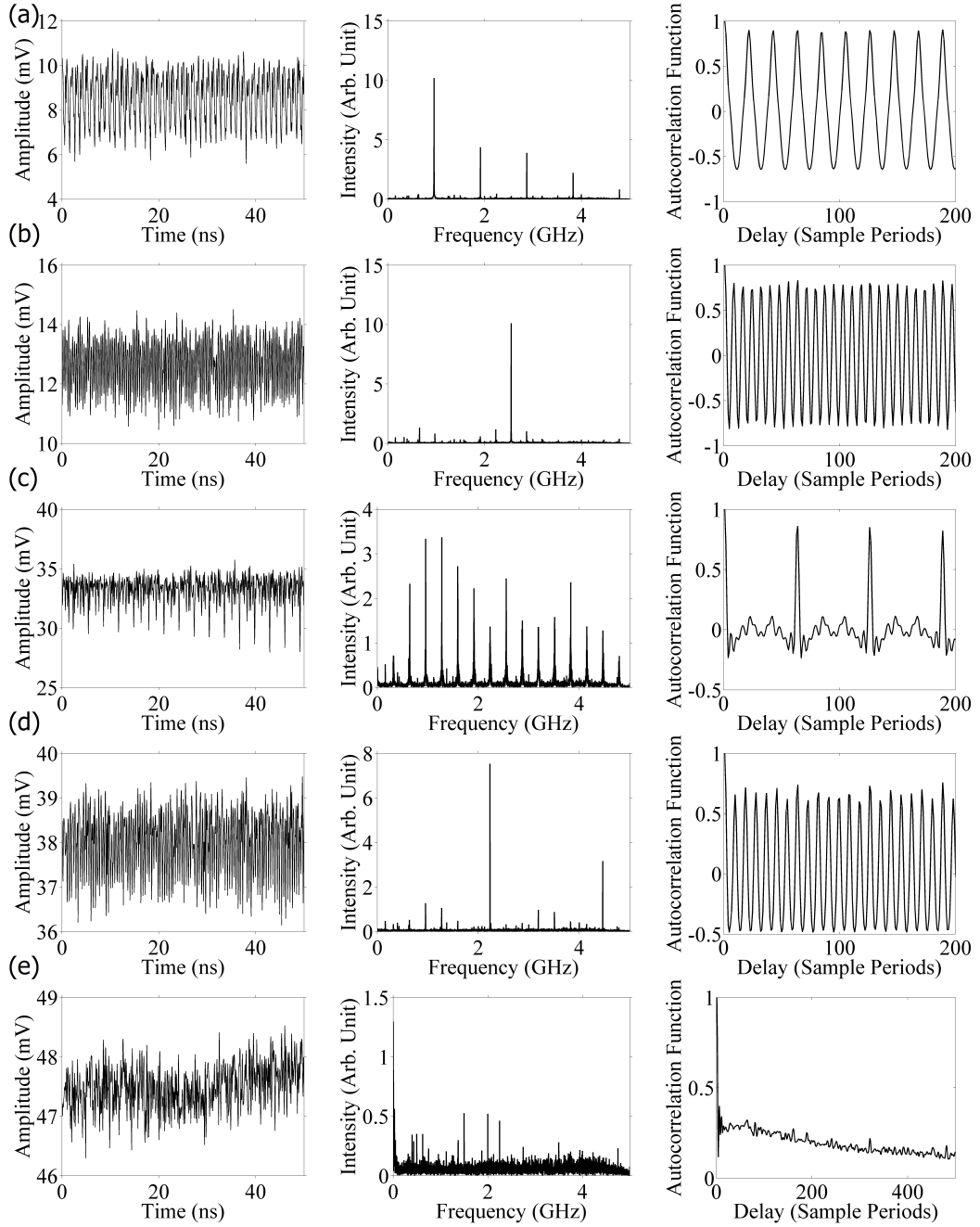
Figure 6.26: Time-series with corresponding FFT spectra and autocorrelation functions for different regions of the parameter space as marked in Fig. 6.23(b). One sample period=50 ps. The FSF level was 97.5% (0.75 V) and the injection current was (a) 1=44 mA, (b) 2=47 mA, (c) 3=70 mA, and (d) 4=78 mA. The FSF level was 99.5% (0.98 V) and the injection current was (e) 5=100 mA.

RF spectra but the envelope previously described does not appear in this region either. The PE values in these two regions are comparable with that of Sec. 6.4.2. In both regions, the laser is strongly single mode and the side mode suppression is greatly enhanced (>55 dB) compared to that with low FSF level as illustrated in Fig. 6.24(a). In both regions the FPI spectra show an increase of the laser mode bandwidth (up to about 2.4 GHz) with increasing FSF. However, the bandwidth of the mode decreases with increasing injection current so the maximum bandwidth is obtained at threshold with maximum FSF in region 1. In region 3, the external cavity delay is strongly affecting the dynamics of the system as shown in Fig. 6.26(c), where the RF spectrum shows strong peaks located at multiples of the external cavity frequency (318.4 MHz), right up to the bandwidth limit of the measurement equipment. This is also confirmed by the presence of strong peaks in the ACF in Fig. 6.26(c) with a delay directly related to the delay introduced by the external cavity. The laser becomes multi-mode, see Fig. 6.24(a), and the PE values (≈ 0.97) increase gradually towards 1 in Fig. 6.23(b). The region marked 4 in Fig. 6.23(b) shows dynamics similar to that observed in region 2 as seen in Fig. 6.26(b) and (d). The RF spectrum shows a strong peak located at about 2 GHz ($7f_e$ and the ACF shows oscillations with a delay corresponding to the frequency of this peak. There is still no sign of the external cavity delay in the ACF even though higher amplitude peaks do appear at this delay. The dominant frequency of the peak in the RF spectra is >2 GHz as depicted in Fig. 6.22(b). These thin bands corresponding to this region appear for a broad range of FSF levels (90%-100%) and injection currents (68 mA-82 mA). In this region, the laser is single mode but emitting at a longer wavelength (around 835 nm) than in region 2. Stable operation of the laser is achieved with much higher FSF level ($\approx 99\%$) than in Sec. 6.4.2, see region 5 in Fig. 6.23(b). Both the FFT spectrum and the ACF in Fig. 6.26(e) show no sign of periodic dynamics in the time-series which is also confirmed by having PE values close to 1 in this region. Despite the laser being cw in this region, Fig. 6.24(a) shows a clear tendency to a strong multi-mode operation of the laser as observed in the pink region in the top right corner of the map. High levels of FSF affect the dynamics of the system similarly to what was observed in Sec. 6.4.2 with the exception of a new region, marked 4 in Fig. 6.23(b), which, despite being in region 3, shows the same dynamics as

in region 2. Region 5 now occurs at much higher FSF levels (>98%) than in Sec. 6.4.2. Periodic time-series associated with lower PE values and single mode operation of the laser are related to regions 1 and 2 while region 3 is still strongly affected by the external cavity delay. However a new region, i.e. 4, appears clearly in the PE map and shows dynamics similar to that observed in region 2. Region 5, where the external cavity delay does not affect the dynamics of the system, now occurs at higher FSF levels.

6.4.4   480 MHz Cavity Roundtrip Frequency

This section introduces the results obtained with the shortest external cavity length matching a multiple of the AOM frequency shift, physically possible due to the space constraint. The external cavity is now set up such that it is three times the AOM frequency shift, i.e. 478.1 MHz. The resonance condition was determined by following the procedure described in Sec. 6.1.5. The data collection was similar to that in Sec. 6.4.2 and 6.4.3 and the same figures were produced in order to allow comparison between different external cavity lengths.

The color map of the RF spectra as a function of FSF level depicted in Fig. 6.27(a) shows strong peaks located at 157.7 MHz, 318.4 MHz and 478.1 MHz. The strongest peak is located at 157.7 MHz and the weakest at 478.1 MHz. In this case both peaks, at 318.4 MHz and 478.1 MHz, only appear in the RF spectra with FSF levels up to 12%. The peak at 157.7 MHz is, however, present for a broad range of FSF levels, appearing at around 0.4% all the way up to 100%. This observation reinforces the fact that this feature is a direct pickup from the AOM power supply. As observed in longer cavity lengths, the temporal dynamics are not affected by low FSF levels but the system shows some instabilities close to threshold (see the region circled in black in the PE map in Fig. 6.28(b)). In this region the laser is strongly multi-mode, see Fig. 6.29(a), the RMS amplitude is slightly higher than in the cw operation range and the PE values are below 0.97. For higher injection currents, $\geq 82 \ mA$, the output power of the system becomes more stable with lower RMS amplitudes and higher PE values associated with single mode operation of the laser. Note that the emission wavelength of the
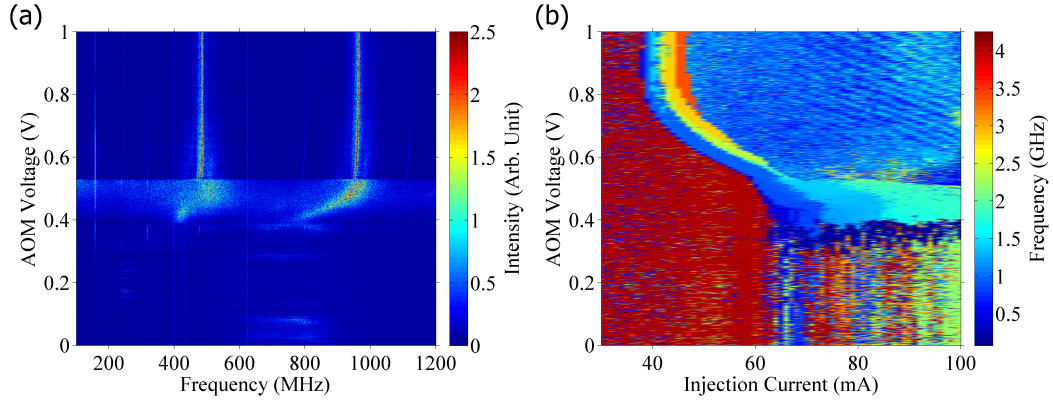
Figure 6.27: (a) Map of the FFTs of the output power time-series for increasing FSF at 70 mA. (b) Map of the dominant frequency of the FFTs of the output power time-series as a function of FSF and injection current.

main mode of the laser increases with increasing injection current as illustrated in Fig. 6.29(b). As already observed in both Sec. 6.4.2 and 6.4.3 the linewidth of the laser broadens with increasing FSF. The FPI spectra indicate a broadening of up to ≈ 300 MHz with an FSF level of 1.5% before the laser starts emitting on several longitudinal modes. Note that at this FSF level, i.e. 1.5%, the side mode suppression is still high (≈ 20 dB) and therefore cannot be observed in Fig. 6.29(a) as the threshold is set at 15 dB. Strong multi-mode emission, with a side mode suppression ≤ 15 dB, only occurs with an FSF level of about 8% (0.38 V) as seen in Fig. 6.29(a). This external cavity length shares the same dynamics as the two cavity lengths already investigated in Sec. 6.4.2 and 6.4.3. Temporal dynamics are moderately affected at low injection currents, ≤ 82 mA, but remain unaffected beyond this point. However, as described before, the system shows spectral broadening and multi-longitudinal mode operation with low FSF level.

Beyond an FSF level of 12%, new dynamics arise in the system. The sharp, strong peak located at 478.1 MHz in Fig. 6.27(a) is now replaced by a broad, low amplitude peak centered around the same frequency. The coherence collapse regime, associated with medium FSF levels, now ranges from 12% up to an FSF level of 45% as illustrated in Fig. 6.28. The reduced upper value is believed to

(a)

(b)
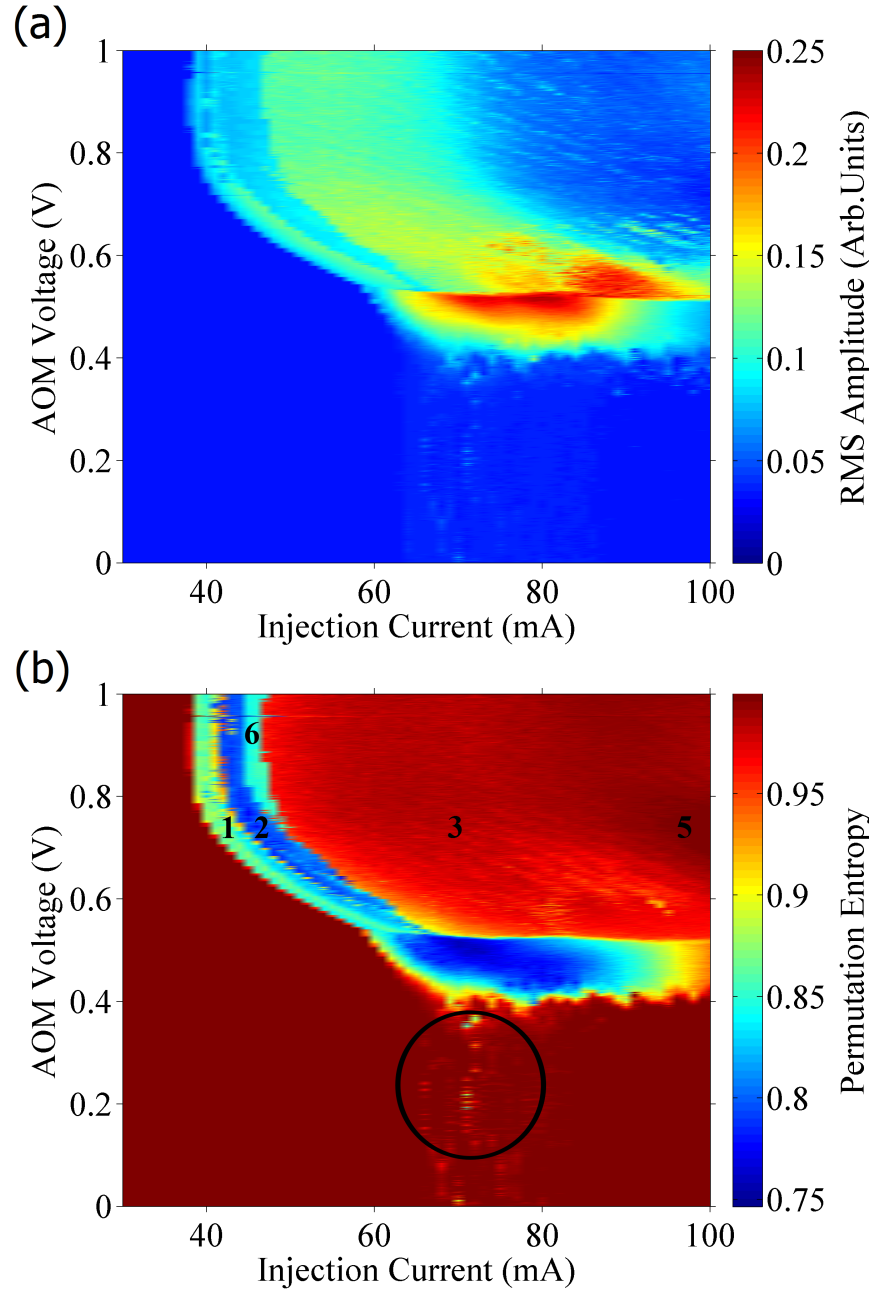
Figure 6.28: (a) Dynamic map of the RMS amplitude of the output power time-series as a function of FSF and injection current. (b) Dynamic map of the normalized permutation entropy ($D = 5$, $\tau = 2$) as a function of FSF and injection current. The numbers 1, 2, 3, 5 and 6 refer to five distinct regions where the dynamics are noticeably different. The circle highlights another region where the dynamics are different.
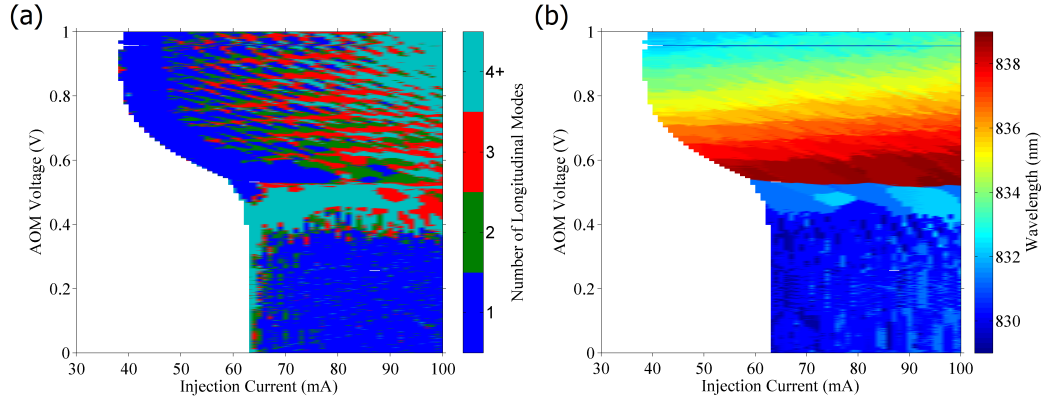
Figure 6.29: (a) Map of the number of longitudinal modes lasing as a function of FSF and injection current. The threshold for side mode suppression was set at 15 dB. (b) Map of the emission wavelength of the main lasing mode as a function of FSF and injection current.

result from the coupling coefficient of the optical feedback to the laser chip. It is higher in the shorter cavity because the beam divergence has less effect in the smaller cavity. This regime is characterized by high RMS amplitude and low PE values. A time-series and its corresponding FFT illustrating this regime is depicted in Fig. 6.30. The FFT spectrum shows broad, low amplitude peaks with low power at high frequencies (>2 GHz) and separated by the external cavity frequency roundtrip, see Fig. 6.25(b). Both transitions, to and from the coherence collapse regime, are abrupt and occur within the resolution limit of the equipment, i.e. AOM voltage step resolution (0.001 V). This regime is also associated with multi-mode operation of the laser on at least 3 longitudinal modes as seen in Fig. 6.29(a). The emission wavelength of the main mode is stable at 832 nm with increasing injection current and FSF, see Fig. 6.24(b), but increases a little with increasing injection current (lighter blue region beyond 85 mA). However, the shift towards longer wavelengths in this region is sudden and not gradual as expected from a free running semiconductor laser with increasing injection current. It is in this region that the first threshold reduction of about 4 mA with 45% FSF level occurs as seen in Fig. 6.29. The optical spectra from the FPI show a gradual broadening of the laser linewidth of up to 1.87 GHz with 45% FSF level. However, as discussed previously, the laser is emitting on multiple longitudinal modes
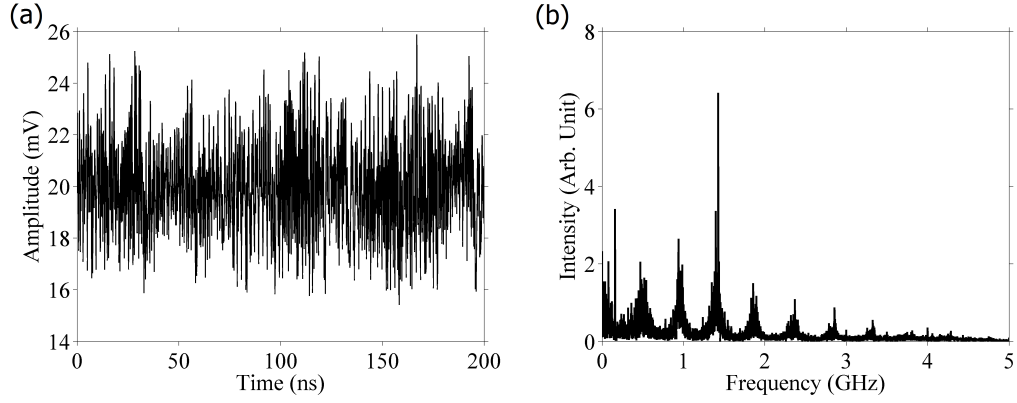
Figure 6.30:   (a) Output power time-series with an FSF level of 43.6% (0.52 V) at 70 mA and (b) corresponding FFT spectrum.

in this region which means that overlap of FSF broadened features associated with these longitudinal modes may be increasing the apparent laser bandwidth observed in the FPI spectra. In this configuration, the dynamics of the system are strongly affected by medium FSF levels as reported in Sec. 6.4.2 and 6.4.3. The system enters the coherence collapse regime and shows high RMS amplitude as well as lower PE values. The RF spectra show broad, low amplitude peaks separated by the external cavity frequency. This region is also associated with strong multi-mode operation of the laser and a moderate reduction of threshold.

Once the FSF level reaches 45% (0.525 V), the dynamics show a transition to the high FSF levels region. The effect of the FSF on the system is now more pronounced and this is illustrated by sharp, high amplitude peaks separated by the external cavity roundtrip frequency in Fig. 6.27(a). A large threshold reduction of about 25 mA is observed with maximum FSF as depicted in Fig. 6.29. The rate at which the threshold current decreases is higher than in the coherence collapse region. The emission wavelength of the main lasing mode abruptly shifts towards longer wavelengths ($\geq 838\ nm$) once the FSF level reaches 45%, see Fig. 6.29(b). Then as FSF further increases a gradual shift occurs towards shorter wavelengths up to maximum FSF level where the emission takes place at about 832 nm. The two competing effects already observed in longer cavity lengths also

occur in this region. The FSF shifts the emission towards shorter wavelengths whereas the injection current shifts it in the opposite direction as illustrated by the different color bands with positive slopes in Fig. 6.29(b). It is, however, clear that the FSF is the dominant effect here as it induces the largest shift on the emission wavelength. Five regions have been identified where the PE values are significantly different, they are marked 1, 2, 3, 5 and 6 in Fig. 6.23(b), four of which have already been identified and described in Sec. 6.4.2 and 6.4.3. The new region, marked 6 in Fig. 6.28(b), is associated with PE values similar to that found in region 1. Figure 6.31 shows time-series with corresponding FFT spectra and ACF for each region marked in Fig. 6.28(b). Regions 1 and 2 have already been identified in Sec. 6.4.2 and 6.4.3 and show similar dynamics here. Region 1 shows cw with periodic dynamics in the time-series as illustrated in the ACF in Fig. 6.31(a). The delay of the oscillations in the ACF corresponds to the frequency of the main frequency component in the FFT spectrum. The PE values are significantly lower than that of the fundamental noise in this region and are about 0.85. The main frequency component in the RF spectra is still <1 GHz ($2f_e$ as depicted in Fig. 6.27(b) and corresponds to a multiple of the external cavity roundtrip frequency. Region 2, see Fig. 6.28(b), shows similar dynamics with periodicity on a cw baseline in the time-series but it is associated with different PE values and different main frequency components in the RF spectra. In Fig. 6.31(b), the delay of the oscillations in the ACF also corresponds to the frequency of the main peak observed in the RF spectrum. However, the main peak in the RF spectra is now located at frequencies >2 GHz ($4f_e$ as seen in Fig. 6.27(b). The PE values associated with region 2 are lower than that found in region 1 and are about 0.80. In both regions the laser is strongly single mode with a much larger side mode suppression >55 dB than the free running laser (>20 dB), and is operating cw. However, the laser is probably operating on several external cavity modes but this hypothesis could not be confirmed as the spectra recorded by the FPI show a broad band modeless output (>1.7 GHz and up to 2.4 GHz) which could potentially be a chirped comb of frequencies that are not resolved due to the slow scanning rate of the Fabry-Perot compared to the frequency shift rate of the intracavity light field. Region 3 is strongly affected by the external cavity delay and the corresponding RF spectra show
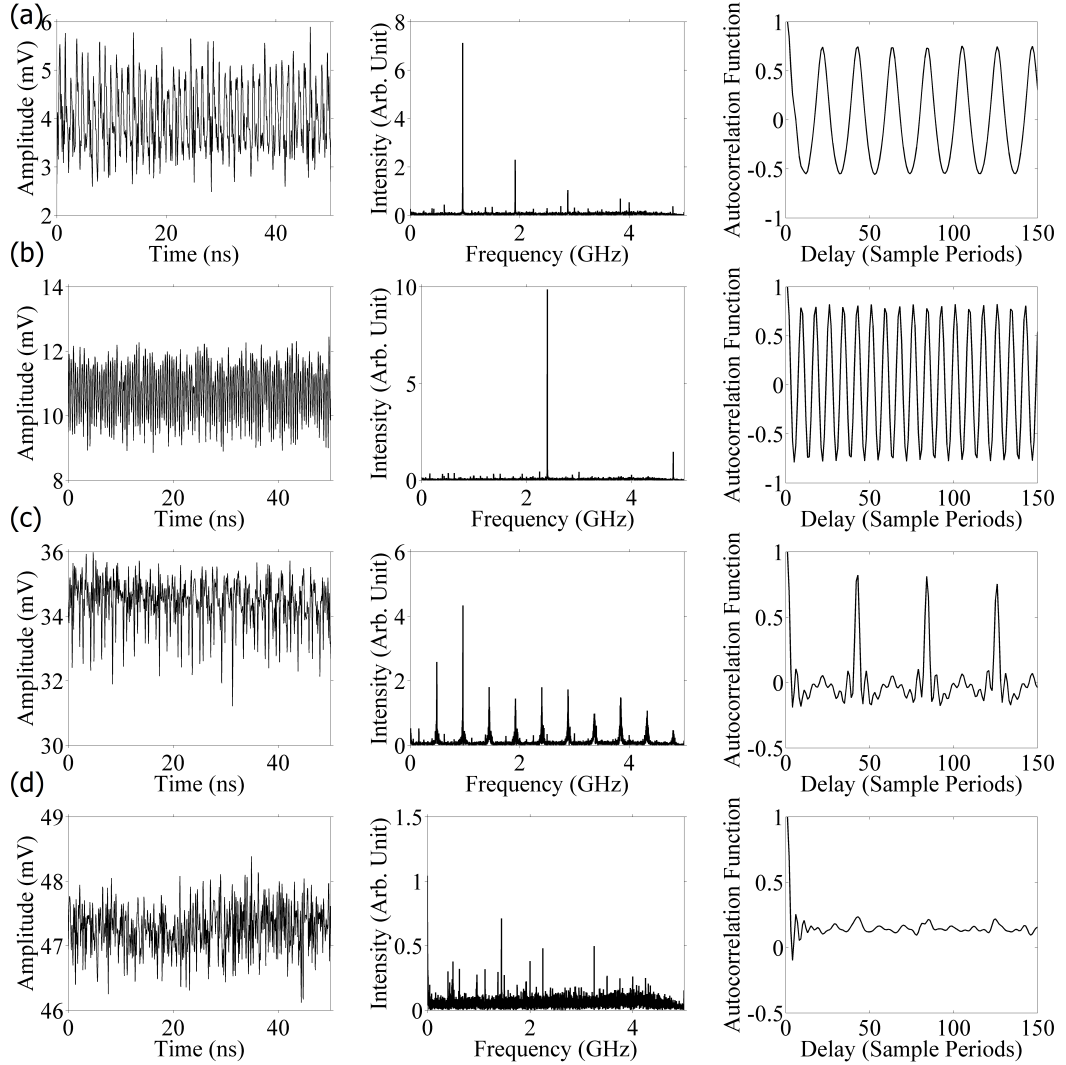
Figure 6.31: Output power time-series and corresponding FFT spectra and autocorrelation function for different regions of the parameter space as marked in Fig. 6.28(b). One sample period=50 ps. The FSF level was 97.5% (0.75 V) and the injection current was (a) 1=40 mA, (b) 2=44 mA, (c) 3=70 mA and (d) 5=100 mA.

strong peaks separated by the external cavity frequency (478.1 MHz) right up to the bandwidth limit of the measurement equipment as seen in Fig. 6.31(c). In this region the laser starts emitting on several longitudinal modes with increasing injection current as depicted in Fig. 6.29(a). The PE values gradually increase
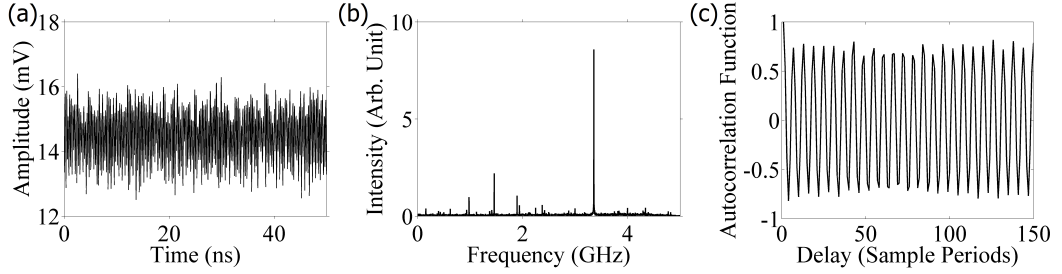
Figure 6.32: (a) Output power time-series with an FSF level of 99.8% (0.90 V) at 45 mA and (b) corresponding FFT spectrum and (c) ACF. One sample period=50 ps.

with increasing injection current until they reach 0.99 corresponding to region 5 in Fig. 6.28(b). In region 5 the PE values are >0.99 and the dynamics of the system are not affected by the external cavity delay anymore as seen in Fig. 6.31(d). This region is associated with multi-mode operation of the laser, see Fig. 6.29(a), low RMS amplitude as seen in Fig. 6.28(a) and high output power indicating cw operation of the laser. In this external cavity setup another region has been identified and is marked 6 in Fig. 6.28(b). This region appears with higher FSF levels (>99%) as a band where the PE values are about 0.85 in Fig. 6.28(b). In this region, periodic time-series on a cw level are observed and the dynamics are similar to that found in region 2 as seen in Fig. 6.32(c). The delay of the oscillations in the ACF are also related to the main peak in the RF spectrum. The location of the main frequency component is however >3 GHz ($7f_e$) as seen in Fig. 6.27(b). In these 3 regions (1, 2 and 6), the system shows periodicity in the time-series on a cw level with the period of the oscillations gradually increasing with injection current until it reaches region 3 where the dynamics are dominated by the external cavity delay. The dynamics observed in both regions, 1 and 2, and 3 suggest that there is a competition between FSF and delayed feedback. These regions are also associated with strong single mode operation of the laser. High levels of FSF affect the system in a similar way to Sec. 6.4.2 and 6.4.3 with the exception of region 6 which shows similar dynamics to regions 1 and 2 and is associated with periodic time-series on a cw baseline and single mode operation of the laser. The dynamics in region 3 are affected by the delay introduced by

the external cavity while region 5 shows sign of external cavity dynamics but is associated with multi-mode, cw operation of the laser and high PE values.

6.4.4.1   Dual Wavelength Emission

Despite the new region marked 6 in Fig. 6.28(b), another regime of operation was observed when this external cavity length was setup. Within a small range of FSF levels ($\approx 0.02\ V$), the laser was able to operate at the same time, within the resolution of the equipment, on two different wavelengths separated by about 10 nm. More surprisingly, the two wavelengths were located at about 831 nm and then at about 841 nm where the gain is very low (see Fig. 6.6). Figure 6.33 shows an optical spectrum from the OSA at 70 mA with 60% FSF level. The modes are located at 831.2 nm (mode 1) and 841.4 nm (mode 2), which corresponds to a separation of 25 longitudinal modes, and the power difference between the two lines is 5.91 dB.

This phenomenon had not been observed previously as the wavelength span of the OSA was set to be between 829 nm and 839 nm. It is also a rather unstable phenomenon that could be observed from seconds to minutes depending on the parameters, and was very sensitive to FSF alignment. It would always occur within the same FSF level range but never at the same level. The relatively slow sweep time of 16 ms (16 nm wavelength span) of the OSA does not allow the characterization of the fast temporal dynamics of the two modes. It is indeed not possible to know whether the two modes are lasing at the same time or not. In order to verify that, the experimental setup was modified such that the two spectral components could be individually coupled to a fast photodetector. Because of the large spectral separation between the two peaks, i.e. $\approx 10\ nm$, a simple diffraction grating was used to physically separate the two wavelengths so that easy coupling could be achieved. Dynamics up to 4 GHz, i.e. the bandwidth limit of the oscilloscope, could then be investigated in each spectral component. Figure 6.34 shows 3 sections of a typical time-series and corresponding RF spectra of each beam illustrating the different dynamics found in the same time trace for the two modes. Note that a small time offset between the two signals could result from a different optical path between the two beams or different cable lengths from
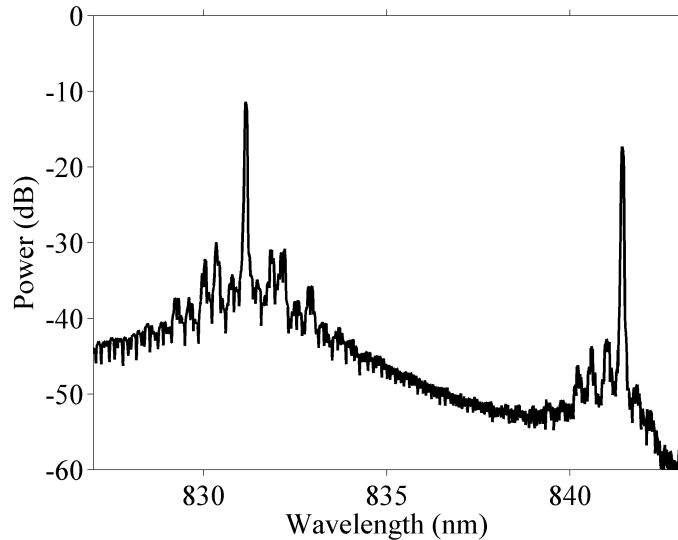
Figure 6.33: Optical spectrum from the OSA at 70 mA with an FSF level of 60%.

the detector to the oscilloscope. For clarity the signal associated with mode 1 was offset by 5 mV. In Fig. 6.34 modes 1 (831.2 nm) and 2 (841.4 nm) are represented by black and blue curves, respectively. Note that because of the losses introduced by the diffraction grating the dc components in both signals are rather low. The noise floor was measured at 2 mV which means that the dc component associated with mode 2 (about 3 mV) in Fig. 6.34 is just above the noise floor when the laser is emitting at this wavelength. In Fig. 6.34(a) mode 1 shows maximum dc amplitude whereas mode 2 is close to the noise level. Mode 2 is showing period doubling behavior compared with mode 1 dynamics as illustrated in the FFT spectrum where the main blue peak is twice the frequency of the main black peak. The situation is different in Fig. 6.34(b) as the dc amplitude of mode 2 increases up to 4 mV while the amplitude in mode 1 decreases to 4 mV. In this region, period tripling occurs as illustrated in the FFT. Even though it can be regarded as such, one has to be careful when stating frequency tripling as there are some other strong frequency components in the signal. Mode 1 shows slower dynamics while mode 2 is still exhibiting some fast dynamics. It is worth mentioning that the amplitude drop in mode 2 occurs at the exact same time the increase in mode
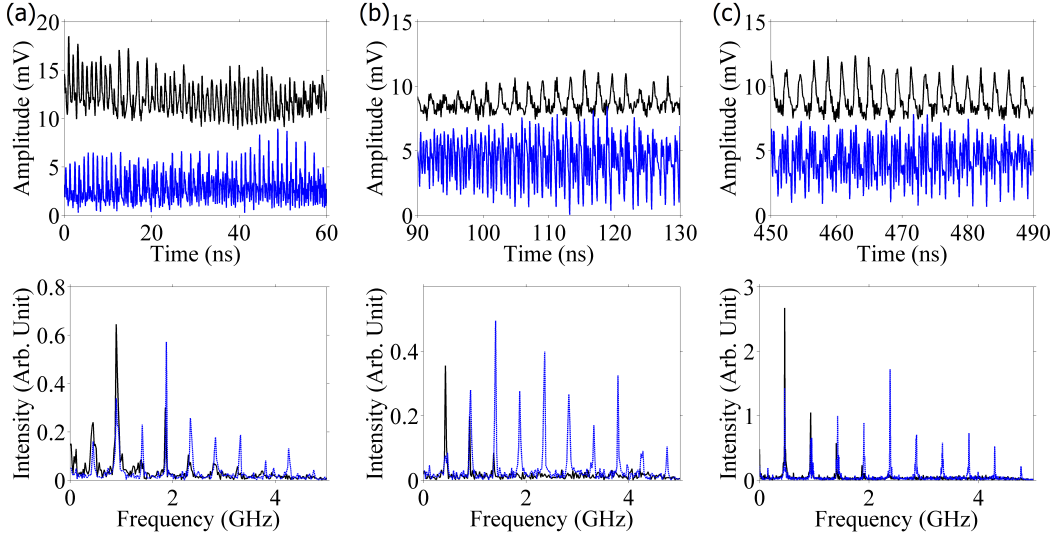
Figure 6.34:   Black line: Mode 1 (831.2 nm). Blue line: Mode 2 (841.4 nm). Sections of the output power time-series and corresponding RF spectra at 70 mA with an FSF level of 60.8%. (a), (b) and (c) illustrate different time intervals of the same time-series.

1 happens, considering the time delay introduced by the optical path difference between the two beams. Figure 6.34(c) illustrates a situation where, both modes have the same dc amplitude. The dynamics of mode 1 seem more regular than in (b) as seen in the FFT spectrum where the main black peak has a higher amplitude than in Fig. 6.34(b). However, the dynamics associated with mode 2 occur at faster time scales as illustrated in the FFT spectrum where the main peak is located well above 2 GHz. This means that mode 2 shows a strong frequency quintupling. However, other frequency components indicate that the dynamics are not only dominated by this frequency. These observations lead to the conclusion that both modes are emitting at the same time. Even though they show anticorrelated power, both modes are on at the same time. However, it is possible that switching occurs between the two modes at time-scales higher than the bandwidth of the oscilloscope, i.e. 4 GHz. As the laser was aging, mode 1 became weaker until lasing at 831 nm did not occur anymore but only occurred at 841 nm. The laser eventually died a few weeks later and no further investigation on this peculiar phenomenon could be carried out. In order to check whether this

phenomenon was affecting the dynamics of the system or not, a second identical laser was set-up and showed the same dynamics associated with the same FSF levels but no sign of a dual wavelength emission. This indicated that this one laser probably showed the two wavelengths lasing as an artefact of aging and was a pre-failure phenomenon.

6.4.5   Non Resonant Cavity

The results obtained with an external cavity which does not match a multiple of the AOM frequency shift are presented in this section. The frequency shift of the AOM is assumed to be f_e=157.7 MHz. The external cavity frequency roundtrip is now 249.3 MHz which corresponds to $1.58f_e$ and is therefore considered non-resonant. The data collection was similar to that in Sec. 6.4.2, 6.4.3 and 6.4.4 and the same figures were produced in order to allow comparison between different external cavity lengths.

Figure 6.35(a) shows a color map of the RF spectra as a function of FSF. A low amplitude peak located at 157.7 MHz associated with low FSF level appears, then decreases in amplitude until the system reaches an FSF level of 37% (0.5 V) where it becomes strong and then decreases gradually with increasing FSF. This confirms that the sharp peak, and its multiples, are related to the AOM frequency and not with the external cavity roundtrip frequency. Note that the peak located at 318.4 MHz is very low in amplitude and does not appear clearly in the map. The temporal dynamics of the system are not affected much by low FSF level as illustrated in Fig. 6.36(a), the RMS amplitude does not vary significantly in this region and stays very low. However, the system is a little more stable when the laser is operated at higher injection currents (>85 mA). In this parameter space mode hopping of the laser is completely absent. The PE map shown in Fig. 6.36(b) reinforces this observation where PE values close to 1 are observed in this region with the exception of lower values near threshold. These low instabilities close to threshold are associated with multi-mode operation (most probably mode hopping) of the laser as depicted in Fig. 6.37(a) which contrasts with the single mode operation of the device at high currents and low
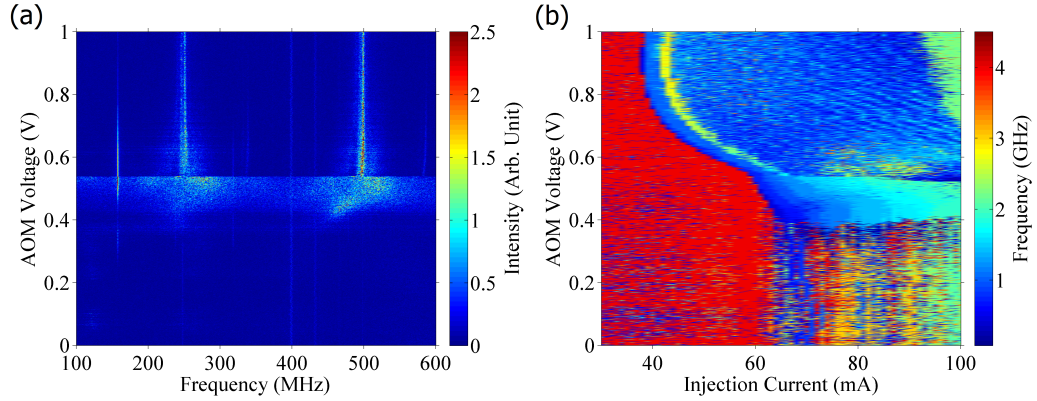
Figure 6.35: (a) Map of the FFTs of the output power time-series for increasing FSF at 70 mA. (b) Map of the dominant frequency of the FFTs of the output power time-series as a function of FSF and injection current.

FSF level. The expected gradual increase in the emission wavelength of the laser with increasing injection current is also observed as illustrated in Fig. 6.36(b). Spectra recorded with the FPI show a gradual broadening of up to 300 MHz of the laser mode associated with very low levels of FSF ($\leq 1.5\%$) while single mode operation of the laser is maintained. Beyond an FSF level of 1.5% the laser starts emitting on several longitudinal modes with a gradual increase of the power in the side modes with increasing FSF. The observations reported here are similar to what has been observed in the different resonant cavity configurations. The dynamics of the system are not influenced much by low levels of FSF. Temporally, the time-series show some periodicity on a cw level and spectrally the laser shows instabilities, i.e. mode hopping. This region is located near threshold and is associated with low injection currents as previously observed in the resonant cases. The spectral behavior of the main longitudinal mode is, however, significantly affected by low FSF level and the laser line shows FSF dependent broadening of a few hundred MHz before the device starts lasing on several longitudinal modes.

A significant change in the dynamics of the system occurs when the FSF level reaches 15% (0.42 V). A broad, low amplitude peak centered at 249.3 MHz appears in Fig. 6.35(a). The coherence collapse regime occurs with mid range FSF level with switch levels at 15% (0.42 V) and 55% (0.55 V) as seen in Fig. 6.36
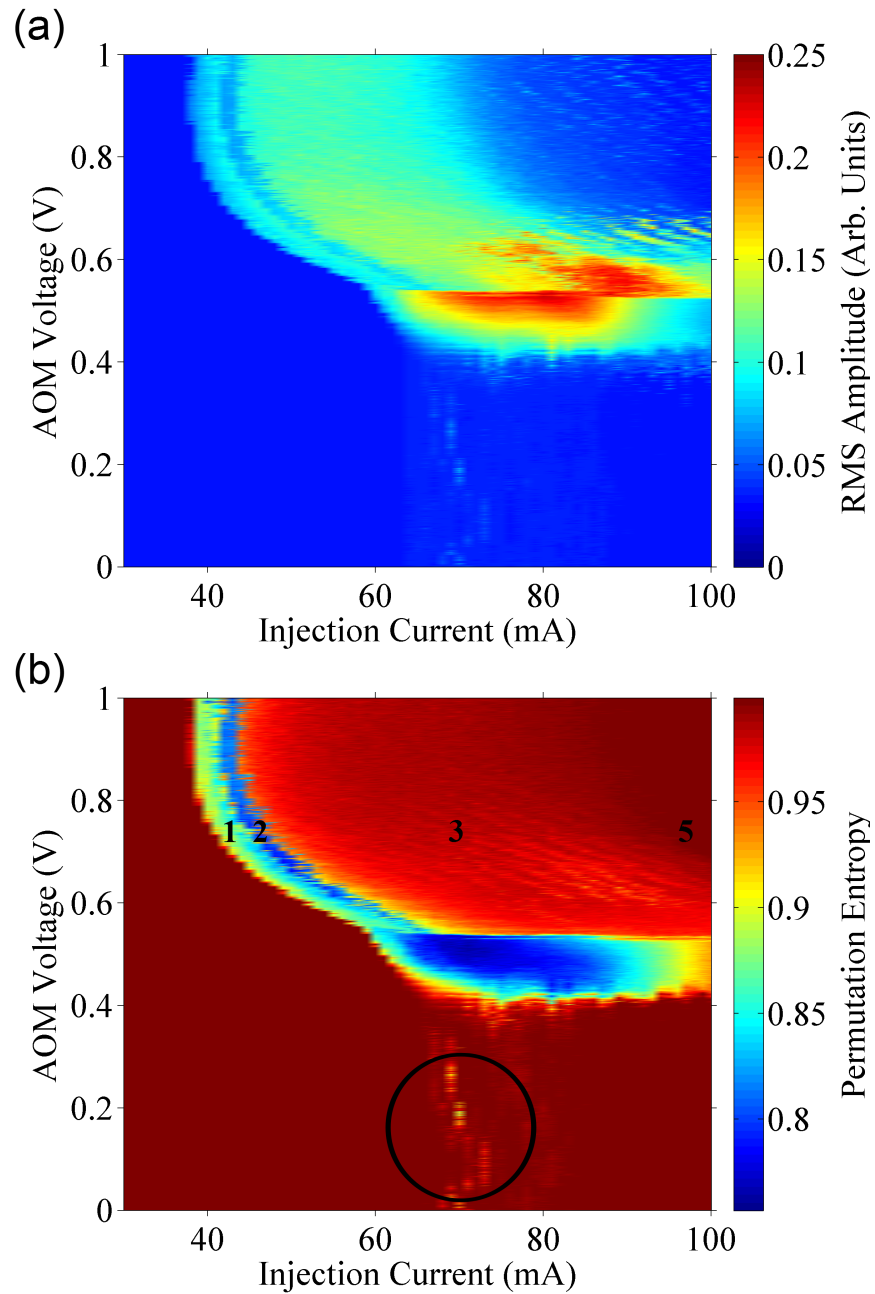
Figure 6.36: (a) Map of the RMS amplitude of the output power time-series as a function of FSF and injection current. (b) Map of the normalized permutation entropy ($D = 5$, $\tau = 2$) as a function of FSF and injection current.
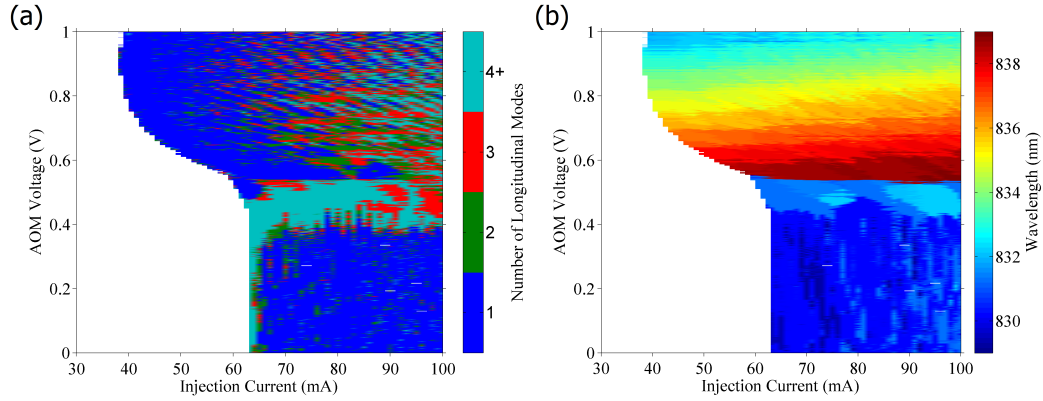
Figure 6.37:   (a) Map of the number of longitudinal modes lasing as a function of FSF and injection current. The threshold for side mode suppression was set at 15 dB. (b) Map of the emission wavelength of the main lasing mode as a function of FSF and injection current.

for this system. This region shows high instability corresponding to high RMS amplitude in Fig. 6.36(a) and low PE values (<0.8) in Fig. 6.36(b). A time-series, and its corresponding RF spectrum, extracted from the coherence collapse regime are shown in Fig. 6.38. The RF spectrum shows broad, low amplitude peaks with low power at high frequencies (>2 GHz) and separated by the external cavity frequency roundtrip, see Fig. 6.38(b). Both transitions, to and from the coherence collapse regime, are abrupt and occur within the resolution limit of the equipment, i.e. the AOM voltage step resolution (0.001 V). The coherence collapse regime is also associated with multi-mode operation of the laser as depicted in Fig. 6.37(a). The PE values are related to the number of longitudinal modes the laser is emitting on, small PE values correspond to a strong multi-mode emission (≥ 4 longitudinal modes) whereas larger PE values are associated with 3 longitudinal modes, as seen by comparing Fig. 6.36(b) and Fig. 6.37(a). In this region the dominant frequency of the RF spectra increases with increasing injection current, see Fig. 6.35(b). A threshold reduction of 4 mA is also observed in Fig. 6.37 and indicates that FSF has a bigger impact in this region. This region is also associated with a stabilization of the emission wavelength of the main lasing mode as illustrated in Fig. 6.37(b). The optical spectra recorded with the FPI show a gradual broadening of the laser linewidth of up to 1.84 GHz with 55%
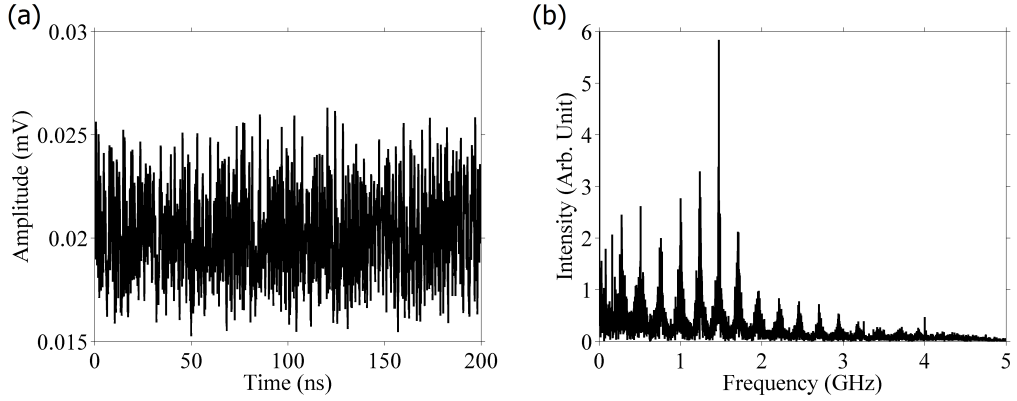
Figure 6.38:   (a) Output power time-series with an FSF level of 47% (0.525 V) at 70 mA and (b) corresponding FFT spectrum.

FSF level which is comparable to observations made in Sec. 6.4.2, 6.4.3 and 6.4.4. Note that within this moderate range of FSF level, i.e. 15%-55%, the laser is strongly multi-mode as depicted in Fig. 6.37(a). As reported earlier, for the case of resonant cavities, the system shows similar dynamics. The system enters the coherence collapse region illustrated by high RMS amplitude and low PE values. The external cavity delay has a significant effect depicted in the RF spectra by broad, low amplitude peaks separated by the external cavity frequency. Higher levels of FSF also mean a small threshold reduction as well as a strong multi-mode operation of the laser.

High levels of FSF, i.e. >55%, lead to a change in the dynamics of the system. In this case, similarities with resonant cavity configurations are quite pronounced. The external cavity delay now has a strong influence on the dynamics and is the dominant effect in most of the parameter space investigated here. This is illustrated in Fig. 6.35(a) where high FSF level is associated with strong, high amplitude peaks separated by the external cavity roundtrip frequency. The transition from the coherence collapse region is abrupt and is characterized by a sudden shift ($\approx 6\ nm$) of the emission wavelength towards longer wavelengths as depicted in Fig. 6.37(b). Then the emission wavelength gradually decreases with increasing FSF while higher injection currents slightly balance this effect by shifting the

emission towards longer wavelengths. A threshold reduction of at most 21 mA is observed in Fig. 6.37. Four regions, marked 1, 2, 3 and 5, with significantly different PE values have been identified in Fig. 6.36(b). These four regions have already been introduced in Sec. 6.4.2, however small differences distinguish both cavity configurations.

Regions 1 and 2 have already been identified in Sec. 6.4.2, 6.4.3 and 6.4.4 and show similar dynamics here. Region 1 is characterized by periodic time-series as illustrated in the ACF in Fig. 6.39(a). The period of the oscillations in the ACF corresponds to the frequency of the main frequency component in the RF spectrum. The latter corresponds to a multiple of the external cavity roundtrip frequency and is located at frequencies <1 GHz ($2f_e$) as depicted in Fig. 6.35(b). The PE values are about 0.87 in this region. Region 2 is associated with lower PE values, about 0.79, and faster dynamics. The delay corresponding to the period of the oscillations in the ACF is also related to the frequency of the main frequency component in the RF spectra, see Fig. 6.39(b). However, the main peak in the RF spectrum is now located at frequencies >2 GHz ($10f_e$) as seen in Fig. 6.35(b) and 6.39(b). In both regions, i.e. 1 and 2, the laser is operating on a single longitudinal mode as illustrated in Fig. 6.37(a) and exhibits a large side mode suppression (>55 dB). Similar observations have been made in Sec. 6.4.2, 6.4.3 and 6.4.4. However, in this case the system shows inconsistency in the dynamics in region 2. This can be seen in Fig. 6.36(b) where the PE values oscillate between 0.79 and 0.95 in region 2. The laser, however, remains single mode. In region 3 the dynamics are dominated by the delay introduced by the external cavity. The RF spectra show sharp, high amplitude peaks separated by the external cavity roundtrip frequency as seen Fig. 6.39(c). The PE values gradually increase from 0.92 up to ≈ 1 with increasing injection current. This increase in PE values is related to the number of longitudinal modes the laser is emitting on as depicted in Fig. 6.37(a). Region 5 is associated with PE values close to 1 and is not affected by the external cavity delay as seen in Fig. 6.39(d). In this region the laser is multi-mode and operates cw as seen in Fig. 6.36(a) where the RMS amplitude is low. High FSF level is associated with different dynamics which depend on the system parameters. Regions 1 and 2 show periodic time-series on a cw baseline with single mode operation of the laser associated with low PE values and low RMS
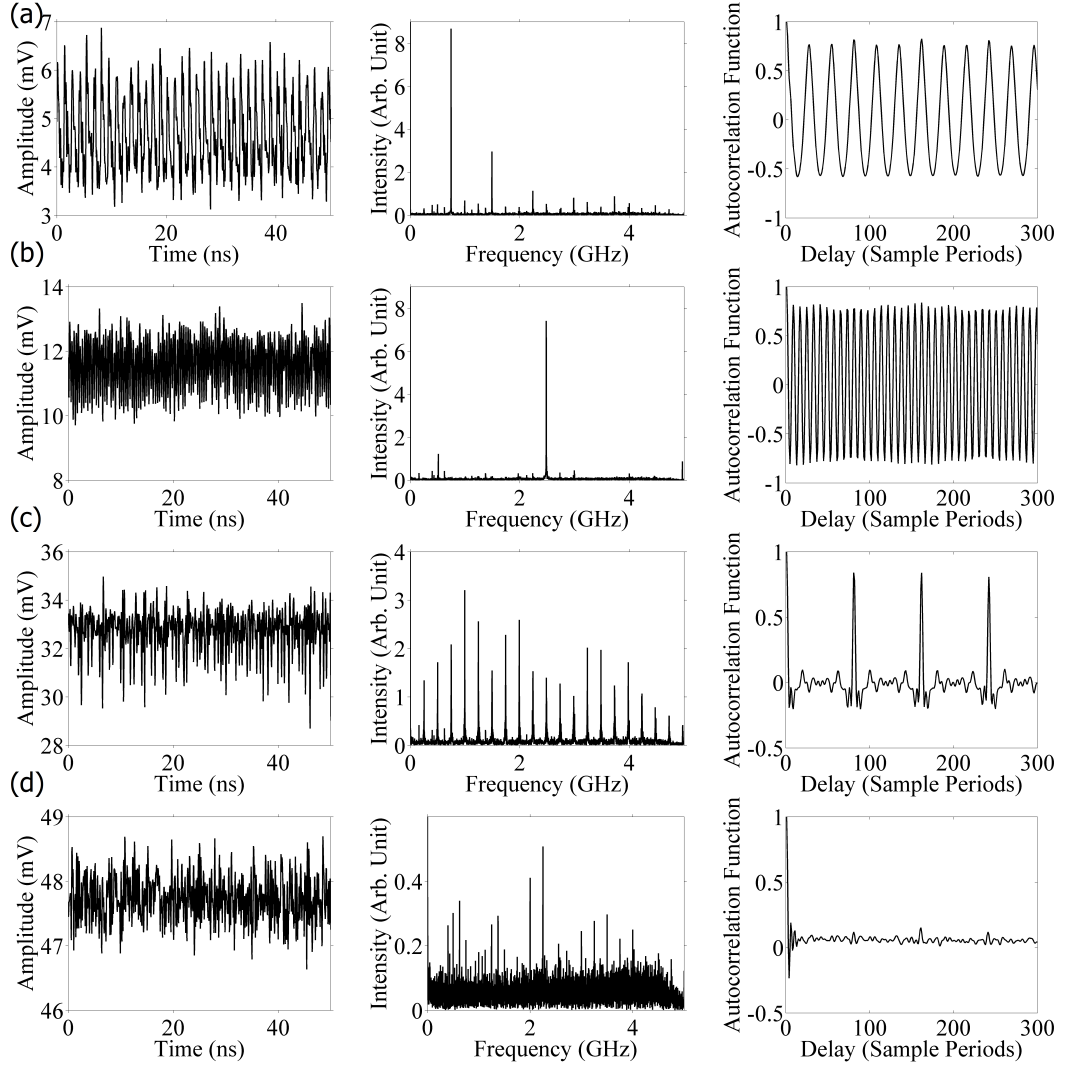
Figure 6.39:   Output power time-series and corresponding FFT spectra and autocorrelation function for different regions of the parameter space as marked in Fig. 6.36(b). One sample period=50 ps. The FSF level was 97.5% (0.75 V) and the injection current was (a) 1=41 mA, (b) 2=45 mA, (c) 3=70 mA and (d) 5=100 mA.

amplitude. These regions are also associated with a low dc level indicating that the laser is operating cw with low amplitude periodic oscillations. The ACF show that the period is very well defined but its amplitude follows more of a chaotic behavior. Region 3 shows dynamics strongly dominated by the external cavity

delay while region 5 exhibits noisy time-series and cw, multi-mode operation of the laser.

6.4.6 Discussion

Four different cavity configurations were investigated, 3 of which are resonant with the AOM frequency shift. The 3 resonant cavities show similar behavior with high levels of FSF, the same basic observations have been made with low levels of FSF and the only difference comes from the FSF level required to reach the coherence collapse regime. The variations in the transition to the coherence collapse regime, i.e. 12% ±1%, are, however, small and are probably related to the increase in FSF strength associated with shorter cavity lengths. Indeed, because of the beam divergence, the longer cavity lengths suffer from higher losses when the beam travels back through the AOM as described in Sec. 6.1.2. When medium FSF level is applied to the system the dynamics are the same regardless of the external cavity length or the resonance condition. The FSF range over which the coherence collapse occurs is slightly different, but again it is probably due to the beam divergence. This explanation is consistent with the results previously introduced as the system transitions from the coherence collapse region at the medium to high FSF regime with an FSF level of 57%, 55%, 53% and 45% corresponding to a cavity roundtrip frequency of 160 MHz, 249 MHz, 320 MHz and 480 MHz, respectively. However, a few differences arise between the different cavity configurations with high FSF levels. The first difference, which is also probably related to the FSF strength, is the stability and the injection range at which regions 1 and 2 appear. The two longer cavities, i.e. 160 MHz and 249 MHz, show instabilities in region 2 with PE values varying from 0.78 to 0.95. The range of injection currents at which region 2 appears is also very small (about 1 mA) whereas it is ≥ 2 mA for the two shorter cavities. The shortest cavity of 480 MHz shows periodic time-series on a cw level over a range of 6 mA in injection current associated with high FSF level >99%. The external cavity corresponding to a roundtrip frequency of 320 MHz shows periodic modulations in the time-series for system parameters that do not show such dynamics in the other external cavity configurations. The high resolution maps illustrating the

dynamics of the system do not show any significant difference between the resonant and non-resonant cases, the dominant effect seems to be the FSF strength. Regardless of the cavity length the dynamics in region 1 always occur at frequencies about 1 GHz, which mean that a shorter cavity would be required to match these frequencies. However, the experimental setup does not allow the characterization of such short external cavities, as explained in Sec. 6.1.5.

Experimental results reported in the literature show a direct effect of the resonance condition on the dynamics of the system. Early reports described the generation of short pulses in a dye laser system [27, 30, 31] in which the external cavity was resonant with the AOM frequency shift. Pulses with a repetition rate corresponding to multiples of the fundamental cavity frequency were observed. The same system also showed a broadband modeless output when the external cavity was non-resonant [97, 99]. However, pulsed output has also been reported in a non resonant cavity configuration with a titanium-sapphire as a gain medium [114]. If a single frequency seed laser is injected into such a broadband FSF laser system a comb of modes spaced by the laser cavity roundtrip frequency shift is generated [105]. Fiber laser based FSF systems in a non resonant cavity configuration have also been reported, such as a short pulsed Er:fiber laser at 1.55 μm [32].

The gain in semiconductor lasers is sufficiently different, i.e. large group velocity dispersion or short carrier lifetime make mode-locking a difficult exercise, than that of previously introduced FSF systems that different dynamics such as chaotic behavior are quite likely to occur [259] in a semiconductor-laser-based FSF laser system. Despite the fact that the system shows dynamics which are not affected by the resonance condition of the external cavity, these two cases will be differentiated. Previous studies on FSF semiconductor laser systems were differentiated by the type of diode laser used in the experiment. More specifically, the intracavity facet reflectance (IFR) was the main difference between them and was brought forward to explain the different behaviors observed experimentally. As presented in the previous sections, the 3 regimes of FSF (low, medium and high FSF levels) will be discussed separately.

6.4 Experimental Results of the Effects of the Cavity Length on the Dynamics of the System

All studies conducted on FSF semiconductor laser systems are at least 10 years old and did not characterize the dynamics with high resolution. Traditionally, system behavior was tracked manually by observation of optical and/or RF spectra but recent major developments in the field of collecting and analyzing output power time-series from nonlinear laser systems now allow high density maps to be generated. The previous studies covered at most 1, low resolution, FSF regime but did not include any detailed analysis of the system. Therefore, the maps previously reported in this chapter are a new tool which give new insights into the dynamics of such systems and pave the way for increased understanding of the nature of the electric field emanating from such sources. The results are not an obvious fit with available theories so new theoretical developments will be needed to explain them.

Low levels of FSF do not affect the temporal dynamic behavior of the system, however, they influence the spectral bandwidth. Strong alteration of the spectral behavior of a semiconductor laser with low FSF level was reported in [28]. The authors used first an infrared (IR) diode laser with an IFR of 32%. They reported a broadening of the laser mode up to 5 GHz with FSF levels above 35% associated with single longitudinal mode operation of the laser. Figure 6.40 illustrates the output spectrum for different levels of external feedback of the IR laser diode and is extracted from [28]. The linewidth of the laser can be estimated as 100 MHz with an FSF level of 5.8% as seen in Fig. 6.40 from [28]. However, the second visible laser diode with FSF exhibited a more drastic broadening where small FSF levels (below 3%) caused a broadening of up to 3 GHz to the main laser mode. The spectral broadening observed in our system does not match quantitatively with the observations of Richter and Hansch. A gradual broadening of up to 300 MHz of the laser mode associated with FSF levels ($\leq 1.5\%$) while single longitudinal mode operation of the laser is observed in our experiment which indicates that the devices they used were more stable to the onset of multi-longitudinal mode operation. The main laser mode output power drop associated with FSF reported in [28] was also observed in our experiment. Several groups observed this spectral broadening with increasing FSF and most of them managed to achieve single mode operation of the laser with FSF levels greater than 1.5%. Martin et al.
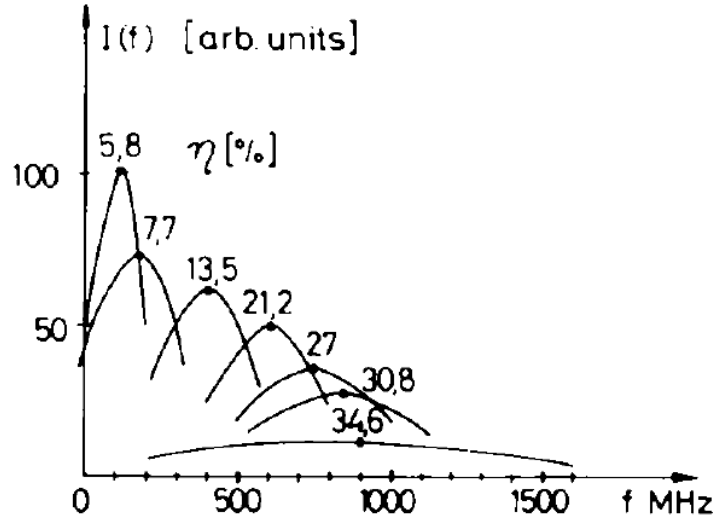
Figure 6.40: Frequency shift and line shape at the output of the infrared diode laser (IRDL) versus diffraction efficiency η of the AOM. Extracted from Ref. [28].

used a visible diode laser (IFR of 20%) with FSF and reported a broadening of 180 MHz with an FSF level of 0.002% [251]. A broadening of modes spaced by the frequency shift of the AOM has also been observed in [103] for low levels of FSF, i.e. below 12%. Willis and coauthors worked with 3 different external cavity designs and observed, in the same external cavity configuration, a broadening of 500 MHz for an FSF level of about 1% before the diode laser (IFR of 4.5%) started emitting on multiple longitudinal modes, as illustrated in Fig. 6.41. The same study also reported an increase in noise of the laser when operated with injection currents close to threshold. Willis et al. improved the side mode suppression by introducing a frequency-selective element inside the external cavity where the plane mirror was replaced by a diffraction grating. This led to a broadening of about 7.5 GHz with an FSF level of 6% associated with single mode operation of the laser. It would be expected to achieve single mode emission with higher FSF levels by using a DFB FSF system, the spectral selectivity of such diodes should allow the device to be operated at much higher FSF level without exciting longitudinal modes of the laser. Surprisingly, the bandwidths of a DFB FSF system reported in [104] were only on the order of several hundreds of MHz with
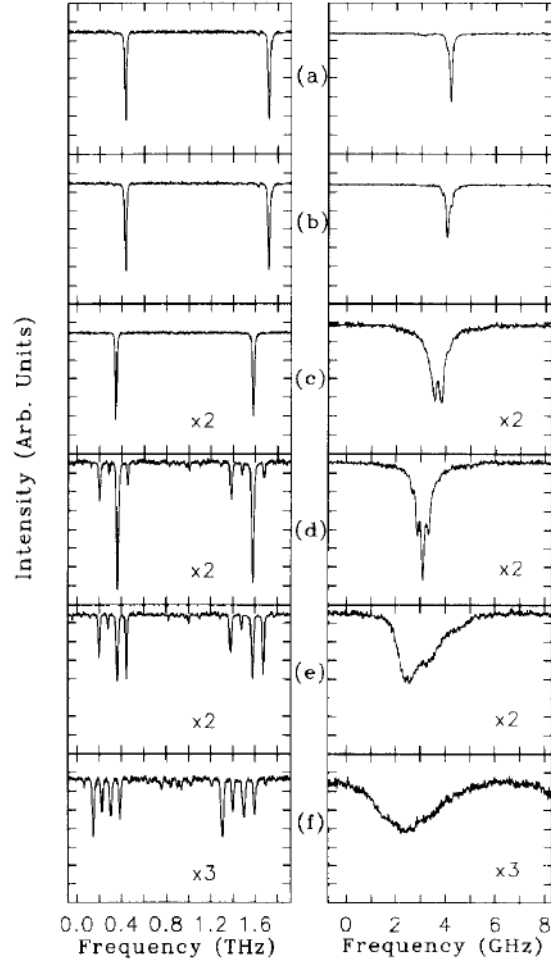
Figure 6.41: The optical frequency spectra of the FSF external cavity diode laser introduced in Ref. [103]. The diffraction efficiency η (and RF power to the AOM) in each case is (a) 0.08% (3.2 mW), (b) 0.26% (10 mW), (c) 0.83% (32 mW), (d) 1.04% (40 mW), (e) 1.3% (50 mW). (f) 2.6% (100 mW). Extracted from Ref. [103].

an FSF level of 0.1%.

The experimental results reported in this chapter match qualitatively the observations made in the literature on similar systems but go well beyond the published literature. It has been shown that low FSF levels induce a gradual broadening of the laser mode with increasing FSF until the laser starts operating on multiple longitudinal modes. This broadening associated with single mode op-

eration of the laser is different in each system reported in the literature. Both the bandwidth and the rate at which the broadening occurs are different and probably related to the specific laser device gain medium and the diode laser system cavity configuration. Also, the maximum diffraction efficiency η of the AOM can be significantly different between the various crystals commonly used in AOMs. The beam shape, geometry of the external cavity and alignment of the AOM can also alter the diffraction efficiency, thus misleading the reader when comparing FSF levels between different studies. The FSF level threshold at which multi-mode operation occurs is related to the IFR of the diode and Ref. [260] showed that a low IFR is required in order to increase this threshold and therefore increase the bandwidth of the laser mode. The IFR of the laser used in our experiment is unknown but the fact that the diode becomes multi-mode with an FSF level of 1.5% indicates that the IFR is comparable to that in [103], i.e. about 4%. This is consistent with the standard high/low reflectivity coatings of standard commercial lasers.

The medium FSF level range is not well documented in the literature as most studies have been focused on low FSF levels [103, 251]. Nevertheless, Richter and Hansch reported a broadening of the laser linewidth up to several GHz associated multi-longitudinal mode operation of the visible diode with medium FSF level (11%). The IR diode showed a broadening of 5 GHz while maintaining a single mode operation of the laser as seen in Fig. 6.40. Beyond a certain FSF level, multi-mode operation is a characteristic feature of Fabry-Perot semiconductor laser systems with FSF. However, no temporal data was ever reported in the literature which makes it difficult to interpret any regimes of instabilities. The analysis of the data reported in this chapter allows a better identification of regions exhibiting different temporal behavior. This study is the most comprehensive experimental study a semiconductor-laser-based FSF laser system. Spectral data alone is not enough to fully characterize the dynamics of the system. Indeed, as seen previously, multi-mode operation of the laser does not always correspond to different temporal behavior, i.e. regions identified in both PE and RMS maps do not exactly match with regions showing very distinct behavior in the spectral maps even though a strong correlation can be established. Careful interpretation

of all these different maps allowed us to identify, with very high precision, the coherence collapse region. The work of Benoist contrasted conventional optical feedback and FSF and noted the suppression of phase dependent linewidth variation of the lasing mode using FSF [104]. Measurements of the RMS noise level, of the photodetected output power as a function of feedback level indicated that a transition to the coherence collapse dynamical regime occurred in both systems. This regime of operation has been well documented in the sequence of regimes observed for a semiconductor laser with optical feedback from an external mirror [5]. In the FSF system the transition was not the expected discontinuous switch at a single feedback level reported in the Benoist et al. study. The transition was more gradual. However, the increase in noise level was about 20 dBm/Hz in both cases. This research suggests that FSF does not dominate nor significantly modify the usual coherence collapse nonlinear dynamics that occurs in these systems and which is predicted reasonably well by the Lang-Kobayashi rate equation model [4]. However, Benoist's work does not specify what the resolution of the FSF level was and this makes it difficult to compare results with our experiment. The transition into and out of the coherence collapse region always occurs within the resolution limit of the equipment which corresponds to a change in the FSF level of about 0.2%, depending on the actual FSF level at which the transition occurs as discussed in Sec. 6.4.2. It is clear that the transition is similar to that of a conventional optical feedback system. The time-series extracted from this region show broad external cavity peaks in the RF spectra, with less power at higher frequencies (>2 GHz). Similar behavior has been reported in [39, 240] using the same characterization tools. The sharp transitions surrounding the coherence collapse region may suggest that this regime of operation "interrupts or disturbs" FSF behavior which otherwise would be a continuum of FSF dynamic behavior. These results suggest that this region of the parameter space, i.e. the coherence collapse, can be predicted and modeled by using the Lang-Kobayashi rate equation model [4].

The third region of the parameter space investigated where the system shows significantly different dynamics is associated with high levels of FSF. In this region the device exhibits a broadening of the laser linewidth (regions 1, 6) and is often

operating multi-mode (regions 3, 5) depending on the injection current. Richter and Hansch reported the broadening of the laser linewidth up to 1 THz with an FSF level of 80%. This, however, was associated with multi-mode operation of the diode. In a similar configuration but with a lower IFR (8×10^{-5}%) Sato and co-authors achieved a spectral broadening of 780 GHz with an FSF level of 90% [260] also associated with a multi-mode emission. Single mode operation of the laser with high FSF levels was only achieved by using an external cavity with a diffraction grating as a reflective element instead of a plane mirror. The frequency narrowing of the bandwidth of the feedback provided by a diffraction grating allows much higher FSF levels to be fed back to the laser than a plane mirror. Sato et al. demonstrated the influence of the spectral selectivity on the isolation of side modes and showed that with a grating providing a high selectivity (1800 lines/mm) it was possible to achieve a spectral bandwidth of 12 GHz while achieving single mode emission of the laser. They also managed to obtain a broadening of 15 GHz using a diode with a lower IFR of 10^{-5}%. Lim and co-workers achieved a linewidth broadening of 5 GHz along with a tunability of 8 nm associated with single mode operation of the laser by using a laser diode with an IFR of about 4% in a Littman-Metcalf cavity configuration in which the AOM is placed between the diffraction grating and the external reflecting mirror [124]. A comparable spectral broadening of 5.28 GHz was obtained in Ref. [245]. Following the observations of [260] and comparing them with earlier studies seems to indicate that two main conditions are required in order to achieve spectral broadening while single mode operation of the laser is maintained. While a high spectral selectivity is necessary to maintain a single mode operation of the laser at high FSF level, a low IFR is also required to suppress multiple longitudinal modes of the laser. Sato and co-workers demonstrated that an IFR $<4 \times 10^{-6}$% is sufficient for the system to behave as a one segment cavity, thus avoiding multiple chip mode operation. The results presented in this chapter have been produced with high resolution data and the amount of details that these high density maps show have no equivalent in the literature. It is because the system has been analyzed in such a complete way that it is now possible to identify regions of the parameter space where the system shows significantly different complexity and behavior. This allows us to distinguish a region where the laser is strongly

single mode and associated with high FSF level (>47%) even though multi-mode operation was already achieved with low FSF level (1.5%). The fact that the system shows such abrupt transitions between the different complexity regions is an indicator that unless high resolution dynamic maps are generated it is not possible to have a complete understanding of the dynamics of the system.

Single mode operation of the laser was achieved with either low FSF level, i.e. <12%, or high FSF level (>47%). This work reports the first observation of single longitudinal mode operation of the device when operated with high levels of feedback provided by a plane mirror (regions 1, 2 and 6) in a semiconductor laser FSF system. A broad laser linewidth of up to 2.4 GHz has been observed with single longitudinal mode operation of the laser. This is the first observation of such a broadband single longitudinal mode output with a semiconductor-laser-based FSF system without using frequency selective feedback. However, when the system is driven with high levels of FSF the laser needs to be operated close to threshold in order to remain single mode. The power in the mode remains high but higher average power is achieved when multi-mode operation of the laser is observed in region 5. The threshold current for the solitary device is about 57 mA and drops to about 33 mA with maximum FSF. This operation below the free running laser threshold may explain why this region of the parameter space has not been investigated in the literature so far. The relatively small injection range at which single mode operation is observed is also a limiting factor. In this region the laser linewidth broadens up to 2.4 GHz but no features spaced by the AOM frequency are observed in the FPI spectra. However, the scanning rate of the FPI (about 10^{13} Hz/s) is much slower than the frequency shift rate inside the external cavity (about 10^{17} Hz/s for an external cavity length of about 30 cm) which means that the observation of a chirped comb of frequencies separated by the AOM frequency was not possible. Yoshizawa and co-authors demonstrated that, regardless of the resonance condition of the external cavity, a chirped frequency comb output with a comb spacing corresponding to the AOM frequency was observed and that the chirping rate was linearly decreasing with increasing cavity length [245]. From these observations a longer cavity of about 2.5 m was set up but because of the beam divergence a longer external cavity could not be used as the minimum amount of FSF required for the system to

go beyond the coherence collapse region was not satisfied. Increasing the cavity length did not allow us to observe any mode structure in the FPI spectra therefore in order to investigate the internal structure of the spectra the output of the laser was coupled to a fixed, i.e. non scanning, FPI. It has been reported in different solid state FSF systems that if the laser exhibits a chirped frequency comb output then a periodical pulse train whose repetition interval is inversely proportional to the round-trip frequency shift, while the output power stays constant, is observed [98, 117, 118, 119]. However, it is expected that the time interval between the pulses is about 6 ns therefore it is necessary to observe the signal with a detector having a good sensitivity and a response time <6 ns which is not the case as the PMT used in the experiment has a response time of about 25 ns. Therefore, the internal structure of the spectra could not be observed in the experiment but it is with good confidence that one believes that, at least in these regions, the system shows a chirped frequency comb output. The characteristic signs associated with this behavior, i.e. spectral broadening with single mode emission, are observed in the experiment and this reinforces this theory. Also the periodic oscillations associated with sharp frequency components in the corresponding RF spectra has to be the result of a beating between several external cavity modes, since the laser is operating single mode in these regions, which supports the chirped frequency comb output model.

Numerous studies [106, 142, 144, 145, 146, 147, 148, 149, 150, 151, 247, 261] have demonstrated the use of a chirped comb of frequencies for optical frequency domain ranging, i.e. accurate distance measurement. In the experiment, the output power time-series show periodic oscillations on a low amplitude cw baseline and this regime has also been observed in a titanium sapphire FSF system for a certain pump power [114]. Bonnet et al. demonstrated a range of different dynamical regimes with increasing pump power. Starting at low pump powers it operated cw then transitioned through sustained spiking, low frequency pulsation with a zero baseline, high frequency pulsations on a cw baseline, and finally to cw output again at high pump powers. They also observed that the transition from cw to mode-locking is associated with a significant broadening (2 GHz) of the laser linewidth. In our experiment the transition from high frequency pulsations on a cw baseline to cw output is accompanied with a broadening of

about 0.8 GHz. However, the system does not show mode-locking but shows an increase in the repetition rate of the pulsations while their modulation depth decreases slightly, which matches the observations of [114]. The main difference between the laser system in [114] and our system, despite the gain medium, is the addition of an etalon with an FSR of 200 GHz inside the gain cavity which restricts the emission to a single transmission order of the resonator. Naturally, in our case, the integration in the external cavity of an element that could reduce the effective gain bandwidth of the laser cavity should be the first step towards short pulse generation. This could be achieved by using a frequency selective element rather than a high reflectivity mirror to close the external cavity.

The behavior observed in [114] has also been observed in [262] where a ring dye laser FSF system showed increasing pulse repetition rates (associated with the external cavity roundtrip time) with increasing pump power. In these regions, where the system exhibits periodic time-series, the RF spectra show strong peaks located at multiples of the external cavity frequency which has also been observed in a dye FSF laser seeded by a single-mode stabilized dye laser and in a diode-pumped Nd:YVO FSF system [117, 263]. However, in [263] the peaks were observed at frequencies corresponding to common multiples between the external cavity frequency roundtrip and the AOM frequency which in our case would lead to the appearance of RF frequencies below the gigahertz range in the four external cavity configurations investigated. Because it was not possible to resolve the internal structure of the optical spectra it is assumed that the chirp rate is related to the AOM frequency. However, the frequency spacing between the modes seems to be related to the external cavity frequency as discussed in Sec. 6.4.5. Indeed, the peaks in the RF spectra for the non resonant cavity are located at multiples of the external cavity frequency and are not associated with the AOM frequency which means that if beating between two modes occurs then these modes are spaced by the external cavity frequency. This observation agrees with the work of Paul et al. in which, by using the unique properties of FSF lasers, they managed to demonstrate accurate distance measurement with a DFB FSF system [146, 147]. The loss of periodic oscillations in the time-series associated with increasing injection current is accompanied by a much higher cw baseline level and irregular spiky output in the time-series. This, eventually leads to cw operation of

the laser for the highest injection currents. This behavior is documented in [114], however, the transition from periodic time-series to cw output is not detailed but the maps presented in this chapter indicate that this is a sharp transition. The transition from regions 1, 2 and 6 to region 3 is sharp and the reasonably well defined oscillations on a cw level suddenly change to a more irregular spiky output in region 3. Then the time-series show decreasing oscillation amplitude with increasing injection current. The PE values increase smoothly until they reach 1 and high power cw output is obtained. These results are a great source of information on semiconductor-laser-based FSF systems. They pave the way for theorists to investigate the effect of FSF on a semiconductor laser. What has been observed so far suggests that there is a competing effect between FSF and conventional optical feedback with certain levels of FSF, i.e. medium and high levels of FSF. The dynamics of the system are completely dominated by FSF when low levels of FSF are fed back to the laser. Then for higher levels of FSF the system seems to be dominated by conventional optical feedback (COF). The coherence collapse regime seems to disrupt the FSF behavior of the system and the dynamics resemble that of a semiconductor laser system with COF in the coherence collapse region. Finally, when high levels of FSF are applied the two effects, i.e. FSF and COF, compete and show characteristics features specific to each kind of feedback. Close to threshold, FSF dominates the dynamics with well defined oscillations on a cw level then COF becomes more prominent with increasing injection current. The level of details this study shows may be used to understand and model the different dynamics observed in this system.

6.5 Conventional Optical Feedback

In this section the dynamics of a semiconductor laser with conventional optical feedback (COF) are investigated. The same setup previously described in Sec. 6.1.1 was used. The only difference lies in the type of feedback utilized. The zeroth order beam of the AOM is now used for feedback which means that the light fed back to the laser diode does not experience any frequency shift. The system is therefore considered as a conventional optical feedback system and is

203
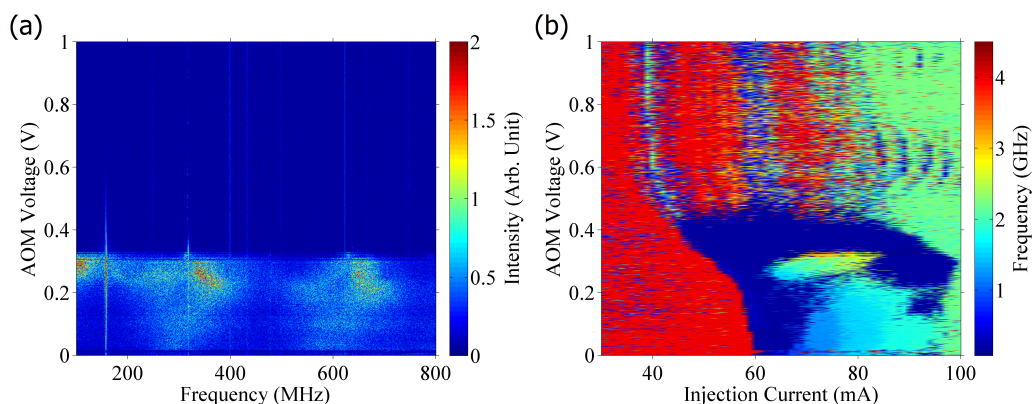
Figure 6.42: (a) Map of the FFTs of the output power time-series for increasing feedback at 70 mA. (b) Map of the dominant frequency of the FFTs of the output power time-series as a function of feedback and injection current.

expected to show dynamics well documented in the literature [5]. The same dynamic maps were produced with the same resolution in order to allow comparison with the FSF laser system. However, because the first order diffraction beam of the AOM can not achieve 100% efficiency a small portion of the light is still transmitted through the zeroth order even when maximum voltage is applied as depicted in Fig. 6.4. Therefore, voltages should not be used when comparing feedback levels between FSF and COF systems. The external cavity length does not affect the dynamics of COF systems, therefore the external cavity corresponding to a roundtrip frequency of 320 MHz will be discussed here. Similar maps have been generated in [39, 240] with an identical laser diode and AOM. The maps presented in these studies were generated with a different resolution, 0.1 mA and 0.01 V steps in injection and feedback level, respectively. A comparable parameter space was investigated and thus allows for direct comparison between both studies.

Figure 6.42(a) shows a color map of the RF spectra as a function of feedback at 70 mA. A strong, sharp peak located at 157.7 MHz appears with low feedback levels (<32%) and gradually decreases in intensity with increasing feedback. A second, weaker peak located at 318.4 MHz also appears in Fig. 6.42(a). This low feedback region is also associated with broad, low amplitude peaks centered at

multiples of the external cavity roundtrip frequency. This regime shows distinctive features associated with the coherence collapse regime previously observed in the FSF system. No feature appears in the RF spectra beyond a feedback level of 32%, the remaining peaks are related to noise coming from the oscilloscope. The dominant frequency map illustrated in Fig. 6.42(b) shows the smooth transition from 1 GHz up to 2 GHz in the coherence collapse region and has also been observed in the FSF system. The coherence collapse region can be seen in the RMS map depicted in Fig. 6.43(a) where it is associated with high RMS amplitude with low feedback level. Two other regions can be identified from Fig. 6.43(a), a first region associated with very low feedback level (<5%) and a second region associated with high injection currents and high feedback levels. The transitions to and from the coherence collapse region are rather abrupt, even though the transition from this region is more gradual. The PE map illustrated in Fig. 6.43(b) shows four distinct regions, marked 1 to 4, where the PE values are significantly different. Region 1 is associated with low PE values (around 0.65) and single mode operation of the laser, see Fig. 6.44(a). In this region below the coherence collapse boundary, the PE values have lower complexity compared to the fundamental noise and the time-series show periodic dynamics as seen in Fig. 6.45(a). The frequency spectra associated with this region show very sharp, very high power peaks separated by approximately 289 MHz which is smaller than the external cavity roundtrip frequency of 318.4 MHz. The oscillation period in the ACF is associated with the frequency of the main RF peak. Region 2 is located in the coherence collapse region and is associated with high RMS amplitude, see Fig. 6.43(a), and PE values of about 0.8 as seen in Fig. 6.43(b). The time-series are noisy and the associated RF spectra exhibit broad peaks separated by the external cavity frequency and low power at high frequencies (>2 GHz), see Fig. 6.45(b). The delay of the low amplitude peak in the ACF corresponds to the frequency of the external cavity frequency. The low amplitude associated with a rapid decrease in power suggests that the oscillations in the output time-series are only weakly correlated with the external cavity delay. In this region the laser is strongly multi-mode as depicted in Fig. 6.44(a) and the higher level of feedback leads to a threshold reduction, see Fig. 6.44(b). The most complex region, which is not associated with cw operation of the laser, is marked 3 in
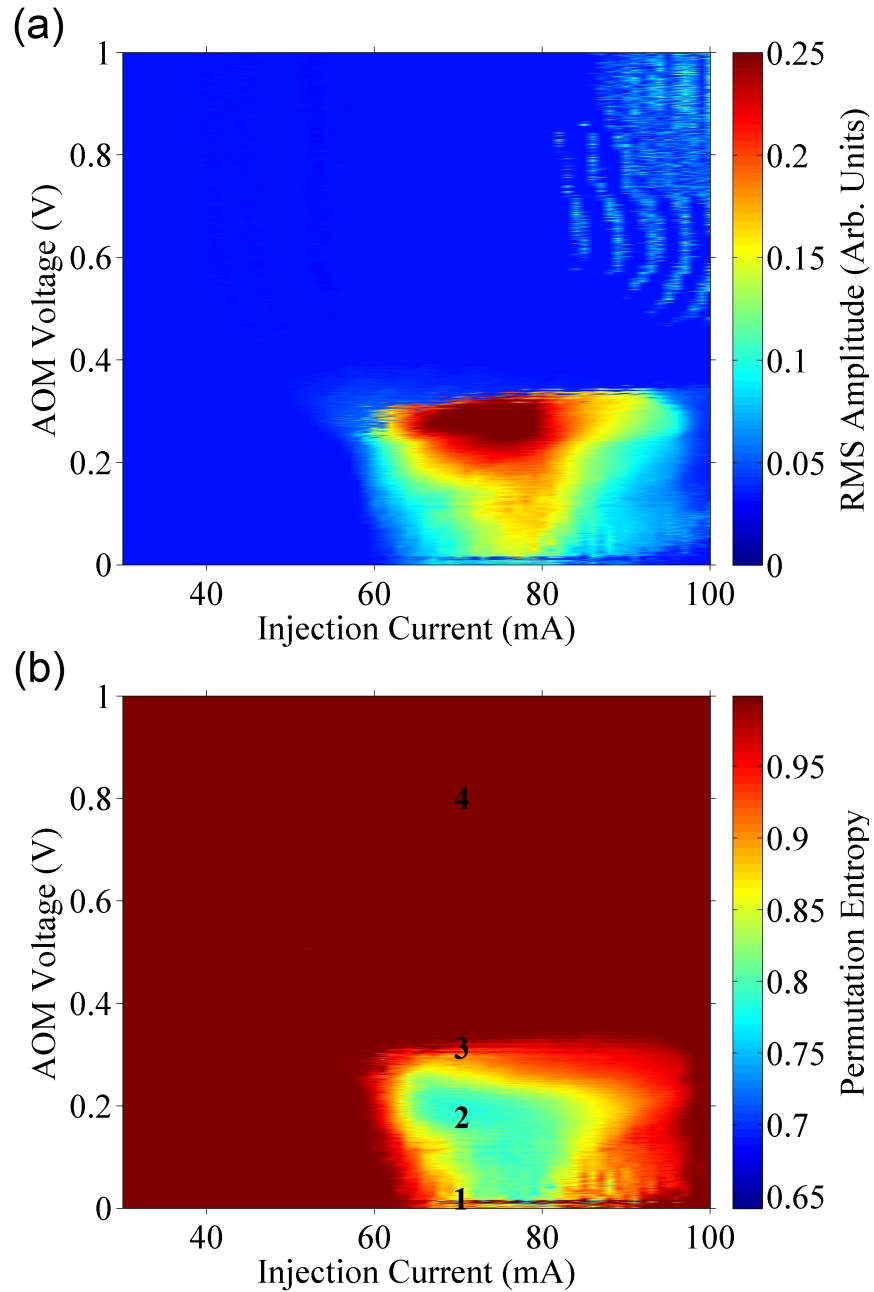
Figure 6.43: (a) Map of the RMS amplitude of the output power time-series as a function of feedback and injection current. (b) Map of the normalized permutation entropy ($D = 5$, $\tau = 2$) as a function of feedback and injection current.
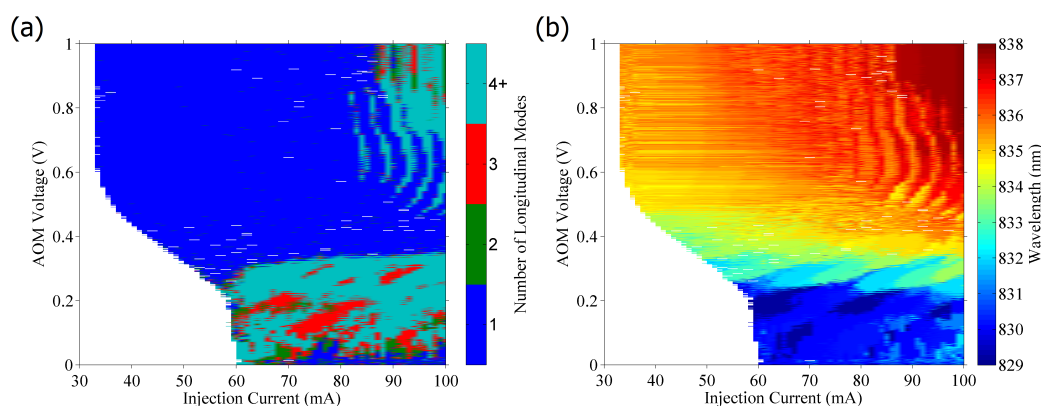
Figure 6.44: (a) Map of the number of longitudinal modes lasing as a function of feedback and injection current. The threshold for side mode suppression was set at 15 dB. (b) Map of the emission wavelength of the main lasing mode as a function of feedback and injection current.

Fig. 6.43(b) and occurs at medium feedback (>30%) with a broad range of injection currents (60-95 mA). Here the output power is dynamically fluctuating and shows low frequency fluctuations as seen in Fig. 6.45(c). The frequency spectra associated with this region reveal sharp, strong peaks separated by the external cavity roundtrip frequency right up to the bandwidth limit of the measurement equipment. The ACF shows high amplitude peaks separated by a delay corresponding to the external cavity frequency. Similarly to region 2, the laser is also operating on multiple longitudinal modes as seen in Fig. 6.44(a). High complexity in the output power time-series of the system means that the laser is operating cw or beyond lasing threshold. Region 4 is associated with feedback levels >32% and PE values close to 1 (≈ 0.99). A typical time-series is shown in Fig. 6.45(d) and its corresponding frequency spectrum shows essentially noise which is also confirmed by the ACF which shows no sign of periodicity in the dynamics of the output power of the laser. The laser is strongly single mode, as illustrated in Fig. 6.44(a) and the threshold is greatly reduced by at most 18 mA with maximum feedback. The emission wavelength of the laser mode increases with increasing feedback and injection current, as illustrated in Fig.6.44(b). There is a region, associated with high feedback and high injection currents, of higher RMS amplitude and multi-mode operation of the laser, as seen in Fig. 6.43(a) and 6.44. However, the
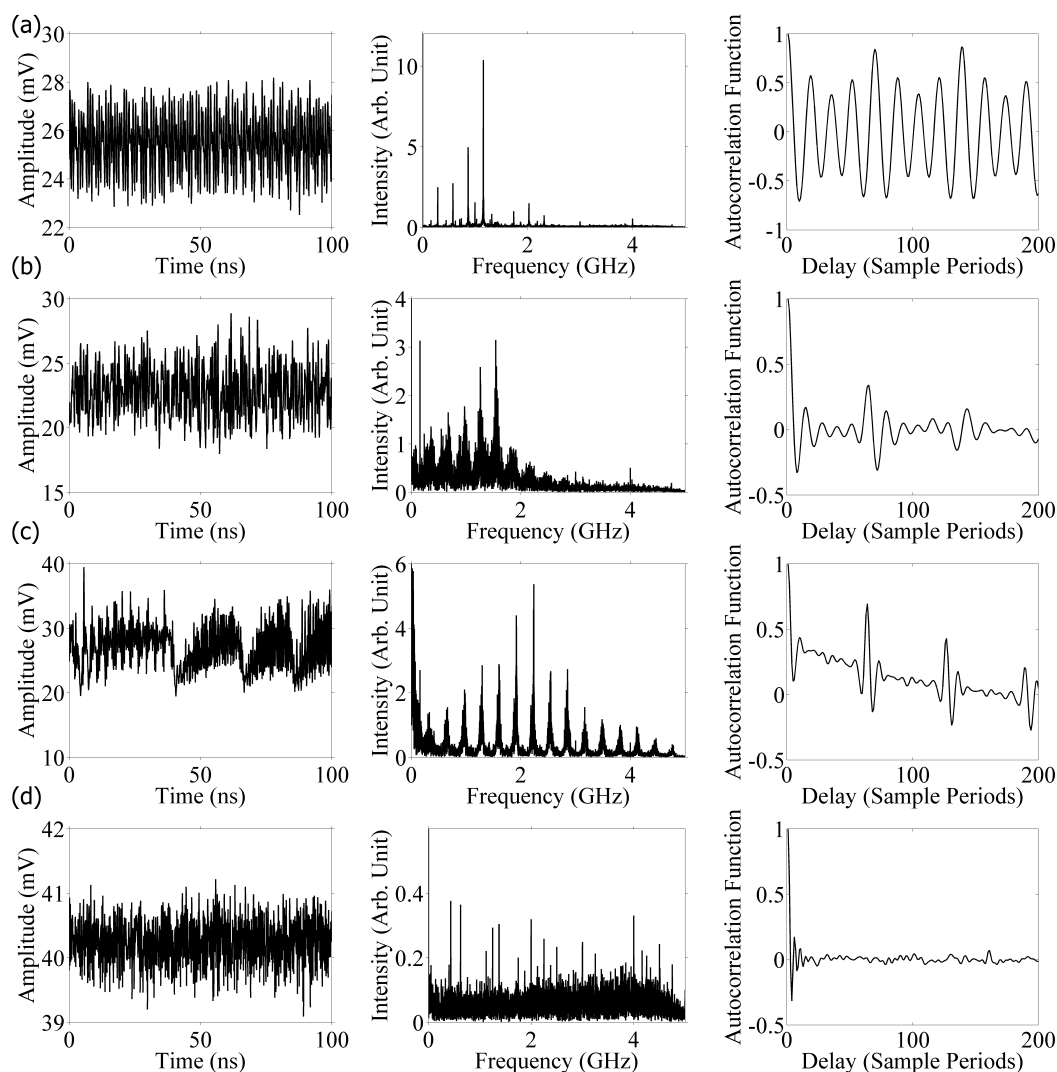
Figure 6.45: Output power time-series and corresponding FFT spectra and autocorrelation function for different regions of the parameter space as marked in Fig. 6.43(b). One sample period=50 ps. The injection current was 70 mA and the feedback level was (a) 1=4%, (b) 2=30%, (c) 3=31% and (d) 5=81%.

PE values associated with this region are close to 1 and the laser operates cw.

The observations reported here for the conventional optical feedback system match that of Ref. [39, 240]. The same dynamics are observed at the same feedback levels and the region of lower complexity, below the coherence collapse

boundary, associated with more regular dynamics, reinforced by the RF spectra showing much sharper peaks than those seen in the coherence collapse region, is also observed in [39]. As reported by Toomey and coauthors the system shows high RMS amplitude for a range of feedback levels and a broad range of injection currents, typically from 60-90 mA with feedback levels between 5% and 30% consistent with coherence collapse. This regime is associated with intensity fluctuations, i.e. low frequency fluctuations, in the output power time-series of the laser resulting in PE values (≈ 0.8) lower than that of fundamental noise observed when the laser is operating either below threshold or cw. This lower complexity indicates more periodic time-series with a strong influence of the external cavity roundtrip frequency on the dynamics. Beyond 32% the system becomes cw and stable over the whole range of injection currents investigated and the lasing threshold is also greatly reduced. This is also the case in Ref. [39, 240] where the stabilizing effect for very high feedback levels is observed over a large range of injection currents. The maps introduced here and the results previously reported in [39] confirm that, at this resolution, there are no unexpected islands of differentiated dynamics within the coherence collapse region.

The dynamics observed for the conventional optical feedback system share some similarities with those of the FSF system. The coherence collapse regime occurs at lower feedback levels in the COF system (5-32%) than in the FSF system (12-45%) but the range of feedback levels at which it happens is comparable. The low feedback region is somewhat different, COF does not show any sign of broadening of the laser mode and the device operates cw on a single longitudinal mode. Within the coherence collapse region, both systems show similar behavior with dynamics dominated by the external cavity delay and strong multi-mode operation of the laser. At higher feedback levels and injection currents away from the lasing threshold the dynamics are similar in both systems. The laser operates cw and the dynamics of the system are no longer influenced by the delay introduced by the external cavity. The main difference in the dynamics between the two systems is the presence of a region of periodic oscillations associated with the external cavity delay in the time-series when the laser operates close to threshold in the FSF system. This suggests that the behavior, in the FSF system, that is dominated by the FSF is only observed at low and high levels

(close to threshold) of feedback power and that FSF does not affect the dynamics of the system in the coherence collapse region although low frequency fluctuations appear with COF. This may indicate that the coherence collapse regime disturbs the FSF dynamics for a range of FSF levels and that COF dynamics dominate in this region then start competing with FSF dynamics for higher levels of FSF. This is also verified in the optical spectra where the threshold does not decrease with low levels of FSF. At these levels of FSF the threshold is expected to be reduced in COF systems and the fact that it reduces in the coherence collapse region is a good indication that COF influences the system in this region. Once the system leaves the coherence collapse regime the threshold reduction rate is similar in both systems. FSF and COF compete with higher levels of FSF. Close to threshold, periodic fluctuations on a cw level are observed in the time-series associated with strong single longitudinal mode operation of the laser in the FSF system. Then at higher injection currents the system seems to be influenced by COF with dynamics associated with the external cavity delay. The emission wavelength of the main laser mode tends to confirm that there are two competing effects with high levels of FSF. COF shifts the emission wavelength towards longer wavelengths whereas FSF shifts it the other direction. The shift induced by FSF is clearly dominating that of the COF. The domination of FSF over COF is more pronounced close to threshold (where supposedly FSF has a bigger impact on the dynamics) where the emission wavelength of the laser is gradually decreasing. The maps generated in this chapter provide new insights into the dynamics of a semiconductor-laser-based FSF system and a great source of information towards the understanding and modeling of such a system.

Chapter 7

Conclusions

In this thesis, we have investigated the dynamics of two external cavity semiconductor laser systems with different types of frequency modified feedback. The first system, based on a VCSEL with feedback from a VBG, has been used to investigate the spatial self-organization of LCSs with synchronized dynamics. Furthermore, the temporal and spectral dynamics of a second system, relying on an EEL with FSF, have been investigated.

In the first experiment we first characterized the external self-imaging cavity. We showed that VBGs work as wavelength lockers for VCSELs similarly to what is found using conventional EELs. A shift of the wavelength emission smaller than 0.03 nm over a range of 200 mA, much smaller than the shift of 0.7 nm measured with feedback from a plane mirror, was observed in the experiment. This shift can be further reduced by increasing the magnification of the imaging system but comes at a cost of increasing size of the system. We demonstrated that beyond threshold, it is possible to stabilize single-wavenumber and narrow bandwidth emission with high fidelity.

We analyzed the effect of deviations of the external cavity from the self-imaging condition (SIC). We demonstrated that the system is remarkably insensitive to deviations from the SIC, even in the millimeter range, for a cavity length in the 100 mm range, thus being beneficial for the robustness of experimental conditions. The self-imaging position allows for best feedback efficiency in terms of both amplitude and phase, thus providing stronger feedback for single LCS. However, controlled deviations from the self-imaging condition may provide

a convenient handle on coupling strength in arrays of lasers and laser solitons [171, 172].

We demonstrated a relatively simple and fast method to characterize quantitatively the disorder in the VCSEL by frequency-selective feedback on scales relevant to devices and laser arrays. We showed that the positions, frequencies and thresholds of the LCSs are dictated by the disorder and as a result LCSs appear at certain locations, i.e. defects, in the VCSEL aperture. The presence of the defects breaks the translational symmetry, fixes the relative distance between solitons and locks the relative phase to values different from $\pi/2$ observed numerically in the absence of defects or experimentally in temporal-longitudinal systems [229]. We demonstrated both experimentally and theoretically that two trapped LCSs in VCSELs with frequency selective feedback display Adler synchronization leading to phase and frequency locking. We showed that locking does not affect the intrinsic properties of the LCSs. This implies that the coupling is weaker than their solitonic properties alone which means that they remain individually controllable. The synchronization is induced by spatial defects where the LCSs are pinned and by changing the frequency of each soliton with respect to that of its neighbor.

The coupling mechanism between two LCSs is not well understood yet. Theoretically it is believed that there is a spatial overlap of the electric fields emerging from the LCSs. However, the experimental observations reported here show phase and frequency locking of two LCSs separated by almost 80 μm which is a distance over which it is not possible to achieve sufficient coupling strength that leads to locking. It seems clear that there exists an additional, different, coupling mechanism. There are several possibilities to explain the provenance of this additional coupling. The most probable reason is that it may be the result of scattering at the VBG in the external cavity which would then favor the overlap of the electric field over larger distances. The results reported in this thesis focus on the self-imaging position but the effects of deviations from this position on coupling strength is interesting. Some time has been spent on quantifying these effects and preliminary results seem to indicate that the strongest locking happens away from the self-imaging position. However, at this point further investigations need to be done in order to use this tool as a way of controlling the coupling strength

between two LCSs in a similar fashion to what has been achieved in large arrays of coupled lasers [171, 264].

Early in the project, before the first systematic characterization of phase and frequency locking, further interesting locking dynamics were observed. High visibility fringes in the far field associated with an optical spectrum showing multiple peaks were observed. The peaks were separated by the external cavity frequency and a fringe visibility higher than 0.5 was observed in the far field. Although the external cavity modes of a single LCS do not have a definite phase relationship, this suggests that the two LCSs oscillate on these external cavity modes together, i.e. the phases are locked at all external cavity modes, and that they show synchronized dynamics. A handle to achieve phase locking of the different external cavity modes of a single LCS could potentially open the door to mode-locked LCS.

Future work should also be focused towards the study of interaction of pinned LCSs from two to multiple elements. In view of the random detuning conditions due to the disorder, it can be anticipated that it is impossible, or at least difficult, to achieve locking of more than two LCSs by a single, global control parameter, i.e. the VBG tilt. It would be necessary to have control over the local values of the detuning in addition to the global one used here. Previous investigations established that the hysteresis loop of a LCS can be shifted independently by local injection of an external beam [193]. The external beam generates or depletes carriers (depending on wavelength), the refractive index changes and this causes a shift of the cavity resonance, with a possible additional thermal effect, which then induces a shift of switching thresholds. It is expected that this will be accompanied by a change in frequency.

In the second experimental system, experimental output time-series measurements have been used to create for the first time high resolution 2D maps of permutation entropy, RF spectra and RMS amplitude as function of FSF and injection current for an FSF semiconductor laser external cavity system. These maps have been used to identify regions of instabilities exhibited by this FSF laser system. Three distinct regimes of operation have been identified corresponding to low, medium and high levels of FSF. Four different cavity configurations were investigated, three of which are resonant with the AOM frequency shift. The

three resonant cavities show similar behavior with high levels of FSF, the same basic observations have been made with low levels of FSF and the only difference comes from the FSF level required to reach the coherence collapse regime.

We showed that low levels of FSF do not affect the temporal dynamics behavior of the system, however, they do influence the spectral bandwidth. A gradual broadening of the laser mode with increasing FSF until the laser starts operating on multiple longitudinal modes is reported. For low levels of FSF the system shows characteristics similar to observations in earlier work [28, 103]. Despite the fact that the laser used here has less side mode suppression, the system shares the same features. A linewidth broadening of up to 300 MHz for an FSF level of 1.5% has been observed as well as a good stability of the system for low FSF levels over the entire range of injection currents studied.

Further increase of FSF causes the RF peak to broaden. In this region the system becomes chaotic for a broad range of FSF levels, typically between 12% and 58%, and injection currents. In this region the FSF laser system behaves in a similar way to conventional optical feedback systems, showing a region of high instability known as the coherence collapse. The differences in the FSF level required to reach this regime observed between the different external cavity configurations are believed to be due to the increase in FSF strength associated with shorter cavity lengths having higher coupling coefficient to the semiconductor laser.

Very high levels of FSF cause the system to be either stable or periodic on a cw baseline depending on the parameters. For high levels of FSF and high injection current the laser becomes stable with a tendency to be emitting on several longitudinal modes. However, close to threshold and for a small range of injection currents, the laser shows periodic oscillations on a cw baseline associated with single longitudinal mode operation. Additionally, preliminary results seem to indicate that in this region the linewidth of the laser broadens up to several GHz. We concluded that the dominant effect on the dynamics of the system seems to be that the FSF strength makes no significant difference between the resonant and non-resonant cases that were observed.

These dynamics were finally compared with those from a conventional optical feedback system. In the latter we found that the coherence collapse regime occurs

over a similar range of feedback levels. Within the coherence collapse region, both systems show similar behavior with dynamics dominated by the external cavity delay and strong multi-mode operation of the laser. At higher feedback levels and injection currents away from the lasing threshold the dynamics are similar in both systems. However, in this region single mode operation is maintained in the COF system. The main difference in the dynamics between the two systems is the presence of a region of periodic oscillations on a cw baseline when the laser operates close to threshold, at high FSF level, in the FSF system. This suggests that the behavior, in the FSF system, that is dominated by the FSF is only observed at low and high FSF levels close to threshold and that FSF does not dominate the dynamics of the system in the coherence collapse region.

The fact that, close to threshold for high levels of FSF, the system shows dynamics similar to those reported in [114] is promising for short pulse generation. The integration in the external cavity of an element that could reduce the effective gain bandwidth of the laser cavity might unlock such dynamics. This could be achieved by using a frequency selective element rather than a high reflectivity mirror to close the external cavity. Three fundamentally different regimes of operation have been identified but more regimes potentially exist in regions of the parameter space not yet accessible with the current setup. Higher FSF levels could be reached by replacing the 50/50 beamsplitter by a 70/30 thus allowing more light to be fed back to the laser. However, the configuration allowing the highest achievable FSF levels is a ring cavity in which the beamsplitter is removed and detection occurs via the zeroth order beam of the AOM. This, along with a frequency selective element, could potentially unlock interesting new dynamics. Nevertheless, at the current stage the maps generated provide new insights into the dynamics of a semiconductor-laser-based FSF system and a great source of information towards the understanding and modeling of such a system.

This thesis adds to the knowledge and understanding of LCSs and FSF systems. The common factor is the possibility of frequency selection and tailoring by adding specific elements in the feedback loop to generate and control dynamics. In the future these two systems could potentially be combined with a view to creating spatial temporal self-localized states, pulsed LCSs.

References

[1] H. Yoshida, Y. Yamashita, M. Kuwabara, and H. Kan, *A 342-nm ultraviolet AlGaN multiple-quantum-well laser diode*, Nature Photonics **2**, 551 (2008).

[2] H. Yoshida *et al.*, *AlGaN-based laser diodes for the short-wavelength ultraviolet region*, New Journal of Physics **11**, 125013 (2009).

[3] J. Faist, *Quantum cascade lasers* (Oxford University Press, England, 2013).

[4] R. Lang and K. Kobayashi, *External optical feedback effects on semiconductor injection laser properties*, IEEE J. Quantum Electron. **16**, 347 (1980).

[5] D. M. Kane and K. A. Shore, *Unlocking dynamical diversity: optical feedback effects on semiconductor lasers* (Wiley, England, 2005).

[6] M. Ito and T. Kimura, *Oscillation properties of AlGaAs DH lasers with an external grating*, Quantum Electronics, IEEE Journal of **16**, 69 (1980).

[7] M. Fleming and A. Mooradian, *Spectral characteristics of external-cavity controlled semiconductor lasers*, Quantum Electronics, IEEE Journal of **17**, 44 (1981).

[8] R. Fox, C. Weimer, L. Hollberg, and G. TuRKt, *The diode laser as a spectroscopic tool*, Spectrochim. Acta Rev. **15**, 291 (1993).

[9] D. O. Caplan, *Laser communication transmitter and receiver design*, Journal of Optical and Fiber Communications Reports **4**, 225 (2007).

[10] P. Zorabedian, W. Trutna, and L. Cutler, *Bistability in grating-tuned external-cavity semiconductor lasers*, Quantum Electronics, IEEE Journal of **23**, 1855 (1987).

[11] M. Giudici, L. Giuggioli, C. Green, and J. Tredicce, *Dynamical behavior of semiconductor lasers with frequency selective optical feedback*, Chaos Solitons and Fractals **10**, 811 (1999).

[12] F. Marino, S. Barland, and S. Balle, *Single-mode operation and transverse-mode control in VCSELs induced by frequency-selective feedback*, IEEE Photon. Technol. Lett. **15**, 789 (2003).

[13] A. Naumenko, N. A. Loiko, M. Sondermann, K. F. Jentsch, and T. Ackemann, *Abrupt turn-on and hysteresis in a VCSEL with frequency-selective optical feedback*, Opt. Commun. **259**, 823 (2006).

[14] G. S. McDonald and W. Firth, *Spatial solitary-wave optical memory*, JOSA B **7**, 1328 (1990).

[15] N. N. Rosanov, *Switching waves, autosolitons, and parallel digital-analogous optical computing*, in *XIV International Conference on Coherent and Nonlinear Optics*, pp. 130–143, International Society for Optics and Photonics, 1992.

[16] W. J. Firth and A. J. Scroggie, *Optical bullet holes: robust controllable localized states of a nonlinear cavity*, Phys. Rev. Lett. **76**, 1623 (1996).

[17] S. Barland *et al.*, *Cavity solitons as pixels in semiconductors*, Nature **419**, 699 (2002).

[18] Y. Tanguy, T. Ackemann, W. J. Firth, and R. Jäger, *Realization of a semiconductor-based cavity soliton laser*, Phys. Rev. Lett. **100**, 013907 (2008).

[19] N. Radwell and T. Ackemann, *Characteristics of laser cavity solitons in a vertical-cavity surface-emitting laser with feedback from a volume Bragg grating*, IEEE J. Quantum Electron. **45**, 1388 (2009).

[20] N. Radwell, *Characteristics of a cavity soliton laser based on a VCSEL with frequency selective feedback*, PhD thesis, The University of Strathclyde, 2010.

[21] D. Cumin and C. P. Unsworth, *Generalising the Kuramoto model for the study of neuronal synchronisation in the brain*, Physica D: Nonlinear Phenomena **226**, 181 (2007).

[22] D. Edmundson and R. Enns, *Robust bistable light bullets*, Optics Letters **17**, 586 (1992).

[23] M. Brambilla, T. Maggipinto, G. Patera, and L. Columbo, *Cavity light bullets: Three-dimensional localized structures in a nonlinear optical resonator*, Physical Review Letters **93**, 203901 (2004).

[24] B. A. Malomed, D. Mihalache, F. Wise, and L. Torner, *Spatiotemporal optical solitons*, Journal of Optics B: Quantum and Semiclassical Optics **7**, R53 (2005).

[25] B. E. Saleh and M. C. Teich, *Fundamentals of Photonics. 2007*.

[26] H. E. Hernández-Figueroa, M. Zamboni-Rached, and E. Recami, *Localized waves* (John Wiley & Sons, 2007).

[27] F. V. Kowalski, J. A. Squier, and J. T. Pinckney, *Pulse generation with an acousto-optic frequency shifter in a passive cavity*, Appl. Phys. Lett. **50**, 711 (1987).

[28] P. I. Richter and T. W. Hansch, *Diode lasers in external cavities with frequency-shifted feedback*, Opt. Commun. **85**, 414 (1991).

[29] I. R. Perry, R. L. Wang, and J. R. M. Barr, *Frequency shifted feedback and frequency comb generation in an Er3+-doped fibre laser*, Opt. Commun. **109**, 187 (1994).

[30] F. V. Kowalski, S. J. Shattil, and P. D. Hale, *Optical pulse generation with a frequency shifted feedback laser*, Appl. Phys. Lett. **53**, 734 (1988).

[31] P. D. Hale and F. V. Kowalski, *Output Characterization of a Frequency Shifted Feedback Laser: Theory and Experiment*, IEEE J. Quantum Electron. **26**, 1845 (1990).

[32] J. M. Sousa and O. G. Okhotnikov, *Short pulse generation and control in Er-doped frequency-shifted-feedback fibre lasers*, Opt. Commun. **183**, 227 (2000).

[33] A. Heidt, J. Burger, J.-N. Maran, and N. Traynor, *High power and high energy ultrashort pulse generation with a frequency shifted feedback fiber laser*, Optics Express **15**, 15892 (2007).

[34] M. P. Nikodem, E. Kluzniak, and K. Abramski, *Wavelength tunability and pulse duration control in frequency shifted feedback Er-doped fiber lasers*, Optics express **17**, 3299 (2009).

[35] L. A. Vazquez-Zuniga and Y. Jeong, *Power-Scalable, Sub-Nanosecond Mode-Locked Erbium-Doped Fiber Laser Based on a Frequency-Shifted-Feedback Ring Cavity Incorporating a Narrow Bandpass Filter*, Journal of the Optical Society of Korea **17**, 177 (2013).

[36] L. A. Jiang, E. P. Ippen, and H. Yokoyama, *Semiconductor mode-locked lasers as pulse sources for high bit rate data transmission*, Journal of Optical and Fiber Communications Reports **2**, 1 (2005).

[37] K. Yvind and J. M. Hvam, *Semiconductor mode-locked lasers for optical communication systems* (Technical University of Denmark, Department of Photonics Engineering, Nanophotonics, 2003).

[38] R. Kaiser and B. Huttl, *Monolithic 40-GHz mode-locked MQW DBR lasers for high-speed optical communication systems*, IEEE Journal of Selected Topics in Quantum Electronics **13**, 125 (2007).

[39] J. P. Toomey and D. M. Kane, *Mapping the dynamic complexity of a semiconductor laser with optical feedback using permutation entropy*, Opt. Express **22**, 1713 (2014).

[40] LaserMarketplace2013, *http://www.laserfocusworld.com/articles/print/volume-49/issue-01/features/laser-marketplace-2013-laser-markets-rise-above-global-headwinds.html*, 2013.

[41] D. A. Neamen and B. Pevzner, *Semiconductor physics and devices: basic principles* (McGraw-Hill New York, 2003).

[42] R. N. Hall, G. E. Fenner, J. D. Kingsley, T. J. Soltys, and R. O. Carlson, *Coherent Light Emission from Ga-As Junctions*, Phys. Rev. Lett **9**, 366 (1962).

[43] N. Holonyak Jr and S. Bevacqua, *Coherent (visible) light emission from Ga (As1- xPx) junctions*, Applied Physics Letters **1**, 82 (1962).

[44] T. Quist *et al.*, *Semiconductor maser of GaAs*, Applied Physics Letters **1**, 91 (1962).

[45] I. Hayashi, M. B. Panish, P. W. Foy, and S. Sumski, *Junction lasers which operate continuously at room temperature*, Applied Physics Letters **17**, 109 (1970).

[46] I. Melngailis, *Longitudinal injection-plasma laser of InSb*, Applied Physics Letters **6**, 59 (1965).

[47] K. Iga, *Surface-emitting laser-its birth and generation of new optoelectronics field*, IEEE Journal of Selected Topics in Quantum Electronics **6**, 1201 (2000).

[48] K. Iga, *Vertical-cavity surface-emitting laser: its conception and evolution*, Japanese Journal of Applied Physics **47**, 1 (2008).

[49] H. Moench and G. Derra, *High Power VCSEL Systems*, Laser Technik Journal **11**, 43 (2014).

[50] R. F. Broom, E. Mohn, C. Risch, and R. Salathe, *Microwave self-modulation of a diode laser coupled to an external cavity*, Quantum Electronics, IEEE Journal of **6**, 328 (1970).

[51] T. Morikawa, Y. Mitsuhashi, J. Shimada, and Y. Kojima, *Return-beam-induced oscillations in self-coupled semiconductor lasers*, Electronics Letters **12**, 435 (1976).

[52] R. W. Tkach and A. R. Chraplyvy, *Regimes of feedback effects in 1.5-µm distributed feedback lasers*, Journal of Lightwave Technology **4**, 1655 (1986).

[53] P. Laurent, A. Clairon, and C. Breant, *Frequency noise analysis of optically self-locked diode lasers*, Quantum Electronics, IEEE Journal of **25**, 1131 (1989).

[54] C. E. Wieman and L. Hollberg, *Using diode lasers for atomic physics*, Review of Scientific Instruments **62**, 1 (1991).

[55] A. Laurent, P. Chanclou, M. Thual, J. Lostec, and M. Gadonna, *Double external cavity laser diode for DWDM applications*, Journal of Optics A: Pure and Applied Optics **2**, L6 (2000).

[56] F. Favre and D. Guen, *Spectral properties of a semiconductor laser coupled to a single mode fiber resonator*, Quantum Electronics, IEEE Journal of **21**, 1937 (1985).

[57] E. Brinkmeyer, W. Brennecke, M. Zürn, and R. Ulrich, *Fibre Bragg reflector for mode selection and line-narrowing of injection lasers*, Electronics Letters **22**, 134 (1986).

[58] M. Kozuma, M. Kourogi, M. Ohtsu, and H. Hori, *Frequency stabilization, linewidth reduction, and fine detuning of a semiconductor laser by using velocity-selective optical pumping of atomic resonance line*, Applied Physics Letters **61**, 1895 (1992).

[59] C. Yan, X. Wang, and J. McInerney, *Multistability in grating-tuned external-cavity semiconductor lasers*, Quantum Electronics, IEEE Journal of **32**, 813 (1996).

[60] A. P. Fischer, O. K. Andersen, M. Yousefi, S. Stolte, and D. Lenstra, *Experimental and theoretical study of filtered optical feedback in a semiconductor laser*, Quantum Electronics, IEEE Journal of **36**, 375 (2000).

[61] A. Naumenko, P. Besnard, N. Loiko, G. Ughetto, and J. Bertreux, *Characteristics of a semiconductor laser coupled with a fiber Bragg grating with arbitrary amount of feedback*, Quantum Electronics, IEEE Journal of **39**, 1216 (2003).

[62] P. Zorabedian, *Axial-mode instability in tunable external-cavity semiconductor lasers*, Quantum Electronics, IEEE Journal of **30**, 1542 (1994).

[63] M. Yousefi and D. Lenstra, *Dynamical behavior of a semiconductor laser with filtered external optical feedback*, Quantum Electronics, IEEE Journal of **35**, 970 (1999).

[64] J. S. Russell, *Report on waves*, in *14th meeting of the British Association for the Advancement of Science*, volume 311, p. 390, 1844.

[65] A. C. Newell, *Solitons in mathematics and physics* (SIAM, 1985).

[66] G. I. Stegeman and M. Segev, *Optical spatial solitons and their interactions: universality and diversity*, Science **286**, 1518 (1999).

[67] M. Segev, *Solitons: a universal phenomenon of self-trapped wave packets*, Opt. & Photon. News **13**, 27 (2002), Introduction to special issue on Solitons.

[68] S. Trillo and W. Torruellas, *Spatial solitons* (Springer, 2001).

[69] W. J. Firth and C. O. Weiss, *Cavity and feedback solitons*, Opt. Photon. News **13**, 54 (2002).

[70] N. Akhmediev and A. Ankiewicz, editors, *Dissipative soliton*Lecture Notes in Physics (Springer, Berlin, 2005).

[71] M. Brambilla, L. A. Lugiato, F. Prati, L. Spinelli, and W. J. Firth, *Spatial soliton pixels in semiconductor devices*, Phys. Rev. Lett. **79**, 2042 (1997).

[72] F. Pedaci *et al.*, *All-optical delay line using semiconductor cavity solitons*, Appl. Phys. Lett. **92**, 011101 (2008).

[73] C. McIntyre, A. M. Yao, G. L. Oppo, F. Prati, and G. Tissoni, *All-optical delay line based on a cavity soliton laser with injection*, Phys. Rev. A **81**, 013838 (2010).

[74] R. Neubecker, G.-L. Oppo, B. Thuering, and T. Tschudi, *Pattern formation in a liquid-crystal light valve with feedback, including polarization, saturation, and internal threshold effects*, Physical Review A **52**, 791 (1995).

[75] W. Lange, T. Ackemann, A. Aumann, E. Buthe, and Y. A. Logvin, *Atomic vapors–A versatile tool in studies of optical pattern formation*, Chaos Solitons and Fractals **10**, 617 (1999).

[76] S. Barbay, R. Kuszelewicz, and J. Tredicce, *Cavity solitons in vcsel devices*, Advances in Optical Technologies **2011**, 628761 (2011).

[77] X. Hachair *et al.*, *Cavity solitons in broad-area vertical-cavity surface-emitting lasers below threshold*, Phys. Rev. A **69**, 043817 (2004).

[78] S. Barbay *et al.*, *Incoherent and coherent writing and erasure of cavity solitons in an optically pumped semiconductor amplifier*, Opt. Lett. **31**, 1504 (2006).

[79] S. Barbay and R. Kuszelewicz, *Physical model for the incoherent writing/erasure of cavity solitons in semiconductor optical amplifiers*, Optics Express **15**, 12457 (2007).

[80] M. Haelterman and G. Vitrant, *Drift instability and spatiotemporal dissipative structures in a nonlinear Fabry-Perot resonator under oblique incidence*, J. Opt. Soc. Am. B **9**, 1563 (1992).

[81] J. P. Seipenbusch, T. Ackemann, B. Schäpers, B. Berge, and W. Lange, *Drift instability and locking behavior of optical patterns*, Phys. Rev. A **56**, R4401 (1997).

[82] A. M. C. Dawes, L. Illing, S. M. Clark, and D. J. Gauthier, *All-Optical Switching in Rubidium Vapor*, Science **308**, 672 (2005).

[83] F. Pedaci, G. Tissoni, S. Barland, M. Giudici, and J. R. Tredicce, *Mapping local defects of extended media using localized structures*, Appl. Phys. Lett. **93**, 111104 (2008).

[84] Z. G. Pan *et al.*, *Optical injection induced polarization bistability in vertical-cavity surface-emitting lasers*, Applied Physics Letters **63**, 2999 (1993).

[85] Y. Hong, K. Shore, A. Larsson, M. Ghisoni, and J. Halonen, *Pure frequency-polarisation bistability in vertical cavity surface-emitting semiconductor laser subject to optical injection*, Electronics Letters **36**, 2019 (2000).

[86] A. Naumenko, N. Loiko, and T. Ackemann, *Analysis of bistability conditions between lasing and nonlasing states for a vertical-cavity surface-emitting laser with frequency-selective optical feedback using an envelope approximation*, Physical Review A **76**, 023802 (2007).

[87] Y. Tanguy, N. Radwell, T. Ackemann, and R. Jäger, *Characteristics of cavity solitons and drifting excitations in broad-area vertical-cavity surface-emitting lasers with frequency-selective feedback*, Phys. Rev. A **78**, 023810 (2008).

[88] P. V. Paulau, D. Gomila, T. Ackemann, N. A. Loiko, and W. J. Firth, *Self-localized structures in vertical-cavity surface-emitting lasers with external feedback*, Phys. Rev. E **78**, 016212 (2008).

[89] K. Rokushima and J. Yamakita, *Analysis of anisotropic dielectric gratings*, JOSA **73**, 901 (1983).

[90] S. Barbay, X. Hachair, T. Elsass, I. Sagnes, and R. Kuszelewicz, *Homoclinic snaking in a semiconductor-based optical system*, Phys. Rev. Lett. **101**, 253902 (2008).

[91] P. Genevet, S. Barland, M. Giudici, and J. R. Tredicce, *Cavity Soliton Laser Based on Mutually Coupled Semiconductor Microresonators*, Phys. Rev. Lett. **101**, 123905 (2008).

[92] P. Genevet, B. Barland, M. Giudici, and J. R. Tredicce, *Stationary localized structures and pulsing structures in a cavity soliton laser*, Phys. Rev. A **79**, 033819 (2009).

[93] C. Harder, K. Lau, and A. Yariv, *Bistability and pulsations in cw semiconductor lasers with a controlled amount of saturable absorption*, Applied Physics Letters **39**, 382 (1981).

[94] C. Harder, K. Y. Lau, and A. Yariv, *Bistability and pulsations in semiconductor lasers with inhomogeneous current injection*, Quantum Electronics, IEEE Journal of **18**, 1351 (1982).

[95] T. Elsass *et al.*, *Control of cavity solitons and dynamical states in a monolithic vertical cavity laser with saturable absorber*, The European Physical Journal D **59**, 91 (2010).

[96] T. Elsass *et al.*, *Fast manipulation of laser localized structures in a monolithic vertical cavity with saturable absorber*, Appl. Phys. B **98**, 327 (2010).

[97] F. V. Kowalski, P. D. Hale, and S. J. Shattil, *Broadband continuous-wave laser*, Opt. Lett. **13**, 622 (1988).

[98] S. Balle, I. Littler, K. Bergmann, and F. V. Kowalski, *Frequency Shifted Feedback Dye Laser Operating at a Small Shift Frequency*, Optics Comm. **102**, 166 (1993).

[99] I. Littler, S. Balle, and K. Bergmann, *The CW modeless laser: Spectral control, performance data and build-up dynamics*, Opt. Commun. **88**, 514 (1992).

[100] D. J. Taylor, S. E. Harris, S. T. K. Nieh, and T. W. Hansch, *Electronic Tuning of a Dye Laser Using the AcoustoOptic Filter*, Appl. Phys. Lett. **19**, 269 (1971).

[101] G. L. Bourdet, R. A. Muller, G. M. Mullot, and J.-Y. Vinet, *Short pulse generation by use of an active multipass interferometer*, IEEE Journal of Quantum Electronics **24**, 580 (1988).

[102] I. Littler and J. H. Eschner, *The cw modeless laser: model calculations of an active frequency shifted feedback cavity*, Opt. Commun. **87**, 44 (1992).

[103] A. P. Willis, A. I. Ferguson, and D. M. Kane, *External cavity laser diodes with frequency-shifted feedback*, Opt. Commun. **116**, 87 (1995).

[104] K. W. Benoist, *The Influence of External Frequency Shifted Feedback on a DFB Semiconductor Laser*, IEEE P. Techn. Lett. **8**, 25 (1996).

[105] I. Littler and K. Bergmann, *Generation of multi-frequency laser emission using an active frequency shifted feedback cavity*, Opt. Commun. **88**, 524 (1992).

[106] J. R. M. Barr, G. Y. Liang, and M. W. Phillips, *Accurate optical frequency-interval measurement by use of nonresonant frequency comb generation*, Optics Letters **18**, 1010 (1993).

[107] S. K. Kim, M. J. Chu, and J. H. Lee, *Wideband multiwavelength erbium-doped fiber ring laser with frequency shifted feedback*, Opt. Commun. **190**, 291 (2001).

[108] J.-N. Maran, S. LaRochelle, and P. Besnard, *C-band multi-wavelength frequency-shifted erbium-doped fiber laser*, Opt. Commun. **218**, 81 (2003).

[109] S.-U. Alam and A. Grudinin, *Tunable picosecond frequency-shifted feedback fiber laser at 1550 nm*, Photonics Technology Letters, IEEE **16**, 2012 (2004).

[110] V. Ogurtsov *et al.*, *Experimental characterization of an Yb3+-doped fiber ring laser with frequency-shifted feedback*, Opt. Commun. **266**, 627 (2006).

[111] H. Y. Ryu, H. S. Moon, and H. S. Suh, *Optical frequency comb generator based on actively mode-locked fiber ring laser using an acousto-optic modulator with injection-seeding*, Optics Express **15**, 11396 (2007).

[112] L. A. Vazquez-Zuniga and Y. Jeong, *Study of a mode-locked erbium-doped frequency-shifted-feedback fiber laser incorporating a broad bandpass filter: Experimental results*, Optics Communications **306**, 1 (2013).

[113] L. A. Vazquez-Zuniga and Y. Jeong, *Study of a mode-locked erbium-doped frequency-shifted-feedback fiber laser incorporating a broad bandpass filter: Numerical results*, Optics Communications **322**, 54 (2014).

[114] G. Bonnet, S. Balle, T. Kraft, and K. Bergmann, *Dynamics and self-modelocking of a titanium-sapphire laser with intracavity frequency shifted feedback*, Opt. Commun. **123**, 790 (1996).

[115] M. Stellpflug, G. Bonnet, B. W. Shore, and K. Bergmann, *Dynamics of frequency shifted feedback lasers: simulation studies*, Opt. Express **11**, 2060 (2003).

[116] K. Nakamura, T. Miyahara, and H. Ito, *Observation of a highly phase-correlated chirped frequency comb output from a frequency-shifted feedback laser*, Appl. Phys. Lett. **72**, 2631 (1998).

[117] K. Kasahara, K. Nakamura, M. Sato, and H. Ito, *Dynamic properties of an all solid-state frequency-shifted feedback laser*, IEEE J. Quantum Electron. **34**, 190 (1998).

[118] K. Nakamura, K. Kasahara, M. Sato, and H. Ito, *Interferometric studies on a diode-pumped Nd:YVO, laser with frequency-shifted feedback*, Opt. Commun. **121**, 137 (1995).

[119] K. Nakamura *et al.*, *Spectral Characteristics of an All Solid-state Frequency-Shifted Feedback Laser*, IEEE J. Quantum Electron. **33**, 103 (1997).

[120] F. V. Kowalski, K. Nakamura, and H. Ito, *Frequency shifted feedback lasers: continuous or stepwise frequency chirped output?*, Opt. Commun. **147**, 103 (1998).

[121] H. Guillet de Chatellus, E. Lacot, W. Glastre, O. Jacquin, and O. Hugon, *The hypothesis of the moving comb in frequency shifted feedback lasers*, Opt. Commun. **284**, 4965 (2011).

[122] R. G. Smith, *Use of the Acoustooptic Light Deflector as an Optical Isolator*, IEEE J. Quantum Electron. **9**, 545 (1973).

[123] B. Furch, A. L. Scholtz, and W. R. Leeb, *Isolation and frequency conversion properties of acoustooptic modulators*, Applied Optics **21**, 2344 (1982).

[124] M. J. Lim, C. I. Sukenik, T. H. Stievater, P. H. Bucksbaum, and R. S. Conti, *Improved design of a frequency-shifted feedback diode laser for optical pumping at high magnetic field*, Opt. Commun. **147**, 99 (1998).

[125] J.-N. Maran, R. Slavk, S. LaRochelle, and M. Karasek, *Chromatic Dispersion Measurement Using a Multiwavelength Frequency-Shifted Feedback Fiber Laser*, IEEE Transaction on Instrum. and Measurment **53**, 67 (2004).

[126] L. Cohen, *Comparison of single-mode fiber dispersion measurement techniques*, Journal of Lightwave Technology **3**, 958 (1985).

[127] S. Ryu, Y. Horiuchi, and K. Mochizuki, *Novel chromatic dispersion measurement method over continuous gigahertz tuning range*, Journal of Lightwave Technology **7**, 1177 (1989).

[128] M. Froggatt, *Distributed measurement of the complex modulation of a photoinduced Bragg grating in an optical fiber*, Applied Optics **35**, 5162 (1996).

[129] J. Von Der Weid, R. Passy, G. Mussi, and N. Gisin, *On the characterization of optical fiber network components with optical frequency domain reflectometry*, Journal of Lightwave Technology **15**, 1131 (1997).

[130] S. Yun, G. Tearney, J. de Boer, N. Iftimia, and B. Bouma, *High-speed optical frequency-domain imaging*, Optics Express **11**, 2953 (2003).

[131] M. Froggatt and J. Moore, *High-spatial-resolution distributed strain measurement in optical fiber with Rayleigh scatter*, Applied Optics **37**, 1735 (1998).

[132] D. Uttam and B. Culshaw, *Precision time domain reflectometry in optical fiber systems using a frequency modulated continuous wave ranging technique*, Journal of Lightwave Technology **3**, 971 (1985).

[133] H. Barfuss and E. Brinkmeyer, *Modified optical frequency domain reflectometry with high spatial resolution for components of integrated optic systems*, Journal of Lightwave Technology **7**, 3 (1989).

[134] R. Passy, N. Gisin, J.-P. Von der Weid, and H. Gilgen, *Experimental and theoretical investigations of coherent OFDR with semiconductor laser sources*, Journal of Lightwave Technology **12**, 1622 (1994).

[135] R. Passy, N. Gisin, and J. Von der Weid, *High-sensitivity-coherent optical frequency-domain reflectometry for characterization of fiber-optic network components*, IEEE Photonics Technology Letters **7**, 667 (1995).

[136] G. Mussi, N. Gisin, R. Passy, and J. Von der Weid, *–152.5 dB sensitivity high dynamic-range optical frequency-domain reflectometry*, Electronics Letters **32**, 926 (1996).

[137] B. Golubovic, B. Bouma, G. Tearney, and J. Fujimoto, *Optical frequency-domain reflectometry using rapid wavelength tuning of a Cr4+:forsterite laser*, Optics Letters **22**, 1704 (1997).

[138] B. Huttner, J. Reecht, N. Gisin, R. Passy, and J. Von der Weid, *Local birefringence measurements in single-mode fibers with coherent optical frequency-domain reflectometry*, Photonics Technology Letters, IEEE **10**, 1458 (1998).

[139] U. Glombitza and E. Brinkmeyer, *Coherent frequency-domain reflectometry for characterization of single-mode integrated-optical waveguides*, Journal of Lightwave Technology **11**, 1377 (1993).

[140] S. Chinn, E. Swanson, and J. Fujimoto, *Optical coherence tomography using a frequency-tunable optical source*, Optics Letters **22**, 340 (1997).

[141] K. Nakamura, T. Miyahara, M. Yoshida, T. Hara, and H. Ito, *A new technique of optical ranging by a frequency-shifted feedback laser*, Photonics Technology Letters, IEEE **10**, 1772 (1998).

[142] K. Nakamura, T. Hara, M. Yoshida, T. Miyahara, and H. Ito, *Optical Frequency Domain Ranging by a Frequency-Shifted Feedback Laser*, IEEE J. Quantum Electron. **36**, 305 (2000).

[143] M. Yoshida, K. Nakamura, T. Miyahara, and H. Ito, *Erbium-doped fiber laser with a frequency-shifted feedback; Oscillation characteristicds and application to reflectometry*, in *Tech. Dig. CLEO*, p. 157, 1998.

[144] L. P. Yatsenko, B. W. Shore, and K. Bergmann, *Ranging and interferometry with a frequency shifted feedback laser*, Opt. Commun. **242**, 581 (2004).

[145] V. V. Ogurtsov *et al.*, *High accuracy ranging with Yb3+-doped fiber-ring frequency-shifted feedback laser with phase-modulated seed*, Opt. Commun. **266**, 266 (2006).

[146] J. Paul, Y. Hong, P. S. Spencer, I. Pierce, and K. A. Shore, *Optical frequency-domain ranging using a frequencyshifted feedback distributed-feedback laser*, IET Optoelectron. **1**, 277 (2007).

[147] J. Paul, Y. Hong, P. S. Spencer, I. Pierce, and K. A. Shore, *Simple and Accurate Optical Frequency Domain Ranging Using Off-the-Shelf DFB Lasers Subject to Frequency-Shifted Optical Feedback*, IEEE P. Techn. Lett. **19**, 1708 (2007).

[148] V. V. Ogurtsov *et al.*, *An all-fiber frequency-shifted feedback laser for optical ranging; signal variation with distance*, Opt. Commun. **281**, 1679 (2008).

[149] L. P. Yatsenko, B. W. Shore, and K. Bergmann, *An intuitive picture of the physics underlying optical ranging using frequency shifted feedback lasers seeded by a phase-modulated field*, Opt. Commun. **282**, 2212 (2009).

[150] L. P. Yatsenko, B. W. Shore, and K. Bergmann, *Coherence in the output spectrum of frequency shifted feedback lasers*, Opt. Commun. **282**, 300 (2009).

[151] J. P. Pique, *Pulsed frequency shifted feedback laser for accurate long distance measurements: Beat order determination*, Opt. Commun. **286**, 233 (2013).

[152] C. Bandt and B. Pompe, *Permutation entropy: a natural complexity measure for time series*, Physical Review Letters **88**, 174102 (2002).

[153] M. Grabherr *et al.*, *Bottom-emitting VCSELs for high-CW optical output power*, IEEE Photon. Technol. Lett. **10**, 1061 (1998).

[154] M. Grabherr *et al.*, *High-Power VCSEL's: Single Devices and Densely Packed 2-D-Arrays*, IEEE J. Sel. Top. Quantum Electron. **5**, 495 (1999).

[155] M. Schulz-Ruhtenberg, Y. Tanguy, K. F. Huang, R. Jäger, and T. Ackemann, *Control of the spatial emission structure of broad-area vertical-cavity surface emitting lasers by feedback*, J. Phys. D: Appl Phys. **42**, 055101 (2009).

[156] E. Averlant, M. Tlidi, H. Thienpont, T. Ackemann, and K. Panajotov, *Experimental observation of localized structures in medium size VCSELs*, Optics Express **22**, 762 (2014).

[157] M. Schulz-Ruhtenberg, Y. Tanguy, R. Jäger, and T. Ackemann, *Length scales and polarization properties of annular standing waves in circular broad-area vertical-cavity surface-emitting lasers*, Appl. Phys. B **97**, 397 (2009).

[158] Optigrate, 2010, OptiGrate Corp, 3267 Progress Drive, Orlando, Florida 32826.

[159] I. V. Ciapurin, V. I. Smirnov, and L. B. Glebov, *Modeling of phase volume diffractive gratings, part 1: transmitting sinusoidal uniform gratings*, Optical Engineering **45**, 015802 (2006).

[160] P. Genevet, S. Barland, M. Giudici, and J. R. Tredicce, *Bistable and addressable localized vortices in semiconductor lasers*, Phys. Rev. Lett. **104**, 223902 (2010).

[161] J. Jimenez, Y. Noblet, P. V. Paulau, D. Gomila, and T. Ackemann, *Observation of laser vortex solitons in a self-focusing semiconductor laser*, Journal of Optics **15**, 044011 (2013).

[162] T. Ackemann and W. J. Firth, *Dissipative Solitons in Pattern-forming Nonlinear Optical Systems: Cavity Solitons and Feedback Solitons*, in *Dissipative solitons*, edited by N. Akhmediev and A. Ankiewicz, volume 661 of *Lecture Notes in Physics*, pp. 55–100, Springer, Berlin, 2005.

[163] N. Radwell *et al.*, *Switching spatial dissipative solitons in a VCSEL with frequency selective feedback*, The European Physical Journal D **59**, 121 (2010).

[164] N. N. Rosanov, *Switching waves, autosolitons, and parallel digital-analogous optical computing*, Proc. SPIE **1840**, 130 (1991).

[165] B. L. Volodin *et al.*, *Wavelength stabilization and spectrum narrowing of high-power multimode laser diodes and arrays by use of volume Bragg gratings*, Opt. Lett. **29**, 1891 (2004).

[166] M. Maiwald *et al.*, *Wavelength-Stabilized Compact Diode Laser System on a Microoptical Bench With 1.5-W Optical Output Power at 671 nm*, IEEE Photon. Tech. Lett. **20**, 1627 (2008).

[167] F. Kroeger, I. Breunig, and K. Buse, *Frequency stabilization and output power undulations of diode lasers with feedback by volume holographic gratings*, Appl. Phys. B **95**, 603608 (2009).

[168] Y. K. Chembo, S. K. Mandre, I. Fischer, W. Elsäßer, and P. Colet, *Controlling the emission properties of multimode vertical-cavity surface-emitting lasers via polarization and frequency-selective feedback*, Phys. Rev. A **79**, 013817 (2009).

[169] T. Ackemann, G.-L. Oppo, and W. J. Firth, *Fundamentals and Applications of Spatial Dissipative Solitons in Photonic Devices*, Adv. Atom. Mol. Opt. Phys. **57**, 323 (2009).

[170] M. Nixon *et al.*, *Synchronized Cluster Formation in Coupled Laser Networks*, Phys. Rev. Lett. **106**, 223901 (2011).

[171] M. Nixon, E. Ronen, and A. A. Friesem, *Geometric Frustration in Large Arrays of Coupled Lasers*, in *Frontiers in Optics*, p. FWAA2, Optical Society of America, 2011.

[172] P. V. Paulau *et al.*, *Adler synchronization of spatial laser solitons pinned by defects*, Phys. Rev. Lett. **108**, 213904 (2012).

[173] M. Schulz-Ruhtenberg, I. Babushkin, N. A. Loiko, T. Ackemann, and K. F. Huang, *Transverse patterns and length-scale selection in vertical-cavity surface-emitting lasers with a large square aperture*, Appl. Phys. B **81**, 945 (2005).

[174] J. Collins and A. Stuart, *Lens-system diffraction integral written in terms of matrix optics*, JOSA **60**, 1168 (1970).

[175] H. Q. Hou *et al.*, *Highly uniform and reproducible vertical-cavity surface-emitting lasers grown by metalorganic vapor phase epitaxy with in situ reflectometry*, IEEE Photon. Tech. Lett. **8**, 1285 (1996).

[176] M. Gurioli *et al.*, *Weak Localization of Light in a Disordered Microcavity*, Phys. Rev. Lett. **94**, 183901 (2005).

[177] H. Pier and E. Kapon, *Photon localization in lattices of coupled vertical-cavity surface-emitting lasers with dimensionalities between one and two*, Opt. Lett. **22**, 546 (1997).

[178] L. D. A. Lundeberg, G. P. Lousberg, D. L. Boiko, and E. Kapon, *Spatial coherence measurements in arrays of coupled vertical cavity surface emitting lasers*, Appl. Phys. Lett. **90**, 021103 (2007).

[179] S. Hegarty, G. Huyet, J. G. McInerney, and K. D. Choquette, *Pattern formation in the transverse section of a laser with a large Fresnel number*, Phys. Rev. Lett. **82**, 1434 (1999).

[180] I. Babushkin, M. Schulz-Ruhtenberg, N. A. Loiko, K. F. Huang, and T. Ackemann, *Coupling of polarization and spatial degrees of freedom of highly divergent emission in broad-area square vertical-cavity surface-emitting lasers*, Phys. Rev. Lett. **100**, 213901 (2008).

[181] J. Kasprzak *et al.*, *BoseEinstein condensation of exciton polaritons*, Nature **443**, 409 (2006).

[182] D. Sanvitto *et al.*, *Spatial structure and stability of the macroscopically occupied polariton state in the microcavity optical parametric oscillator*, Phys. Rev. B **73**, 241308(R) (2006).

[183] R. Kuszelewicz, I. Ganne, I. Sagnes, and G. Slekys, *Optical self-organization in bulk and multiquantum well GaAlAs microresonators*, Phys. Rev. Lett. **84**, 6006 (2000).

[184] T. Ackemann *et al.*, *Spatial mode structure of bottom-emitting broad-area vertical-cavity surface-emitting lasers*, J. Opt. B: Quantum Semiclass. Opt. **2**, 406 (2000).

[185] S. Barland, O. Piro, M. Giudici, J. R. Tredicce, and S. Balle, *Experimental evidence of van der Pol -Fitzhugh -Nagumo dynamics in semiconductor optical amplifiers*, Phys. Rev. E **68**, 036209 (2003).

[186] J. L. Oudar, R. Kuszelewicz, B. G. Sfez, J. C. Michel, and R. Planel, *Prospects for further threshold reduction in bistable microresonators*, Opt. Quantum Elect. **24**, S193 (1992).

[187] D. I. Babic and S. W. Corzine, *Analytic expression for the reflection delay, penetration depth, and adsorptance of quarter-wave dielectric mirrors*, IEEE J. Quantum Electron. **28**, 514 (1992).

[188] J.-P. Weber, K. Malloy, and S. Wang, *Effects of layer thickness variations on vertical-cavity surface-emitting DBR semiconductor lasers*, IEEE Photon. Tech. Lett. **2**, 162 (1990).

[189] L. Spinelli, G. Tissoni, M. Brambilla, F. Prati, and L. A. Lugiato, *Spatial solitons in semiconductor microcavities*, Phys. Rev. A **58**, 2542 (1998).

[190] S. Barland, F. Marino, M. Giudici, J. Tredicce, and S. Balle, *In situ measurement of cavity length variation across the transverse section of broad-area vertical-cavity surface-emitting lasers*, Appl. Phys. Lett. **83**, 2303 (2003).

[191] R. Michalzik, M. Grabherr, and K. J. Ebeling, *High-power VCSELs: Modeling and experimental characterization*, Proc. SPIE **3286**, 206 (1998).

[192] L. A. Coldren and S. W. Corzine, *Diode Lasers and Photonic Integrated Circuits* (Wiley, New York, 1995).

[193] N. Radwell, P. Rose, C. Cleff, C. Denz, and T. Ackemann, *Compensation of spatial inhomogeneities in a cavity soliton laser using a spatial light modulator*, Opt. Exp. **18**, 23121 (2010).

[194] T. Ackemann, N. Radwell, Y. Noblet, and R. Jäger, *Disorder mapping in VCSELs using frequency-selective feedback*, Optics Letters **37**, 1079 (2012).

[195] R. Adler, *A Study of Locking Phenomena in Oscillators*, Proc. IRE **34**, 351 (1946).

[196] H. Haken, *A nonlinear theory of laser noise and coherence*, Zeitschrift fur Physik **181**, 96 (1964).

[197] J. W. Crowe and W. E. Ahearn, *External cavity coupling and phase locking of gallium arsenide injection lasers*, IEEE J. Quantum Electron. **4**, 169 (1968).

[198] Z. Jiang and M. McCall, *A Theoretical Study of Coupled Laser Systems*, J. Mod. Opt. **39**, 159 (1992).

[199] L. Fabiny, P. Colet, R. Roy, and D. Lenstra, *Coherence and phase dynamics of spatially coupled solid-state lasers*, Physical Review A **47**, 4287 (1993).

[200] M. Möller, B. Forsmann, and W. Lange, *Amplitude instability in coupled Nd:YVO₄ microchip lasers*, Chaos, Solitons & Fractals **10**, 825 (1999).

[201] Y. Kuramoto, *Self-entrainment of a population of coupled non-linear oscillators*, in *International symposium on mathematical problems in theoretical physics*, pp. 420–422, Springer, 1975.

[202] S. H. Strogatz, *From Kuramoto to Crawford: exploring the onset of synchronization in populations of coupled oscillators*, Physica D: Nonlinear Phenomena **143**, 1 (2000).

[203] A. Pikovsky, M. Rosenblum, and J. Kurths, *Synchronization - A universal concept in nonlinear sciences* volume 12 of *Cambridge Nonlinear Science Series* (Cambridge University Press, Cambridge, 2001).

[204] C. J. Buczek, R. J. Freiberg, and M. L. Skolnick, *Laser injection locking*, Proceedings of the IEEE **61**, 1411 (1973).

[205] P. Coullet, D. Daboussy, and J. R. Tredicce, *Optical excitable waves*, Phys. Rev. E **58**, 5347 (1998).

[206] D. Goulding *et al.*, *Excitability in a quantum dot semiconductor laser with optical injection*, Physical Review Letters **98**, 153903 (2007).

[207] J. Thévenin, M. Romanelli, M. Vallet, M. Brunel, and T. Erneux, *Resonance assisted synchronization of coupled oscillators: frequency locking without phase locking*, Physical Review Letters **107**, 104101 (2011).

[208] S. H. Strogatz and I. Stewart, *Coupled oscillators and biological synchronization*, Scientific American **269**, 102 (1993).

[209] D. C. Michaels, E. P. Matyas, and J. Jalife, *Mechanisms of sinoatrial pacemaker synchronization: a new hypothesis.*, Circulation Research **61**, 704 (1987).

[210] T. J. Walker, *Acoustic synchrony: two mechanisms in the snowy tree cricket*, Science **166**, 891 (1969).

[211] J. Garcia-Ojalvo, M. B. Elowitz, and S. H. Strogatz, *Modeling a synthetic multicellular clock: repressilators coupled by quorum sensing*, Proceedings of the National Academy of Sciences of the United States of America **101**, 10955 (2004).

[212] S. H. Strogatz, D. M. Abrams, A. McRobie, B. Eckhardt, and E. Ott, *Theoretical mechanics: Crowd synchrony on the Millennium Bridge*, Nature **438**, 43 (2005).

[213] K. Shockley, M.-V. Santana, and C. A. Fowler, *Mutual interpersonal postural constraints are involved in cooperative conversation.*, Journal of Experimental Psychology: Human Perception and Performance **29**, 326 (2003).

[214] K. Shockley, A. A. Baker, M. J. Richardson, and C. A. Fowler, *Articulatory constraints on interpersonal postural coordination.*, Journal of Experimental Psychology: Human Perception and Performance **33**, 201 (2007).

[215] A. Z. Zivotofsky and J. M. Hausdorff, *The sensory feedback mechanisms enabling couples to walk synchronously: An initial investigation*, Journal of Neuroengineering and Rehabilitation **4**, 28 (2007).

[216] N. R. van Ulzen, C. J. Lamoth, A. Daffertshofer, G. R. Semin, and P. J. Beek, *Characteristics of instructed and uninstructed interpersonal coordination while walking side-by-side*, Neuroscience Letters **432**, 88 (2008).

[217] J. N. Cappella and S. Planalp, *Talk and silence sequences in informal conversations III: Interspeaker influence*, Human Communication Research **7**, 117 (1981).

[218] M. M. Louwerse, R. Dale, E. G. Bard, and P. Jeuniaux, *Behavior matching in multimodal communication is synchronized*, Cognitive Science **36**, 1404 (2012).

[219] J. J. Raftery *et al.*, *In-phase evanescent coupling of two-dimensional arrays of defect cavities in photonic crystal vertical cavity surface emitting lasers*, Appl. Phys. Lett. **89**, 081119 (2006).

[220] R. A. York and R. C. Compton, *Quasi-optical power combining using mutually synchronized oscillator arrays*, Microwave Theory and Techniques, IEEE Transactions on **39**, 1000 (1991).

[221] P. Colet and R. Roy, *Digital communication with synchronized chaotic lasers*, Optics Letters **19**, 2056 (1994).

[222] G. D. VanWiggeren and R. Roy, *Communication with chaotic lasers*, Science **279**, 1198 (1998).

[223] A. Argyris *et al.*, *Chaos-based communications at high bit rates using commercial fibre-optic links*, Nature **438**, 343 (2005).

[224] Y. Tanguy, T. Ackemann, and R. Jäger, *Characteristics of switching dynamics in a semiconductor-based cavity-soliton laser*, Optics Express **15**, 16773 (2007).

[225] C. McIntyre, *Dynamics and interactions of cavity solitons in photonic devices*, PhD thesis, The University of Strathclyde, 2013.

[226] A. J. Scroggie, W. J. Firth, and G.-L. Oppo, *Cavity Soliton Laser with Frequency Selective Feedback*, Phys. Rev. A **80**, 013829 (2009).

[227] M. Giudici, S. Balle, T. Ackemann, S. Barland, and J. R. Tredicce, *Effects of Optical Feedback on Vertical-Cavity Surface-Emitting Lasers: Experiment and Model*, J. Opt. Soc. Am. B **16**, 2114 (1999).

[228] P. V. Paulau, D. Gomila, P. Colet, B. A. Malomed, and W. J. Firth, *From one-to two-dimensional solitons in the Ginzburg-Landau model of lasers with frequency-selective feedback*, Physical Review E **84**, 036213 (2011).

[229] P. Grelu and N. Akhmediev, *Dissipative solitons for mode-locked lasers*, Nature Photonics **6**, 84 (2012).

[230] D. Maydan, *Acoustooptical Pulse Modulators*, IEEE J. Quantum Electron. **6**, 15 (1970).

[231] G. N. Gibson, R. Klank, F. Gibson, and B. E. Bouma, *Electro-optically cavity-dumped ultrashort-pulse Ti: sapphire oscillator*, Optics Letters **21**, 1055 (1996).

[232] M. Hofer, M. E. Fermann, F. Haberl, M. H. Ober, and A. J. Schmidt, *Mode locking with cross-phase and self-phase modulation*, Optics Letters **16**, 502 (1991).

[233] R. G. Driggers, *Encyclopedia of optical engineering* (CRC press, 2003).

[234] J. M. Lawrence and D. M. Kane, *Influence of the angular alignment of the optical feedback field on external cavity diode laser characteristics*, Opt. Commun. **159**, 316 (1999).

[235] K. F. Jentsch, M. Sondermann, and T. Ackemann, *Analysis and optimization of coupling to external cavities in feedback experiments with vertical-cavity surface-emitting lasers*, Opt. Commun. **281**, 1396 (2008).

[236] J. L. Saltich, *An Optical Spectrum Analyzer* (University of Illinois at Urbana-Champaign, USA, 1967).

[237] G. Hernndez, *Fabry-Perot Interferometers* (Cambridge University Press, England, 1988).

[238] J. Sacher, D. Baums, P. Panknin, W. Elssser, and E. O. Gbel, *Intensity instabilities of semiconductor lasers under current modulation, external light injection, and delayed feedback*, Phys. Rev. E **45**, 1893 (1992).

[239] P. Besnard, B. Meziane, and G. M. Stephan, *Feedback phenomena in a semiconductor laser induced by distant reflectors*, IEEE J. Quantum Electron. **29**, 1271 (1993).

[240] J. P. Toomey, D. M. Kane, M. W. Lee, and K. A. Shore, *Nonlinear dynamics of semiconductor lasers with feedback and modulation*, Opt. Express **18**, 16955 (2010).

[241] C. Voumard, *External-cavity-controlled 32-MHz narrow-band cw GaAlAs-diode lasers*, Optics Letters **1**, 61 (1977).

[242] C. Risch, C. Voumard, F. K. Reinhart, and R. Salathe, *External-cavity-induced nonlinearities in the light versus current characteristic of (Ga, Al)*

As continuous-wave diode lasers, IEEE J. Quantum Electron. **13**, 692 (1977).

[243] I. Littler, S. Balle, and K. Bergmann, *Continuous-wave laser without frequency-domain-mode structure: investigation of emission properties and buildup dynamics,* J. Opt. Soc. Am. B **8**, 1412 (1991).

[244] G. L. Bourdet, *Short-pulse generation at 10 µm in an active cw-injected ring laser cavity,* Applied Optics **42**, 5457 (2003).

[245] A. Yoshizawa and H. Tsuchida, *Chirped-comb generation in frequency-shifted feedback laser diodes with a large frequency shift,* Opt. Commun. **155**, 51 (1998).

[246] L. P. Yatsenko, B. W. Shore, and K. Bergmann, *Theory of a frequency-shifted feedback laser,* Opt. Commun. **236**, 183 (2004).

[247] M. Yoshida, K. Nakamura, and H. Ito, *A New Method for Measurement of Group Velocity Dispersion of Optical Fibers by Using a Frequency-Shifted Feedback Fiber Laser,* IEEE P. Techn. Lett. **13**, 227 (2001).

[248] P. Saltz and W. Streifer, *Transient analysis of an electronically tunable dye laser-Part I: Simulation study,* IEEE J. Quantum Electron. **8**, 893 (1972).

[249] W. Streifer and P. Saltz, *Transient analysis of an electronically tunable dye laser-part II: Analytic study,* IEEE J. Quantum Electron. **9**, 563 (1973).

[250] W. Streifer and J. R. Whinnery, *Analysis of a dye Laser Tuned by Acousto-Optic Filter,* Applied Physics Letters **17**, 335 (1970).

[251] J. Martin, Y. Zhao, S. Balle, K. Bergmann, and M. P. Fewell, *Visible-wavelength diode laser with weak frequency-shifted optical feedback,* Opt. Commun. **112**, 109 (1994).

[252] K. A. Shore and D. M. Kane, *Comb generation bandwidth for frequency-shifted feedback semiconductor lasers,* IEEE J. Quantum Electron. **35**, 1053 (1999).

[253] D. Lenstra, B. Verbeek, and A. Den Boef, *Coherence collapse in single-mode semiconductor lasers due to optical feedback*, IEEE J. Quantum Electron. **21**, 674 (1985).

[254] C. E. Shannon, *A note on the concept of entropy*, Bell System Tech. J **27**, 379 (1948).

[255] H. Kantz and T. Schreiber, *Nonlinear time series analysis* (Cambridge university press, 2004).

[256] Y. Cao, W. Tung, J. B. Gao, V. A. Protopopescu, and L. M. Hively, *Detecting dynamical changes in time series using the permutation entropy*, Physical Review E **70**, 046217 (2004).

[257] M. Staniek and K. Lehnertz, *Parameter selection for permutation entropy measurements*, International Journal of Bifurcation and Chaos **17**, 3729 (2007).

[258] E. A. Avrutin, J. H. Marsh, and E. L. Portnoi, *Monolithic and multi-GigaHertz mode-locked semiconductor lasers: Constructions, experiments, models and applications*, IEE Proceedings-Optoelectronics **147**, 251 (2000).

[259] M. Yousefi *et al.*, *New role for nonlinear dynamics and chaos in integrated semiconductor laser technology*, Physical Review Letters **98**, 044101 (2007).

[260] S. Sato and M. Kawasaki, *Wide spectral width of frequency-shifted-feedback semiconductor laser*, in *ROMOPTO 2003: Seventh Conference on Optics*, pp. 90–97, International Society for Optics and Photonics, 2004.

[261] K. A. Shore and D. M. Kane, *Optimum modulation frequency for FM seeded FSF laser ranging*, in *Optoelectronics, IEE Proceedings*, volume 153, pp. 284–286, IET, 2006.

[262] S. Balle and K. Bergmann, *Self-pulsing and instabilities in a unidirectional ring dye laser with intracavity frequency shift*, Opt. Commun. **116**, 136 (1995).

[263] H. Guillet de Chatellus *et al.*, *Generation of ultrahigh and tunable repetition rates in CW injection-seeded frequency-shifted feedback lasers*, Optics Express **21**, 15065 (2013).

[264] M. Nixon *et al.*, *Controlling synchronization in large laser networks*, Physical Review Letters **108**, 214101 (2012).